MASARYKOVA UNIVERZITA
PŘÍRODOVĚDECKÁ FAKULTA
ÚSTAV TEORETICKÉ FYZIKY A ASTROFYZIKY

Magnetohydrodynamické vlny a oscilace ve sluneční koróně

HABILITAČNÍ PRÁCE

Obor: Teoretická fyzika a astrofyzika

Petr Jelínek

Brno 2017

Abstract This habilitation thesis is devoted to studies of waves and oscillations in solar corona. Waves and oscillations in solar corona are currently very topical, because different types of waves and oscillations are observed using the probes and satellites within the solar atmosphere. In this thesis the results obtained mainly by numerical simulations of magnetohydrodynamics (MHD) are presented. In several cases, these results are confirmed by direct ground-based observations, mainly using the solar radiotelescope RT5 of the solar physics department of Astronomical Institute of Academy of Sciences of the Czech Republic in Ondřejov. We present the results from our own numerical simulations in different coronal structures, for example simple magnetic slabs, neutral (Harris) current-sheet or opened magnetic structures. Such studies are very important for the understanding of wave processes taking place in the solar atmosphere, because they could help us to clarify not yet fully understood and explained problem of solar corona heating. This thesis consist of three main parts as follows: introduction to the problem of waves and oscillations in solar atmosphere, commented collection of author's papers and finally, enclosed papers as published in journals.

Abstrakt Předložená habilitační práce se věnuje studiu vln a oscilací ve sluneční koróně. Téma vln a oscilací ve sluneční koróně je v současné době velice aktuální, neboť různé typy vln a oscilací jsou přímo ve sluneční atmosféře pozorovány pomocí družic. V předložené práci jsou popsány výsledky, získané především numerickým řešením rovnic magnetohydrodynamiky (MHD), které jsou v několika případech potvrzené i přímými pozorováními, zejména pomocí radioteleskopu RT5 slunečního oddělení AsÚ AV ČR v Ondřejově. Jsou zde prezentovány numerické simulace v různých koronálních strukturách, ať už se jedná o jednoduché magnetické smyčky, neutrální proudovou vrstvu a nebo otevřené struktury. Tyto studie jsou velmi důležité pro pochopení vlnových procesů odehrávajících se ve sluneční atmosféře, neboť by mohly pomoci k objasnění zatím ne zcela pochopeného a vysvětleného problému ohřevu sluneční koróny. Tuto habilitační práci tvoří úvod do problematiky vln a oscilací ve sluneční atmosféře, komentovaný přehled publikovaných prací autora a konečně přiložené práce autora tak, jak byly v daném časopise publikovány.

Obsah

Předmluva

Slunce je objektem na obloze, který fascinoval a byl předmětem zájmu lidstva již od nepaměti. První zmínky o jeho pozorování můžeme najít v Číně již 2000 let př.n.l. a zhruba 600 let př.n.l. v Řecku. Různé kultury uctívaly Slunce jako božstva a pohlížely na něj jako na životodárnou hvězdu, zásobující naši Zemi světlem a teplem. V tomto smyslu má pro nás Slunce i dnes naprosto stejný význam, ovšem náš pohled se podstatně změnil hlavně díky pokročilým technikám pozorování, poskytujícím detailnější informace. Při pozorování ze Země jsme ovšem značně ovlivněni atmosférou, která propouští víceméně pouze viditelné záření a část záření v rádiovém oboru spektra. Z tohoto důvodu, se společně s rozvíjející se technikou, Slunce začalo pozorovat z kosmického prostoru, kde zemská atmosféra již pozorování neovlivňuje. Za počátek jeho pozorování z kosmu lze považovat rok 1973, kdy byla vypuštěna družice Skylab. Od té doby byla vypuštěna celá řada dalších kosmických družic, které podstatně rozšířily soubor našich vědomostí, můžeme jmenovat například družice SOHO, TRACE, Hinode, STEREO nebo v únoru 2010 vypuštěnou družici SDO. Napozorovaná data z těchto kosmických družic, v různých oborech elektromagnetického spektra, např. gamma záření, tvrdého a měkkého rentgenového záření, extrémně ultrafialového záření, významně pomohla pochopit některé fyzikální procesy, odehrávající se na Slunci. Dnes díky pozorováním, ať už pozemským nebo kosmickým s jistotou víme, že Slunce není zdaleka tak klidné, jak by se na první pohled mohlo zdát. Lze zde pozorovat celou řadu fyzikálních procesů, které mohou, a to dokonce velmi významně, ovlivňovat život na Zemi. Významnost těchto jevů spočívá, zejména v dnešní době, na závislosti lidstva na technických a elektronických přístrojích, které mohou různé procesy na Slunci ovlivňovat, případně dokonce i poškodit.

Díky našemu detailnějšímu poznání Slunce o něm máme obrovské množství informací, nicméně v souvislosti s tím se vynořila i spousta nových problémů. Například jedním z takových velice intenzivně zkoumaných, a zatím ne zcela dokonale popsaných a pochopených jevů ve sluneční fyzice, je ohřev sluneční koróny. Možným kandidátem, i když ne zcela jediným, zodpovědným za tento tzv. koronální ohřev, jsou pravděpodobně magnetoakustické vlny. Magnetoakustické vlny jsou mimo jiné velmi důležitým diagnostickým nástrojem, který nám, podobně jako v seismologii pomáhá odhalovat vlastnosti prostředí, ve kterém se vlny šíří. Mnoho poznatků o vlnách, šířících se sluneční atmosférou máme z již zmíněných pozorování. Na druhou stranu, velmi významnou a nezastupitelnou roli také hraje teoretický popis, zejména pak numerické simulace.

Předložená habilitační práce se zabývá numerickými simulacemi šíření magnetohydrodynamických (MHD) vln ve sluneční atmosféře, na základě MHD popisu plazmatu. Základem práce je modelování vln v různých koronálních strukturách, pomocí různých numerických kódů a algoritmů. V modelech pro jednoduchou magnetickou smyčku se MHD rovnice řeší za pomoci dvoukrokového Lax-Wendroffova algoritmu s umělým vyhlazováním, zatímco pro jiné, složitější struktury, například neutrální proudovou vrstvu (tzv. *Harris current-sheet*) nebo otevřené magnetické struktury, se používá numerický kód FLASH, využívající Riemannovy řešiče, který je modulární, využívá paralelizaci a adaptivní zjemňování výpočetní sítě.

Předložená habilitační práce rozdělena do dvou hlavních částí. V první části je nastíněn úvod do problematiky, včetně současného stavu výzkumu vln a oscilací ve sluneční atmosféře. Ve druhé části jsou prezentovány komentované vlastní výsledky, kterých jsme našimi numerickými simulacemi dosáhli a v několika případech také porovnali s pozorováními. V příloze jsou pak uvedeny kopie plných textů odborných článků, které jsou komentovány ve zmíněné druhé části habilitační práce.

Kapitola 1

Úvod do problému vln a oscilací ve sluneční koróně

V této kapitole popíšeme jednotlivé vrstvy atmosféry Slunce. Podrobněji se budeme věnovat pro nás nejdůležitější části – sluneční koróně, tj. oblasti, pro kterou jsme nejčastěji prováděli naše numerické výpočty šíření (magnetohydrodynamických) MHD vln. V další části se budeme věnovat zejména různým typům MHD vln, se kterými se ve sluneční atmosféře můžeme setkat.

1.1 Co je sluneční koróna?

Jednoduše můžeme říci, že sluneční koróna je nejsvrchnější částí sluneční atmosféry, složená z téměř úplně ionizovaného velmi řídkého vodíkového plazmatu (např. Priest 1982; Aschwanden 2005). Nemá pevně ohraničenou vnější hranici a zasahuje do meziplanetárního prostoru, kde plynule přechází ve sluneční vítr. Její tvar je nepravidelný a značně se mění společně se sluneční aktivitou. Sluneční korónu nemůžeme pozorovat pouhým okem, protože za normálních okolností je přezářena denním slunečním svitem. Můžeme ji ovšem běžně pozorovat během slunečních zatmění nebo uměle pomocí koronografu, poprvé sestrojeného v roce 1930 B. Lyotem (1897-1952). Teplota v koróně se pohybuje od několika stovek tisíc Kelvinů v tzv. klidných oblastech, až po několik desítek miliónů Kelvinů ve slunečních erupcích.

Sluneční koróna leží nad částečně ionizovanou a relativně chladnou částí sluneční atmosféry, nazývanou chromosféra. V této oblasti se teplota pohybuje od několika málo tisíc Kelvinů (tzv. oblast teplotního minima v nízké chromosféře) až po zhruba $20000\ \mathrm{K}$ v oblastech vysoké chromosféry. Tloušťka chromosféry se pohybuje zhruba kolem $2000 - 2500\ \mathrm{km}$.

Mezi korónou a chromosférou se nachází další, poměrně význačná část sluneční atmosféry – přechodová oblast (vrstva). Přechodová vrstva je velmi dobře pozorovatelná v ultrafialové oblasti spektra, například pomocí družice TRACE (Golub et al. 1999; Handy et al. 1999) a její tloušťka se odhaduje v řádu několika stovek kilometrů. Tato vrstva je velmi zajímavá tím, že na takto poměrně malé vzdálenosti narůstá teplota ze zmíněných zhruba $20000\ \mathrm{K}$ v oblastech vysoké chromosféry na $1 - 2\ \mathrm{MK}$ v koróně. Průběh teploty a hustoty (koncentrace) částic v různých vrstvách sluneční atmosféry, podle tzv. VAL-C modelu (Vernazza et al. 1981; Avrett & Loeser 2008), je zobrazen na obrázku 1.1.

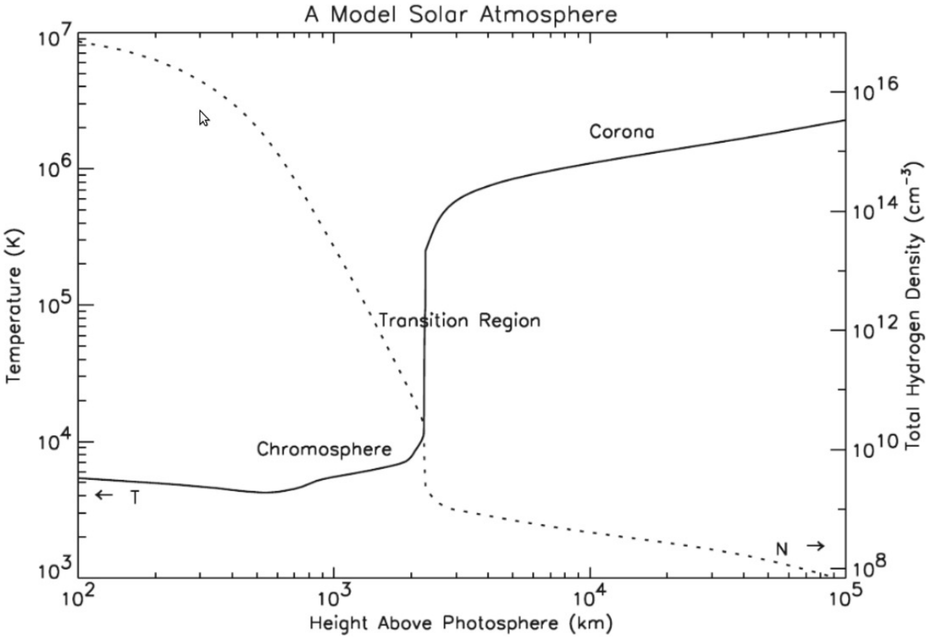

Obr. 1.1: Průběh teploty a hustoty (koncentrace) částic v jednotlivých vrstvách sluneční atmosféry podle tzv. VAL-C modelu (Vernazza et al. 1981), včetně naznačné přechodové oblasti. Převzato z (Golub & Pasachoff 2009).

Sluneční korónu je možné rozdělit na tři části, podle toho jaký v dané výšce nad slunečním povrchem dominuje emisní mechanismus (např. Antia et al. 2003; Golub & Pasachoff 2009). Setkáme se zde tak s tzv. K-korónou (kontinuum), dále E-korónou (emisní) a F-korónou (Fraunhoferova). Během sluneč-

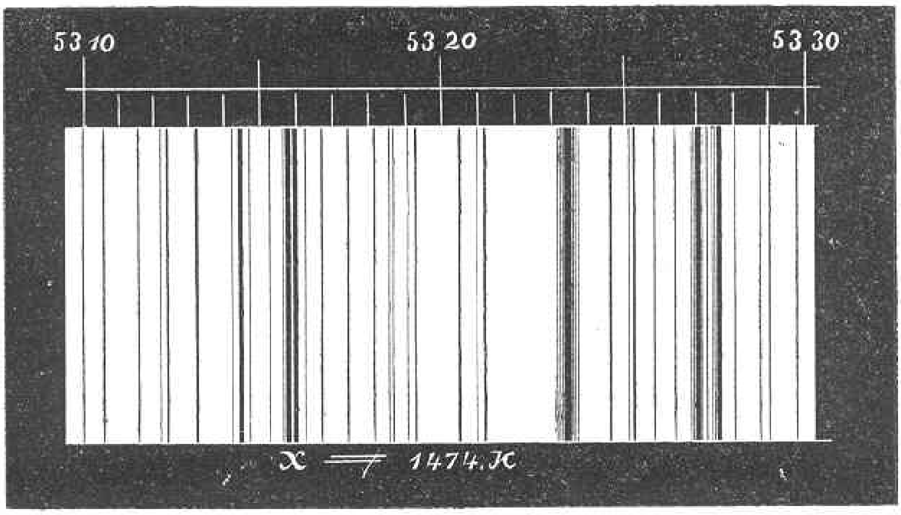

Obr. 1.2: Historická fotografie spektra koróny v okolí zelené emisní čáry o vlnové délce 530,3 nm, připisované nově objevenému prvku – koróniu. Reprodukováno z knihy: A. C. Young, The Sun, druhé vydání 1896, Obr. 93 (s. 258). Zdroj: `http://www.astro.umontreal.ca/~paulchar`.

ního zatmění dne 7. srpna 1869, viditelného v severní Americe, dva američtí astronomové, A. C. Young (1834-1908) a W. Harkness (1837-1903), nezávisle na sobě objevili ve spektru koróny zelené emisní čáry o vlnové délce 530,3 nm (obrázek 1.2, Young 1896). Po dalších zhruba 70 let zůstávaly tyto čáry ve sluneční fyzice záhadou. Prvním vysvětlením bylo, že tyto čáry pocházejí z dosud neobjeveného prvku, který dokonce dostal název – korónium (Billings 1966; Severny 2004; Golub & Pasachoff 2009). Teprve v roce 1943 přišel švédský fyzik B. Edlén (1906-1993) se správným vysvětlením, že se jedná o čáry několikrát ionizovaných atomů těžkých prvků. Identifikoval tak poprvé čtyři emisní čáry ve sluneční koróně, pocházející z Fe X, Fe XI, Ca XII a Ca XIII. Ve všech Edlén identifikoval 19 z tehdy známých 24 emisních čar ve sluneční koróně. Tím se podařilo vysvětlit původ těchto emisních čar a vyvrátit existenci korónia. Nicméně, vyvstal zde nový problém, a to existence takovýchto několikrát ionizovaných atomů těžkých prvků. Toho je možné docílit v prostředí s velmi vysokou teplotou. Znamená to tedy, že koróna musí mít teplotu mnohonásobně vyšší, než viditelná fotosféra – milión Kelvinů i více. Tato vysoká teplota vysvětluje ale i další fakt, proč je koróna poměrně rozsáhlým útvarem. Pokud by měla koróna teplotu fotosféry, pak by tzv. ekvivalentní výška (angl. *scale height*), daná vztahem (Priest 1982):

$$\lambda = \frac{k_{\mathrm{B}}T}{mg}, \tag{1.1}$$

byla pouze kolem $150\ \mathrm{km}$, což znamená, že ve vzdálenosti slunečního poloměru by hustota byla v podstatě nulová. Nicméně, pokud použijeme teplotu vyšší (řádu miliónu kelvinů, odhadovaných v koróně), pak dostáváme evivalentní výšku kolem $10^5\ \mathrm{km}$, což již odpovídá skutečným hodnotám.

Další částí sluneční koróny je K-koróna. Zde převládá lineárně polarizovaná spojitá emise způsobená rozptylem fotosférického záření na rychlých volných elektronech.

Poslední částí je F-koróna, která vzniká rozptylem světla na pomalých prachových částicích. Ve spektru F-koróny můžeme pozorovat absorpční čáry Fraunhoferova spektra. Zasahuje až do meziplanetárního prostoru a velmi často ji můžeme pozorovat v podobě tzv. zodiakálního (zvířetníkového) světla kolem ekliptiky. Mnozí autoři neuvažují F-korónu za regulérní součást sluneční koróny, proto se provádějí pozorování převážně E- a K-koróny.

Teplota v celé sluneční atmosféře není homogenní (Aschwanden 2005). Můžeme pozorovat chladnější místa, oblasti tzv. koronálních děr, kde převládá otevřená konfigurace magnetického pole a teplota je zde $T \leq 1\ \mathrm{MK}$. V oblastech s uzavřeným magnetickým polem, o kterých mluvíme jako o tzv. klidných oblastech, je teplota přibližně $T \approx 1 - 2\ \mathrm{MK}$. A nakonec v nejteplejších aktivních oblastech mohou teploty nabývat hodnot $T \approx 2 - 6\ \mathrm{MK}$. Jak již bylo řečeno v úvodu, vysoká teplota v koróně (o dva až tři řády vyšší než fotosféra) a velký teplotní gradient v přechodové vrstvě není dosud uspokojivě vysvětlen. Existují některé teorie a pokusy o vysvětlení tohoto jevu, jako např. procesy rekonexe magnetického pole nebo ohřev pomocí magnetoakustických vln ve slunečním plazmatu.

Je třeba ještě zmínit, že ve sluneční koróně hraje velmi důležitou roli magnetické pole. Z toho důvodu se ve fyzice sluneční koróny zavádí tzv. plazma-β parametr. Tento parametr je definován jako poměr kinetického a magnetického tlaku, takže můžeme napsat (např. Priest 1982; Aschwanden 2005):

$$\beta = \frac{p_{\mathrm{kin}}}{p_{\mathrm{mag}}} = \frac{nk_{\mathrm{B}}T}{\frac{B^2}{2\mu_0}} = \frac{2}{\gamma}\left(\frac{c_{\mathrm{s}}}{c_{\mathrm{A}}}\right)^2, \tag{1.2}$$

kde γ je adiabatický koeficient, c_{s} je rychlost zvuku a c_{A} je Alfvénova rychlost.

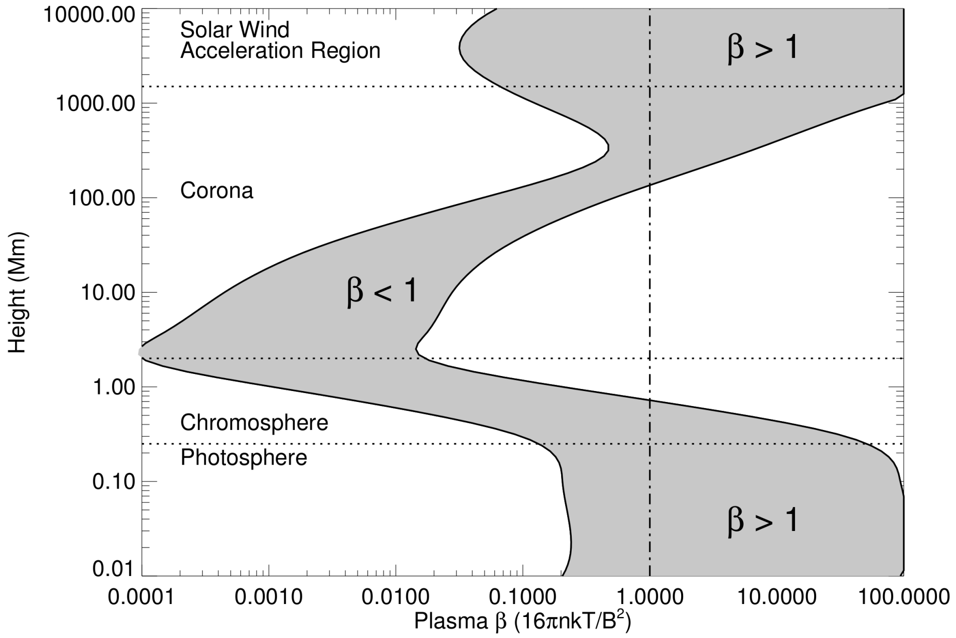

Obr. 1.3: Plazma-β parametr ve sluneční koróně pro dvě různé hodnoty magnetického pole – 2500 G (křivka nalevo) a 100 G (křivka napravo). Převzato z (Aschwanden 2005).

Jak se mění tento parametr ve sluneční atmosféře, ukazuje obrázek 1.3. Z obrázku je patrné, že pro velkou část sluneční koróny platí $\beta < 1$, tedy převládá v ní magnetický tlak, zatímco pro fotosféru, část chromosféry a vnější koróny platí $\beta > 1$. Magnetické pole v koróně, jak již bylo napsáno, hraje velmi podstatnou roli a v zásadě řídí procesy, které se v koróně odehrávají. Nicméně, jak je z obrázku vidět, i v koróně může být plazma-β parametr být větší než jedna, tzn. magnetické pole je zde velmi malé. To se stává například v případě tzv. „magnetických kaspů“, kde převládají tlakové síly (díky velmi vysoké teplotě), magnetické pole je velmi malé, a plazma tak může volně unikat do prostoru podél magnetických siločar.

Podle konfigurace magnetického pole můžeme rozlišit dva druhy útvarů na Slunci. Pokud je magnetické pole uzavřené, tak struktury mají tvar smyček se zjasněním u zakotvení, kde emitují v oboru EUV a měkkého rentgenového záření. Typicky mají smyčky poloměr až do 10 Mm a poloměr trubice se odhaduje na zhruba 1 Mm. Stále se také diskutuje o tom, že smyčka není jednolitým útvarem, ale že se skládá z několika menších smyček, které zatím pouze nedokážeme za použití současné techniky rozlišit (např. Nakariakov et al. 2016).

Smyčky jsou obvykle koncentrovány poblíž určitých míst (např. v blízkosti slunečních skvrn) a jsou součástí tzv. aktivních oblastí. V případě otevřených magnetických polí jsou magnetické útvary vyplněny hustým plazmatem a často se nacházejí v blízkosti koronálních děr, kde můžeme pozorovat jasnější útvary nazývané v odborné literatuře jako *coronal plumes*, a jimiž unikají částice rychlého slunečního větru, např. (Nakariakov & Verwichte 2005). Je také možné ještě pozorovat další útvary, které se dají považovat za kombinaci obou zmíněných útvarů, a to jsou tzv. *coronal streamers*, které jsou zdrojem pomalého slunečního větru. Všechny popsané útvary jsou schématicky vyobrazeny na obrázku 1.4.

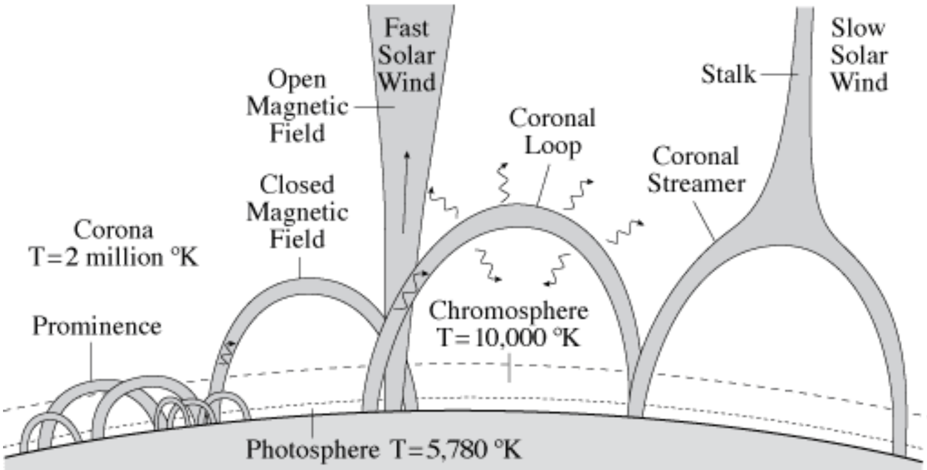

Obr. 1.4: Schématické zobrazení sluneční atmosféry a v ní pozorovatelných útvarů (koronální smyčky, otevřené struktury a tzv. *coronal streamers*). Zdroj: `https://ase.tufts.edu`.

1.2 MHD vlny ve sluneční koróně

Magnetohydrodynamické (MHD) vlny můžeme najít v různých typech plazmatu, které je nejen astrofyzikálního původu (Roberts 2000). MHD vlny byly detekovány například i ve fúzních zařízeních typu Tokamak (Rosenbluth & Rutherford 1975; Sharapov et al. 2002), dále také v magnetosféře Země, ve slunečním větru a v mnoha strukturách pozorovaných ve sluneční atmosféře, např. v koronálních smyčkách, v blízkosti slunečních skvrn, slunečních protuberancích a také v souvislosti se slunečními erupcemi a výrony koronální hmoty

(CME), např. (Nakariakov & Verwichte 2005; De Moortel & Nakariakov 2012; Nakariakov et al. 2016).

V posledních letech je studium MHD vln a oscilací ve sluneční koróně jedním z nejdynamičtěji se rozvíjejících směrů sluneční fyziky, ovšem o vlnách a oscilacích ve sluneční koróně se ve sluneční fyzice diskutuje už několik desetiletí. Teprve ale ke konci 90. let minulého století nám přístroje s vysokým rozlišením, pozorující v EUV oboru spektra, na palubách moderních družic umožnily tyto vlny pozorovat přímo. Zejména vypuštění družic SOHO[1] a TRACE[2] způsobilo doslova revoluci v pozorování jevů spojených s vlnami a oscilacemi. Můžeme zmínit například objev a následné pozorování tzv. EIT vln v roce 1996 (Veronig et al. 2011; Nitta et al. 2013) a detailnější pozorování Moretonových vln (Thompson et al. 1998; Harra et al. 2011), které byly objeveny poprvé mnohem dříve – již v roce 1960. Oba typy vln jsou spojeny se slunečními erupcemi a jsou stále předmětem odborných diskuzí, neboť jejich vzájemná souvislost nám ještě není zcela jasná. Dále to jsou vlny v koronálních smyčkách (Berghmans & Clette 1999; Aschwanden et al. 1999; De Moortel et al. 2002), *kink* oscilace ve smyčkách generované slunečními erupcemi (Nakariakov et al. 1999; Aschwanden et al. 2002), podélné stojaté vlny v koronálních smyčkách (Kliem et al. 2002; Wang et al. 2002). Existuje také mnoho pozemských pozorování v rádiovém oboru spektra (např. Mészárosová et al. 2008, 2009a,b,c, 2011). V únoru 2010 byla vypuštěna družice SDO[3], která za pomoci přístroje AIA tyto vlny pozoruje s velkým časovým a prostorovým rozlišením. Díky tomuto přístroji byly dokonce objeveny nové dva druhy vln v koróně, rychle se pohybující kvaziperiodické vlnové balíky (*quasi-periodic wave trains*) (Liu et al. 2011) a pomalu tlumené stojaté *kink* oscilace s malou amplitudou (Anfinogentov et al. 2013; Nisticò et al. 2013a).

MHD vlny byly také podrobeny analýze v mnoha teoretických a numerických studiích, např. (Roberts 1981a,b), poslední výsledky numerických studií shrnuje (např. Pascoe 2014). Z velkého množství typů vln různí autoři studovali například postupné vlny (De Moortel et al. 2000), pomalé stojaté magnetoakustické vlny (Ofman & Wang 2002; Selwa et al. 2005; Zaqarashvili et al. 2005; Selwa et al. 2007; Jelínek & Karlický 2009, 2010) a pomalé postupné magneto-

---

[1] https://sohowww.nascom.nasa.gov/

[2] http://www.lmsal.com/TRACE/

[3] http://sdo.gsfc.nasa.gov/

akustické vlny v koronálních smyčkách s efekty gravitace, viskozity a tepelné vodivosti (Nakariakov et al. 2000; Tsiklauri & Nakariakov 2001). Dále to jsou studie rychlých magnetoakustických vln v koronálních smyčkách v tzv. *kink* módu (Nakariakov et al. 1999; Wang & Solanki 2004; Andries et al. 2005; Pascoe et al. 2009, 2010; Yu et al. 2015) a tzv. *sausage* módu (Nakariakov et al. 2003; Melnikov et al. 2005; Pascoe et al. 2007, 2009; Jelínek & Karlický 2012; Jelínek et al. 2012; Yu et al. 2015).

Během intenzivního výzkumu vln a oscilací ve sluneční koróně bylo potvrzeno či přímo objeveno velké množství různých vln a jejich módů a není proto ani možné je do detailu zde všechny popsat. Pro další přehled výsledků jak z pozorování, tak výsledků analytických nebo numerických je možné nahlédnout například do (Zaitsev & Stepanov 2008; Banerjee et al. 2011; Patsourakos & Vourlidas 2012; De Moortel & Nakariakov 2012; Stepanov et al. 2012a; Mathioudakis et al. 2013; Liu & Ofman 2014).

Jak již bylo dříve řečeno, hlavním důvodem intenzivního výzkumu MHD vln a oscilací ve sluneční koróně je pochopení a vysvětlení zcela zásadního problému sluneční fyziky a to ohřevu sluneční koróny. Dalším důvodem je například pochopení mechanismu generování rychlého slunečního větru, fyzikálních mechanismů uvolňování energie při slunečních erupcích a použití vln k diagnostice plazmatu, ve kterém se vlny šíří. Podobně jako u Země, kdy pomocí seismologie můžeme zjistit mnoho o zemském tělese, tak i díky vlnám v koróně se můžeme dozvědět více o její struktuře a proto se v této oblasti výzkumu velmi často setkáváme s pojmem koronální seismologie (Nakariakov 2004; Nakariakov & Verwichte 2004; De Moortel & Nakariakov 2012; Stepanov et al. 2012a,b).

1.2.1 Typy vln a oscilací ve sluneční koróně

V této části obecně popíšeme některé typy vln a oscilací, které se nejčastěji vyskytují a souvisejí s autorovým výzkumem.

V plynech vnímáme zvuk díky periodickému zhušťování a zřeďování prostředí, ve kterém se vlna pohybuje. Taková vlna se šíří v kulových vlnoplochách a charakteristickou rychlostí šíření takového rozruchu je rychlost zvuku daná vztahem, (např. Goedbloed & Poedts 2004):

$$c_\mathrm{s} = \sqrt{\gamma \frac{p}{\varrho}} = \sqrt{\frac{\gamma k_\mathrm{B}}{m} T}. \tag{1.3}$$

V plazmatu se díky přítomnosti magnetického pole objevuje jiná charakteristická rychlost, známá jako Alfvénova, (např. Goedbloed & Poedts 2004):

$$c_\mathrm{A} = \frac{B}{\sqrt{\mu_0 \varrho}}. \tag{1.4}$$

Nicméně v plazmatu, na rozdíl od vzduchu, kde pozorujeme šíření zvuku v podobě jedné kulové vlnoplochy, se takové vlnoplochy vyskytují tři. Jedná se o vlnoplochy Alfvénových vln, pohybující se již zmíněnou Alfvénovou rychlostí a vlnoplochy tzv. pomalých a rychlých magnetoakustických vln, např. (Chen 1974; Priest 1982; Goossens 2003). Vzájemné vztahy mezi rychlostí zvuku (c_s), Alfvénovou rychlostí (c_A) a rychlostí pro pomalou (c_sl) a rychlou (c_f) magnetoakustickou vlnu jsou následující:

$$\frac{1}{c_\mathrm{sl}^2} = \frac{1}{c_\mathrm{s}^2} + \frac{1}{c_\mathrm{A}^2} \qquad\qquad c_\mathrm{f}^2 = c_\mathrm{s}^2 + c_\mathrm{A}^2. \tag{1.5}$$

Abychom dostali konkrétní vyjádření, popisující vlnoplochy, ve kterých se MHD vlny v plazmatu šíří, je třeba najít disperzní relaci $\omega = \omega(\mathbf{k})$. Ta má následující tvar (Priest 1982; Aschwanden 2005; Kulsrud 2005):

$$-\omega^2 \delta\mathbf{v} + (c_\mathrm{s}^2 + c_\mathrm{A}^2)(\mathbf{k}\cdot\delta\mathbf{v})\mathbf{k} + (\mathbf{k}\cdot\mathbf{c}_\mathrm{A})[(\mathbf{k}\cdot\mathbf{c}_\mathrm{A})\delta\mathbf{v} - (\mathbf{c}_\mathrm{A}\cdot\delta\mathbf{v})\mathbf{k} - (\mathbf{k}\cdot\delta\mathbf{v})\mathbf{c}_\mathrm{A}] = 0. \tag{1.6}$$

Řešením výše uvedené rovnice dostaneme tři řešení, tzv. magnetoakustický komplex, která odpovídají vyjádření fázových rychlostí zmíněných typů MHD vln – pomalé, rychlé a Alfvénově, viz obrázek 1.5.

Alfvénovy vlny

Alfvénovy vlny jsou vlnami čistě magnetickými, jediným zdrojem těchto vln je magnetické pole. Jedná se o příčnou vlnu, porucha magnetického pole je kolmá k původnímu magnetickému poli. Důležité je, že tyto vlny neovlivňují nijak hustotu a tlak prostředí, ve kterém se pohybují. Tyto vlny jsou vysoce anizotropní, což dobře prezentuje graf fázové, ale zejména grupové rychlosti, obrázek

1.5. Grupovou rychlostí se pohybují pouze podél magnetických siločar, to znamená že pouze podél těchto siločar mohou přenášet energii. Fázovou rychlost můžeme vyjádřit jako (Priest 1982; Goossens 2003):

$$c_{\mathrm{f,A}}^2 = c_{\mathrm{A}}^2 \cos^2(\theta). \tag{1.7}$$

Tato rychlost se mění od rychlosti $c_{\mathrm{A,f}} = c_{\mathrm{A}}$ podél magnetického pole až po $c_{\mathrm{A,f}} = 0$ kolmo k němu. Pokud bychom měli přehledně shrnout vlastnosti Alfvénových vln, můžeme napsat:

- jsou závislé pouze na magnetickém poli
- nezpůsobují změny v hustotě a tlaku prostředí, ve kterém se pohybují
- jsou anizotropní a nepohybují se kolmo k magnetickému poli
- přenos energie se děje pouze podél magnetických siločar, a to Alfvénovou rychlostí

Pomalé magnetoakustické vlny

Dalším z řešení rovnice (1.6) je fázová rychlost pomalých magnetoakustických vln (Priest 1982; Goossens 2003):

$$v_{\mathrm{f,S}}^2 = \frac{1}{2}\left(c_{\mathrm{s}}^2 + c_{\mathrm{A}}^2\right) - \frac{1}{2}\sqrt{\left(c_{\mathrm{s}}^2 + c_{\mathrm{A}}^2\right)^2 - 4c_{\mathrm{s}}^2 c_{\mathrm{A}}^2 \cos^2\theta}. \tag{1.8}$$

Vlastnosti pomalých magnetoakustických vln je možné shrnout následovně:

- jsou závislé nejen na magnetickém poli, ale též na tlakových silách
- způsobují změny v hustotě a tlaku prostředí, ve kterém se pohybují
- tlak plazmatu a magnetický tlak jsou v protifázi
- jsou velmi anizotropní a nemohou se pohybovat kolmo k siločarám magnetického pole
- přenos energie je tedy anizotropní a děje se pouze v malých oblastech kolem magnetických siločar

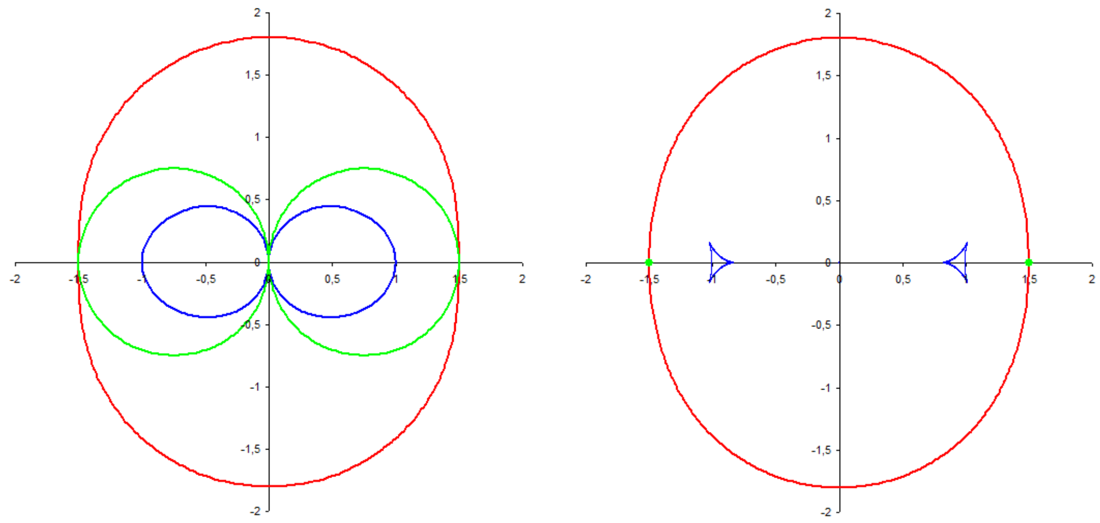

Obr. 1.5: Polární diagramy fázové (vlevo) a grupové rychlosti (vpravo) pro $c_\mathrm{A} = 1.5c_\mathrm{s}$. Červená barva odpovídá rychlé, zelená pomalé magnetoakustické vlně a modrá Alfvénově vlně. Magnetické pole je orientováno vodorovně. Zdroj: autor.

Rychlé magnetoakustické vlny

Jako poslední řešení dostáváme pro rychlé magnetoakustické vlny fázovou rychlost jako (Priest 1982; Goossens 2003):

$$v_{\mathrm{f,F}}^2 = \frac{1}{2}\left(c_\mathrm{s}^2 + c_\mathrm{A}^2\right) + \frac{1}{2}\sqrt{\left(c_\mathrm{s}^2 + c_\mathrm{A}^2\right)^2 - 4c_\mathrm{s}^2 c_\mathrm{A}^2 \cos^2\theta}. \tag{1.9}$$

Podobně jako v předchozích případech shrneme vlastnosti rychlých magnetoakustických vln:

- jsou závislé nejen na magnetickém poli, ale též na tlakových silách
- způsobují změny v hustotě a tlaku prostředí, ve kterém se pohybují
- tlak plazmatu a magnetický tlak jsou ve fázi
- jsou izotropní, nicméně snadněji se pohybují ve směru kolmém k magnetickému poli
- přenos energie je izotropní

V literatuře se velmi často objevují různá označení vln, která mohou být poněkud matoucí. Alfvénovy vlny jsou vlny nekompresní, v anglické literatuře označovány také jako *incompressible* nebo *shear Alfvén waves*. Pomalé magnetoakustické vlny jsou někdy označovány jako *slow Alfvén waves*. U posledního typu, tedy rychlé magnetoakustické vlny, se můžeme setkat v jistém případě s pojmem *compressible Alfvén wave*. S tímto označením se setkáme v aproximaci tzv. *cold plasma limit*, kdy platí, že Alfvénova rychlost c_A je mnohem větší, než rychlost zvuková, $c_\mathrm{s} \approx 0$. Z rovnice (1.9) pak vyplývá, že fázová rychlost rychlé magnetoakustické vlny $v_\mathrm{f,F} = c_\mathrm{A}$, tedy rychlá vlna (která je sama o sobě kompresní – projevuje se změnami v tlaku, hustotě, atd.) se pohybuje Alfvénovou rychlostí, proto je tedy nazývána kompresní Alfvénovou vlnou.

Entropická vlna

V případě entropické vlny (nebo módu) rychlost plazmatu, stejně jako magnetické pole i tlak zůstávají beze změny, zatímco jedinou fyzikální veličinou, která se mění, je hustota a entropie. Entropická vlna je tedy charakterizována tím, že se nepohybuje a její fázová rychlost (nebo frekvence) je nulová, např. (Goedbloed & Poedts 2004; Goedbloed et al. 2010). Protože s hustotou a tlakem je entropie spojena vztahem, např. (Landau & Lifshitz 1987):

$$S \sim \ln \left(p\rho^{-\gamma}\right), \tag{1.10}$$

mění se společně s hustotou i tato veličina.

Velmi často tuto vlnu zanedbávají ve svých studiích i autoři, kteří se MHD vlnami zabývají. Je to proto, že se ukazuje, že entropická vlna je poměrně rychle utlumena efektem tepelné vodivosti plazmatu. Je také velmi dobře známo, že tepelná vodivost napříč a kolmo k magnetickému poli je značně odlišná (Priest 1982; Golub & Pasachoff 2009):

$$\frac{k_\perp}{k_\parallel} = 2 \times 10^{-31} \frac{n^2}{T^3 B^2}, \tag{1.11}$$

kde $k_\parallel$ se dá vyjádřit jako:

$$k_\parallel = 1.8 \times 10^{-10} \frac{T^{5/2}}{\ln \Lambda} \; \left[\mathrm{W} \cdot \mathrm{m}^{-1} \cdot \mathrm{K}^{-1}\right]. \tag{1.12}$$

Zde $\ln \Lambda$ je tzv. Coulombův logaritmus, jehož hodnota je většinou mezi čísly $5 - 20$. Typické hodnoty pro koeficient tepelné vodivosti jsou $4 \times 10^{-11} T^{5/2}$ pro oblast fotosféry, $10^{-11} T^{5/2}$, pro chromosféru a $9 \times 10^{-12} T^{5/2}$ pro korónu. Z tohoto důvodu se dost často setkáváme v literatuře pouze se vztahem $k_{\|} = 10^{-11}T^{5/2}$ nezávisle na místě ve sluneční atmosféře. Zatímco je tedy tepelná vodivost kolmo na směr magnetického pole velmi malá, ve směru magnetického pole je velká a tato vlna tak může být velice rychle utlumena.

Nicméně, někteří autoři se problémem entropického módu zabývali podrobněji (při zanedbání efektu tepelné vodivosti), např. (Murawski et al. 2011; Jelínek et al. 2015a) a ukázali, že entropická vlna v magnetickém X-bodu může být nepřímým důkazem nanoerupcí nebo dokonce erupcí ve sluneční atmosféře.

1.2.2 MHD vlny v koronálních smyčkách

Dosud se popis týkal pouze šíření rovinných vln v homogenním neomezeném prostředí. Vzhledem k tomu, že například sluneční erupce jsou doprovázeny vznikem tzv. poerupčních smyček a též další útvary na Slunci můžeme ve formě smyček pozorovat, jeví se taková struktura jako nejjednodušší a zároveň nejpřirozenější vlnovod.

Skutečně se ukazuje, že útvar v podobě válce je velmi dobrým vlnovodem pro akustické (a v případě s magnetickým polem, magnetoakustické) vlny a nadto existence takového vlnovodu velmi silně ovlivňuje šíření vln.

Disperzní relace pro vlny šířící se magnetickým vlnovodem válcového tvaru má ve válcových souřadnicích následující tvar (Roberts et al. 1984; Aschwanden 2005; Kulsrud 2005):

$$\rho_0(k^2c_{\mathrm{A}}^2 - \omega^2)m_{\mathrm{e}}\frac{K_n'(m_{\mathrm{e}}a)}{K_n(m_{\mathrm{e}}a)} = \rho_e(k^2c_{\mathrm{Ae}}^2 - \omega^2)n_0\frac{J_n'(n_0a)}{J_n(n_0a)}, \tag{1.13}$$

kde

$$n_0^2 = \frac{(\omega^2 - k^2c_{\mathrm{A}}^2)(\omega^2 - k^2c_{\mathrm{s0}}^2)}{(c_{\mathrm{s0}}^2 + c_{\mathrm{A}}^2)(\omega^2 - k^2c_{\mathrm{t}}^2)}, \tag{1.14}$$

a

$$m_{\mathrm{e}}^2 = \frac{(k^2c_{\mathrm{se}}^2 - \omega^2)(k^2c_{\mathrm{Ae}}^2 - \omega^2)}{(c_{\mathrm{se}}^2 + c_{\mathrm{Ae}}^2)(k^2c_{\mathrm{te}}^2 - \omega^2)}. \tag{1.15}$$

V rovnici (1.13) jsou J_n, K_n Besselovy funkce n-tého řádu, a J_n', K_n' jejich derivace, k je vlnový vektor podél magnetického pole a ω je frekvence. Rovnice (1.13) byla odvozena za předpokladu, že $m_{\mathrm{e}} > 0$, což znamená, že se žádné vlny nedostanou mimo válcový vlnovod, takže všechny pohyby se odehrávají pouze v magnetické smyčce. Řád n Besselových funkcí definuje mód oscilací a tím geometrii oscilující smyčky. Na obrázku 1.6 je vidět příčný řez takovou smyčkou pro různé hodnoty čísla n.

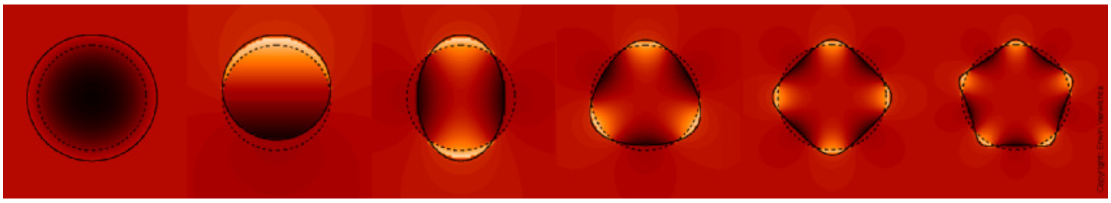

Obr. 1.6: Příčný řez smyčkou zobrazující různé módy oscilací. Zleva pro $n = 0$ (*sausage*), $n = 1$ (*kink*) a $n \geq 2$ vyšší módy oscilací. Zdroj: `http://www2.warwick.ac.uk`.

V rovnicích (1.14) a (1.15) se vyskytuje veličina c_t, tzv. *tube speed*, definovaná jako (Goedbloed & Poedts 2004):

$$c_\mathrm{t} = \frac{c_\mathrm{s} c_\mathrm{A}}{(c_\mathrm{s}^2 + c_\mathrm{A}^2)^{1/2}}. \tag{1.16}$$

Sausage mód Tento typ vln dostaneme pro $n = 0$. Jedná se o symetrické pulzace celé smyčky, přičemž v okolí osy symetrie zůstává prostředí nenarušeno. Tyto vlny mívají podle výsledků získaných z pozorování typické periody v rozmezí $0.5 - 10\ \mathrm{s}$. Odhad periody vlny můžeme provést na základě znalosti délky smyčky L jako:

$$P = \frac{2L}{v_\mathrm{ph}}, \tag{1.17}$$

přičemž platí $c_\mathrm{A} < v_\mathrm{ph} < c_\mathrm{Ae}$, kde c_A, resp. c_Ae je Alfvénova rychlost uvnitř, resp. vně smyčky (Goedbloed & Poedts 2004; Aschwanden 2005). Pokud je poměr hustot smyčky a prostředí, ve kterém se nachází velmi velký, pak pro periodu vlny v *sausage* módu můžeme napsat následující podmínku:

$$P < \frac{2\pi w}{j_0 c_\mathrm{A}} \approx \frac{2.62 w}{c_\mathrm{A}}, \tag{1.18}$$

kde j_0 je Besselova funkce a w pološířka smyčky (Goedbloed & Poedts 2004; Aschwanden 2005).

Kink mód *Kink* mód dostáváme pro případ, kdy je $n = 1$. Oproti předchozímu módu je tento příčnou vlnou. Poprvé byl *kink* mód pozorován pomocí družice TRACE 14. července 1998 jako oscilace koronální smyčky krátce po sluneční erupci, přičemž oscilace byly způsobeny velmi pravděpodobně právě touto erupcí (Aschwanden et al. 1999; Nakariakov et al. 1999; Schrijver et al. 1999). Po tomto objevu se *kink* oscilace staly objektem intenzivního výzkumu jak teoretického, tak z hlediska pozorování. Detailním rozborem této události se ukázalo, že se jedná o stojatý *kink* mód oscilací koronální smyčky. Nakonec se z pozorování podařilo odhalit i existenci postupných rychlých *kink* vln v otevřených strukturách. Bližší informace je možné nalézt např. v (Nakariakov & Verwichte 2005).

Torzní mód V homogenním neomezeném prostředí s magnetickým polem tedy v podstatě existují čtyři druhy MHD vln – pomalé a rychlé magnetoakustické vlny, Alfvénovy vlny a entropické vlny.

Ukazuje se ale, že u Alfvénových vln by měl existovat mód, který se nazývá torzní. Tyto tzv. Alfvénovy torzní vlny by měly být schopny uvolňovat energii ve sluneční atmosféře mnohem účinněji, než „klasické" Alfvénovy vlny. Obecně se Alfvénovy vlny pozorují velice špatně, neboť již víme, že v prostředí kudy procházejí nemění ani hustotu ani tlak a jsou tzv. „nekompresní". Na druhou stranu torzní Alfvénovy vlny se dají detekovat ze spektrálních pozorování, protože způsobují červený i modrý Dopplerův posuv spektrálních čar zároveň, což vede k jejich rozšíření. Kromě tohoto rozšíření spektrálních čar se ale chovají úplně stejně jako normální Alfvénovy vlny, to znamená, že při pohledu na smyčku, kudy tyto vlny procházejí nepozorujeme jakoukoliv změnu polohy ani tvaru smyčky.

1.2.3 Impulzivně generované rychlé MHD vlny

S impulzivně generovanými rychlými MHD vlnami se ve sluneční atmosféře setkáme velmi často, neboť zdrojem těchto vln jsou sluneční erupce, které tak mohou být zdrojem vln na jednom nebo i více místech, například v koronální smyčce. V práci (Roberts et al. 1984) autoři uvádí, že postupné vlny, spíše než stojaté, se objeví všude tam, kde jsou poruchy vyvolány impulzivně. Rozruch vyvolaný takovým pulzem je interpretován jako superpozice (Fourierův integrál) rovinných vln přes všechna ω a k. Obecně tak vznikne pravidelná posloupnost vlnových balíků, které obsahují mnoho vlnových délek a mají disperzní chrakter, někdy také nazývaná *wave train*. Celý vlnový signál se skládá

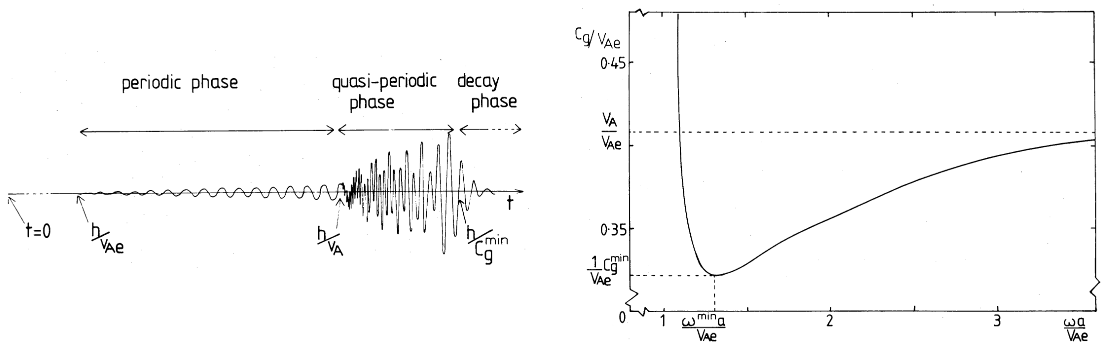

Obr. 1.7: Časový vývoj signálu impulzivně generované rychlé vlny, pohybující se v koronální smyčce a disperzní diagram grupové rychlosti pro tento typ vln. Převzato z (Roberts et al. 1984).

ze tří fází (Roberts et al. 1984). Okamžik prvního příchodu signálu odpovídá času $t_{\mathrm{p}} = h/c_{\mathrm{Ae}}$, tuto fázi nazýváme jako periodickou. Během této fáze mírně narůstá jak frekvence, tak amplituda až do okamžiku $t_{\mathrm{qp}} = h/c_{\mathrm{A}}$, kdy „přijde“ od zdroje signál s vysokou frekvencí. Výsledkem je silný nárůst amplitudy a oscilace, které takto vzniknou, se nazývají kvaziperiodické. Tato tzv. kvaziperiodická fáze trvá do okamžiku $t_{\mathrm{dp}} = h/c_{\mathrm{g}}^{\mathrm{min}}$, kde $c_{\mathrm{g}}^{\mathrm{min}}$ je minimální hodnota grupové rychlosti. V okamžiku času t_{dp} začíná další fáze, tzv. útlumová, někdy také nazývaná jako Airyho fáze, kdy se poměrně rychle snižuje amplituda těchto oscilací a oscilace jsou utlumeny, viz obrázek 1.7. *Wave trains* se pohybují podél magnetického pole rychlostí odpovídající zhruba $1\ \mathrm{Mm} \cdot \mathrm{s}^{-1}$, tedy o řád vyšší rychlostí, než je hodnota rychlosti zvuku v daném prostředí a jejich perioda je okolo jedné minuty (Liu et al. 2012). Tyto závěry byly potvrzeny i pozorováním jak ve viditelném oboru spektra, tak na rádiových vlnách, např. (Mészárosová et al. 2009b). Pomocí pozorování byly tyto vlny interpretovány jako rychlé magnetoakustické vlny (Ofman et al. 2011) a detailní analýza pozorování odhalila, že vlny jsou generovány náhlým (impulzivním) uvolněním energie (Yuan et al. 2013) a to, že kvaziperiodická část vlnového signálu má svůj základ v disperzních efektech.

Fyzikální mechanismy těchto disperzních efektů v kontextu rychlých magnetoakustických vln byly podrobněji zkoumány mnoha autory, např. (Murawski & Roberts 1993; Nakariakov et al. 2004; Pascoe et al. 2007) nebo (Yu et al. 2016, 2017). Waveletová spektra rychlých *wave trains* ukázala charakteristický tvar, který dostal dokonce i svůj vlastní název *crazy tadpole* (Nakariakov et al. 2004). Je to proto, že waveletová analýza (Farge 1992; Torrence & Compo 1998) vlnového signálu ukazuje, že nejdříve přijde ocásek „pulce“, obsahující úzké pásmo vlnových délek, a teprve potom se objeví hlava, která obsahuje široké pásmo vlnových délek.

Numerickými MHD simulacemi vzniku a šíření rychlých *wave trains* ve 2D, konkrétně v magnetické struktuře vějířového charakteru (angl. *magnetic funnel*) se zabýval například (Pascoe et al. 2013). Získané výsledky jsou v souladu s pozorováními *wave trains*. Autor této práce se také podobnými 2D studiemi v různých magnetických strukurách zabýval, např. (Karlický et al. 2011; Jelínek & Karlický 2012; Jelínek & Murawski 2013; Karlický et al. 2013; Mészárosová et al. 2014). Podrobnější popis těchto a dalších autorových prací je uveden v následující kapitole.

Kapitola 2

Numerické simulace MHD vln ve sluneční koróně

V této části habilitační práce jsou stručně popsány a okomentovány výsledky, týkající se šíření MHD vln v různých strukurách ve sluneční koróně, kterých jsme dosáhli pomocí našich numerických simulací. Pro jednoduchost jsme se zabývali téměř výhradně MHD numerickými simulacemi ve 2D, které jsme později vylepšili přidáním reálného VAL-C teplotního profilu (Vernazza et al. 1981; Avrett & Loeser 2008) a gravitačního pole. I přes jisté zjednodušení těchto modelů oproti reálným procesům ve třech rozměrech jsme dosáhli poměrně zajímavých výsledků a protože jsme zkoumali rychlé impulzivně generované vlny, nalezli u všech vlnových signálů charakteristické *tadpoles* v rámci waveletové analýzy, viz předchozí kapitola. Na druhou stranu jsme si samozřejmě vědomi, že 2D modely mají jistá omezení a nezahrnují efekty, které by ve výsledku mohly šíření vln ovlivňovat. Takovým jevem může být například tzv. *mode coupling* rychlých a Alfvénových vln, stejně tak do jisté míry srovnání numerických a napozorovných dat v důsledku interpretace 3D signálu ve 2D prostoru, např. (Gruszecki et al. 2012; Antolin & Van Doorsselaere 2013; Nisticò et al. 2013b).

V habilitační práci uvádíme tři význačné struktury, které jsme podrobně zkoumali – smyčka v magnetickém poli a bez magnetického pole (Jelínek & Karlický 2009, 2010; Mészárosová et al. 2014; Jelínek & Karlický 2015; Karlický & Jelínek 2016), neutrální proudová vrstva v literatuře označovaná jako tzv. *Harris current-sheet* (Karlický et al. 2011; Jelínek & Karlický 2012; Jelínek et al.

2012; Karlický et al. 2013; Mészárosová et al. 2014; Jelínek et al. 2015b), magnetický nulový bod (Jelínek et al. 2015a) a konečně otevřená magnetická struktura se zakřivenými magnetickými siločarami (Jelínek & Murawski 2013).

Předložená práce se zabývá numerickými simulacemi MHD vln ve sluneční koróně, na kterých jsme společně převážně s M. Karlickým z AsÚ AV ČR v Ondřejově začali spolupracovat v roce 2008. Do té doby, a během svého doktorského studia, se autor zabýval taktéž numerickými simulacemi, ale převážně procesů v nízkoteplotním laboratorním plazmatu. Z toho důvodu jsou v seznamu autorových publikací zařazeny i tyto práce, které ale nejsou dále nijak komentovány. Během svého ročního pobytu na Astronomickém ústavu vídeňské univerzity v letech 2009 – 2010 se autor také již zabýval numerickými simulacemi MHD vln, ale v tzv. galaktickém halu. Z této spolupráce vznikla publikace (Jelínek & Hensler 2011), která je uvedena pouze v seznamu literatury bez bližšího komentáře, neboť autor se dále již podobnými simulacemi nezabýval.

2.1 Numerické kódy

V době, kdy jsme začínali provádět simulace vln a oscilací ve sluneční koróně se tímto problémem z numerického hlediska nikdo u nás systematicky nezabýval. Ve světě existuje několik silných a uznávaných skupin, které mají v tomto oboru značný ohlas, např. univerzity ve Warwicku, St. Andrews a v Sheffieldu ve Velké Británii nebo v Leuvenu v Belgii. Tyto skupiny mají velmi často vlastní numerické kódy, které během let postupně vyvíjejí a lidé mimo skupinu na daném pracovišti se k nim obtížně dostávají. Jejich další nevýhodou je fakt, že velmi často jsou to kódy „ušité na míru“ konkrétním problémům řešeným v té které skupině. Z tohoto důvodu byl autor habilitační práce nucen začít využívat kódy vlastní. První numerický kód byl založen na starším kódu používaným M. Karlickým pro simulace rekonexe magnetického pole. Tento kód, původně napsaný v jazyce FORTRAN 77 byl přepsán autorem do jazyka FORTRAN 90/95 a postupně upraven do podoby vhodné pro simulace šíření vln ve sluneční koróně. Kód je založen na řešení soustavy MHD rovnic v tzv. konzervativním tvaru pomocí dvoukrokového Lax-Wendroffova algoritmu s umělým vyhlazováním (Sato & Hayashi 1979; Murawski 2002; Chung 2002). Ukázalo se, že tento kód je plně dostačující pro řešení široké škály jednodušších problémů, ovšem nedostačoval již v okamžiku, kdy bylo nutné například zavést do problémů gravitační pole, atd. Mimo jiné také z tohoto důvodu autor v roce 2010 navázal bližší spolupráci s prof. K. Murawskim z Katedry teoretické fyziky fakulty matematiky, fyziky a informatiky na Univerzitě Marie Curie-Skłodowské (UMCS) v Lublinu v Polsku, přičemž tato spolupráce úspěšně pokračuje dosud. Na UMCS v Lublinu existuje malá skupina, zabývající se problémy MHD vln a oscilací ve sluneční koróně a používající numerický kód FLASH, se kterým se zde autor seznámil a ve kterém vznikla většina zde prezentovaných výsledků. V započaté zahraniční spolupráci autor pokračoval i pobytem na Katolické univerzitě v Leuvenu ve skupině prof. T. Van Doorsselaere (březen-květen 2015), na základě čehož vznikla společná práce, zaslaná do časopisu *The Astrophysical Journal*.

2.1.1 FLASH

V současné době existuje celá řada numerických kódů použitelných k MHD výpočtům, např. PLUTO, Athena, ZEUS, VAC a další[1]. Numerický kód FLASH[2], který je vyvíjen na univerzitě v Chicagu je v současné době v komunitě zabývající se vlnami a oscilacemi v plazmatu poměrně dobře znám. Původně byl kód vyvíjen jako hydrodynamický, nyní je použitelný i pro MHD a nebo relativistické MHD (RMHD) výpočty. FLASH je napsaný v programovacím jazyce FORTRAN 90/95, je paralelizovaný a využívá tzv. Adaptive Mesh Refinement (AMR), tedy automatické zjemňování výpočetní sítě v místech s velkými skoky v různých veličinách (např. tlak, hustota, teplota, atd.), to znamená tam, kde by mohlo docházet k velkým numerickým chybám. Jedná se o kód volně šiřitelný, modulární a otevřený, tj. každý uživatel po registraci může volně části kódů upravovat a přispívat tak k celkovému vývoji. V současnosti je v něm možné využívat kartézské, cylindrické a sférické geometrie ve všech třech rozměrech. Je zde také možné provádět výpočty se započtením gravitace a zdrojových členů, např. *thermal conduction*, *heating* nebo *cooling term*. FLASH má i částicový modul a je možné provádět i například výpočty v kosmologii. V současnosti se zřejmě jedná o nejuniverzálnější numerický kód použitelný pro celou škálu astrofyzikálních aplikací.

---

[1] http://www.astrosim.net/

[2] http://flash.uchicago.edu/site/flashcode/

2.2 Studované struktury

2.2.1 Magnetická smyčka

V počátcích naší práce v oblasti MHD vln a oscilací jsme se zaměřili, z numerického hlediska, na poměrně jednoduchou strukturu ve sluneční koróně a to smyčku, reprezentovanou jako jednorozměrnou a nebo dvourozměrnou strukturu.

V publikaci **(Jelínek & Karlický 2009)** jsme se zabývali numerickými simulacemi impulzivně generovaných stojatých vln v uzavřené smyčce. Protože se v našem případě jednalo o první výpočty tohoto druhu, celý problém byl zjednodušen zanedbáním magnetického pole, z tohoto důvodu jsme vygenerovali tedy pouze akustické vlny. Celý problém byl řešen pouze v jednom rozměru, nicméně i tak se podařilo získat poměrně zajímavé výsledky. Především jsme ověřili správnost našeho numerického kódu srovnáním výsledků získaných v práci (Selwa et al. 2005). Z výpočtů je možné udělat si představu, jakým způsobem jsou generovány akustické vlny ve sluneční koróně v závislosti na poloze počátečního pulzu a také jakým způsobem dochází k úbytku energie směrem do hustších vrstev sluneční atmosféry.

Oproti předchozí práci jsme v **(Jelínek & Karlický 2010)** vytvořili numerický model smyčky v magnetickém poli ve dvou dimenzích. Ideální MHD rovnice byly řešeny pomocí Lax-Wendroffova algoritmu s umělým vyhlazováním (Sato & Hayashi 1979; Kliem et al. 2000) v programovacím jazyce FORTRAN 90/95. Protože hlavním cílem práce bylo podrobně prozkoumat chování impulzivně generovaných tzv. *wave trains*, autor také vytvořil program pro numerické výpočty disperzních relací, což je zejména důležité pro zjištění velikostí fázové a grupové rychlosti šířících se vln (Roberts 1981b; Smith et al. 1997). Za použití obou kódů jsme zjišťovali chování magnetoakustických vln v závislosti na tzv. plazma-β parametru, tedy velikosti magnetického pole orientovaného podél smyčky. Získaná data byla analyzována waveletovou metodou (Farge 1992; Torrence & Compo 1998). V souvislosti se změnou velikosti magnetického pole byla zjištěna změna tvaru tzv. *tadpole*, viz (Katsiyannis et al. 2003; Nakariakov et al. 2005), jeho velikost a příchod signálu do detekčního bodu. Tato práce tak byla vylepšením předchozích výpočtů a sloužila jako solidní základ pro naše následující, komplikovanější výpočty.

Ogrodowczyk & Murawski (2007) ve své práci zkoumali chování rychlých magnetoakustických vln v případě dvou paralelních magnetických *slabů*. Základní myšlenkou naší další práce **(Jelínek & Karlický 2015)** bylo pokusit se zjistit, jak se budou rychlé magnetoakustické vlny chovat také ve struktuře dvou *slabů*, které budou ale vnořeny jeden do druhého. Vytvořili jsme tedy strukturu o různých hustotách a hustotních profilech s různě velkým, i když stejně orientovaným magnetickým polem. Vycházeli jsme z teoretických předpokladů, že v každém takto vzniklém strukturovaném vlnovodu se bude šířit magnetoakustická vlna o odlišné periodě, neboť jak již bylo napsáno dříve, perioda je přímo úměrná pološířce struktury a nepřímo úměrná Alfvénově rychlosti. Tyto závěry byly potvrzeny, neboť analýzou vlnového signálu pomocí waveletové metody jsme zjistili dvě periody blízké teoreticky vypočítaným hodnotám. Byly také potvrzeny závěry z našich předchozích prací (Jelínek & Karlický 2012; Mészárosová et al. 2014) a to, že tvar signálu podstatně závisí na kvalitě vlnovodu. Tato zjištění mohou být velmi důležitá pro vysvětlení některých pozorování, kde byly detekovány dvě hlavní periody vlnového signálu, neboť se předpokládá, že magnetická smyčka, kterou reprezentujeme v našich modelech jako *slab* není jednoduchá, ale je strukturovaná, tj. skládá se z více struktur podobného typu, např. (Peter et al. 2013; Brooks et al. 2013; Nakariakov et al. 2016).

V naší nedávno publikované práci **(Karlický & Jelínek 2016)** jsme se zaměřili na numerické simulace kvazi-periodických procesů, generovaných teplotním (tlakovým) pulzem ve smyčce. Jednalo se o model s gravitačně stratifikovanou sluneční atmosférou a byl použit teplotní profil podle VAL-C modelu. Magnetické pole bylo generováno podobně jako v práci (Konkol et al. 2012). Na počátku výpočtu byl vygenerován tlakový (teplotní) pulz v obou zakotveních smyčky. Následkem takových pulzů se plazma z nižších vrstev atmosféry začalo pohybovat podél magnetických siločar. Vytvořily se rázové vlny, které se setkaly na vrcholu smyčky, kde se vytvořila oblast hustého a horkého plazmatu (Falewicz et al. 2015). Po této vzájemné interakci na vrcholu smyčky se tyto rázové vlny pohybovaly dále podél magnetických siločar směrem k přechodové oblasti a hustším vrstvám sluneční atmosféry. Poté byly odraženy a pohybovaly se opět v opačném směru. Ve výsledku se tyto rázové vlny „přetransformovaly" v pomalé magnetoakustické vlny, jak bylo zjištěno z rozložení magnetického a kinetického tlaku, které jsou oba v protifázi (např. Priest 1982; Aschwanden 2005). Pomocí waveletové analýzy jsme se pokusili odhadnout periody těchto pomalých magnetoakustických vln, kde jsme pro různé polohy detekčních bodů dospěli k hodnotám $40 - 170$ s, což potvrzuje i naše dřívější zjištění pro jedoduché *slaby* a to, že perioda a tvar signálu silně závisí na poloze detekčního a perturbačního bodu (Jelínek & Karlický 2012; Jelínek et al. 2012; Mészárosová et al. 2014).

2.2.2 Neutrální proudová vrstva a magnetický nulový bod

V práci **(Karlický et al. 2011)** jsme se zabývali numerickými simulacemi rychlých magnetoakustických vln a generování tzv. *narrowband dm-spikes* (Jiřička et al. 2001), přičemž výsedky byly přímo porovnávány s pozorováním ondřejovským radiospektrografem RT5. Původní myšlenkou práce bylo vysvětlit vznik *dm-spikes* generováním MHD vln ve struktuře tzv. *Harrisova curent-sheetu*, protože se jedná o strukturu vyskytující se během slunečních erupcí. Z pozorování byly určeny periody pozorovaných vln a k numerickému výpočtu jsme použili 2D MHD model, zmíněný v předchozím odstavci, ale bez započtení gravitačního pole. Jak je v práci popsáno, dosáhli jsme velmi dobré shody výsledků pozorování s výsledky z numerického modelu. V modelu jsme zanedbávali vnitřní strukturu *current-sheetu*, kde se objevuje stále větší počet dalších proudových vrstev a plazmoidů až na velikostech řádově několika metrů (Bárta et al. 2010, 2011), ale použii jsme tzv. *global current-sheet*. Proto velice důležitým výsledkem z numerických výpočtů byla představa o velikosti takového globálního *current-sheetu*, stejně jako odhady vzdálenosti perturbačního a detekčního bodu, na kterém závisí tvar a tím pádem struktura (*tadpole*) detekovaného signálu.

Práce **(Jelínek & Karlický 2012)** je věnována šíření rychlých magnetoakustických vln ve struktuře *Harrisova current-sheetu*. Z literatury, například (Roberts 1981a; Edwin & Roberts 1982; Roberts et al. 1984), je velmi dobře známa a popsána teorie šíření vln v jednoduchých magnetických *slabech*. My jsme se pokusili najít analogii mezi zmíněnými strukturami a výsledky porovnat. Abychom co nejlépe mohli analyzovat signál v detekčních bodech podél osy *current-sheetu*, počítali jsme i fázové a grupové rychlosti šířících se vln, které sloužily k odhadu příchodu prvního signálu do detekčního bodu a dalších významných bodů signálu – periodická, kvaziperiodická a útlumová fáze signálu (Roberts et al. 1984). Z globálního hlediska nebyly zjištěny velké rozdíly mezi šířením signálu v magnetickém *slabu* nebo v *current-sheetu*. Změny se projevovaly nejvíce samozřejmě v okolí středu obou struktur, což je dáno především rozdílnou konfigurací magnetického pole – v centru *current-sheetu* je nulové magnetické pole. Z hlediska pozorování jsme nalezli dvě důležitá zjištění a to, že stejně jako v případě jednoduchého *slabu* i pro *Harris current-sheet* platí vztah pro periodu signálu uvedený např. v (Roberts et al. 1984) až na multiplikativní konstantu. Z toho vyplývá, že ze zjištěných period vlnového signálu z pozorování je možné alespoň zhruba odhadnout velikost pozorované struktury. Dalším podstatným zjištěním je fakt, že *tadpoles* získané z waveletové analýzy ukazují jejich prodloužení a jejich pozdější detekci v závislosti na vzdálenosti perturbačního a detekčního bodu. To je důležité pro zjištění vzdálenosti mezi rádiovým zdrojem, jehož signál pozorováním zkoumáme a místa, kde byl takový signál vygenerován.

Rozšířením předchozí práce je **(Jelínek et al. 2012)**. V tomto případě jsme *current-sheet* umístili do gravitačního pole a sledovali jak se mění perioda a tvar detekovaného signálu. Bylo zjištěno, že perioda signálu se v gravitačním poli zvyšuje a signál získává nepravidelnější tvar. První vlastnost je dána tím, že oproti *current-sheetu* bez gravitačního pole, kde pro popis magnetického pole stačí pouze jeho vertikální složka, v gravitačním poli je třeba zavést ještě horizontální složku, která způsobí rozšiřování magnetických siločar společně s rostoucí výškou nad slunečním povrchem. Z toho důvodu má celá struktura divergentní charakter a protože perioda je přímo úměrná šířce (pološířce) takové struktury, jak bylo ověřeno v (Jelínek & Karlický 2012), následkem toho roste i perioda signálu. Nepravidelnost signálu je dána tím, že gravitačně stratifikovaná atmosféra má v každé vrstvě jiné disperzní vlastnosti a vlna se tak šíří v každé takové vrstvě rozdílně. V další části výpočtu byla změněna počáteční teplota. Tím jsme dostali rozdílné výsledky odpovídající teorii ve smyslu toho, že s klesající počáteční teplotou narůstá perioda detekovaného signálu z důvodu nárůstu hustoty a tím pádem změny Alfvénovy rychlosti, jíž je perioda signálu přímo úměrná. Hlavním cílem této práce tedy bylo vytvořit realističtější model *current-sheetu*, odpovídající skutečnosti a tím pádem docílit lepšího porovnání s pozorováními.

Práce **(Karlický et al. 2013)** se zabývá možností generování tzv. *fiber bursts* (Jiřička et al. 2001) pomocí rychlých magnetoakustických vln. V této práci jsme vytvořili dva modely – semiempirický a numerický MHD model. Smyslem obou modelů bylo vygenerovat struktury, připomínající právě *fiber bursts*, srovnatelné s pozorováními. V semiempirickém modelu je magnetoakustická vlna (konkrétně rychlá jako *sausage* mód) vygenerována pomocí perturbace magnetického pole a tlaku (hustoty) ve fázi. To je rozdíl oproti modelu prezentovanému v práci (Kuznetsov 2006), kde se vlna generuje perturbacemi zmíněných veličin v protifázi. V této části modelu se tedy vygeneroval vlnový balík, který se následně překryl s počátečním profilem hustoty a magnetického pole. Z předpokládané rádiové emise se následně vypočítalo rádiové spektrum, které bylo srovnatelné s pozorováním. V případě numerických MHD simulací jsme pro lepší porovnání získaných výsledků s pozorováními využili náš vylepšený MHD model *Harrisova current-sheetu* v gravitačně stratifikované sluneční atmosféře. Pro vygenerování vlny jsme použili rychlostní pulz gaussovského profilu (Nakariakov et al. 2004, 2005). Takto vygenerovanou vlnu jsme nechali volně šířit prostředím. Podobně jako v předchozím případě jsme vypočítali rádiové spektrum. Z naší práce vyplynulo důležité zjištění, že rychlé magnetoakustické vlny, pohybující se podél *current-sheetu* mohou vysvětlit existenci *fiber bursts*. Tento závěr jsme učinili na základě obou zmíněných modelů. Nicméně, mezi oběma modely jsou důležité rozdíly. Semiempirický model je výpočetně jednodušší a rychlejší, na druhou stranu neobsahuje mnoho fyzikálních procesů, neboť na počátku máme předpis, který již během výpočtu nelze měnit. V případě MHD simulací je situace odlišná. Jedná se sice o mnohem výpočetně náročnejší postup, ale jsou zde zahrnuty procesy které výslednou vlnu podstatně ovlivňují, například disperze prostředí, atd. Protože se v podstatě jedná o selfkonzistentní model, dostaneme z tohoto důvodu mnohem realističtější výsledky, které jsou snadněji porovnatelné s pozorováními. Nevýhodou MHD simulací, který jsme v tomto případě pozorovali, je úbytek energie ze systému, který je způsobený nedokonalostmi na hranicích vlnovodu, ve kterém se vlny šíří. Z toho důvodu pak nebylo možné vytvořit větší počet *fiber bursts*, které jsou známy z pozorování, neboť vlna která je generuje se poměrně rychle utlumí.

Další rozšíření našich modelů, týkajících se *Harrisova current-sheetu* a magnetických smyček (Jelínek & Karlický 2010, 2012; Jelínek et al. 2012), zejména o podrobnější parametrické studie prezentuje práce **(Mészárosová et al. 2014)**. V tomto případě byl použit starší model bez gravitačně stratifikované sluneční atmosféry a bez VAL-C modelu teplotního profilu. Zjišťovali jsme vliv změny velikosti počátečního pulzu na šířící se MHD vlny a dále například interakci dvou protichůdných vln. V modelu jsme pozorovali také pomalé magnetoakustické vlny (Nakariakov et al. 2000; Tsiklauri & Nakariakov 2001; Selwa et al. 2007). Zatímco rychlé magnetoakustické vlny se pohybovaly víceméně stejným způsobem jak v magnetické smyčce, tak v *current-sheetu* (Jelínek et al. 2012), pro případ pomalých magnetoakustických vln jsme zjistili změny v jejich tvaru a šíření pro oba typy magnetických struktur. Dále jsme v našich simulacích pozorovali také další vlnový mód, nazývaný jako entropický (Murawski et al. 2011), kterým jsme se podrobněji zabývali v práci popsané v následujícím odstavci.

V práci **(Jelínek et al. 2015a)** jsme se věnovali numerickým MHD simulacím entropické vlny, vygenerované v magnetickém nulovém bodě. Opět jsme používali naše vylepšené numerické modely s gravitačně stratifikovanou sluneční atmosférou a teplotním profilem atmosféry podle VAL-C modelu. Struktura magnetického pole odpovídala (Parnell et al. 1997) a na rozdíl od našich předchozích prací jsme počáteční pulz generovali v tlaku a to jak s kladnou, tak se zápornou amplitudou. Tlakový pulz magnetickém nulovém bodě odpovídá náhlému ohřevu, resp. ochlazení plazmatu, tedy uvolnění energie a akumulace plazmatu, resp. teplotní nestabilitě, která má za následek „nasátí“ plazmatu z okolí. V obou případech jsme pozorovali vznik entropické vlny. Tato vlna je v ideálním prostředí charakterizována nulovým pohybem (Goedbloed & Poedts 2004). V důsledku působení gravitačního pole se vlna v případě záporného počátečního tlakového pulzu začala pohybovat směrem k povrchu Slunce a v druhém případě – kladný počáteční pulz v tlaku – díky vztlakové síle směrem do vyšších vrstev sluneční atmosféry. Oba pohyby byly ale silně omezovány magnetickou tenzí (Lorentzovou silou). V obou případech je také velmi dobře patrná rozvíjející se Rayleigh-Taylorova nestabilita a co je nejdůležitější, podstatný nárůst elektrického proudu v magnetickém nulovém bodě, což může vést k uvolňování magnetické energie a následnému ohřevu okolního plazmatu.

Spojením pozorování a numerických simulací je práce **(Jelínek et al. 2015b)**, ve které jsme se zabývali Alfvénovými vlnami. Tyto vlny jsou všudypřítomné ve sluneční atmosféře (např. De Pontieu et al. 2007; Tomczyk et al. 2007; Jess et al. 2009; Mathioudakis et al. 2013) a numericky se jimi v poslední době zabývali např. (Chmielewski et al. 2013, 2014; Jelínek et al. 2015b). Jak již bylo napsáno v úvodní kapitole, Alfvénovy vlny jsou nekompresní, takže je není možné detekovat jako například periodické změny v hustotě, tlaku, atd. Tento typ vln je ale možné odhalit pomocí spektroskopických metod, kdy díky turbulencím dojde k rozšíření spektrálních čar, které je dobře pozorovatelné. Cílem práce bylo tedy vytvořit model, kde by byly Alfvénovy vlny přítomny a výsledky porovnat s pozorováním. Využili jsme opět naše 2D modely s gravitačně stratifikovanou sluneční atmosférou a teplotním profilem podle VAL-C modelu. Na počátku výpočtu jsme vygenerovali pulz v rychlosti, tentokrát ovšem ve směru osy z, kolmé k rovině výpočetní oblasti, ve skutečnosti se tedy jednalo o 2.5D model.

2.2.3 Otevřená struktura

Tématu otevřené magnetické struktury se věnuje práce **(Jelínek & Murawski 2013)**. Za otevřenou magnetickou strukturu můžeme samozřejmě považovat i *current-sheet*, nicméně ve zmíněné práci se jedná o magnetickou strukturu, nacházející se například v blízkosti sluneční skvrny, magnetické pole má tedy „vějířovitý“ charakter. V této práci jsme prováděli 2D numerické simulace šíření magnetoakustických vln v gravitačně stratifikované sluneční atmosféře podle VAL-C modelu. Počáteční pulz byl generován v horizontálním směru nad a pod přechodovou oblastí. V případě vygenerování horizontálního pulzu bylo zjištěno, že po určitém čase dojde ke konverzi horizontálního pobybu na pohyb vertikální, který vytvoří výtrysk plazmatu nad přechodovou oblastí, doprovázený několika menšími výtrysky a dojde k rozkmitání přechodové oblasti v blízkém okolí původního pulzu. Na druhou stranu vygenerováním pulzu nad přechodovou oblastí došlo k vytvoření víru a chladnější plazma se začalo pohybovat do vyšších částí sluneční atmosféry, zatímco teplejší směrem k povrchu. Po určité době bylo v modelu opět možné pozorovat oscilace přechodové oblasti. V obou případech jsme se snažili odhadnout periodu takových oscilací a dospěli jsme k hodnotě 180 s, tedy zhruba k tříminutovým oscilacím, pozorovaných nad slunečními skvrnami, například v UV/EUV emisi pomocí družice SDO/AIA a rádiové emisi pomocí NoRH.

2.3 Přehledová studie o vlnách a oscilacích

V letech 2013-2015 v rámci projektu „MHD Oscillations in the Solar Corona and Earth's Magnetosphere: Towards Consolidated Understanding" ISSI ve švýcarském Bernu a několika institucí vznikla společná práce **(Nakariakov et al. 2016)**. Práce je velmi obsáhlým přehledem stavu výzkumu MHD vln ve sluneční koróně a v zemské magnetosféře. Z tohoto důvodu v přehledu komentovaných prací (příloha B) jsou uvedeny pouze vybrané pasáže publikace. Hlavním cílem práce bylo podat ucelený přehled odborníkům z obou oblastí, neboť velmi často obě skupiny řeší podobné nebo dokonce stejné problémy, ale například terminologie je zcela odlišná. Tato práce si tedy klade za cíl jakési sjednocení vědomostí a znalostí z obou oborů ve světle současného stavu výzkumu.

2.4 Další cíle

V současné době je jedna práce, která již prošla recenzí, zaslána do časopisu *The Astrophysical Journal*. Ve stádiu rozpracování jsou další tři publikace týkající se vln a oscilací ve sluneční atmosféře, přičemž jedna je ke dnešnímu dni připravena k odeslání do časopisu *Space Science Reviews* a další dvě práce se předpokládají zaslat do *The Astrophysical Journal* a *Monthly Notices of the Royal Astronomical Society*.

Do budoucna bychom se dále chtěli v našich numerických simulacích zaměřit hlavně na výpočty se zavedením zdrojových členů, tj. zahrnout ve výpočtech například člen ohřevu, radiačních ztrát, atd. Naším dalším hlavním cílem je vytvářet a používat modely ve třech dimenzích, na čemž jsme již začali pracovat v současné době, ve spolupráci s AsÚ AV ČR v Ondřejově a UMCS v Lublinu v Polsku, v rámci standardního grantového projektu GAČR 16-13277S řešeného v letech $2016-2018$, jehož je autor předložené habilitační práce hlavním řešitelem.

Kapitola 3

Závěr

Předložená habilitační práce je věnována problému magnetoakustických vln ve sluneční atmosféře. První část je rešeršního charakteru, kde se autor snažil stručně popsat úvod do problematiky magnetoakustických vln v plazmatu. Ve druhé části jsou shrnuty výsledky, kterých bylo pomocí numerických simulací dosaženo. Problematika MHD vln ve sluneční atmosféře je poměrně široká a společně s rozvojem pozorování mimo Zemi (zejména družice SDO nebo SOHO) je zde tlak na numerické výpočty a teoretická vysvětlení jako podpory pozorovaných jevů. Na druhou stranu, společně s rychlým vývojem výpočetní techniky a kvalitních numerických kódů, lze těmto požadavkům velmi dobře vyhovět.

Jak již bylo uvedeno dříve, u nás se systematicky výzkumem MHD vln ve sluneční atmosféře, zejména z numerického hlediska, nikdo dlouhodobě nezabývá. Z tohoto důvodu bylo navázáno autorem množství zejména zahraničních kontaktů ve skupinách, které se již tradičně tímto problémem zabývají. Autor strávil několik měsíců na jednotlivých pracovištích, aby získal co nejvíce zkušeností, které by pak mohl samostatně aplikovat pro řešení těchto problémů v budoucnu. Je možné konstatovat, že se tento cíl poměrně dobře podařilo splnit, neboť v posledních letech se podařilo publikovat několik zásadních prací a autor je již akceptován vědeckou komunitou v tomto oboru, o čemž svědčí například nárůst citací v posledních letech, případně přednášky a semináře konané na zahraničních univerzitách a ústavech – KU Leuven v Belgii, UMCS Lublin v Polsku nebo ISSI Bern ve Švýcarsku.

Mimo to, autor v minulých letech přednesl několik popularizačních přednášek, týkajících se sluneční fyziky a vln a oscilací ve sluneční koróně a to jak na středních, tak i vysokých školách. Jako příklad můžeme uvést Gymnázium Český Krumlov, Gymnázium J. V. Jirsíka v Českých Budějovicích, Gymnázium v Jihlavě, Gymnázium v Písku, z vysokých škol pak MU v Brně, UJEP v Ústí nad Labem, Univerzita v Pardubicích a samozřejmě také Jihočeská univerzita v Českých Budějovicích. Autor vedl či konzultoval práce některých středoškolských studentů (např. J. Měšťan a J. Kotek z Gymnázia v Písku – Projekt „Catch a Star“, rok 2007 nebo M. Kosobud z Česko-anglického gymnázia v Č. Budějovicích v rámci projektu Amavet, rok 2012).

Během svého působení na Jihočeské univerzitě autor úspěšně vedl několik bakalářských a magisterských prací, věnovaných numerickým simulacím magnetoakustických vln v různých magnetických strukturách ve sluneční atmosféře. I přesto, že na Přírodovědecké fakultě JU v Českých Budějovicích není možné přímo studovat fyziku plazmatu nebo astronomii a astrofyziku, se autor pokusil ve studentech vzbudit zájem o velmi zajímavou problematiku vln a oscilací ve sluneční koróně. Z tohoto důvodu vytvořil nový jednosemestrální volitelný kurz UFY/PFA – Plazmová fyzika a astrofyzika, navazující na autorem přednášený povinný kurz UFY/AST – Astronomie a astrofyzika. Tento kurz pokrývá základy fyziky plazmatu, částečně sluneční fyziku a konečně problém vln a oscilací v plazmatu, nejen slunečním. Pro lepší orientaci studentů v těchto zajímavých, ale obtížných problémech autor napsal skripta „Magnetohydrodynamické vlny a oscilace ve sluneční koróně“.

Seznam obrázků

Literatura

Andries, J., Goossens, M., Hollweg, J. V., Arregui, I., & Van Doorsselaere, T. 2005, A&A, 430, 1109

Anfinogentov, S., Nisticò, G., & Nakariakov, V. M. 2013, A&A, 560, A107

Antia, H. M., Bhatnagar, A., & Ulmschneider, P., eds. 2003, Lecture Notes in Physics, Berlin Springer Verlag, Vol. 619, Lectures on Solar Physics, 1

Antolin, P. & Van Doorsselaere, T. 2013, A&A, 555, A74

Aschwanden, M. J. 2005, Physics of the Solar Corona. An Introduction with Problems and Solutions (2nd edition)

Aschwanden, M. J., de Pontieu, B., Schrijver, C. J., & Title, A. M. 2002, Sol. Phys., 206, 99

Aschwanden, M. J., Fletcher, L., Schrijver, C. J., & Alexander, D. 1999, ApJ, 520, 880

Avrett, E. H. & Loeser, R. 2008, ApJS, 175, 229

Banerjee, D., Gupta, G. R., & Teriaca, L. 2011, Space Sci. Rev., 158, 267

Bárta, M., Büchner, J., & Karlický, M. 2010, Advances in Space Research, 45, 10

Bárta, M., Büchner, J., Karlický, M., & Skála, J. 2011, ApJ, 737, 24

Berghmans, D. & Clette, F. 1999, Sol. Phys., 186, 207

Billings, D. E. 1966, A guide to the solar corona, New York: Academic Press

Brooks, D. H., Warren, H. P., Ugarte-Urra, I., & Winebarger, A. R. 2013, ApJ, 772, L19

Chen, F. F. 1974, Introduction to plasma physics, New York: Plenum Press

Chmielewski, P., Murawski, K., Musielak, Z. E., & Srivastava, A. K. 2014, ApJ, 793, 43

Chmielewski, P., Srivastava, A. K., Murawski, K., & Musielak, Z. E. 2013, MNRAS, 428, 40

Chung, T. J. 2002, Computational Fluid Dynamics, 1036

De Moortel, I., Ireland, J., Hood, A. W., & Walsh, R. W. 2002, A&A, 387, L13

De Moortel, I., Ireland, J., & Walsh, R. W. 2000, A&A, 355, L23

De Moortel, I. & Nakariakov, V. M. 2012, Philosophical Transactions of the Royal Society of London Series A, 370, 3193

De Pontieu, B., McIntosh, S. W., Carlsson, M., et al. 2007, Science, 318, 1574

Edwin, P. M. & Roberts, B. 1982, Sol. Phys., 76, 239

Falewicz, R., Rudawy, P., Murawski, K., & Srivastava, A. K. 2015, ApJ, 813, 70

Farge, M. 1992, Annual Review of Fluid Mechanics, 24, 395

Goedbloed, J. P., Keppens, R., & Poedts, S. 2010, Advanced Magnetohydrodynamics

Goedbloed, J. P. H. & Poedts, S. 2004, Principles of Magnetohydrodynamics

Golub, L., Bookbinder, J., Deluca, E., et al. 1999, Physics of Plasmas, 6, 2205

Golub, L. & Pasachoff, J. M. 2009, The Solar Corona, Cambridge University Press

Goossens, M., ed. 2003, Astrophysics and Space Science Library, Vol. 294, An introduction to plasma astrophysics and magnetohydrodynamics

Gruszecki, M., Nakariakov, V. M., & Van Doorsselaere, T. 2012, A&A, 543, A12

Handy, B. N., Acton, L. W., Kankelborg, C. C., et al. 1999, Sol. Phys., 187, 229

Harra, L. K., Sterling, A. C., Gömöry, P., & Veronig, A. 2011, ApJ, 737, L4

Jess, D. B., Mathioudakis, M., Erdélyi, R., et al. 2009, Science, 323, 1582

Jiřička, K., Karlický, M., Mészárosová, H., & Snížek, V. 2001, A&A, 375, 243

Katsiyannis, A. C., Williams, D. R., McAteer, R. T. J., et al. 2003, A&A, 406, 709

Kliem, B., Dammasch, I. E., Curdt, W., & Wilhelm, K. 2002, ApJ, 568, L61

Kliem, B., Karlický, M., & Benz, A. O. 2000, A&A, 360, 715

Konkol, P., Murawski, K., & Zaqarashvili, T. V. 2012, A&A, 537, A96

Kulsrud, R. M. 2005, Plasma physics for astrophysics, Princeton University Press

Kuznetsov, A. A. 2006, Sol. Phys., 237, 153

Landau, L. D. & Lifshitz, E. M. 1987, Fluid Mechanics, Second Edition: Volume 6 (Course of Theoretical Physics), 2nd edn., Course of theoretical physics / by L. D. Landau and E. M. Lifshitz, Vol. 6 (Butterworth-Heinemann)

Liu, W. & Ofman, L. 2014, Sol. Phys., 289, 3233

Liu, W., Ofman, L., Nitta, N. V., et al. 2012, ApJ, 753, 52

Liu, W., Title, A. M., Zhao, J., et al. 2011, ApJ, 736, L13

Mathioudakis, M., Jess, D. B., & Erdélyi, R. 2013, Space Sci. Rev., 175, 1

Melnikov, V. F., Reznikova, V. E., Shibasaki, K., & Nakariakov, V. M. 2005, A&A, 439, 727

Mészárosová, H., Karlický, M., & Rybák, J. 2011, Sol. Phys., 273, 393

Mészárosová, H., Karlický, M., Rybák, J., & Jiřička, K. 2009a, A&A, 502, L13

Mészárosová, H., Karlický, M., Rybák, J., & Jiřička, K. 2009b, ApJ, 697, L108

Mészárosová, H., Sawant, H. S., Cecatto, J. R., et al. 2009c, Advances in Space Research, 43, 1479

Mészárosová, H., Sawant, H. S., Cecatto, J. R., et al. 2008, in European Solar Physics Meeting, Vol. 12, European Solar Physics Meeting, ed. H. Peter, 2.105

Murawski, K. 2002, Analytical and Numerical Methods for Wave Propagation in Fluid Media, Series on stability, vibration, and control of systems (World Scientific)

Murawski, K. & Roberts, B. 1993, Sol. Phys., 144, 255

Murawski, K., Zaqarashvili, T. V., & Nakariakov, V. M. 2011, A&A, 533, A18

Nakariakov, V. M. 2004, in Astronomical Society of the Pacific Conference Series, Vol. 325, The Solar-B Mission and the Forefront of Solar Physics, ed. T. Sakurai & T. Sekii, 253

Nakariakov, V. M., Arber, T. D., Ault, C. E., et al. 2004, MNRAS, 349, 705

Nakariakov, V. M., Melnikov, V. F., & Reznikova, V. E. 2003, A&A, 412, L7

Nakariakov, V. M., Ofman, L., Deluca, E. E., Roberts, B., & Davila, J. M. 1999, Science, 285, 862

Nakariakov, V. M., Pascoe, D. J., & Arber, T. D. 2005, Space Sci. Rev., 121, 115

Nakariakov, V. M. & Verwichte, E. 2004, Astronomy and Geophysics, 45, 4.26

Nakariakov, V. M. & Verwichte, E. 2005, Living Reviews in Solar Physics, 2

Nakariakov, V. M., Verwichte, E., Berghmans, D., & Robbrecht, E. 2000, A&A, 362, 1151

Nisticò, G., Nakariakov, V. M., & Verwichte, E. 2013a, A&A, 552, A57

Nisticò, G., Verwichte, E., & Nakariakov, V. 2013b, Entropy, 15, 4520

Nitta, N. V., Schrijver, C. J., Title, A. M., & Liu, W. 2013, ApJ, 776, 58

Ofman, L., Liu, W., Title, A., & Aschwanden, M. 2011, ApJ, 740, L33

Ofman, L. & Wang, T. 2002, ApJ, 580, L85

Ogrodowczyk, R. & Murawski, K. 2007, A&A, 461, 1133

Parnell, C. E., Neukirch, T., Smith, J. M., & Priest, E. R. 1997, Geophysical and Astrophysical Fluid Dynamics, 84, 245

Pascoe, D. J. 2014, Research in Astronomy and Astrophysics, 14, 805

Pascoe, D. J., Nakariakov, V. M., & Arber, T. D. 2007, A&A, 461, 1149

Pascoe, D. J., Nakariakov, V. M., Arber, T. D., & Murawski, K. 2009, A&A, 494, 1119

Pascoe, D. J., Nakariakov, V. M., & Kupriyanova, E. G. 2013, A&A, 560, A97

Pascoe, D. J., Wright, A. N., & De Moortel, I. 2010, ApJ, 711, 990

Patsourakos, S. & Vourlidas, A. 2012, Sol. Phys., 281, 187

Peter, H., Bingert, S., Klimchuk, J. A., et al. 2013, A&A, 556, A104

Priest, E. R. 1982, Solar magneto-hydrodynamics,Dordrecht, Holland ; Boston: D. Reidel Pub. Co. ; Hingham

Roberts, B. 1981a, Sol. Phys., 69, 39

Roberts, B. 1981b, Sol. Phys., 69, 27

Roberts, B. 2000, Magnetohydrodynamic Waves, Encyclopedia of Astronomy and Astrophysics, ed. P. Murdin

Roberts, B., Edwin, P. M., & Benz, A. O. 1984, ApJ, 279, 857

Rosenbluth, M. N. & Rutherford, P. H. 1975, Physical Review Letters, 34, 1428

Sato, T. & Hayashi, T. 1979, Physics of Fluids, 22, 1189

Schrijver, C. J., Title, A. M., Berger, T. E., et al. 1999, Sol. Phys., 187, 261

Selwa, M., Murawski, K., & Solanki, S. K. 2005, A&A, 436, 701

Selwa, M., Ofman, L., & Murawski, K. 2007, ApJ, 668, L83

Severny, A. B. 2004, Solar Physics (University Press of the Pacific)

Sharapov, S. E., Alper, B., Berk, H. L., et al. 2002, Physics of Plasmas, 9, 2027

Smith, J. M., Roberts, B., & Oliver, R. 1997, A&A, 327, 377

Stepanov, A. V., Zaitsev, V. V., & Nakariakov, V. M. 2012a, Physics Uspekhi, 55, A04

Stepanov, A. V., Zaitsev, V. V., & Nakariakov, V. M. 2012b, Stellar Coronal Seismology as a Diagnostic Tool for Flare Plasma, Wiley-VCH Verlag GmbH Co. KGaA, Weinheim, Germany

Tajima, T., Sakai, J., Nakajima, H., et al. 1987, ApJ, 321, 1031

Takasao, S. & Shibata, K. 2016, ApJ, 823, 150

Thompson, B. J., Plunkett, S. P., Gurman, J. B., et al. 1998, Geophys. Res. Lett., 25, 2465

Tomczyk, S., McIntosh, S. W., Keil, S. L., et al. 2007, Science, 317, 1192

Torrence, C. & Compo, G. P. 1998, Bulletin of the American Meteorological Society, 79, 61

Tsiklauri, D. & Nakariakov, V. M. 2001, A&A, 379, 1106

Vernazza, J. E., Avrett, E. H., & Loeser, R. 1981, ApJS, 45, 635

Veronig, A. M., Gömöry, P., Kienreich, I. W., et al. 2011, ApJ, 743, L10

Wang, T., Solanki, S. K., Curdt, W., Innes, D. E., & Dammasch, I. E. 2002, ApJ, 574, L101

Wang, T. J. & Solanki, S. K. 2004, A&A, 421, L33

Yang, L., Zhang, L., He, J., et al. 2015, ApJ, 800, 111

Young, C. A. 1896, The Sun, New York, D. Appleton and company, 1896. New and rev. ed.

Yu, H., Li, B., Chen, S.-X., & Guo, M.-Z. 2015, ApJ, 814, 60

Yu, H., Li, B., Chen, S.-X., Xiong, M., & Guo, M.-Z. 2016, ApJ, 833, 51

Yu, H., Li, B., Chen, S.-X., Xiong, M., & Guo, M.-Z. 2017, ApJ, 836, 1

Yuan, D., Shen, Y., Liu, Y., et al. 2013, A&A, 554, A144

Zaitsev, V. V. & Stepanov, A. V. 2008, Physics Uspekhi, 51, 1123

Zaqarashvili, T. V., Oliver, R., & Ballester, J. L. 2005, A&A, 433, 357

Příloha A

Seznam všech autorových publikovaných prací

V následujícím seznamu jsou uvedeny veškeré autorovy práce indexované v databázi Web of Science a NASA ADS. Seznam je rozdělen do dvou částí – v první jsou publikace, které se se přímo týkají numerických simulací vln a oscilací ve sluneční koróně. Ve druhé části jsou pak uvedeny práce, zabývající se numerickými simulacemi v nízkoteplotním plazmatu a jedna práce, popisující šíření MHD vln v galaktickém halu. U každé práce je též uveden IF časopisu v roce vydání publikace a odhadovaný autorův podíl na práci.

Aktuální seznam všech autorových publikací je možné nalézt na stránkách: `http://www.researcherid.com/rid/D-4612-2014`.

A.1 Numerické simulace – vlny a oscilace ve sluneční koróně

[J1] Jelínek, P. & Karlický, M. 2009, Eur. Phys. J. D, 54, 305. (IF = 1.42), 80 %. → str. 50

[J2] Jelínek, P. & Karlický, M. 2010, IEEE Trans. Plasma Sci., 38, 2243. (IF = 1.07), 80 %. → str. 57

[J3] Karlický, M., Jelínek, P., & Mészárosová, H. 2011, A&A, 529, A96. (IF = 4.587), 40 %. → str. 63

[J4] Jelínek, P. & Karlický, M. 2012, A&A, 537, A46. (IF = 5.084), 90 %. → str. 69

[J5] Jelínek, P., Karlický, M., & Murawski, K. 2012, A&A, 546, A49. (IF = 5.084), 80 %. → str. 79

[J6] Karlický, M., Mészárosová, H., & Jelínek, P. 2013, A&A, 550, A1. (IF = 4.479), 30 %. → str. 88

[J7] Jelínek, P. & Murawski, K. 2013, MNRAS, 434, 2347. (IF = 5.226), 90 %. → str. 95

[J8] Mészárosová, H., Karlický, M., Jelínek, P., & Rybák, J. 2014, ApJ, 788, 44. (IF = 5.993), 40 %. → str. 103

[J9] Jelínek, P., Srivastava, A. K., Murawski, K., Kayshap, P., & Dwivedi, B. N. 2015, A&A, 581, A131. (IF = 4.387), 70 %. → str. 113

[J10] Jelínek, P., Karlický, M., & Murawski, K. 2015, ApJ, 812, 105. (IF = 5.993), 80 %. → str. 124

[J11] Jelínek, P. & Karlický, M. 2015, CEAB, 39, 51. 90 %. → str. 133

[J12] Nakariakov, V. M., Pilipenko, V., Heilig, B., et al. 2016, Space Sci. Rev., 200, 75. (IF = 7.242), 10 %. → str. 141

[J13] Karlický, M. & Jelínek, P. 2016, A&A, 590, A4. (IF = 5.185), 50 %. → str. 178

A.2 Numerické simulace – ostatní publikace

[J14] Hrach, R., Jelínek, P., Šimek, J., Bařina, O., & Vicher, M. 2004, Czech. J. Phys., 54, C671. (IF = 0.29), 40 %.

[J15] Jelínek, P., Šimek, J., & Hrach, R. 2006, Czech. J. Phys., 56, B809. (IF = 0.57), 80 %.

[J16] Jelínek, P. & Hrach, R. 2007, J. Phys.: Conf. Ser., 63, 012010, 90 %.

[J17] Šimek, J., Hrach, R., & Jelínek, P. 2007, Comp. Phys. Commun., 177, 137. (IF = 1.84), 20 %.

[J18] Jelínek, P., Hrach, R., & Bartoš, P. 2007, Vacuum, 82, 240. (IF = 0.88), 80 %.

[J19] Bartoš, P., Hrach, R., & Jelínek, P. 2007, Vacuum, 82, 220. (IF = 0.88), 20 %.

[J20] Jelínek, P., Virostko, P., Hubička, Z., & Bartoš, P. 2007, in American Institute of Physics Conference Series, Vol. 963, Computational Methods in Science and Engineering, ed. G. Maroulis & T. E. Simos, 1240–1243. 80 %.

[J21] Bartoš, P., Hrach, R., & Jelínek, P. 2008, Contrib. Plasma Phys., 48, 406. (IF = 1.19), 20 %.

[J22] Bartoš, P., Blažek, J., Jelínek, P., & Špatenka, P. 2009, Eur. Phys. J. D, 54, 319. (IF = 1.42), 20 %.

[J23] Jelínek, P. & Hensler, G. 2011, Comp. Phys. Commun., 182, 1784. (IF = 3.268), 90 %.

Příloha B

Kopie zahrnutých prací

V této části předložené habilitační práce jsou uvedeny všechny autorovy práce, týkající se numerických simulací vln a oscilací ve sluneční atmosféře tak, jak byly publikovány v daném časopise. Pouze poslední článek je kopií z ArXivu, neboť v době podání habilitační práce článek sice prošel recenzí, ale nebyl ještě publikován.

Eur. Phys. J. D (2009)
DOI: 10.1140/epjd/e2009-00124-7

THE EUROPEAN
PHYSICAL JOURNAL D

Regular Article

Computational study of impulsively generated standing slow acoustic waves in a solar coronal loop

P. Jelínek[1,a] and M. Karlický[2]

[1] University of South Bohemia, Faculty of Science, Branišovská 31, 370 05 České Budějovice, Czech Republic
[2] Astronomical Institute, Academy of Sciences of the Czech Republic, v. v. i., Fričova 258, 251 65 Ondřejov, Czech Republic

Received 3rd September 2008 / Received in final form 7 January 2009

Abstract. We numerically investigated standing slow acoustic waves impulsively excited in a solar coronal loop by gas pressure and mass density perturbations in one-dimensional space. The corresponding computer model is described by the hydrodynamic equations that are solved numerically by means of the so-called flux limiters methods on uniformly structured mesh. We discuss the fundamental mode and the first harmonic mode which are generated in dependence on position of the initial perturbation in the numerical box. We show how the standing slow acoustic waves are generated in the corona, where they are trapped in space between two dense layers as in the resonator, and how their energy leaks from the corona to the dense layers. We found that this leakage increases with the decrease of the density jump at the transition region. We also studied the case when the perturbation is initiated at the transition region. We found that even in this case the standing wave is formed, but their energetics is influenced by the evaporation of the plasma from the transition region into the corona.

PACS. 95.30.Lz Hydrodynamics – 94.20.wf Plasma waves and instabilities – 96.60.pf Coronal loops, streamers – 52.65.-y Plasma simulation

1 Introduction

Oscillations in solar coronal loops have been observed for a few decades. The importance of such oscillations lies in their potential for the diagnostics of solar coronal structure (magnetic field, plasma density, etc.). The waves in coronal loops were studied both observationally and theoretically [1].

The various oscillation modes in coronal loops were observed with highly sensitive instruments such as SUMER (SOHO) and TRACE. The observed oscillations include propagating [2] and standing [3] slow magnetosonic waves, as well as a branch of fast magnetosonic waves, horizontal kink [4,5], vertical kink [6] and fast sausage waves [7].

Coronal loop oscillations were studied also analytically, e.g. [8,9]. As analytical studies are unfortunately applicable only for highly idealized situations, numerical simulations are often used for solutions of more complex problems. These studies are based on numerical solutions of the full set of magnetohydrodynamic equations in one- or two-dimensions. Such a numerical approach was undertaken by a number of authors [10–16].

Above mentioned studies are very important in connection with the problem of coronal heating, solar wind acceleration, coronal seismology, etc., because identification of possible mechanisms of the mentioned processes belongs to the unsolved problems in solar physics. In the last two decades there has been intensive theoretical work undertaken to advocate the idea of coronal plasma heating by magnetohydrodynamic waves. In particular, it has been suggested that coronal loops could be heated by dissipation of high frequency slow magnetoacoustic waves [17,18].

In the presented paper we numerically study impulsively generated slow standing waves and energy leakage of these waves from coronal parts of the solar coronal loop, into more dense layers of the solar atmosphere. These studies were performed by means of a numerical code with different numerical schemes. We discuss the fundamental mode and the first harmonic mode, which are both triggered by perturbations in pressure and mass density. Some of the presented results here can be found in [14], where the authors studied among others the dependence of excitation and damping times on initial pulse positions and various mass density contrasts, etc. The FLASH code was used in this case. In our paper, first we verify these results using various numerical schemes and then we study the problem in more details. As a consequence, new aspects of this problem are found.

---

[a] e-mail: `pj@matfyz.cz`

This paper is organized as follows: in Section 2, the hydrodynamic equations are described, the philosophy of its solution is indicated and, at last, some physical assumptions as initial conditions and perturbations are presented. The next section (Sect. 3) shows the numerical results obtained by means of our computer model accompanied by discussion. Finally, we present some conclusions and future plans in Section 4.

2 Numerical model

2.1 Mathematical background

In our model we describe plasma dynamics in a coronal loop by the hydrodynamic equations:

$$\frac{\partial \varrho}{\partial t} = - \frac{\partial \varrho v}{\partial x}, \tag{1}$$

$$\varrho \frac{\partial v}{\partial t} + \varrho \left(v \frac{\partial v}{\partial x} \right) = - \frac{\partial p}{\partial x}, \tag{2}$$

$$\frac{\partial U}{\partial t} = - \frac{\partial S}{\partial x}, \tag{3}$$

here, ϱ is a mass density, v flow velocity and p is gas pressure. The plasma energy density U is given by:

$$U = \frac{p}{\gamma - 1} + \frac{\varrho}{2} v^2, \tag{4}$$

with the adiabatic coefficient $\gamma = 5/3$. The flux S is expressed as:

$$S = (U + p)\, v. \tag{5}$$

Taking the coronal loop to be along the x-direction, the velocity v and other plasma quantities only depend on time t and spatial coordinate x.

2.2 Numerical solutions

The hydrodynamic equations (1)–(3) were transformed into a conservation form, $\partial_t \mathbf{\Psi} + \partial_x \mathbf{F}(\mathbf{\Psi}) = 0$, for each of the three integration variables, $\mathbf{\Psi} = (\varrho, \varrho v, U)$ and were solved numerically.

For the numerical solution of equations in conservation form the methods of so-called flux limiters were used, e.g. minmod, van Leer or superbee method, see [19,20]. These numerical methods are able to damp down the oscillations near sharp discontinuities and jumps.

The numerical region was oriented in the x-direction, implemented at $0 \leq x \leq L$ and was covered by a uniform grid with 2500 cells. Open boundary conditions that allow a wave signal freely leave the simulation region were applied. We varied the number of grids to show that obtained results are not affected by this number.

The time step used in our calculations satisfied the Courant-Friedrichs-Levy stability condition in the form

$$\Delta t \leq \frac{CFL \Delta x}{\max(c_s + |v|)}, \tag{6}$$

where $CFL = 0.8$ is called Courant number.

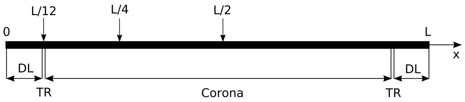

Fig. 1. The sketch of 1-D coronal loop considered to be along the x-axis. The positions of initial pulses and important parts of the coronal loop can be seen.

Table 1. Perturbations parameters.

A_p	A_ϱ	w (m)	x_0 (m)
$0.25p_0, 0.5p_0$	$0.125\varrho_0(x_0)$, $0.250\varrho_0(x_0)$	$L/40$	$L/2, L/4$

2.3 Initial conditions and perturbations

The sketch of the considered 1-D coronal loop is shown in Figure 1. Its main parts are: corona, TR (transition region), and DL (dense layer). The arrows show the positions of initial perturbations at $L/12, L/4$ and $L/2$. In the state of equilibrium, following [14], we assume initial pressure $p_0 = c_s^2 \varrho_0 / \gamma =$ const. and initial plasma velocity $v = 0$. The initial mass density profile of this loop is expressed as the function of the hyperbolic tangent, see also [14]:

$$\varrho(x) = \varrho_0 \left\{ \frac{d}{2} \left[\tanh(s(x - x_\mathrm{t})(x - L + x_\mathrm{t})) + 1 \right] + 1 \right\}, \tag{7}$$

where the quantity $s = 5 \times 10^{-14}$ m^{-1} is the slope of density, $x_\mathrm{t} = 2.842 \times 10^5$ m denotes the position of the transition region, $\varrho_0 = 10^{-12}$ kg m^{-3}, and $d = 10^5 - 10^8$. The sound speed in the solar coronal plasma $c_\mathrm{s} \approx 350$ km s^{-1}, which corresponds to the temperature of solar coronal plasma $T \sim 4 \times 10^6$ K, see e.g. [21]. Initial energy density U_0 was calculated from equation (4).

The length of the coronal loop was $L = 50$ Mm which corresponds to the loop radius of about 16 Mm. The loop foot-points were settled at positions $x = 0$ and $x = L$.

In view of our interest to study impulsively generated slow standing waves in the solar coronal loops, we have launched a pulse in the pressure and mass density in various positions – see Figure 1. The pulse had the following form:

$$\delta f(x, 0) = A_f \exp\left\{ -[(x - x_0)/w]^2 \right\}, \tag{8}$$

here $f = [p, \varrho]$, A_f is the initial amplitude of the pulse, x_0 its initial position and w is the pulse width. Values of these quantities are in Table 1.

Both pulses, i.e. in the pressure and mass density, were generated simultaneously at time $t = 0$ s. Thus, the pressure and mass density profile at this time following the form

$$f(x, 0) = f_0(x, 0) + \delta f(x, 0). \tag{9}$$

The results, presented in the next section (Sect. 3) were calculated for the perturbations parameters $A_p = 0.25p_0$ and $A_\varrho = 0.125\varrho_0(x_0)$, see Table 1.

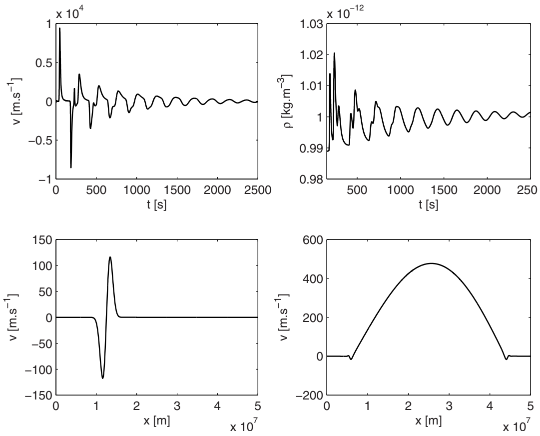

Fig. 2. Time evolution of velocity $v(x = L/4, t)$, mass density $\varrho(x = L/4, t)$ (top panels) and spatial profiles of velocity $v(x, \Delta t)$, $v(x, 7.12\ T_1)$ (bottom panels); all for mass density contrast $d = 10^8$, pulse width $w = L/40$, and initial pulse position $x_0 = L/4$.

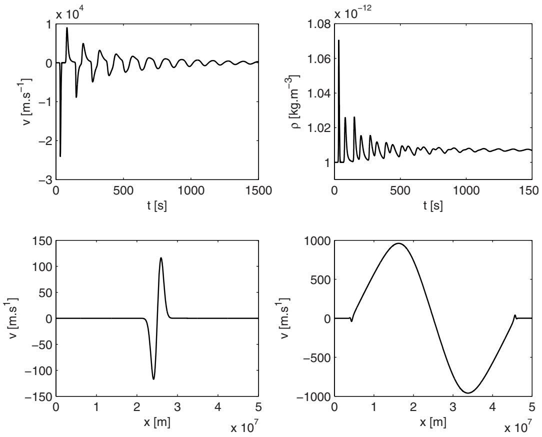

Fig. 3. Time evolution of velocity $v(x = L/4, t)$, mass density $\varrho(x = L/4, t)$ (top panels) and spatial profiles of velocity $v(x, \Delta t)$, $v(x, 7.89\ T_2)$ (bottom panels); all for mass density contrast $d = 10^8$, pulse width $w = L/40$, and initial pulse position $x_0 = L/2$.

3 Results and discussion

First we focused on the numerical methods used for the solution of the set of equations (1)–(3). We have used so-called flux limiter methods which are able to damp down the oscillations near jumps, e.g. in temperature or mass density at the transition region, etc. We tested five flux limiter methods – minmod, van Leer, van Albada, superbee and MC (monotonized central) scheme – for further information see e.g. [19]. During the test calculations, we obtained very similar results for all these methods. In the following we present the results obtained with the monotonized central (MC) scheme which is a compromise between superbee and minmod methods. We also made computations for various number of grids which showed very similar results.

In Figures 2–4, the time evolutions of velocity, mass density and spatial profiles of velocity for various initial pulses positions and in various multiples of the wave periods T_n are presented. The mass density contrast $d = 10^8$ and initial pulse width $w = L/40$ for all depicted results in mentioned figures were used. The corresponding physical process can be described as follows: after the pulse initiation, the acoustic waves in the broadband spectrum are generated. They propagate out from the pulse locations to dense layers of the coronal loop where they are reflected. The reflected waves are trapped in space between two dense layers as in the resonator catalyzing the formation of standing waves. If the initial pulse is generated at $x_0 = L/4$ or $x_0 = L/2$, the fundamental (Fig. 2) or first harmonic mode (Fig. 3) is excited in the final stage. The period T_1 is the wave period for the fundamental mode, the period T_2 is for the first harmonic mode, see equation (10), and time Δt is a time step at the start of calculation, see equation (6). As can be seen in Figures 2 and 3, the fundamental standing wave is about twice as long than the first harmonic mode. In the case of first harmonic mode is noticeable that the standing wave is attenuated more strongly than in the case of fundamental mode. Probably, it is caused by the fact that there can be observed the symmetric energy leakage of the wave into the more dense layers of the solar coronal loop [14].

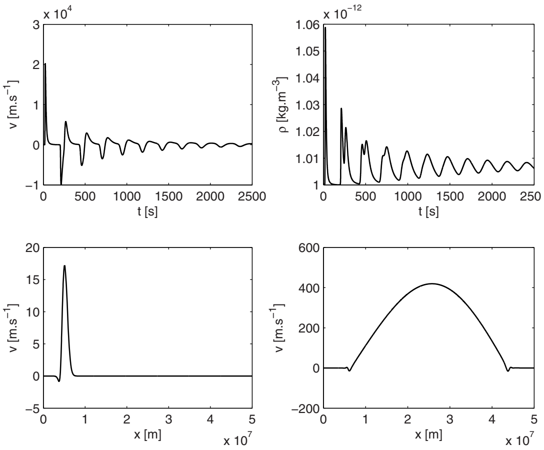

Fig. 4. Time evolution of velocity $v(x = L/4, t)$, mass density $\varrho(x = L/4, t)$ (top panels) and spatial profiles of velocity $v(x, \Delta t)$, $v(x, 18.9\ T_1)$ (bottom panels); all for mass density contrast $d = 10^8$, pulse width $w = L/40$, and initial pulse position $x_0 \approx L/12$.

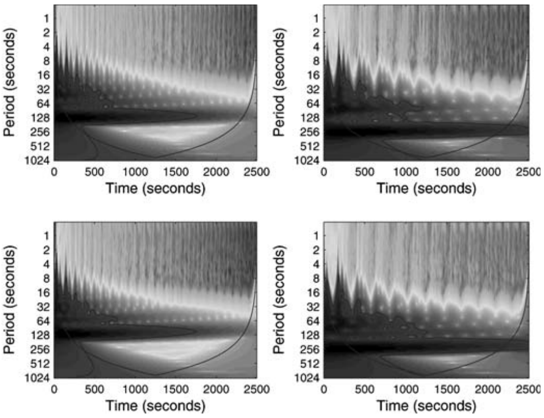

Fig. 5. Wavelet power spectra of velocities v for initial pulse position $x_0 = L/2$ (left) and $x_0 = L/4$ (right), mass density contrast $d = 10^5$ (top panels) and $d = 10^8$ (bottom panels) and pulse width $w = L/40$.

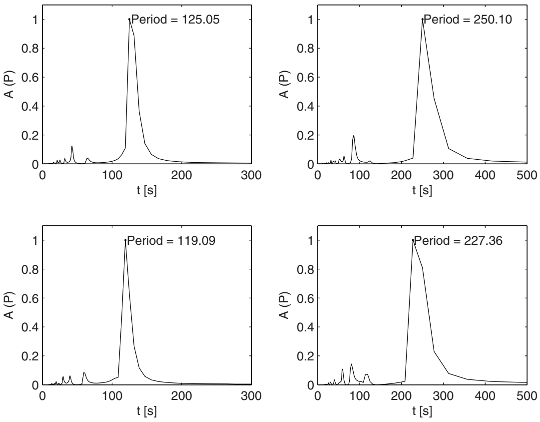

Fig. 6. Fourier power spectra of velocities v for initial pulse position $x_0 = L/2$ (left) and $x_0 = L/4$ (right), mass density contrast $d = 10^5$ (top panels) and $d = 10^8$ (bottom panels) and pulse width $w = L/40$. The amplitude of the power spectrum $A(P)$ is normalized to 1.

Table 2. Effective lengths of the solar coronal loop.

	T_2 $(d = 10^5)$	T_2 $(d = 10^7)$	T_2 $(d = 10^8)$
$L_{\rm eff}$ (Mm)	43.77	41.55	41.68

In Figure 4, similar results as in Figures 2 and 3 are shown, but the initial perturbations in pressure and mass density were launched near the transition region at the position $x_0 \approx L/12$, see Figure 1. As can be seen, the fundamental mode is excited – similarly as in the case with $x_0 = L/4$. The time evolutions of the velocity and mass density are also similar, but the wave is not attenuated so strongly. Note that the velocity of the first perturbation detected at $x = L/4$ (see Fig. 4) is about two times higher than in Figure 2; the same situation, i.e. that the first perturbation of the mass density is higher in Figure 4 than in Figure 2 can be seen.

To show details of a spectral evolution from the initial perturbation to the final standing waves, in Figure 5 the wavelet power spectra of velocities for two mass density contrasts and two initial pulse positions are presented; these cases correspond to those presented in Figures 2 and 3. As seen here the broadband spectrum of the initial perturbation evolves into the narrow spectrum of the standing waves.

These results are in agreement with the corresponding Fourier power spectra, which give more precise values of the periods of standing waves (Fig. 6). The amplitudes of the power spectra $A(P)$ are normalized to 1. As can be seen, the periods for fundamental and first harmonic standing waves were found – see the values in the graphs. The effective loop length $L_{\rm eff}$ can be calculated from the equation for the wave period of a standing wave

$$T_n = \frac{2L_{\rm eff}}{nc_{\rm s}}, \tag{10}$$

where n is the standing wave number and $c_{\rm s}$ is the sound speed. The calculated effective lengths of the coronal loop are presented in Table 2. From the obtained results in the table it is evident that if the mass density contrast d increases, the effective coronal loop length $L_{\rm eff}$ decreases. This effect can be explained by the deeper penetration of the standing wave into more dense layers of the solar atmosphere near the transition region. In the case of mass density contrast $d = 1$, the effective loop length would be equal to the initial coronal loop length L.

The Figures 7–9 present new aspects of our computations. They show the time evolutions of total, pressure and kinetic energies integrated in the whole system ($0 - 50$ Mm – upper panels), integrated in the dense layer ($0 - 4$ Mm – middle panels), and integrated in the corona ($4 - 46$ Mm – bottom panels) for three different locations of the initial pulse. Note that in all cases for total (dashed line) and pressure energy (thick line) is valid y-axis on the left side of the graph, whereas for kinetic energy the right y-axis is used. The x-axis is in the logarithmic scale.

The total energy is calculated as a sum of the pressure and kinetic energy according to equation (4). As expected (due to the high density contrast), the total energy in the whole system is conserved as shown by dashed lines in the upper panels of all figures. In all other panels (middle and bottom) the total energy has practically the same value as the pressure energy because kinetic energy is too small in comparison with it. That is why we show in these panels only the pressure and kinetic energies.

If we compare pressure and kinetic energies computed in the whole simulation region, we can see that while the pressure energy decreases, because of the pressure decrease after the pulse launch, the kinetic energy increases because of a growth of the velocity of perturbed plasma.

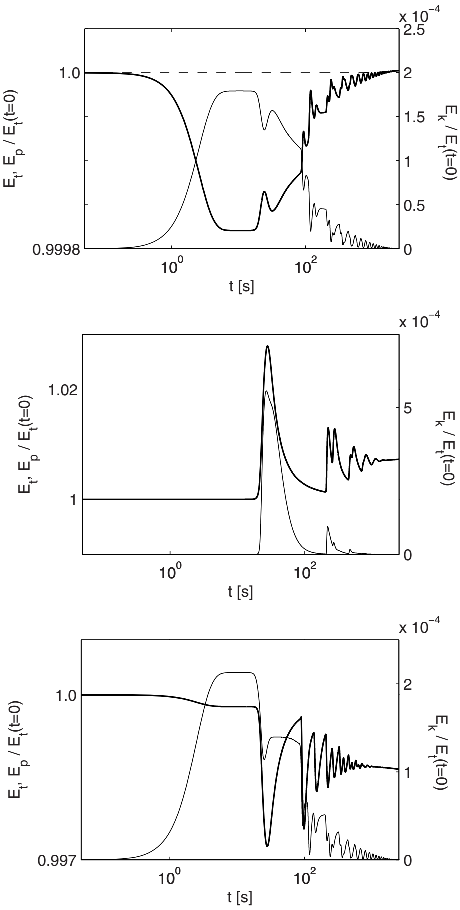

Fig. 7. Time evolution of total energy (dashed line), pressure energy (thick line) and kinetic energy. Upper panel – whole simulation region, middle panel – dense layer, bottom panel – coronal region; all for mass density contrast $d = 10^8$, pulse width $w = L/40$, and initial pulse position $x_0 = L/4$.

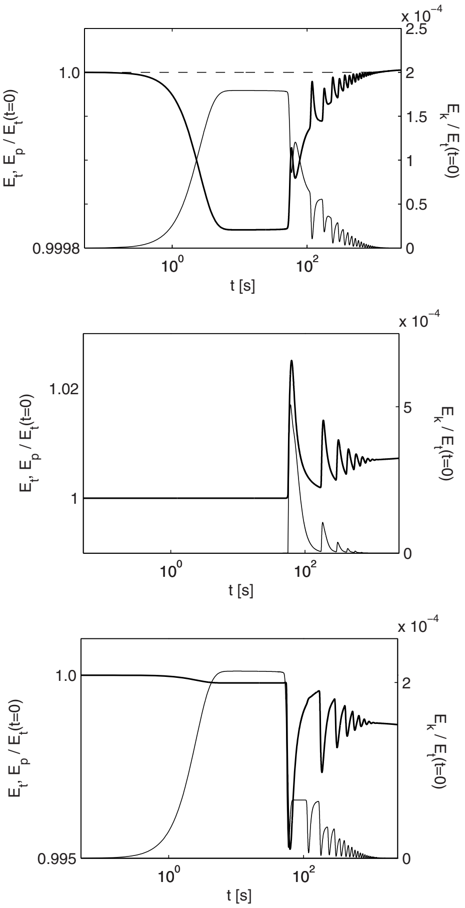

Fig. 8. Time evolution of total energy (dashed line), pressure energy (thick line) and kinetic energy. Upper panel – whole simulation region, middle panel – dense layer, bottom panel – coronal region; all for mass density contrast $d = 10^8$, pulse width $w = L/40$, and initial pulse position $x_0 = L/2$.

Practically the same situation is seen for the kinetic energies in the corona, but for initial pulse positions at $L/2$ and $L/4$ the pressure energy decreases permanently because of a leakage of the energy into dense layers of the solar atmosphere. These results show that the dense layers do not represent ideal reflecting boundaries and thus a part of the energy of these standing waves leaks into the dense layers (see also the pressure energy increase in the dense layer – middle panels in Figs. 7 and 8). We found that this leakage increases with the decrease of the density jump at the transition region.

On the other hand, for initial pulse position near the transition region, i.e. $x_0 \approx L/12$, the pressure energy in the corona increases together with the kinetic energy (Fig. 9). This is different from previous cases because the initial pulse perturbing the loop is located near the transition region and the process is thus influenced by the plasma evaporation, see the density wave moving from the transition region into the corona just after the initial perturbation (Fig. 10). We describe this process with the density wave as the plasma evaporation because it is very similar to that which is caused by the pressure enhancement in the transition layer due to the electron beam bombardment, see [22].

In the cases of the initial pulse positions at $L/4$ and $L/2$, the results for the dense layer of the solar atmosphere show that the pressure and kinetic energies vary simultaneously. It is because during the wave penetration into the dense layer both the velocity and the pressure are perturbed simultaneously. The different situation exists when

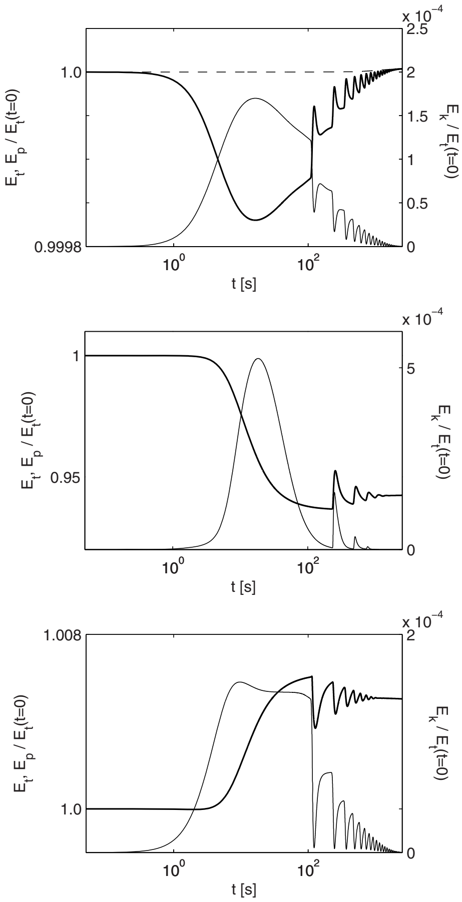

Fig. 9. Time evolution of total energy (dashed line), pressure energy (thick line) and kinetic energy. Upper panel – whole simulation region, middle panel – dense layer, bottom panel – coronal region; all for mass density contrast $d = 10^8$, pulse width $w = L/40$, and initial pulse position at $x_0 \approx L/12$.

the initial pulse is generated near the transition region. The kinetic energy increases too but the pressure energy decreases due to the evaporation process.

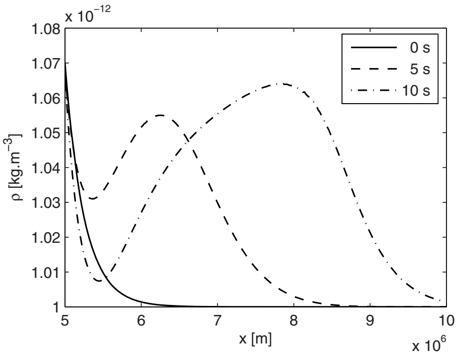

Fig. 10. Time evolution of mass density ρ in a part of solar corona close to the transition region for three subsequent times. Mass density contrast is $d = 10^8$, pulse width $w = L/40$, and initial pulse position $x_0 \approx L/12$.

4 Summary and conclusions

In this paper we considered impulsively generated slow standing waves in a solar coronal loop. The processes are described by the set of one-dimensional hydrodynamic equations that are solved numerically by means of so-called flux limiter methods.

Some results, e.g. time evolutions of velocity, mass density or energy and spatial profiles of velocity for various times are presented. The wavelet spectra show how the broadband spectrum of the initial perturbation change into the narrow spectrum of a standing wave. The fast Fourier transform was used for calculation of the wave period in the fundamental and first harmonic mode. For two types of the pulse initiation (at $L/2$ and $L/4$) we show how the standing slow acoustic waves are generated in the corona, where they are trapped in space between two dense layers as in the resonator, and how their energy leaks from the corona to the dense layers. We found that this leakage increases with the decrease of the density jump at the transition region. We also studied the case when the perturbation is located at the transition region. We found that even in this case the standing wave is formed, but their energetics is influenced by the evaporation of the plasma from the transition region.

Our presented one-dimensional model, based in principle on some results published in paper [14] (partly because of verification of our own numerical code), serves only as the basic model for the description of real physical processes which take place in the solar coronal loops. Hence, the next step in our research will be the development of a more realistic computer model by extension to the two or three spatial dimensions and inclusion before mentioned non-ideal terms – the heating term, cooling term or effects of the gravitational field. By means of this improved computer model, we could investigate effects like attenuation of waves in coronal loops under influence of gravitational force, etc.

This research has been supported by the Grant IAA300030701 of Grant Agency of the Academy of Sciences of the Czech Republic. The authors wish to thank the anonymous referees for valuable comments which improved the quality of the paper. The wavelet analysis was performed using the software written by C. Torrence and G. Compo available at URL http://paos.colorado.edu/research/wavelets.

References

1. M. Aschwanden, *Physics of the Solar Corona* (Springer, Praxis Publ., Chichester, UK, 2004)
2. I. De Moortel, J. Ireland, R.W. Walsh, A.W. Hood, Sol. Phys. **209**, 61 (2002)
3. L. Ofman, T. Wang, Astrophys. J. **580**, L85 (2002)
4. M.J. Aschwanden, L. Fletcher, C.J. Schrijver, D. Alexander, Astrophys. J. **520**, 880 (1999)
5. V.M. Nakariakov, L. Ofman, E.E. Deluca, B. Roberts, J.M. Davila, Science **285**, 862 (1999)
6. T.J. Wang, S.K. Solanki, Astron. Astrophys. **421**, L33 (2004)
7. D.J. Pascoe, V.M. Nakariakov, T.D. Arber, Astron. Astrophys. **461**, 1149 (2007)
8. L. Ofman, Astrophys. J. **568**, L135 (2002)
9. T. Van Doorsselaere, A. Debosscher, J. Andries, S. Poedts, Astron. Astrophys. **424**, 1065 (2004)
10. M. Selwa, K. Murawski, Astron. Astrophys. **425**, 719 (2004)
11. B. Kliem, M. Karlický, A.O. Benz, Astron. Astrophys. **360**, 715 (2000)
12. M. Selwa, L. Ofman, K. Murawski, Astrophys. J. **668**, L83 (2007)
13. K. Murawski, M. Selwa, L. Nocera, Astron. Astrophys. **437**, 687 (2005)
14. M. Selwa, K. Murawski, S.K. Solanki, Astron. Astrophys. **436**, 701 (2005)
15. J. Terradas, R. Oliver, J.L. Ballester, R. Keppens, Astrophys. J. **675**, 875 (2008)
16. R. Ogrodowczyk, K. Murawski, Astron. Astrophys. **467**, 311 (2007)
17. L.J. Porter, J.A. Klimchuk, P.A. Sturrock, Astrophys. J. **435**, 482 (1994)
18. G.B. Laing, P.M. Edwin, Sol. Phys. **161**, 269 (1995)
19. T.J. Chung, *Computational Fluid Dynamics* (Cambridge University Press, New York, USA, 2002)
20. K. Sankaran, L. Martinelli, S.C. Jardin, E.Y. Choueiri, Int. J. Numer. Meth. Eng. **53**, 1415 (2002)
21. E.R. Priest, *Solar Magnetohydrodynamics* (D. Reidel Publishing Company, London, England, 1982)
22. M. Karlický, Sol. Phys. **130**, 347 (1990)

Impulsively Generated Wave Trains in a Solar Coronal Loop

Petr Jelínek and Marian Karlický

***Abstract*—Impulsively generated fast magnetoacoustic wave trains in a solar coronal loop are numerically studied. The problem is considered as 2-D in space, and for the description, the full set of magnetohydrodynamic (MHD) equations is used. The numerical solution of the MHD equations is performed by means of the Lax–Wendroff algorithm on a uniformly structured mesh. The wavelet analysis of the obtained wave trains shows out the typical tadpole shapes, i.e., a narrow tail followed by a broadband head. In this paper, we discuss the propagation speed and periods of the wave trains as well as the shapes of the tadpoles in dependence on the plasma beta parameter. These studies are very important in connection with the observations because the tadpole signatures, firstly discovered during the solar eclipse in 1999 by the SECIS instrument, have been recently recognized also in decimetric type IV radio events by the Ondřejov radiospectrograph.**

***Index Terms*—Coronal loops, magnetohydrodynamics, oscillations, tadpoles, waves.**

I. INTRODUCTION

OSCILLATIONS and waves (fast and slow magnetoacoustic waves and "kink" and "sausage" modes) in solar coronal loops have been observed for a few decades and were studied both observationally and theoretically, as shown, e.g., in [1] and [2].

The various oscillation modes in the coronal loops were observed with highly sensitive instruments such as SUMER (SOHO) and TRACE as well as newer missions, e.g., EIS/Hinode or EUVI/STEREO. The observed oscillations include propagating and standing slow magnetosonic waves, as well as a branch of fast magnetosonic waves, horizontal kink, vertical kink, and fast sausage waves. The importance of such oscillations lies in their potential for the diagnostics of a solar coronal structure (magnetic field, gas density, etc.).

Both observational and theoretical studies are very important in connection with the problem of coronal heating, solar wind acceleration, coronal seismology, etc., because the identification of possible mechanisms of the mentioned processes belongs to the unsolved problems in solar physics. In the last two decades, there has been intensive theoretical work undertaken to advocate the idea of coronal plasma heating by MHD waves. In particular, it has been suggested that the coronal loops could be heated by the dissipation of the high-frequency slow magnetoacoustic waves.

The periodicity of magnetoacoustic modes of the propagating waves is formed by the time evolution of an impulsively generated signal [3]–[7]. One evident source of such a perturbance can be, e.g., the impulsive flare process (providing either single or multiple sources of disturbances). These impulsively generated magnetoacoustic waves are trapped in regions with higher density, i.e., with a low Alfvén speed, and these regions are acting as the waveguides. The amplitude and frequency modulations of these waves predicted in [4] are seen in numerical simulations.

The wavelet analysis of these impulsively generated magnetoacoustic wave trains shows the typical tadpole shape where a narrow-spectrum tail precedes a broadband head. Such tadpole signatures were observed by the SECIS instrument in the 1999 solar-eclipse data [8] and in the dm-radio bursts of gyrosynchrotron emission [9], [10]. They were found also numerically in [11] and [12].

The main aim of this paper is to generalize the results, obtained by [12], accounting for the effects of the finite plasma beta and to analyze a relationship between the initial pulses and resulting tadpoles in dependence on the plasma beta parameter in a wave-guiding solar coronal loop. The further goal is to calculate the phase and group velocities of the impulsively generated wave trains, solving analytical formulas numerically, and to compare them with the results of MHD simulations.

The structure of this paper is as follows. As the motivation of our numerical study, we shortly present in Section II our observations of the solar flares observed by the radiospectrograph in Ondřejov and the example of the detected tadpole patterns. In the first part of Section III, the MHD equations are described, and the philosophy of their numerical solution is indicated. The second part of Section III is devoted to the wave equation for plasma motions and its numerical solutions for the phase and group velocities of the waves in wave-guiding solar coronal loops. In Section IV, some physical assumptions such as initial conditions and initial perturbations are presented. Section V shows the numerical results obtained by means of our computer

Manuscript received November 30, 2009; revised April 20, 2010 and May 25, 2010; accepted May 28, 2010. Date of publication July 12, 2010; date of current version September 10, 2010. This work was supported in part by the Grant Agency of the Academy of Sciences of the Czech Republic under Grant IAA300030701 and in part by the Grant Agency of the Czech Republic under Grant P209/10/1680.

P. Jelínek is with the Department of Physics and Biophysics, Faculty of Science, University of South Bohemia, 370 05 České Budějovice, Czech Republic. He is also with the Department of Solar Physics, Astronomical Institute of Academy of Sciences of the Czech Republic, 251 65 Ondřejov, Czech Republic, and also with the Institute of Astronomy, Faculty of Earth Sciences, Geography, and Astronomy, Vienna University, 1180 Vienna, Austria (e-mail: pj@matfyz.cz).

M. Karlický is with the Department of Solar Physics, Astronomical Institute of Academy of Sciences of the Czech Republic, 251 65 Ondřejov, Czech Republic (e-mail: karlicky@asu.cas.cz).

Color versions of one or more of the figures in this paper are available online at http://ieeexplore.ieee.org.

Digital Object Identifier 10.1109/TPS.2010.2052371

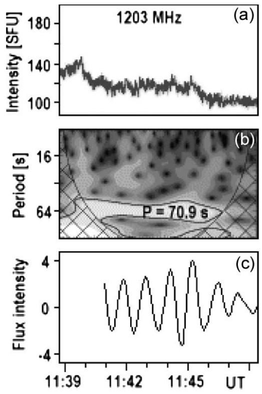

Fig. 1. Example of the tadpole detected in the radio flux on 1203 MHz during the June 13, 2001 solar flare observed by the Ondřejov radiospectrograph [14]. (a) Radio flux record. (b) Wavelet spectrum with the tadpole. (c) Radio flux computed by the inverse transform from the wavelet spectrum for the period range 40–100 s.

model accompanied by a discussion. Finally, we present some conclusions and future plans in Section VI.

II. OBSERVATIONS

In [9], [10], and [13], it was, for the first time, recognized that the wavelet spectra of some solar radio bursts consist the tadpole patterns. An example of such a tadpole with a characteristic period of 70.9 s is shown in Fig. 1.

These tadpoles are interpreted as signatures of the magnetoacoustic wave trains moving along the coronal loops and modulating the gyrosynchrotron emissions of the radio sources through a variation of the magnetic fields.

III. COMPUTER MODEL

A. Numerical Solutions of MHD Equations

In plasma physics, there exist several methods of how the plasma dynamics can be described and calculated, as shown, e.g., in [15]–[18]. In our computer model, we describe the plasma dynamics in the coronal loop by the ideal MHD equations [19]

$$\begin{aligned} \frac{\partial \varrho}{\partial t} &= -\nabla \cdot (\varrho \mathbf{v}) && (1)\\ \varrho \frac{\partial \mathbf{v}}{\partial t} + \varrho(\mathbf{v}\cdot\nabla)\mathbf{v} &= -\nabla p + \frac{1}{\mu_0}(\nabla \times \mathbf{B}) \times \mathbf{B} && (2)\\ \frac{\partial \mathbf{B}}{\partial t} &= \nabla \times (\mathbf{v} \times \mathbf{B}) && (3)\\ \frac{\partial U}{\partial t} &= -\nabla \boldsymbol{S} && (4)\\ \nabla \cdot \mathbf{B} &= 0. && (5) \end{aligned}$$

Here, ϱ is the mass density, $\mathbf{v}$ is the plasma flow velocity, p is the gas pressure, and $\mathbf{B}$ is the magnetic field. The plasma energy density U is given by

$$U = \frac{p}{\gamma - 1} + \frac{\varrho}{2} v^2 + \frac{B^2}{2\mu_0} \qquad (6)$$

with the adiabatic coefficient $\gamma = 5/3$, and the flux vector $\boldsymbol{S}$ is expressed as

$$\boldsymbol{S} = \left(U + p + \frac{B^2}{2\mu_0} \right) \cdot \mathbf{v} - (\mathbf{v}\cdot\mathbf{B}) \frac{\mathbf{B}}{\mu_0}. \qquad (7)$$

The MHD equations (1)–(4) were transformed into a flux conserving form, i.e.,

$$\frac{\partial \boldsymbol{\Psi}}{\partial t} + \frac{\partial \mathbf{F}(\boldsymbol{\Psi})}{\partial x} + \frac{\partial \mathbf{G}(\boldsymbol{\Psi})}{\partial y} = 0 \qquad (8)$$

where the vector $\boldsymbol{\Psi}$ in our 2-D case means

$$\boldsymbol{\Psi} = \begin{pmatrix} \rho \\ \rho v_{\mathrm{x}} \\ \rho v_{\mathrm{y}} \\ B_{\mathrm{x}} \\ B_{\mathrm{y}} \\ U \end{pmatrix}. \qquad (9)$$

The vector functions $\mathbf{F}(\boldsymbol{\Psi})$ and $\mathbf{G}(\boldsymbol{\Psi})$ are too complex to be presented here; for them, see, e.g., [20] or [21].

For the numerical solution of this type of equations, the two-step Lax–Wendroff algorithm [21] was used. The numerical region was oriented in the xy plane (see Fig. 2), implemented at $0 \leq x \leq L$ and $0 \leq y \leq H$, and covered by a uniform grid with 1250 cells × 300 cells. Open-boundary conditions were applied, and the time step satisfied the Courant–Friedrichs–Lewy condition in the form [21]

$$\Delta t \leq \frac{\mathrm{CFL} \cdot \Delta x}{\max\left(c_{\mathrm{s}} + |\mathbf{v}|\right)} \qquad (10)$$

where $\mathrm{CFL} = 0.8$ is called the Courant number.

B. Calculations of Phase and Group Velocities

For the calculation of the phase and group velocities of plasma waves in a solar coronal loop, we numerically solved the wave equation for plasma motions [22]–[25], where the equilibrium parameters of the loop are nonuniform along the y-coordinate

$$\frac{d}{dy}\left[f(y) \frac{dv_{\mathrm{y}}}{dy} \right] + \varrho \left(\omega^2 - k_{\mathrm{x}} v_{\mathrm{Alf}}^2 \right) v_{\mathrm{y}} = 0 \qquad (11)$$

where v_{y} is the velocity component normal to the magnetic field, ω is the frequency, k_{x} is the longitudinal wavenumber along the sheet, and the Alfvén speed $v_{\mathrm{Alf}}^2 = B^2/\mu_0\varrho$. The function $f(y)$ is expressed as

$$f(y) = \frac{\varrho c_{\mathrm{f}}^2 \left(\omega^2 - k_{\mathrm{x}}^2 c_{\mathrm{T}}^2 \right)}{\left(\omega^2 - k_{\mathrm{x}}^2 c_{\mathrm{s}}^2 \right)} \qquad (12)$$

where the tube speed c_{T} and fast speed c_{f} are implied as $c_{\mathrm{T}} = c_{\mathrm{s}} v_{\mathrm{Alf}} / (c_{\mathrm{s}}^2 + v_{\mathrm{Alf}}^2)^{1/2}$ and $c_{\mathrm{f}} = (c_{\mathrm{s}}^2 + v_{\mathrm{Alf}}^2)^{1/2}$, respectively. The singular point of (11) is called the cusp resonance or cusp singularity but not usually seen in the numerical simulations of the fast magnetoacoustic waves, as shown, e.g., in [26].

The second-order ordinary differential equation (11) is rewritten in terms of two first-order equations in the new functions ξ_1 and ξ_2

$$\xi_1 = f(y)\frac{dv_{\mathrm{y}}}{dy}, \qquad \xi_2 = v_{\mathrm{y}} \tag{13}$$

such that

$$\frac{d\xi_1}{dy} = \varrho\left(k_{\mathrm{x}} v_{\mathrm{Alf}}^2 - \omega^2\right)\xi_2 \tag{14}$$

$$\frac{d\xi_2}{dy} = \frac{\xi_1}{f(y)}. \tag{15}$$

The boundary conditions at the point $y = 0$ for the kink mode are given by $\xi_1 = 0$ and $\xi_2 = c$, and the sausage mode satisfies the conditions $\xi_1 = cf(0)$ and $\xi_2 = 0$, whereas the constant c is arbitrary.

To obtain a solution of (11), we used a fixed value of k_{x} and integrated between $y = 0$ and $y = y_{\max}$ the two first-order equations (14) and (15) by means of the Runge–Kutta fourth-order method. The exact value of the frequency ω was obtained by the bisection method when the velocity v_{y} satisfied the boundary condition at the second point $v_{\mathrm{y}}(y = y_{\max}) = 0$ for both wave modes (kink and sausage modes).

IV. INITIAL CONDITIONS AND PERTURBATIONS

The sketch of the considered 2-D solar coronal loop is shown in Fig. 2. The arrows show the positions of the initial perturbation at (L/6, H/2), the point where the data were recorded (L/2, H/2) and the orientation of the magnetic field.

The solar coronal loop in our computer model is represented by the slab with a width $w = 2$ Mm and a mass density $\varrho_{\mathrm{sl}} = d \cdot \varrho_0$, where we imposed that $d = 5$. This slab is embedded in a magnetic environment with the magnetic field given by the plasma beta parameter, as shown in Table I. Between the plasma beta parameter and the magnetic field, the relation is well known as

$$\beta = \frac{p}{p_{\mathrm{mag}}} = \frac{2\mu_0 p}{B^2}. \tag{16}$$

The magnetic field is parallel to the x-axis (see Fig. 2) and is assumed to be a constant in the whole simulation region. The mass density of the magnetic environment is $\varrho_0 = 1 \times 10^{-12}$ kg $\cdot$ m^{-3}, i.e., the corresponding electron plasma density is $n_{\mathrm{e}} \approx 6 \times 10^8$ cm^{-3} which is in agreement with the electron plasma density in the solar corona [1].

In the state of equilibrium, we assume an initial pressure $p_0 = c_{\mathrm{s}}^2 \varrho_0/\gamma = \mathrm{const.}$ and an initial plasma velocity $\mathbf{v} = 0$. Equilibrium demands that the pressure (plasma plus magnetic) is uniform, i.e.,

$$p + \frac{B^2}{2\mu_0} = \mathrm{const.} \tag{17}$$

The mass density profile in the solar coronal loop along the x-axis is considered to be a constant, and in the y-axis, the mass density profile is expressed by the formula [27]

$$\varrho(x, y) = \varrho_0 + (\varrho_{\mathrm{sl}} - \varrho_0) \cdot \mathrm{sech}^2\left[\left(\frac{y}{w}\right)^{\alpha}\right]. \tag{18}$$

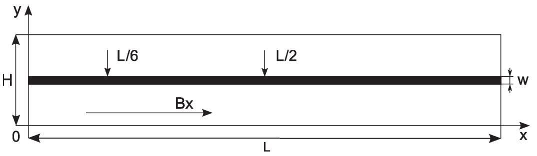

Fig. 2. Sketch of 2-D coronal loop considered to be along the x-axis. Positions of initial pulses and important parts of the coronal loop can be seen.

The power index α determines the steepness of the profile. The cases when the power index α equals either unity or infinity correspond to the symmetric Epstein profile or to the step function profile, respectively [12]. We used $\alpha = 8$ in our calculations.

The sound speed in the coronal plasma $c_{\mathrm{s}} \sim 166 \cdot T^{1/2} = 166$ km $\cdot$ s^{-1} [19], where the temperature of a solar coronal plasma $T = 1 \times 10^6$ K. The magnetic field, given by the plasma beta $B_0 = \mathrm{const.}$ and the initial energy density U_0, was calculated from (6).

As we simulate only a part of the solar coronal loop, the real length size of the computational box was $L = 100$ Mm, and the width was $H = 24$ Mm.

In view of our interest to study the impulsively generated wave trains in solar coronal loops, we have launched a pulse in the velocity in the y-axis direction. The point where the velocity was perturbed was located in (L/6, H/2) (see Fig. 2), and the pulse had the following form [11], [12]

$$v_{\mathrm{y}} = A_0 \cdot y \cdot \exp\left(-\frac{x^2}{\lambda_{\mathrm{x}}^2}\right) \cdot \exp\left(-\frac{y^2}{\lambda_{\mathrm{y}}^2}\right). \tag{19}$$

Here, A_0 is the initial amplitude of the pulse; $\lambda_{\mathrm{x}} = 1.5$ Mm and $\lambda_{\mathrm{y}} = 0.5$ Mm are the widths in the longitudinal and transverse directions, respectively. The pulse in the velocity was generated at the start of the numerical simulation at a time $t = 0$ s.

V. RESULTS

In the first part of this section, we present the results obtained by means of the 2-D MHD numerical simulations (see Figs. 3 and 4), and the second part contains the results (see Fig. 5) concerning the calculations of the phase and group velocities.

A. MHD Modeling of Impulsively Generated Wave Trains

In Table I, for various plasma betas, besides the Alfvén speed inside the slab (v_{Ai}) and outside the magnetic environment (v_{Ae}), we present the time interval dt between the start of the perturbation and the first signal detection (at the detection point) as well as the corresponding wave signal velocities expressed in ratios with the Alfvén ones (v/v_{Ai} and v/v_{Ae}).

The detection point was settled in the position at the x-axis $x = \mathrm{L}/2$ and at the y-axis $y = \mathrm{H}/2$, i.e., the distance between the point where the initial pulse was launched and the detection point was approximately 33 Mm.

TABLE I

beta	$v_{\rm Ai}$ [km/s]	$v_{\rm Ae}$ [km/s]	$v/v_{\rm Ai}$	$v/v_{\rm Ae}$	dt [s]
0.148	299	660	2.78	1.25	40.15
0.448	172	380	2.81	1.27	68.98
0.648	143	320	2.82	1.26	82.61
0.848	125	280	2.84	1.27	93.89

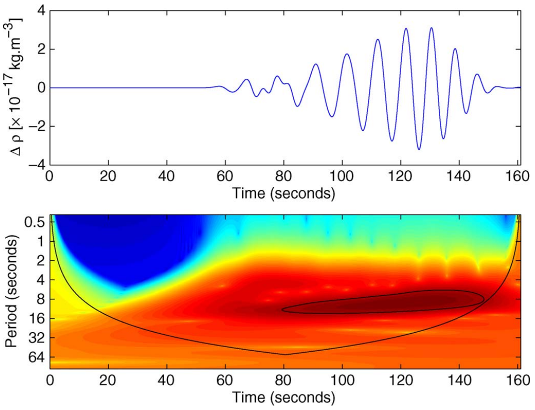

Fig. 3. Time evolution of (top panel) mass density $\varrho(x = \mathrm{L}/2,\ y = \mathrm{H}/2,\ t)$ and (bottom panel) corresponding wavelet analysis of this signal for the plasma $\beta = 0.148$. Mass density contrast $d = 5$, pulse size $\lambda_{\rm x} = 0.015$ L, $\lambda_{\rm y} = 0.021$ H, and initial pulse position $x_0 = \mathrm{L}/6$, $y_0 = \mathrm{H}/2$.

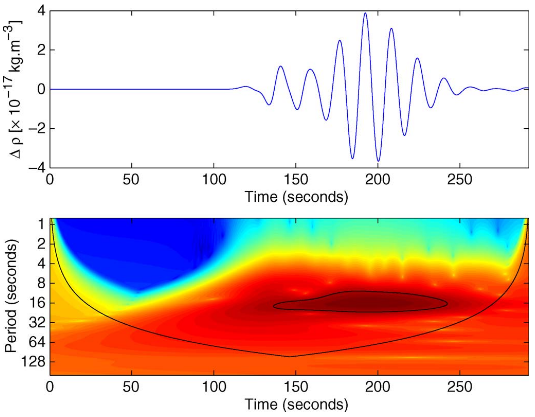

Fig. 4. Time evolution of (top panel) mass density $\varrho(x = \mathrm{L}/2,\ y = \mathrm{H}/2,\ t)$ and (bottom panel) corresponding wavelet analysis of this signal for the plasma $\beta = 0.648$. Mass density contrast $d = 5$, pulse size $\lambda_{\rm x} = 0.015$ L, $\lambda_{\rm y} = 0.021$ H, and initial pulse position $x_0 = \mathrm{L}/6$, $y_0 = \mathrm{H}/2$.

The next two figures (see Figs. 3 and 4) present the time evolution of the mass density in the detection point (top panels) and the corresponding wavelet analysis of the signal for two different plasma beta parameters (bottom panels).

The different forms of the incoming signal are evident as well as the various shapes of the tadpoles in dependence of the plasma beta parameter. By comparison of both figures, it is noticeable that the period of the signal increases with a higher plasma beta parameter.

B. Calculations of Phase and Group Velocities

In the last figure (see Fig. 5), the results obtained by the numerical calculation of (11) are shown.

Here, the group and phase velocities or the mass density for various wave modes (kink and sausage)—top panels and right lower panel, respectively, as well as the velocity $v_{\rm y}$ for different wavenumbers $k_{\rm x}$ can be seen.

VI. DISCUSSION AND CONCLUSION

In this paper, we numerically studied the impulsively generated wave trains in a solar coronal loop. Generally, this paper consists of three main parts.

The first part of this paper presents shortly our observations of the solar radio bursts and the obtained tadpole patterns and serves as the motivation of our numerical studies of the impulsively generated wave trains presented here.

The second part of this paper deals with the numerical simulations of the impulsively generated wave trains in solar coronal loops by means of solution 2-D MHD equations.

Finally, in the third part, we numerically calculated the wave equation for the plasma motion and obtained the group and phase velocities and other physical quantities, e.g., plasma velocity, plasma density, etc. This part of this paper serves as the motivation for our further study of waves under various geometrical or physical conditions.

The magnetoacoustic waves are described by the set of ideal MHD equations that are solved numerically by means of the two-step Lax–Wendroff integration scheme. We numerically studied the propagation of the signal in the solar coronal slab in dependence on the plasma beta parameter (i.e., in dependence of different magnetic fields oriented along the solar coronal loop). The obtained numerical data were analyzed by the wavelet method.

The change of the typical tadpole shape can be seen as the plasma beta parameter changes, as shown in Figs. 3 and 4. It was found that, with the increase of the plasma beta parameter, the time (dt) of the first signal arrival to a distant location increases, but the ratios of the propagation velocity with the Alfvén velocity inside and outside of the slab remain nearly the same (see Table I).

The further goal was to calculate the dispersion relation to obtain the phase and group speeds of the signal, and other physical characteristics for the kink and sausage modes, as shown in Fig. 5. This procedure allows us to estimate the speeds of the waves in solar coronal loops in various physical and geometrical configurations. These calculations presented here serve as the motivation for our further studies, and the calculations of the dispersion relations for various magnetic and geometrical configurations of solar coronal loops will be presented in our next research work.

For simplification, in this paper, we considered the model with a slab geometry. However, for the coronal loops, a cylindrical geometry is more natural. Furthermore, as shown by [25] and [28], in the long wavelength limit, the slab and cylinder models give different results for the kink mode, and that issue should be taken into account in the interpretation of

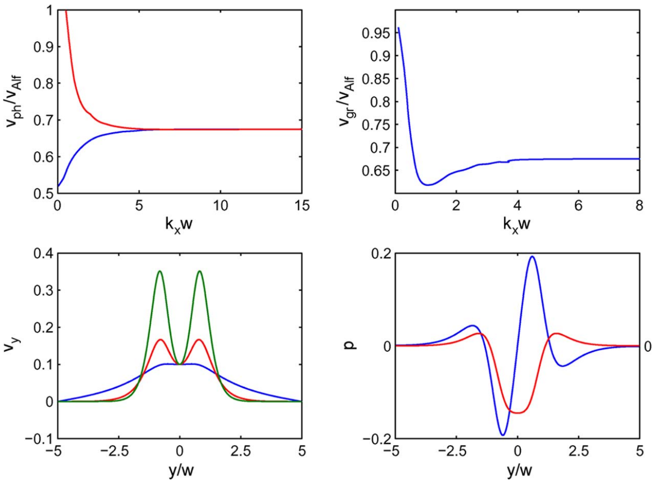

Fig. 5. (Left upper panel) Phase and (right upper panel) group speeds for (red line) kink and (blue line) sausage modes. (Left lower panel) Velocity v_y—calculated for sausage mode—for (blue, red, and green lines) $k_x w = 1, 2, 3$. (Right lower panel) Mass density for (red line) kink and (blue line) sausage modes.

the observational results. However, we are not only interested about the coronal loops; our interest is also about the current sheets [29], which, as indicated by our radio observations, could be also the waveguides of the magnetoacoustic waves. In such cases, the slab model is natural, and as made in the present simulations, we also considered higher values of the plasma beta parameter than that usually assumed in the corona.

The numerical models presented here are, in reality, the numerical tools considered for our extended study of wave trains in flare coronal loops. Varying the coronal loop structure, we plan to make a parametric study of wave trains using the presented MHD model. We will try to find the best fit between the observed parameters and the model results. To check the reality of our modeling, we will also utilize the knowledge in the phase and group velocities of specific wave modes in the considered coronal loop structure. In this way, we expect to obtain important information about the coronal loops as well as about the propagating wave trains.

Acknowledgment

The authors would like to thank the anonymous referees for the valuable comments which improved the quality of this paper. The wavelet analysis was performed using the software written by C. Torrence and G. Compo which is available at URL http://paos.colorado.edu/research/wavelets.

References

[1] M. Aschwanden, *Physics of the Solar Corona*. Chichester, U.K.: Springer-Verlag, 2004.

[2] P. Jelínek and M. Karlický, “Computational study of impulsively generated standing slow acoustic waves in a solar coronal loop,” *Eur. Phys. J. D*, vol. 54, no. 2, pp. 305–311, Aug. 2009.

[3] B. Roberts, P. M. Edwin, and A. O. Benz, “Fast pulsations in the solar corona,” *Nature*, vol. 305, no. 5936, pp. 688–690, Oct. 1983.

[4] B. Roberts, P. M. Edwin, and A. O. Benz, “On coronal oscillations,” *Astrophys. J.*, vol. 279, pp. 857–865, Apr. 1984.

[5] K. Murawski and B. Roberts, “Numerical simulations of fast MHD waves in a coronal plasma. II—Impulsively generated linear waves,” *Sol. Phys.*, vol. 144, no. 1, pp. 101–112, 1993.

[6] K. Murawski and B. Roberts, “Numerical simulations of fast MHD waves in a coronal plasma. IV—Impulsively generated nonlinear waves,” *Sol. Phys.*, vol. 145, no. 1, pp. 65–75, 1993.

[7] K. Murawski and B. Roberts, “Time signatures of impulsively generated waves in a coronal plasma,” *Sol. Phys.*, vol. 151, no. 2, pp. 305–317, May 1994.

[8] A. C. Katsiyannis, D. R. Williams, R. T. J. McAteer, P. T. Gallagher, F. P. Keenan, and F. Murtagh, “Eclipse observations of high-frequency oscillations in active region coronal loops,” *Astron. Astrophys.*, vol. 406, no. 2, pp. 709–714, Aug. 2003.

[9] H. Mészárosová, H. S. Sawant, J. R. Cecatto, J. Rybák, M. Karlický, F. C. R. Fernandes, M. C. de Andrade, and K. Jiřička, “Coronal fast wave trains of the decimetric type IV radio event observed during the decay phase of the June 6, 2000 flare,” *Adv. Space Res.*, vol. 43, no. 10, pp. 1479–1483, May 2009.

[10] H. Mészárosová, M. Karlický, J. Rybák, and K. Jiřička, “Tadpoles in wavelet spectra of a solar decimetric radio burst,” *Astrophys. J.*, vol. 697, no. 2, p. L108, Jun. 2009.

[11] V. M. Nakariakov, D. J. Pascoe, and T. D. Arber, “Short quasi-periodic MHD waves in coronal structures,” *Space Sci. Rev.*, vol. 121, no. 1–4, pp. 115–125, Nov. 2005.

[12] V. M. Nakariakov, T. D. Arber, C. E. Ault, A. C. Katsiyannis, D. R. Williams, and F. P. Keenan, “Time signatures of impulsively generated coronal fast wave trains,” *Mon. Not. R. Astron. Soc.*, vol. 349, no. 2, pp. 705–709, 2004.

[13] H. Mészárosová, M. Karlický, J. Rybák, and K. Jiřička, “Drifting tadpoles in wavelet spectra of decimetric radio emission of fiber bursts,” *Astron. Astrophys.*, vol. 502, no. 2, pp. L13–L15, 2009.

[14] K. Jiřička, M. Karlický, O. Kepka, and A. Tlamicha, “Fast drift burst observations with the new Ondřejov radiospectrograph,” *Sol. Phys.*, vol. 147, no. 1, pp. 203–206, Sep. 1993.

[15] P. Jelínek, J. Šimek, and R. Hrach, “Computational study of processes in plasma sheaths surrounding probes of various geometries,” *Czech. J. Phys.*, vol. 56, pp. B809–B814, Oct. 2006.

[16] P. Jelínek, R. Hrach, and P. Bartoš, “Techniques for computational study of plasma–solid interaction at higher pressures,” *Vacuum*, vol. 82, no. 2, pp. 240–243, Oct. 2007.

[17] P. Bartoš and R. Hrach, “The influence of collision effects in DC glow discharge in argon plasma on the sheath formation,” *Czech. J. Phys.*, vol. 56, pt. 4, Suppl. B, pp. B638–B643, 2006.

[18] R. Hrach, P. Bartoš, and V. Hrachová, “Computational study of plasma-surface interaction in plasma-assisted technologies,” *Eur. Phys. J. D*, vol. 54, no. 2, pp. 417–423, Aug. 2009.

[19] E. R. Priest, *Solar Magnetohydrodynamics*. London, U.K.: Reidel, 1982.

[20] K. Sankaran, L. Martinelli, S. C. Jardin, and E. Y. Choueiri, "A flux-limited numerical method for solving the MHD equations to simulate propulsive plasma flows," *Int. J. Numer. Methods Eng.*, vol. 53, pp. 1415–1432, 2002.

[21] T. J. Chung, *Computational Fluid Dynamics*. New York: Cambridge Univ. Press, 2002.

[22] J. M. Smith, B. Roberts, and R. Oliver, "Magnetoacoustic wave propagation in current sheets," *Astron. Astrophys.*, vol. 327, pp. 377–387, 1997.

[23] B. Roberts, "Wave propagation in a magnetically structured atmosphere I: Surface waves at a magnetic interface," *Sol. Phys.*, vol. 69, no. 1, pp. 27–38, Jan. 1981.

[24] B. Roberts, "Wave propagation in a magnetically structured atmosphere II: Waves in a magnetic slab," *Sol. Phys.*, vol. 69, no. 1, pp. 39–56, Jan. 1981.

[25] P. M. Edwin and B. Roberts, "Wave propagation in a magnetically structured atmosphere III: The slab in a magnetic environment," *Sol. Phys.*, vol. 76, no. 2, pp. 239–259, Mar. 1982.

[26] V. I. Zhukov, "Wave transformation at the cusp resonance in a finite conductivity isothermal atmosphere permeated by a nearly horizontal magnetic field," *Astrophys. Space Sci.*, vol. 154, no. 2, pp. 247–254, Apr. 1989.

[27] V. M. Nakariakov and B. Roberts, "On fast magnetosonic coronal pulsations," *Sol. Phys.*, vol. 159, no. 2, pp. 399–402, Jul. 1995.

[28] P. M. Edwin and B. Roberts, "Wave propagation in a magnetic cylinder," *Sol. Phys.*, vol. 88, no. 1/2, pp. 179–191, Oct. 1983.

[29] P. M. Edwin, B. Roberts, and W. J. Hughes, "Dispersive ducting of MHD waves in the plasma sheet: A source of Pi2 wave bursts," *Geophys. Res. Lett.*, vol. 13, no. 4, pp. 373–376, 1986.

Petr Jelínek was born in Písek, Czech Republic, in 1979. He received the Ph.D. degree from Charles University in Prague, Prague, Czech Republic, in 2007.

Since 2009, he has been an Assistant Professor with the Department of Physics and Biophysics, Faculty of Science, University of South Bohemia, České Budějovice, Czech Republic. He is also currently a Postdoctoral Research Fellow with the Institute of Astronomy, Faculty of Earth Sciences, Geography, and Astronomy, Vienna University, Vienna, Austria, and also currently has a part-time job with the the Department of Solar Physics, Astronomical Institute of Academy of Sciences of the Czech Republic, Ondřejov, Czech Republic.

Marian Karlický was born in Frýdek-Místek, Czech Republic, in 1949. He received the CSc. and DrSc. degrees from the Academy of Sciences of the Czech Republic, Ondřejov, Czech Republic, in 1981 and 1992, respectively.

He was an Associate Professor with Charles University in Prague, Prague, Czech Republic. Since 1974, he has been with the Astronomical Institute, Academy of Sciences of the Czech Republic.

A&A 529, A96 (2011)
DOI: 10.1051/0004-6361/201016171

Astronomy & Astrophysics

Magnetoacoustic waves in the narrowband dm-spikes sources

M. Karlický[1], P. Jelínek[2], and H. Mészárosová[1]

[1] Astronomical Institute of the Academy of Sciences of the Czech Republic, 25165 Ondřejov, Czech Republic
e-mail: `karlicky@asu.cas.cz`
[2] University of South Bohemia, Faculty of Science, 37005 České Budějovice, Czech Republic

Received 19 November 2010 / Accepted 22 February 2011

ABSTRACT

Aims. A new type of analysis of the narrowband dm-spikes in solar radio radiation is introduced to look for magnetoacoustic waves in their sources.
Methods. The Fourier and wavelet methods were used. For the first time, the tadpole structures in the wavelet spectra of this radio emission were searched for.
Results. Fifteen groups of the narrowband dm-spikes, observed during solar flares, were selected and analyzed by the Fourier and wavelet analysis methods. We found that the mean Fourier spectra of these spikes in frequency space are the powerlaws with a power-law index in the range $-1.2 - -1.8$. Furthermore, their wavelet spectra based on time series reveal tadpoles at some frequencies, which indicates the presence of magnetoacoustic waves. These waves are interpreted as propagating through a source of the narrowband dm-spikes. It is proposed that the spikes are generated by driven coalescence and fragmentation processes in turbulent reconnection outflow. This interpretation is supported by a simultaneous observation of drifting pulsating structures (DPSs) and spikes. Finally, modeling of the magnetoacoustic waves and tadpoles in the Harris current sheet supports this interpretation.

Key words. Sun: corona – Sun: flares – Sun: radio radiation

1. Introduction

The radio narrowband decimetric spikes belong to the most interesting radio bursts with exceptionally high brightness temperatures ($T_\mathrm{b} \approx 10^{15}$ K) and short durations ($\leq$0.1 s, see the review by Benz 1986). Their observational characteristics have been described in many papers (e.g. Slottje 1981; Karlický 1984; Fu et al. 1985; Stähli & Magun 1986; Benz et al. 1982; Zlobec & Karlický 1998; Mészárosová et al. 2003). On the other hand, the theoretical models can be divided into two groups: a) those based on the plasma emission and acceleration processes (Kuijpers et al. 1981; Tajima et al. 1990; Wentzel 1991; Bárta & Karlický 2001), and b) those based on the electron-cyclotron maser (Holman et al. 1980; Melrose & Dulk 1982; Vlahos & Sharma 1984; Winglee et al. 1988; Aschwanden 1990; Fleishman & Yastrebov 1994; Fleishman & Melnikov 1998). To distinguish between these two types of models, polarization and harmonic structures of the spikes have also been studied (Güdel 1990; Güdel & Zlobec 1991; Krucker & Benz 1994).

Searching for a characteristic bandwidth of individual spikes Karlický et al. (1996, 2000) found that the Fourier transform of the dynamic spectra of spikes have a power-law form with power-law indices close to $-5/3$. Based on these results, Bárta & Karlický (2001) propose that the spikes are generated in turbulent reconnection outflows at positions where the upper hybrid frequency is equal to the low harmonics of the electron cyclotron frequency (double resonance). The instability is driven by electron beams accelerated in the reconnection diffusion region. However, new findings of the cascading (fragmented) reconnection (Bárta et al. 2010a,b) lead us to a partial modification of this model, as seen the following.

Recently, Mészárosová et al. (2009a,b) used a new technique based on the wavelet analysis, to detect, for the first time, the tadpoles in the wavelet spectra (interpreted as the magnetoacoustic waves) in some radio sources. The magnetoacoustic waves are trapped in regions with higher density that act as waveguides. If these waves are impulsively triggered at some given location, then at some distance from the initiation site, these propagating waves (owing to their dispersion characteristics) can be detected as the tadpole structure in their wavelet spectra; for details, see e.g. Nakariakov et al. (2004).

Because the magnetoacoustic waves can be easily triggered in the reconnection and because we proposed that the spikes are generated during the reconnection process (Bárta & Karlický 2001), we decided to search for the magnetoacoustic waves in the spike sources (tadpoles in the wavelet spectra of radio fluxes), thereby supporting our model.

As shown in the following, we found these tadpoles (waves) in all studied groups of spikes. Then we simulated these waves and tadpoles in the model with the Harris current sheet. Finally, the results are discussed and a conclusion drawn.

2. Observations and data analysis

We selected 15 dm-radio events with the spikes recorded by the Ondřejov radiospectrograph (Jiřička et al. 1993) during the years 1997–2003 in the frequency range 0.8–2.0 MHz. The times of their observations, GOES X-ray, and Hα characteristics of associated events are presented in Table 1. A typical example of these spikes, observed at 12:45:10–12:45:53 UT in 2003 August 5, is shown in Fig. 1.

First, we analyzed all of the selected groups of spikes (Table 1) using the same method as described in the paper by Karlický et al. (1996). The radiospectrograms were resampled

Table 1. Radio events with the narrowband dm-spikes and characteristics of associated flares.

No.	Flare	Radio Start [UT]	End [UT]	GOES Start [UT]	Max [UT]	End [UT]	X-ray Imp.	Optic. Imp.	Hα Position	NOAA AR #
1	1997 Sep. 12	16:05	16:07	16:00	16:06	16:17	C6.0			
2	1997 Nov. 3	09:05	09:06	09:03	09:10	09:13	M1.4			
3	2000 Feb. 22	13:00	13:02	12:46	12:49	13:21	C2.1			
4	2000 Apr. 15	13:40	13:41	13:38	13:43	13:50	C3.0	SF	S22 E29	8955
5	2000 May 15	10:48	10:50	10:46	10:50	10:56	M1.2			
6	2000 May 30	10:29	10:31	09:54	10:18	10:40	C8.6			
7	2000 Jul. 8a	07:32	07:34	07:29	07:34	07:39	C6.1	1N	N17 W07	9070
8	2000 Jul. 8b	07:58	08:00	07:29	07:34	07:39	C6.1	SF	S22 E15	9073
9	2001 Mar. 25	11:07	11:09	10:33	11:16	11:20	M2.6	1N	N21 E59	9401
10	2001 Mar. 28	12:07	12:26	12:03	12:10	12:17	C6.0			
11	2002 Dec. 20a	10:47	10:49	10:45	10:49	10:53	C1.2			
12	2002 Dec. 20b	11:26	11:28	11:25	11:28	11:30	C2.7			
13	2003 Mar. 18	12:06	12:08	11:51	12:08	12:20	X.1.5	1B	S15 W46	10314
14	2003 Jun. 10	08:34	08:37	08:34	08:37	08:40	M2.7	1N	N12 W44	10375
15	2003 Aug. 5	12:45	12:46	12:43	12:49	12:51	M1.7	SN	S16 E33	10424

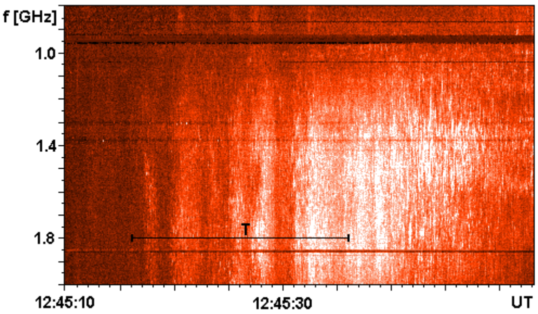

Fig. 1. Typical radio dynamic spectrum (0.8–2.0 GHz) showing the narrowband dm-spikes observed by the Ondřejov radiospectrograph at 12:45:10–12:45:53 UT on 2003 August 5. Tadpole wavelet patterns were recognized in the time interval T (12:45:16–12:45:36 UT).

along the frequency axis according to the formula

$$z(f) = H_\mathrm{n} \ln \frac{f}{f_0}, \tag{1}$$

where $z(f)$ is the height in the solar atmosphere in dependence on frequency f, H_n is the density height-scale for the radio emission by the plasma emission mechanism, and $f_0 = 2$ GHz in our case (for details see Karlický et al. 1996). After that, the spectrum areas for spikes and background noise were chosen and the time-averaged power spectra along the height axis $P(k)$ (where the wavenumber k is in units of H_n^{-1}) were computed. The power spectra at high wavenumbers (here for $\log\ k > 2.5$) are likely to be affected by the background noise. Therefore the power spectra were “corrected” for the background noise contribution by subtracting this component. This is not a precise method, but it can help us to estimate the behavior of the signal power spectra also at high wave numbers.

The computed power-law index for all spikes groups (second column in Table 2) ranges from −1.2 to −1.8 (−1.5 on average). An example of the 1-D Fourier spectrum versus the distance scale k (after the substraction of the noise power spectra) for the 2003 August 5 event is presented in Fig. 2. The straight dashed line with the power-law index −5/3 is added for comparison.

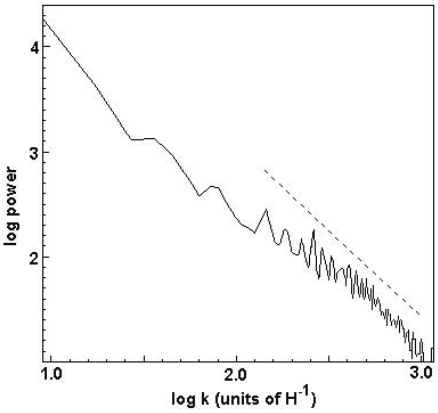

Fig. 2. The 1-D Fourier spectrum for the 2003 August 5 event versus the distance scale k (see text). The straight dashed line denotes the line with the power-law index −5/3 for comparison.

Table 2. Power-law indices of the Fourier spectra of the narrowband dm-spikes and parameters of associated wavelet tadpoles.

No.	Spikes Power-law index of spikes	Tadpoles Start time [UT]	Duration [s]	Period [s]
1	−1.8	16:05:55	20	5.1
2	−1.2	09:07:10	32	5.7
3	−1.4	13:00:49	13	3.6
4	−1.7	13:40:09	27	5.8
5	−1.3	10:48:33	09	3.3
6	−1.3	10:29:55	18	4.1
7	−1.3	07:32:50	23	5.0
8	−1.3	07:58:51	10	3.4
9	−1.7	11:07:48	13	3.8
10	−1.5	12:08:10	16	6.0
11	−1.6	10:47:59	16	3.3
12	−1.6	11:26:42	25	6.5
13	−1.8	12:07:01	23	5.5
14	−1.7	08:35:51	31	4.9
15	−1.4	12:45:16	20	6.3
mean	−1.5		20	4.8

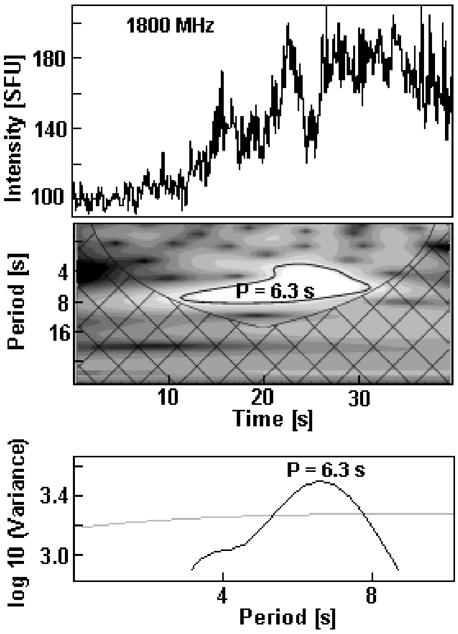

Fig. 3. Typical example of the tadpole detected at the radio frequency 1800 MHz in the interval T (see Fig. 1). *Upper panel* shows original time series (2003 August 5 event). *Middle panel* shows its wavelet power spectrum with the tadpole pattern (characteristic period P = 6.3 s) outlined by a contour at the 99% confidence level. *Bottom panel* shows the global wavelet spectrum (black line) with the maximum for the period P = 6.3 s. The gray line means the 99% significance level.

Then, we searched for tadpoles in the wavelet spectra as signatures of magnetoacoustic waves in all spikes events (Table 1) at all recorded frequencies. We used the methods described in the papers by Mészárosová et al. (2009a,b). To be sure that these tadpoles belong to studied spikes we focused only on the dominant tadpoles with the shortest characteristic periods $P < 10$ s. The basic characteristics of these tadpoles are in Table 2. The tadpole period P and duration range from 3.4 to 6.5 s (4.8 s on average) and from 9 to 32 s (20 s on average), respectively. A typical example is presented in Fig. 3 where the upper panel shows the radio flux observed on 1800 MHz during the 2003 August 5 event in the interval T, see Fig. 1. Middle panel shows its wavelet power spectrum with the tadpole pattern (characteristic period P = 6.3 s) outlined by contour at the 99% confidence level. Bottom panel shows the global wavelet spectrum (black line) with the maximum for the period P = 6.3 s. The gray line means the 99% significance level.

3. Modeling of magnetoacoustic waves and tadpoles in the narrowband dm-spikes sources

3.1. Interpreting the narrowband dm-spikes

As presented above the mean Fourier spectra (made along the frequency) in all studied groups of spikes are the power-law ones with the power-law index in the range −1.2–−1.8. This (for larger set of spike events than in previous studies) confirms our previous result (Karlický et al. 1996, 2000) that these spectra have a power-law index close to −5/3 (=−1.66), which in known as the Kolmogorov index of MHD turbulence.

An entirely new result is that in all spike events (at least at limited ranges of frequencies) we found the tadpoles, which indicate the presence of propagating magnetoacoustic waves. Their mean period is about 5 s. Because the magnetoacoustic waves are a natural part of the turbulent outflow, we consider these waves as those supporting the model of spikes in the region of the magnetic reconnection outflows (Bárta & Karlický 2001).

To interpret these results we propose the model shown in Fig. 4. It is based on "the standard" CSHKP flare model (e.g. Magara et al. 1996 and references therein). In accordance with Shibata and Tanuma (2001), the global current sheet is stretched by rising magnetic rope and fragmented by the tearing-mode instability to smaller and smaller plasmoids (in 2-D O-type magnetic field structures, in 3-D magnetic ropes) and current sheets. This fragmentation (cascading) process produces very narrow current sheets (down to a few meters) with very high current densities, where the anomalous resistivity is generated and fast reconnection occurs. Moreover, in the model, the plasmoids are accumulated and compressed in turbulent reconnection-plasma outflows, especially in the region above the flare loop arcade. These plasmoids have different sizes. They are driven by outflows to interact and coalesce into larger ones and are also fragmented into smaller plasmoids. That is to say, a new current sheet is formed between two merging plasmoids and new smaller plasmoids are generated in this current sheet, on smaller and smaller spatial scales. We called this process driven coalescences and fragmentations (Fig. 4). For more details, see Bárta et al. (2010b).

Furthermore, Karlický & Bárta (2007) and (Karlický et al. 2010) have shown that each coalescence process accelerates electrons that generate plasma waves, as well as the electromagnetic ones. Considering all these facts, we propose that the narrowband dm-spikes are generated by the driven coalescence and fragmentation processes of plasmoids in the turbulent reconnection outflows. The observation shown in Fig. 5 supports this interpretation. As seen here, the drifting pulsating structures (DPSs) at the 1.0–1.8 GHz frequency range drift towards higher frequencies (towards lower heights in the solar atmosphere), where the spikes are observed. The DPSs indicate the plasmoids moving downwards in the solar atmosphere (Bárta et al. 2008a,b), towards the spikes source, in agreement with the scenario presented in Fig. 4.

Furthermore, we assume that the global reconnection process can be perturbed by e.g. some inhomogeneity in the reconnection inflows and thus to generate magnetoacoustic waves propagating into the spikes source (see Fig. 4). These waves can easily modulate the coalescence processes among plasmoids and thus to modulate electron acceleration and subsequent production of spikes.

To support this interpretation, we take the Harris current sheet as a simple model of the magnetic field and density structure of the global current sheet, which includes reconnection outflows. The current sheets, in which the fast reconnection occurs, are only tiny substructures of the global current sheet, and these substructures are neglected in the following computations. The global current sheet is perturbed at one location, and then at some distant location from the first one, the propagating magnetoacoustic waves and the corresponding tadpoles are analyzed. The parameters of tadpoles depend on the parameters of the model. On the other hand, these simulated tadpoles, which fit the observed ones, give us information about parameters of the global current sheet where the spikes are generated.

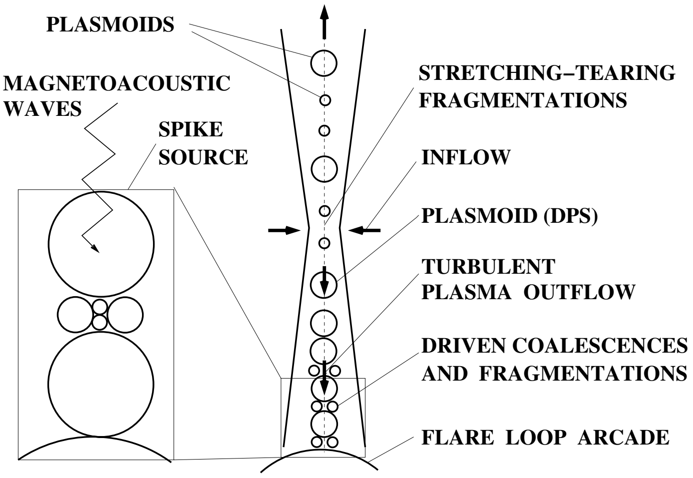

Fig. 4. Scenario of the dm-spike generation in the flare current-sheet reconnection and magnetoacoustic waves propagation. Compare with Fig. 5.

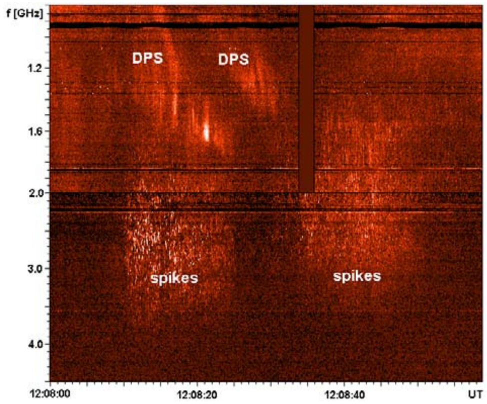

Fig. 5. Composite radio spectrum from two Ondřejov radiospectrographs (0.8–2.0 and 2.0–4.5 GHz) showing the positively drifting pulsating structures (DPSs) and narrowband dm-spikes observed on 2001 March 28. The 0.8–2.0 GHz spectrum was shortly interrupted at 12:08:34–12:08:36 UT. Compare with Fig. 4.

3.2. Numerical model

3.2.1. Model equations

In our model we describe plasma dynamics by the ideal magnetohydrodynamic equations (Priest 1982; Chung 2002):

$$\frac{\partial \varrho}{\partial t} = -\nabla \cdot (\varrho \boldsymbol{v}), \qquad (2)$$

$$\varrho \frac{\partial \boldsymbol{v}}{\partial t} + \varrho (\boldsymbol{v} \cdot \nabla) \boldsymbol{v} = -\nabla p + \frac{1}{\mu_0} (\nabla \times \boldsymbol{B}) \times \boldsymbol{B}, \qquad (3)$$

$$\frac{\partial \boldsymbol{B}}{\partial t} = \nabla \times (\boldsymbol{v} \times \boldsymbol{B}), \qquad (4)$$

$$\frac{\partial U}{\partial t} = -\nabla \boldsymbol{S}, \qquad (5)$$

$$\nabla \cdot \boldsymbol{B} = 0. \qquad (6)$$

Here ϱ is a mass density, $\boldsymbol{v}$ flow velocity, p gas pressure, and $\boldsymbol{B}$ is the magnetic field. The plasma energy density U is given by

$$U = \frac{p}{\gamma - 1} + \frac{\varrho}{2} v^2 + \frac{B^2}{2\mu_0}, \qquad (7)$$

with the adiabatic coefficient $\gamma = 5/3$, and the flux vector $\boldsymbol{S}$ is expressed as

$$\boldsymbol{S} = \left(U + p + \frac{B^2}{2\mu_0} \right) \boldsymbol{v} - (\boldsymbol{v} \cdot \boldsymbol{B}) \frac{\boldsymbol{B}}{\mu_0} \cdot \qquad (8)$$

The magnetohydrodynamic Eqs. (2)–(6) were transformed into a flux conserving form, i.e.,

$$\frac{\partial \boldsymbol{\Psi}}{\partial t} + \frac{\partial \mathbf{F}(\boldsymbol{\Psi})}{\partial x} + \frac{\partial \mathbf{G}(\boldsymbol{\Psi})}{\partial y} = 0, \qquad (9)$$

and were solved numerically. The vector $\boldsymbol{\Psi}$ in our two-dimensional case is expressed as

$$\boldsymbol{\Psi} = \begin{pmatrix} \rho \\ \rho v_x \\ \rho v_y \\ B_x \\ B_y \\ U \end{pmatrix}. \qquad (10)$$

The vector functions $\mathbf{F}(\boldsymbol{\Psi})$ and $\mathbf{G}(\boldsymbol{\Psi})$ are too complex to be presented here, but see them at e.g. (Sankaran 2002; Chung 2002).

For the numerical solution of this type of equation, the modified two step Lax-Wendroff algorithm was used. The numerical region was in the $x - y$-plane, implemented at $0 \leq x \leq L$ and $0 \leq y \leq H$ and was covered by a uniform grid with 1250×300 cells. Open boundary conditions were applied and the time step satisfied the Courant-Friedrichs-Levy condition in the form (Chung 2002):

$$\Delta t \leq \frac{\mathrm{CFL} \Delta x}{\max(c_{\mathrm{s}} + |\boldsymbol{v}|)}, \qquad (11)$$

where CFL = 0.8 is called the Courant number. For more details about such simulations, see the papers by Jelínek & Karlický (2009, 2010).

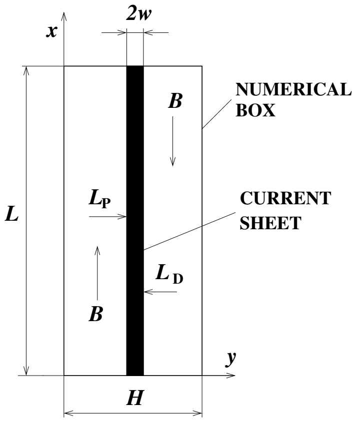

Fig. 6. Sketch of the initial 2-D Harris current sheet considered in simulations. The positions of initial pulse perturbation (L_P) and data collection (L_D) are indicated by the arrows. Compare with Fig. 4.

3.2.2. Model initial conditions

Figure 6 schematically shows the initial 2-D current sheet. The magnetic field in such a current sheet is given by the equation:

$$\boldsymbol{B} = B_{\rm out} \tanh\left(\frac{(y - H/2)}{w}\right)\hat{\boldsymbol{e}}_x, \tag{12}$$

where $B_{\rm out}$ is the magnetic field at $y \to \infty$ and w the half-width of the current sheet. We take the temperature to be the same in the whole numerical box. The plasma density in the current sheet center, where we assume the source of spikes, is determined from the frequency on which the tadpole was found (assuming for simplicity the plasma emission process on the plasma frequency). The other parameters in the current sheet are determined by a choice of the plasma beta parameter β in the region far away from the current sheet ($y \to \infty$). It follows from the equation

$$B_{\rm out} = \sqrt{\frac{2\mu_0 p_{\rm CS}}{1+\beta}}, \tag{13}$$

where $p_{\rm CS}$ is the kinetic pressure in the center of the current sheet. The initial plasma velocity is assumed to be $\boldsymbol{v} = 0$ everywhere in the numerical box.

To generate the magnetoacoustic waves we perturb the current sheet by a pulse in velocities (see Nakariakov et al. 2004):

$$v_y = A_0 \frac{y}{\lambda_x} \exp\left(-\frac{(x - L_{\rm P})}{\lambda_x}\right)^2 \exp\left(-\frac{(y - H/2)}{\lambda_y}\right)^2, \tag{14}$$

where λ_x and λ_y are the dimensions of the pulse in $x-$ and $y-$ axis, and A_0 is the amplitude of the initial pulse. The pulse in the velocity was generated at the start of the numerical simulation at $t = 0$ s. The position of the initial pulse was located at the point ($L_{\rm P}$, $H/2$). On the other hand, the propagating magnetoacoustic waves were detected at the point ($L_{\rm D}$, $H/2$), see Fig. 6.

3.3. Results of numerical simulations

In our simulations we tried to find the best fit of the modeled tadpole with the observed one. Among many possible parameters, we selected some of them as fixed: the temperature is $T = 1 \times 10^7$ K, the plasma beta parameter outside the current sheet is $\beta = 0.1$, the length of the current sheet is $L = 100$ Mm, the plasma density in the current sheet center (at $H/2$) is $n_{\rm e} = 4.0{\times}10^{16}{\rm m}^{-3}$, the location of the initial perturbation is $L_{\rm P} = L/2$, and the parameters of the perturbation pulse are $\lambda_x = 1.0$ Mm, $\lambda_y = 1.5$ Mm, and $A_0 = 1.5{\times}\,10^4$ m s^{-1}.

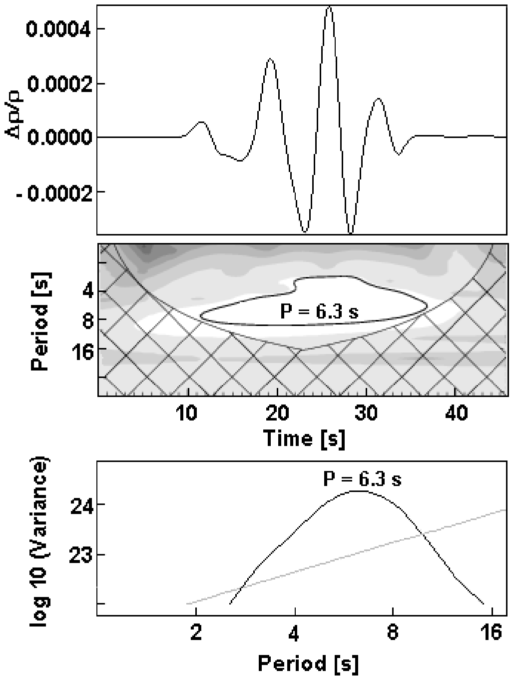

Fig. 7. The modeled tadpole that fits the observed one shown in Fig. 3. *Upper panel* shows a time evolution of the mass density at the detection point (spikes source), where $L_{\rm P} - L_{\rm D} = 8.33$ Mm. *Middle panel* shows the corresponding wavelet power spectrum with the tadpole pattern (characteristic period $P = 6.3$ s) outlined by contour at the 99% confidence level. *Bottom panel* shows the global wavelet spectrum (black line) with the maximum for the period $P = 6.3$ s. The gray line indicates the 99% significance level.

To find the best fit, the halfwidth of the current sheet w and distance between $L_{\rm P}$ and $L_{\rm D}$ are varied. We found that (i) increasing the half-width of the current sheet increases the characteristic period of tadpoles; (ii) decreasing the distance between $L_{\rm P}$ and $L_{\rm D}$ makes the tadpole shorter. With these facts, the "best" fit was found for $w = 1$ Mm and the distance $L_{\rm P} - L_{\rm D} = 8.33$ Mm. The "best" fitted tadpole is shown in Fig. 7 (compare with that in Fig. 3), where the upper panel shows a time evolution of mass density at the detection point, i.e. $\rho(x = L_{\rm D}, y = H/2, t)$. The middle panel shows the corresponding wavelet power spectrum with the tadpole pattern (characteristic period $P = 6.3$ s) outlined by contour at the 99% confidence level. The bottom panel shows the global wavelet spectrum with the maximum for the period $P = 6.3$ s.

4. Discussion and conclusions

For fifteen spikes events we found that their Fourier spectra are power-law spectra with the power-law index in the range of −1.2

to −1.8. Moreover, in all these events we recognized the tadpoles in their wavelet spectra, which indicate the propagating magnetoacoustic waves in the spikes sources. When interpreting these spikes as generated in turbulent reconnection outflows we modeled the magnetoacoustic waves and corresponding tadpoles. We found good agreement between the modeled and observed tadpole for the halfwidth of the current sheet $w = 1$ Mm and for the distance between the location of the perturbation and location of the magnetoacoustic wave detection $L_\mathrm{P} - L_\mathrm{D} = 8.33$ Mm. For other parameters in the model, see the previous section. Although these parameters are not unique, they give us rough information about the sizes of the global flare current sheet. Especially, the period of the tadpoles has a high diagnostic value. Similarly as for the dense slab (Nakariakov et al. 2004), in our case the period was found to be proportional to the half-width of the current sheet.

In our simulations we consider the Harris current sheet, which covers the whole reconnection region including the reconnection plasma outflows, i.e. the global current sheet. Thus, the halfwidth of the current sheet (1000 km), estimated from magnetoacoustic waves, means the half-width of this global current sheet (current layer). This width is of the order of the observed current layers, e.g. by Ciaravella et al. (2002) and Lin et al. (2005). We neglected substructures in this global current sheet given by smaller and smaller plasmoids and narrower and narrower current sheets. Spatial scales of this cascade of current sheets come down to a few meters where the current densities are so high that the anomalous resistivity is generated and fast reconnection occurs. An advantage of this model with multiscale current sheets is that it naturally explains the electron fluxes inferred from hard X-ray observations (from all the acceleration sites). For more details about this scale problem, see Bárta et al. (2010a,b).

Because the magnetoacoustic waves are a part of the turbulent reconnection outflow, we consider their finding on the spike sources as supporting our model of spikes. Based on the new findings (Bárta et al. 2010b) and also on observations, we proposed that the narrowband dm-spikes are generated by driven coalescence and fragmentation processes in turbulent reconnection outflows. (Remark: Generally, these processes can be for the whole reconnection region, i.e. also in the reconnection outflow oriented upwards; therefore, the spikes can also be generated at high coronal altitudes as metric spikes.) The propagating magnetoacoustic waves (indicated by tadpoles) modulate these coalescence processes via a modulation of current densities in interaction regions among plasmoids. These waves modulate an acceleration of electrons and generation of plasma and electromagnetic waves – spikes. The narrowband dm-spikes can thus be considered as a radio signature of the fragmented reconnection in solar flares.

Acknowledgements. This research was supported by the grants IAA300030701 (GA AS CR), P209/10/1680 (GA CR), the research project AV0Z10030501 of the Astronomical Institute AS, and the Centre for Theoretical Astrophysics, Prague. Authors thank Dr. J. Rybák for his help with the wavelet analysis that was performed with software based on tools provided by C. Torrence and G. P. Compo at `http://paos.colorado.edu/research/wavelets`.

References

Aschwanden, M. J. 1990, A&AS, 85, 1141
Bárta, M., & Karlický, M. 2001, A&A, 379, 1045
Bárta, M., Vršnak, B., & Karlický, M. 2008a, A&A, 477, 649
Bárta, M., Karlický, M., & Žemlička, R. 2008b, Sol. Phys., 253, 173
Bárta, M., Büchner, J., & Karlický, M. 2010a, Adv. Space Res., 45, 10
Bárta, M., Büchner, J., Karlický, M., & Skála, J. 2010b, ApJ, submitted [`arXiv:1011.4035B`]
Benz, A. O. 1986, Sol. Phys., 104, 99
Benz, A. O., Zlobec, P., & Jaeggi, M. 1982, A&A, 109, 305
Chung, T. J. 2002, Computat. Fluid Dyn. (New York, USA: Cambridge University Press)
Ciaravella, A., Raymond, J. C., Li, J., et al. 2002, ApJ, 575, 1116
Fleishman, G. D., & Yastrebov, S. G. 1994, Sol. Phys., 154, 361
Fleishman, G. D., & Melnikov, V. F. 1998, Uspechi fizicheskich nauk, 168, 1265 (in Russian)
Fu, Q. J., Li, C. S., & Yin, S. Z. 1985, in Kunming Workshop on Solar Physics and Interplanetary travelling phenomena, ed. C. de Jager, & Chen Biao (Beijing: Science Press), 560
Güdel, M. 1990, A&A, 239, L1
Güdel, M., & Zlobec, P. 1991, A&A, 245, 299
Holman, G. D., Eichler, D., & Kundu, M. 1980, in IAU Symp. 86, ed. M. Kundu, & T. Gergely, 465
Jelínek, P., & Karlický, M. 2009, Eur. Phys. J. D, 54, 305
Jelínek, P., & Karlický, M. 2010, IEEE Trans. Plasma Sci., 38, 2243
Jiřička, K., Karlický, M., Kepka, O., & Tlamicha, A. 1993, Sol. Phys., 147, 203
Karlický, M. 1984, Sol. Phys., 92, 329
Karlický, M., & Bárta, M. 2007, A&A, 464, 735
Karlický, M., Sobotka, M., & Jiřička, K. 1996, Sol. Phys., 168, 375
Karlický, Jiřička, K., & Sobotka, M. 2000, Sol. Phys., 195, 165
Karlický, M., Bárta, M., & Rybák, J. 2010, A&A, 514, A28
Krucker, S., & Benz, A. O. 1994, A&A, 285, 1038
Kuijpers, J., Van der Post, P., & Slottje, C. 1981, A&A, 102, 331
Lin, J., Ko, Y.-K., Sui, L., et al. 2005, ApJ, 622, 1251
Magara, T., Mineshige, S., Yokoyama, T., & Shibata, K. 1996, ApJ, 466, 1054
Melrose, D. B., & Dulk, G. A. 1982, ApJ, 259, 844
Mészárosová, H., Veronig, A., Zlobec, P., & Karlický, M. 2003, A&A, 407, 1115
Mészárosová, H., Karlický, M., Rybák, J., & Jiřička, K. 2009a, ApJ, 697, L108
Mészárosová, H., Karlický, M., Rybák, J., & Jiřička, K. 2009b, A&A, 502, L13
Nakariakov, V. M., Arber, T. D., Ault, C. E., et al. 2004, MNRAS, 349, 705
Priest, E. R. 1982, Sol. Magnetohydrodynamics (London, UK: D. Reidel Publishing Company)
Sankaran, K., Martinelli, L., Jardin, S. C., & Choueiri, E. Y. 2002, Int. J. Numer. Meth. Engng., 53, 1415
Shibata, K., & Tanuma, S. 2001, Earth Planets Space, 53, 473
Slottje, C. 1981, Atlas of Fine Structures of Dynamic Spectra of Solar Type IV-dm and Some Type II Radio Bursts, Dwingeloo Observatory
Stähli, M., & Magun, A. 1986, Sol. Phys., 104, 117
Tajima, T., Benz, A. O., Thaker, M., & Leboeuf, J. N. 1990, ApJ, 353, 666
Vlahos, L., & Sharma, R. R. 1984, ApJ, 290, 347
Winglee, R. R., Dulk, G. A., & Pritchett, P. L. 1988, ApJ, 328, 809
Wentzel, D. G. 1991, ApJ, 373, 285
Zlobec, P., & Karlický, M. 1998, Sol. Phys., 182, 477

A&A 537, A46 (2012)
DOI: 10.1051/0004-6361/201117883

Astronomy & Astrophysics

Magnetoacoustic waves in diagnostics of the flare current sheets

P. Jelínek[1] and M. Karlický[2]

[1] University of South Bohemia, Faculty of Science, Branišovská 10, 370 05 České Budějovice, Czech Republic
e-mail: `pj@matfyz.cz`
[2] Academy of Sciences of the Czech Republic, Astronomical Institute, v. v. i., Fričova 258, 251 65 Ondřejov, Czech Republic
e-mail: `karlicky@asu.cas.cz`

Received 15 August 2011 / Accepted 24 October 2011

ABSTRACT

Aims. To obtain diagnostics tools for solar flare current sheets, we numerically studied impulsively generated magnetoacoustic waves in the Harris current sheet.

Methods. We used two-dimensional (2-D) magnetohydrodynamic (MHD) and wave dispersion models. Tests of these models were performed for waves in the density slab, where analytical solutions are known. In the MHD model, we solved the full set of ideal MHD equations by means of the modified two-step Lax-Wendroff algorithm. The initial perturbation was chosen to generate preferentially the fast sausage magnetoacoustic waves. To determine the dispersion characteristics of MHD waves in the Harris current sheet, we numerically solved the equation of plasma motions by means of the Runge-Kutta fourth order method together with the bisection iteration one. To establish some diagnostics of these waves and their corresponding flare current sheets, we used the wavelet analysis method.

Results. We find that the results of tests of our 2-D MHD and wave dispersion models for the density slab are in good agreement with analytical results. We analyze the magnetoacoustic waves in the current sheet and compare them with those in the density slab. In both cases, for similar geometrical and plasma parameters, we find that wave trains were generated and propagated in a similar way. Their signals registered at selected locations of the Harris current sheet and density slab are also similar. Nevertheless, a dependence of the period of the magnetoacoustic waves on the width of the Harris current sheet differs from that for the density slab. The form of the wave front inside the current sheet similarly differs from that in the density slab. We find that the wavelet spectra of the signals of incoming magnetoacoustic waves at selected locations in the current sheet have the form of wavelet tadpoles. We distinguish that the form of these wavelet tadpoles becomes longer and the heads of the wavelet tadpoles are detected later in time as the distance of the detection point from that of the initial wave perturbation increases. We also find that the wavelet tadpole period depends on the plasma beta parameter. The results are discussed from the point of view of their use as diagnostics of the flare current sheets or flare loops.

Key words. methods: numerical – Sun: flares – Sun: oscillations – Sun: corona – magnetohydrodynamics (MHD)

1. Introduction

Oscillations and magnetohydrodynamic (MHD) plasma waves play a very important role in the many phenomena observed in the solar atmosphere (see e.g. Priest 1982; Aschwanden 2004). These MHD waves and oscillations have been analyzed by theoretical and numerical research Nakariakov et al. (2004, 2005), Selwa & Murawski (2004), Selwa et al. (2005, 2007), or Jelínek & Karlický (2009, 2010). The various oscillation modes in solar coronal loops have been observed with highly sensitive instruments such as SUMER (SoHO) and TRACE, as well as by more recent missions, e.g., EIS/Hinode or EUVI/STEREO. The observed oscillations include propagating waves similar to those of DeMoortel et al. 2002 and slow standing magnetoacoustic waves similar to those described by Ofman & Wang (2002), as well as a branch of fast magnetoacoustic waves, horizontal kink, vertical kink, and fast sausage waves (see e.g. Aschwanden 2004 or Wang & Solanki 2004).

The impulsively generated MHD waves and oscillations can be excited by various processes in the solar corona. The impulsive flare process, which provides either single or multiple sources of disturbances, is the most probable one. The impulsively generated magnetoacoustic waves are trapped in regions of higher density, i.e. in regions with a lower Alfvén speed, which act as waveguides. The periodicity of propagating fast sausage waves is formed by the time evolution of an impulsively generated signal (see Roberts et al. 1983, 1984; and Murawski & Roberts 1994). These waves in a coronal waveguide have three distinct phases: 1) periodic phase (long-period spectral components arrive as the first at observation point); 2) quasi-periodic phase (as both long and short-period spectral components arrive and interact), and finally; 3) decay (or Airy) phase (as the signal passes), (Roberts et al. 1984).

The wavelet analysis of impulsively generated (fast sausage) magnetoacoustic wave trains shows the typical tadpole shape where a narrow-spectrum tail precedes a broadband head. These tadpole signatures (wavelet tadpole) were firstly observed by the SECIS instrument in the 1999 solar-eclipse data (see Katsiyannis et al. 2003). Similarly, Mészárosová et al. (2009a,b) detected, for the first time, the tadpoles in the wavelet spectra in some radio sources, which have also been confirmed numerically, see e.g. Nakariakov et al. (2004, 2005).

Karlický et al. (2011) found the wavelet tadpoles in sources of narrowband dm-spikes. They concluded that these wavelet tadpoles indicate that magnetoacoustic waves propagate in the global current sheet (current layer) in the turbulent reconnection outflows. This paper served as a motivation of a more extended and detailed study of magnetoacoustic (fast sausage) waves in the current sheet. In particular, much interest has been placed on the parameters of the current sheets (e.g. the current sheet width, the plasma beta parameter, and the distance between the wave initiation and detection sites) that influence the detected signal and its corresponding wavelet spectrum. Assuming that these waves modulate the radio fluxes (or even UV fluxes) in various locations of the current sheet, we propose that this knowledge can help us to determine the parameters of flare current sheets. For model tests and comparison, a similar study of the density slab was made. Therefore, a similar method can be used to determine the diagnostics of the density slabs, which correspond to flare loops in coronal conditions.

The structure of the present paper is as follows. Section 2 describes our numerical models, and Sect. 3 contains initial conditions and a form of initial perturbations. In Sect. 4, the numerical results, obtained by means of our computer models, are shown and discussed. Finally, in Sect. 5 our conclusions are presented.

2. Numerical model

2.1. Numerical solutions of MHD equations

In our present model, we describe the plasma dynamics by the ideal magnetohydrodynamic equations (see Priest 1982; Chung 2002)

$$\begin{aligned} \frac{\partial \varrho}{\partial t} &= -\nabla(\varrho \boldsymbol{v}), & (1)\\ \varrho\frac{\partial \boldsymbol{v}}{\partial t} &+ \varrho(\boldsymbol{v}\nabla)\boldsymbol{v} = -\nabla p + \frac{1}{\mu_0}(\nabla\times\boldsymbol{B})\times\boldsymbol{B}, & (2)\\ \frac{\partial \boldsymbol{B}}{\partial t} &= \nabla\times(\boldsymbol{v}\times\boldsymbol{B}), & (3)\\ \frac{\partial U}{\partial t} &= -\nabla\boldsymbol{S}, & (4)\\ \nabla\boldsymbol{B} &= 0, & (5) \end{aligned}$$

where ϱ is a mass density, $\boldsymbol{v}$ is the flow velocity, p is the gas pressure, and $\boldsymbol{B}$ is the magnetic field. The plasma energy density U is given by

$$U = \frac{p}{\gamma - 1} + \frac{\varrho}{2}v^2 + \frac{B^2}{2\mu_0}, \tag{6}$$

where the adiabatic coefficient is $\gamma = 5/3$, and the flux vector $\boldsymbol{S}$ is expressed as

$$\boldsymbol{S} = \left(U + p + \frac{B^2}{2\mu_0}\right)\boldsymbol{v} - (\boldsymbol{v}\boldsymbol{B})\frac{\boldsymbol{B}}{\mu_0}\cdot \tag{7}$$

The magnetohydrodynamic Eqs. (1)–(4) were transformed into a flux conserving form, i.e.

$$\frac{\partial \boldsymbol{\Psi}}{\partial t} + \frac{\partial \boldsymbol{F}(\boldsymbol{\Psi})}{\partial x} + \frac{\partial \boldsymbol{G}(\boldsymbol{\Psi})}{\partial y} = 0, \tag{8}$$

and solved numerically. The vector $\boldsymbol{\Psi}$ in the two-dimensional case is expressed as

$$\boldsymbol{\Psi} = \begin{pmatrix} \rho \\ \rho v_x \\ \rho v_y \\ B_x \\ B_y \\ U \end{pmatrix}. \tag{9}$$

The vector functions $\boldsymbol{F}(\boldsymbol{\Psi})$ and $\boldsymbol{G}(\boldsymbol{\Psi})$ are too complex to be reproduced here, hence for more information we refer to either Sankaran et al. (2002) or Chung (2002).

For the numerical solution of this type of equations, we used the modified two-step Lax-Wendroff algorithm (Kliem et al. 2000). The numerical region was oriented in the x, y-plane, implemented at $0 \leq x \leq L$ and $0 \leq y \leq H$ and covered by a uniform grid with 1250×300 cells. Open boundary conditions were applied and the time step satisfied the Courant-Friedrichs-Levy condition in the form given by Chung (2002)

$$\Delta t \leq \frac{\mathrm{CFL}\Delta x}{\max(c_\mathrm{s} + |\boldsymbol{v}|)}, \tag{10}$$

where CFL = 0.8 is called the Courant number.

To stabilize the-two step Lax-Wendroff numerical scheme, we applied artificial smoothing (see Sato & Hayashi 1979). At each grid point, all variables were replaced after each full time step of the algorithm according to the formula

$$\boldsymbol{\Psi}^n_{i,j} = \lambda\boldsymbol{\Psi}^n_{i,j} + \frac{1-\lambda}{4}(\boldsymbol{\Psi}^n_{i-1,j} + \boldsymbol{\Psi}^n_{i+1,j} + \boldsymbol{\Psi}^n_{i,j-1} + \boldsymbol{\Psi}^n_{i,j+1}), \tag{11}$$

with the coefficient $\lambda = 0.98$ during the simulation (see Kliem et al. 2000).

2.2. Calculations of phase and group speeds

For the calculations of phase and group velocities of plasma waves in current sheets and the density slab, we numerically solved the wave equation for plasma motions, as described by e.g. Smith et al. (1997), Roberts (1981a,b), or Edwin & Roberts (1982, 1983), where the equilibrium parameters of the loop (density and pressure) depend on the y coordinate

$$\frac{\mathrm{d}}{\mathrm{d}y}\left[f(y)\frac{\mathrm{d}v_y}{\mathrm{d}y}\right] + \varrho\left(\omega^2 - k_x v^2_\mathrm{Alf}\right)v_y = 0, \tag{12}$$

where v_y is the velocity component normal to the magnetic field, ω is the frequency, k_x is the longitudinal wavenumber along the sheet, and the Alfvén speed is calculated as $v^2_\mathrm{Alf} = B^2/\mu_0\varrho$.

The function $f(y)$ from Eq. (12) is expressed as

$$f(y) = \frac{\varrho c^2_\mathrm{f}\left(\omega^2 - k^2_x c^2_\mathrm{T}\right)}{\left(\omega^2 - k^2_x c^2_\mathrm{s}\right)}, \tag{13}$$

where $c_\mathrm{s} = (\gamma p/\varrho)^{1/2}$ is the sound speed. The tube speed c_T and fast speed c_f are implied as $c_\mathrm{T} = c_\mathrm{s}v_\mathrm{Alf}/(c^2_\mathrm{s} + v^2_\mathrm{Alf})^{1/2}$ and $c_\mathrm{f} = (c^2_\mathrm{s} + v^2_\mathrm{Alf})^{1/2}$, respectively.

Equation (12) has a singular point called either the cusp resonance or cusp singularity. This point plays an important role in the case of slow magnetoacoustic waves, whereas it is not seen in numerical simulations of the fast magnetoacoustic waves (see e.g. Zhukov 1989).

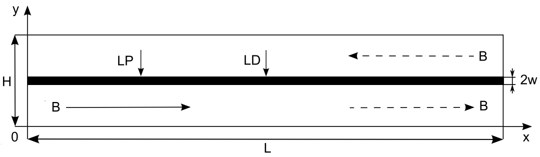

Fig. 1. The sketch of a 2-D Harris current sheet (or density slab) considered to be along the x-axis. Positions of the initial pulse L_P, data collection L_D, and magnetic field orientations are shown.

The second order ordinary differential Eq. (12) is rewritten in terms of two first order equations in the new functions ξ_1 and ξ_2

$$\xi_1 = f(y)\frac{\mathrm{d}v_y}{\mathrm{d}y}, \qquad \xi_2 = v_y, \tag{14}$$

such that

$$\frac{\mathrm{d}\xi_1}{\mathrm{d}y} = \varrho\left(k_x v_{\mathrm{Alf}}^2 - \omega^2\right)\xi_2, \tag{15}$$

and

$$\frac{\mathrm{d}\xi_2}{\mathrm{d}y} = \frac{\xi_1}{f(y)}. \tag{16}$$

The boundary conditions at the point $y = 0$ for the "kink" mode are given by $\xi_1 = 0, \xi_2 = c$. The "sausage" mode satisfies the conditions $\xi_1 = c\,f(0), \xi_2 = 0$, whereas the constant c is arbitrary in both cases.

To obtain a solution of Eq. (12) we used a fixed value of k_x and integrating between $y = 0$ and $y = y_{\max}$ the two first order Eqs. (15) and (16) by means of the Runge-Kutta fourth order method. The exact value of the frequency ω was obtained with the bisection iteration method when the velocity v_y satisfied the boundary condition at the second point $v_y(y = y_{\max}) = 0$ for both wave modes (kink and sausage mode).

3. Initial conditions and perturbations

The sketch of the studied two-dimensional (2-D) solar coronal structure is shown in Fig. 1. The arrows show the positions of the initial perturbation at L_P, the point where the data were detected at L_D, and the orientation of the magnetic field in both of the studied cases, the first the density slab with the parallel magnetic field (solid arrow) and the second the Harris current sheet (dashed arrows).

The length and width of the simulation region, for both studied cases, were $L = 100$ Mm and $H = 24$ Mm, respectively.

In the dense part of the density slab and the whole simulation box of the Harris current sheet, the temperature was assumed to be constant, at $T = 10^7$ K, and the corresponding sound speed is $c_s \approx 166\,T^{1/2} = 525$ km s^{-1} (see Priest 1982). In the state of equilibrium, we assumed the initial plasma velocity $\boldsymbol{v} = 0$ and calculated the initial energy density U_0 from Eq. (6).

In view of our interest in studying impulsively generated wave trains in the solar coronal structures, we launched a pulse in the velocity in the y-axis direction. The point where the velocity is perturbed was located at $(L_P, H/2)$, (see Fig. 1) and the initial velocity pulse followed a (Gaussian) profile (see e.g. Nakariakov et al. 2004, 2005)

$$v_y = A_0\frac{y}{\lambda_x}\exp\left[-\frac{(x - L_P)}{\lambda_x}\right]^2 \exp\left[-\frac{(y - H/2)}{\lambda_y}\right]^2, \tag{17}$$

where $A_0 = 1.5 \times 10^4$ m s^{-1} is the initial amplitude of the pulse, and $\lambda_x = 1.5$ Mm and $\lambda_y = 0.5$ Mm are the widths of the velocity pulse in the longitudinal and transverse directions, respectively. This type of pulse generates preferentially the sausage waves. The initial pulse in the velocity was generated at the start of the numerical simulation at time $t = 0$ s.

3.1. Density slab

The flare loop in this case is represented by a slab with a half-width $w = 1$ Mm. The slab is embedded in a magnetic environment with a magnetic field given by the plasma beta parameter

$$\beta = \frac{p}{p_{\mathrm{mag}}} = \frac{2\mu_0 p}{B^2}, \tag{18}$$

where the plasma beta β is assumed to be 0.1. The magnetic field is parallel to the x-axis (see Fig. 1) and is assumed to be constant in the whole simulation region.

The mass density profile in a flare loop along the x-axis is also considered to be constant, and along the y-axis the mass density profile is expressed by the formula (see Nakariakov & Roberts 1995)

$$\varrho(x, y) = \varrho_0 + (\varrho_{\mathrm{sl}} - \varrho_0)\,\mathrm{sech}^2\left\{\left[\frac{(y - H/2)}{w}\right]^\alpha\right\}, \tag{19}$$

where the power index α determines the steepness of the profile. The cases where the power index α equals either unity or infinity correspond to the symmetric Epstein profile or to the step function profile, respectively (see Nakariakov et al. 2005). In this study, $\alpha = 8$ was used for the calculations. The exact values of the mass density of the magnetic environment ϱ_0, as well as the mass density in the center of the slab ϱ_{sl} is given in Sect. 4.

3.2. Harris current sheet

The magnetic field in this current sheet is given by the equation

$$\boldsymbol{B} = B_{\mathrm{out}}\tanh\left[\frac{(y - H/2)}{w_{\mathrm{cs}}}\right]\hat{\boldsymbol{e}}_x, \tag{20}$$

where B_{out} is the magnetic field at $y \to \infty$ and w_{cs} is the half-width of the current sheet, $w_{\mathrm{cs}} = 1$ Mm.

Magnetic field B_{out} is determined from the equation

$$B_{\mathrm{out}} = \sqrt{\frac{2\mu_0 p_{\mathrm{cs}}}{1 + \beta}}. \tag{21}$$

The kinetic pressure at the center of the current sheet p_{cs} is calculated from the plasma density at the center of the current sheet ϱ_{cs}. We assumed that the plasma beta parameter outside of the current sheet is the same as in the case of density slab, i.e. $\beta = 0.1$.

Because of the zero magnetic field at the center of the current sheet $B_{\mathrm{cs}} = 0$, one can calculate, from the condition of equilibrium, of

$$p + \frac{B^2}{2\mu_0} = \mathrm{const.}, \tag{22}$$

that the distribution of the mass density in the simulation box is as follows

$$\varrho(x, y) = \varrho_{\mathrm{cs}} - \frac{mB_x^2(y)}{2\mu_0 k_B T}, \tag{23}$$

where m is the proton mass, μ_0 is the magnetic permeability, and k_B is the Boltzmann constant.

4. Results

We present our numerically obtained results, firstly for the simple density slab and the Harris current sheet and secondly by comparing the numerical results for both magnetic structures.

4.1. Density slab

We show the results that we obtained for a simple flare loop – density slab in the magnetic field oriented parallel to the slab. We analyzed the incoming signal and compared the calculated period of the wave signal by the wavelet method with the analytical formula. The location of the perturbation point was $L_\mathrm{P} = \{L/6, H/2\}$ and the position of the point where the data were collected was $L_\mathrm{D} = \{L/2, H/2\}$, respectively (see Fig. 1).

To estimate the period of the wave signal, we use the equation provided by Roberts (1984)

$$P = \frac{2\pi w}{j_0 v_\mathrm{Alf}} \sqrt{1 - \frac{\varrho_0}{\varrho_\mathrm{sl}}} \approx 2.6 w / v_\mathrm{Alf}, \tag{24}$$

where ϱ_0 and v_Alf are the values of mass density outside and the Alfvén speed inside the density slab, respectively. The square root in the Eq. (24) can be neglected when $\varrho_\mathrm{sl} \gg \varrho_0$; we then obtain the period in the form shown on the right side of the equation, because $j_0 \approx 2.4$ is the first zero of the Bessel function $J_0(x)$.

In the presented case, the mass density of the magnetic environment is $\varrho_0 = 6.082 \times 10^{-12}$ kg m^{-3} and the mass density at the center of the slab is $\varrho_\mathrm{sl} = 6.688 \times 10^{-11}$ kg m^{-3}, i.e. the mass density ratio $d = \varrho_0/\varrho_\mathrm{sl} \doteq 0.091$. Thus, from Eq. (24) we obtained the period of the wave signal $P \approx 6.8$ s.

In Fig. 2, we also compare the results of different numerical tests. In its upper part, the time evolution of the incoming signal and the times when the first signal is detected T_fs, as well as the time of the decay phase T_dp, is shown. In the middle panel, the global wavelet spectrum of the incoming signal (full line) with the dominant wave period P, and the 99% significance level (dash-dotted line) (see Torrence & Compo 1998) is shown. The most dominant period in this wavelet spectrum is the period $P \approx 7.0$ s. This "mean" period is in good agreement with that given by the analytical Eq. (24), derived for the typical period of oscillation in the density slab. Finally, in the bottom part of the figure, we display the group speed of the wave v_gr.

To asses the quality of our numerical model, we calculated the wave periods for different half-widths of the density slab (see Table 1 second column). The computed values show a linear dependence on the density slab half-width w, which is in agreement with the analytical Eq. (24).

To estimate the time of the decay (Airy) phase of the wave signal, we found the minimum of the group velocity, (see Fig. 2 bottom), $v_\mathrm{gr}^\mathrm{min} = 0.2542 v_\mathrm{Alf,0} = 3.27 \times 10^5$ m s^{-1}, where $v_\mathrm{Alf,0}$ is the Alfvén speed outside the density slab. The time of decay phase is then $T_\mathrm{dp} = |L_\mathrm{D} - L_\mathrm{P}|/v_\mathrm{gr}^\mathrm{min} \approx 102.0$ s (see Roberts et al. 1984). The time, when the first signal arrived is calculated as $T_\mathrm{fs} = |L_\mathrm{D} - L_\mathrm{P}|/v_\mathrm{Alf,0} = 25.9$ s, which should be compared with these values in the upper panel of Fig. 2.

Our presented results served mainly to verify that our numerical code works properly and the numerical results are comparable to the results obtained by means of known analytical formulae. After these successful tests, we applied our numerical codes for the calculations to more complicated structures in the solar corona, such as the Harris current sheet.

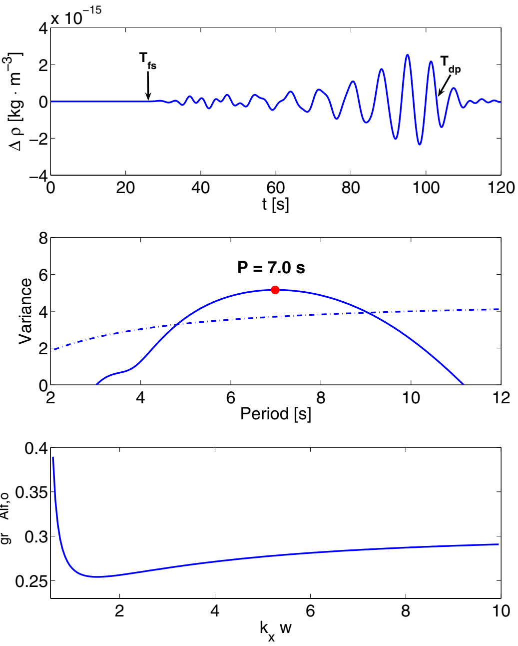

Fig. 2. *Upper panel*: time evolution of the mass density $\varrho(L_\mathrm{D} = \{L/2, H/2\}, t)$. *Middle panel*: the global wavelet spectrum of the incoming signal (full line) with dominant wave period P, and the 99% significance level (dash-dotted line). *Bottom panel*: the group speed of the wave $v_\mathrm{gr} = \mathrm{d}\omega/\mathrm{d}k$ in units of the external Alfvén speed as a function of wave number $k_x w$ (bottom panel). All for the density slab.

Table 1. Wave periods calculated by wavelet analysis for three selected half-widths w.

w [Mm]	P_slab [s]	P_CS [s]
1.00	7.0	6.8
1.25	8.6	7.6
1.50	10.4	8.2

Notes. Periods for the density slab (second column) and for the Harris current sheet (third column) are shown.

4.2. Harris current sheet

We present the numerical results obtained for the Harris current sheet configuration. We compare our results for different widths of the current sheet as well as for different plasma beta parameters.

In this studied case, we used values of the mass density similar to those of simple density slab, i.e. the mass density outside the Harris current sheet was $\varrho_0 = 6.082 \times 10^{-12}$ kg m^{-3} and the mass density at the center of the current sheet was $\varrho_\mathrm{CS} = 6.688 \times 10^{-11}$ kg m^{-3}. The location of the point where the velocity is perturbed was placed at $L_\mathrm{P} = \{L/6, H/2\}$ and the position of the detection point was assumed to be $L_\mathrm{D} = \{L/2, H/2\}$, respectively.

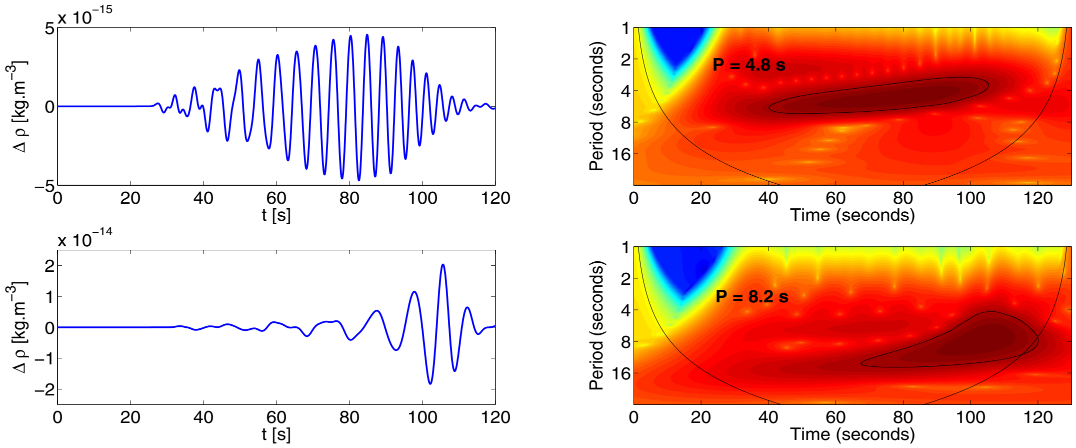

Fig. 3. Comparison of wave signals (*left column*) and corresponding wavelet tadpole shapes (*right column*) for two different widths of the Harris current sheet; $w_{\rm CS} = 0.50$ Mm (*first row*) and $w_{\rm CS} = 1.50$ Mm (*second row*). The data were recorded in the position $L_{\rm D} = \{L/2; H/2\}$.

4.2.1. Current sheet width

In Fig. 3, we compare the of wave signals and the corresponding wavelet tadpole shapes for two different widths of the Harris current sheet. For the calculations, we used the widths of the Harris current sheet $w_{\rm CS} = 0.50$ Mm and $w_{\rm CS} = 1.50$ Mm. The plasma beta parameter was $\beta = 0.1$.

The figure shows that as the width of the Harris current sheet increases, the wave period also increases. However, this increase in the wave period is smaller than that for the density slab, as can be seen comparing the second and third columns of Table 1. Analyzing this difference, we conclude that it is caused by differences in the density and magnetic field profiles of both structures. In the density slab, its boundaries are similar to those of a step function for a broad range of half-widths (as in the analytical approach), while the current sheet profile becomes broader and less steep as the half-width increases. We also analyzed the average propagation speeds in the density slab and current sheet and found that after increasing the widths of both structures their average propagation speeds insides them remain practically the same. The average propagation speeds in the density slab and the current sheet for the same width are comparable. Considering these results and the values of the periods shown in Table 1, we can conclude for the current sheet that, if there is a relation similar to that for the density slab (Eq. (24)), then the constant of the proportionality in this relation for the current sheet is a slowly decreasing function with the increasing width of the current sheet, instead of the constant 2.6 for the density slab (Eq. (24)).

The wavelet analysis of the wave signal also reveals that for higher values of the Harris current sheet half-width, the wavelet tadpoles become shorter and the heads of the wavelet tadpoles are more distinct. These results agree with those presented in Nakariakov et al. (2005), where the longitudinal driver width was varied for a fixed width of the density slab. As shown by Nakariakov et al. (2005), narrower longitudinal drivers produce a broader k-spectrum above the cutoff for wave propagation and thus a broader interval of periods is detected.

4.2.2. Plasma beta parameter

Figure 4 shows the comparison of wave signals and corresponding wavelet tadpole shapes for two different plasma beta parameters. We present the results for plasma beta parameter $\beta = 0.01$ and $\beta = 0.05$, which are typical of values in the solar corona (see Aschwanden 2004).

We found that the higher the plasma beta parameter is, the shorter is the observed wave period. We compare these results with the value of the wave period in Fig. 11 (right column) for a plasma beta parameter $\beta = 0.1$.

We can also see that the changes in the plasma beta parameter have almost no effect at all on the shapes of the wavelet tadpoles. However, the time of the "first" signal is later in the case of a lower value of the plasma beta parameter. This is because when the plasma beta parameter decreases, the external Alfvén speed $v_{\rm Alf,0}$ increases, hence the arrival time of the first signal decreases.

In Fig. 5, we depict the group speeds of the magnetoacoustic waves for two different plasma beta parameters. The graphs show the positions and values of the minimum group speeds $v_{\rm gr,min}$.

The minima of the group speed for the plasma beta parameter of $\beta = 0.05$ were found to be $v_{\rm gr,min} = 0.18 v_{\rm Alf,0} = 3.27 \times 10^5$ m s^{-1}, and for a plasma beta $\beta = 0.10$ the minimal value of the group speed was $v_{\rm gr,min} = 0.26 v_{\rm Alf,0} = 3.34 \times 10^5$ m s^{-1}, respectively. In spite of the different ratio of minimal group speed to external Alfvén speed $v_{\rm gr,min}/v_{\rm Alf,0}$ for both of the studied cases, the time of the decay (Airy) phase is very similar (because of the very similar minimal group speeds $v_{\rm gr,min}$) at $T_{\rm dp} \approx 110$ s (see Fig. 4 for comparison).

4.3. Comparison of the density slab and the Harris current sheet

To compare the numerical results obtained for the density slab and the Harris current sheet, we use the physical quantities $\beta = 0.1$, $w_{\rm sl} = w_{\rm CS} = 1.0$ Mm.

The perturbation point was located at $L_{\rm P} = \{L/6, H/2\}$ for all cases that we studied and compared, whereas the detection

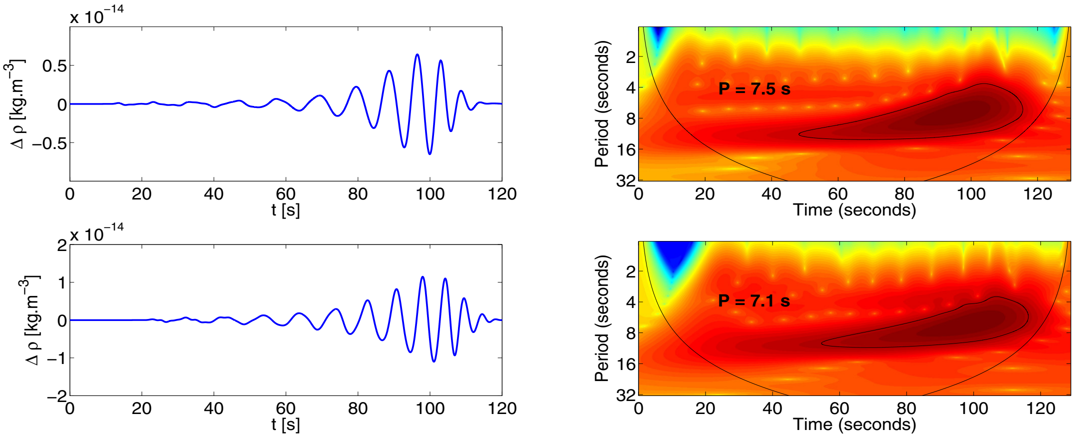

Fig. 4. Comparison of wave signals (*left column*) and corresponding wavelet tadpole shapes (*right column*) for plasma beta parameters $\beta = 0.01$ (*first row*) and $\beta = 0.05$ (*second row*), calculated for the Harris current sheet. The data were recorded in the position $L_{\mathrm{D}} = \{L/2; H/2\}$.

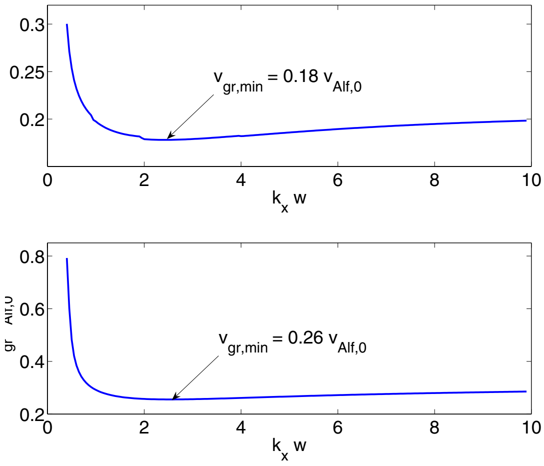

Fig. 5. Group speeds of the waves in units of the external Alfvén speed $v_{\mathrm{Alf},0}$ as the functions of wave number $k_x w$ for plasma beta parameter $\beta = 0.05$ (*upper panel*) and $\beta = 0.10$ (*lower panel*). The minimal values of the group speed v_{gr} are shown by arrows, and calculated for the Harris current sheet.

point L_{D} was placed at several points in the x-y plane to help improve our understanding of the nature of incoming wave signals.

4.3.1. Wave propagation

The numerical results calculated for the density slab (Fig. 6) and the Harris current sheet (Fig. 7) are compared. In both of these figures, we present the pressure variance $\Delta p = p(t) - p(0)$ at various times t during the wave evolution.

Comparing the contours of the pressure variance Δp, we can see that from the global point of view the results are similar. Nevertheless, when we study our results in detail (see e.g. Figs. 8 and 9), we can recognize differences, especially in the central parts of both the structures, where, in the Harris current sheet, the magnetic field, as well as the Alfvén speed is close to zero.

Since the wave evolution in the waveguide is determined by the dispersive properties of the waveguide as a whole, the global similarity of the evolution of both of these structures means that these structures have similar dispersive properties. However, differences found between the central parts of these structures are caused by local differences between the magnetic field and density profiles.

4.3.2. Incoming signals at different detection points

We compare the various wave signals entering the Harris current sheet in Fig. 10. To display the incoming wave signal, we used the time evolution of the mass density variance $\Delta\varrho = \varrho(t) - \varrho(t)$ at the detection point L_{D}. The point L_{D} where the data were collected was placed at six different positions in the numerical box. The three rows correspond to three points in the x-direction ($L/4$, $L/2$, and $3L/4$), whereas the two columns of the figure correspond to two points in y-direction ($H/2$ and $3H/4$).

When we compare the two columns of Fig. 10, it is evident that the signal at the center of the Harris current sheet has the shape, consisting of distinct phases, described in Roberts (1984). Using the wavelet analysis method, the typical tadpole shape was obtained (see Fig. 11). It is also clearly visible that the number of wavelengths depends on the position of the detection point L_{D}. This is again because the first waves to arrive are the fastest ones. The farther away the detection point is, the more waves (long and short period waves) are mixed.

On the other hand, from the second column of both figures we can see that the changes in the density variance here are not as high as at the center of the Harris current sheet. The shapes of these signals also differ from those in the first column. These signals are probably a mixture of several waves.

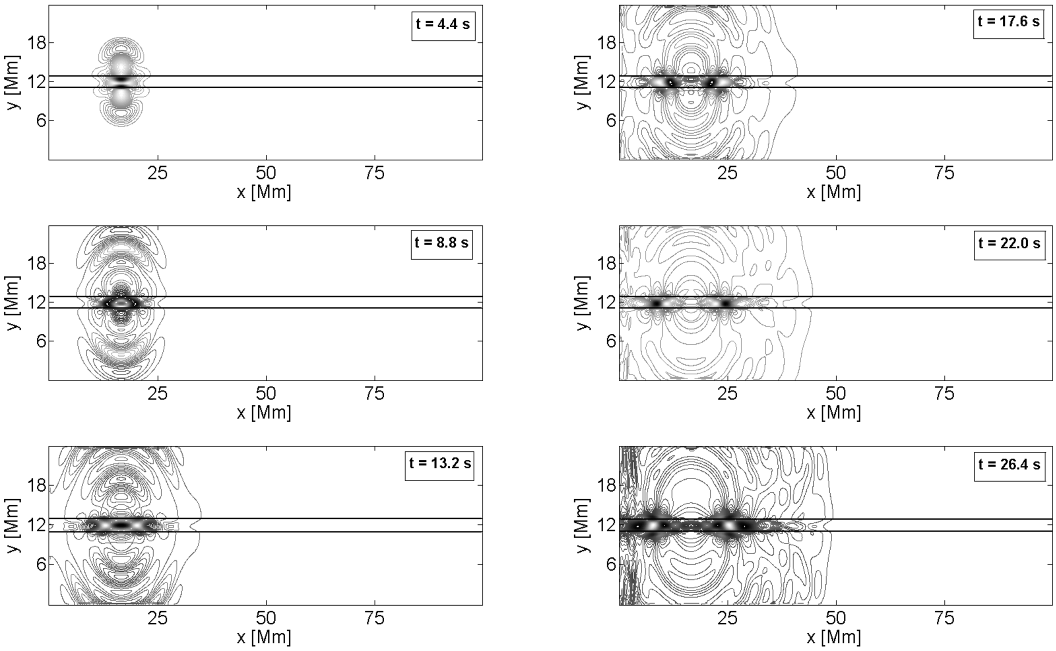

Fig. 6. The time evolution of the pressure variance $\Delta p = p(t) - p(0)$ at various times t, depicted as the contours for the density slab. The borders of the density slab are drawn as the black lines ($w_{\rm sl} = 1.0$ Mm).

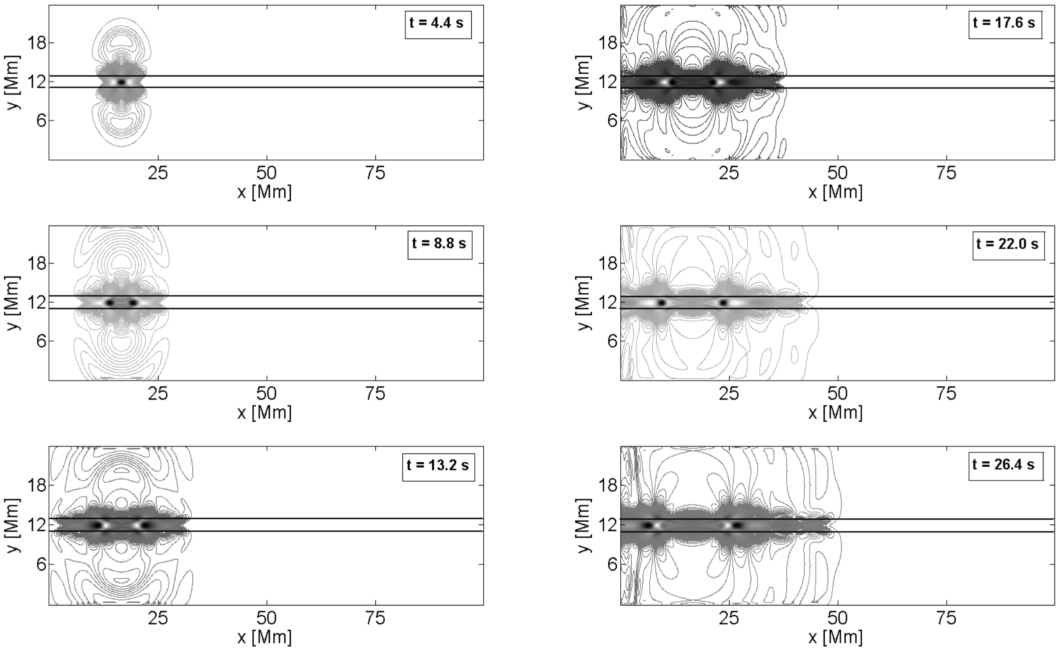

Fig. 7. The time evolution of the pressure variance $\Delta p = p(t) - p(0)$ at various times t, depicted as the contours for the Harris current sheet. The width of the current sheet is bordered by black lines ($w_{\rm CS} = 1.0$ Mm).

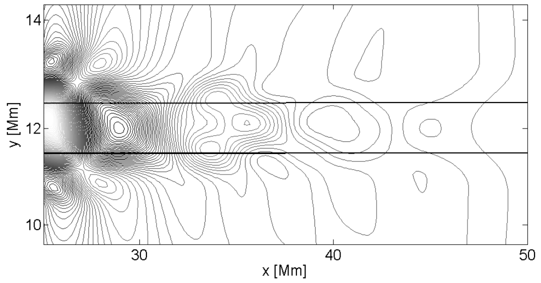

Fig. 8. Detail of the pressure variance Δp at the time $t = 26.4$ s for the density slab. The black lines represent the borders of the density slab ($w_{\rm sl} = 1.0$ Mm).

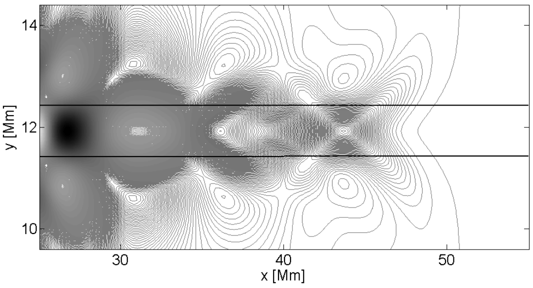

Fig. 9. Detail of the pressure variance Δp for the Harris current sheet at the time $t = 26.4$ s. The black lines represent the borders of the current sheet ($w_{\rm CS} = 1.0$ Mm).

4.3.3. Forms of wavelet tadpoles

Figure 11 shows the wavelet tadpoles calculated by means of the wavelet analysis for three different positions of the detection point, $L_{\rm D} = \{L/4, H/2\}, \{L/2, H/2\}$, and $\{3L/4, H/2\}$, in the density slab and in the Harris current sheet – as shown in the left and right column, respectively.

The shapes of the wavelet tadpoles of both of these structures were found to be very similar at all detection points. This is in good agreement with our previous findings about the behavior of the magnetoacoustic waves close to the center of the Harris current sheet. The form of these wavelet tadpoles becomes longer and the heads and tails of the wavelet tadpoles are detected later in time as the distance $|L_{\rm D} - L_{\rm P}|$ of the detection point increases away from that of the initial wave perturbation. The evolution of the detected signal with time is in good agreement with our expectations based on the analytical expressions for the estimation of the "first signal" arrival as well as the time of the decay (Airy) phase. The prolongations of the wavelet tadpoles, which depend on the location of the detection point $L_{\rm D}$, are due to the mixing of different phases of incoming magnetoacoustic waves and are in ratios of detection and perturbation point distances.

In the same figure, it can be seen that the periods of these wavelet tadpoles partly change because of the way in which they depend on the position of the detection point $L_{\rm D}$. From the global wavelet spectrum, we have found that the periods of the wave signals for the density slab and the Harris current sheet are as follows: $P_{L/4} = 6.8$ s, $P_{L/2} = 7.0$ s, $P_{3L/4} = 7.3$ s and, $P_{L/4} = 6.3$ s, $P_{L/2} = 6.8$ s, $P_{3L/4} = 7.2$ s, respectively.

5. Conclusions

Using the 2-D MHD model, we have studied numerically the propagation of magnetoacoustic waves in two different structures: a) the density slab with the straight magnetic field oriented along this slab; and b) the Harris current sheet. To obtain the phase and group speeds of propagating magnetoacoustic waves, we have numerically solved the wave equation of plasma motions. For the analysis of numerically calculated wave signals, we used the wavelet method.

In the case of the density slab, we compared the results of our numerical computations with analytical expressions. We found that the numerically obtained periods of wave signals, as well as their dependence on the slab half-width, are in good agreement with those calculated using analytical formulae. We compared how the times of the wave signal arrivals depend on the position of the detection point $L_{\rm D}$ using the numerically calculated and analytically derived group speeds of this wave. Since there was good agreement between the numerical and analytical results, we applied the numerical model for the Harris current sheet. The mutual comparisons of the results were made for both of these studied cases.

We found that from a global point of view magnetoacoustic waves in both cases evolve in a similar way. Nevertheless, there are differences in the central parts of these structures because of their different magnetic field profiles. Owing to the same reason, the dependences of the wave period on the half-width of these structures partly differ.

Considering these similarities and differences, one can conclude that without any additional information (e.g. information about the radio source location) it will not be easy to distinguish, in terms of diagnostics, between both of these cases. There may be an opportunity to resolve them in the form of the wavelet spectra derived e.g., in the analysis of the flare radio emission during solar flares (Mészárosová et al. 2009c). In particular, some unusual wavelet tadpoles have already been simulated, as well as observed, that be able to resolve these cases. However, this is beyond the scope of this paper and will be studied in more detail in further studies.

From the point of view of the diagnostics of either flare current sheets or flare loops, the most important measurements and findings are: a) the periods that can be used to estimate the half-width of these structures; and b) that the wavelet tadpoles become longer and their heads are detected later in time when increasing a distance between the detection and perturbation points. Thus, it is possible to estimate a distance between the radio source, for which modulated signal is analyzed, and the region where the magnetoacoustic wave is initiated. In special cases, we can even record the magnetoacoustic wave propagating along the density slab or the current sheet. For example, we can permit the magnetoacoustic wave to propagate along these structures upwards in the solar atmosphere and ensure that this wave modulates the radio emission (produced by the plasma emission mechanism) at lower radio frequencies. The wavelet spectra at these frequencies would then show us how the wavelet tadpoles have shifted in time, corresponding to the propagating magnetoacoustic wave train. Each tadpole corresponds to a specific plasma frequency, i.e. to specific plasma density and height in the solar atmosphere, if some density model of the solar atmosphere is assumed.

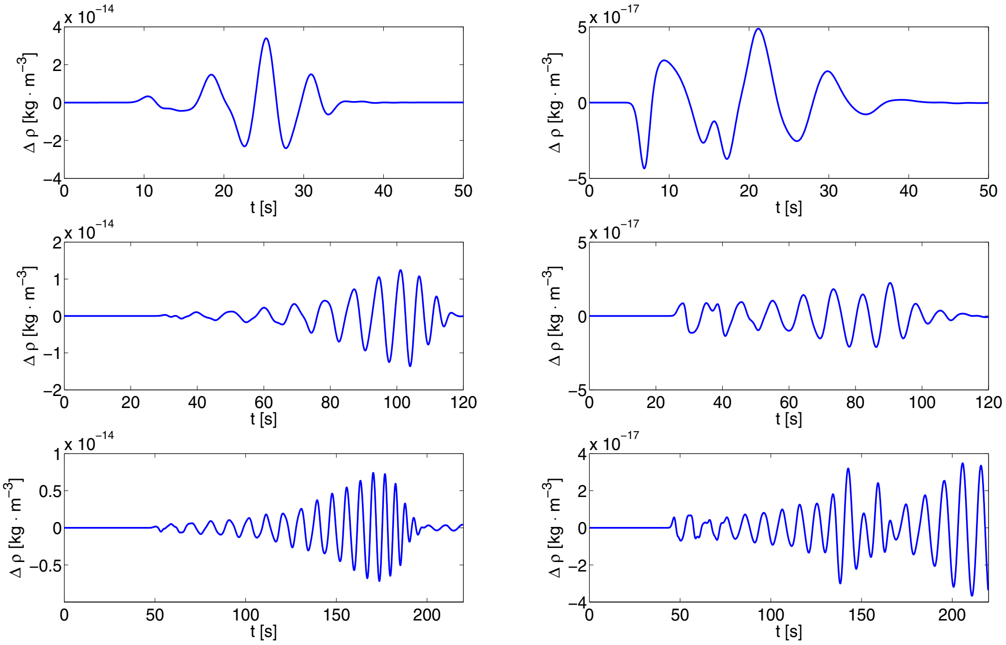

Fig. 10. Comparison of incoming wave signals in selected detection points. The data were recorded in $L_\mathrm{D} = L/4, L/2, 3L/4$ (*upper, middle and lower panel*, respectively). In the *left and right columns*, the results for the center ($H/2$) and 75 Mm ($3H/4$) above the Harris current sheet are shown.

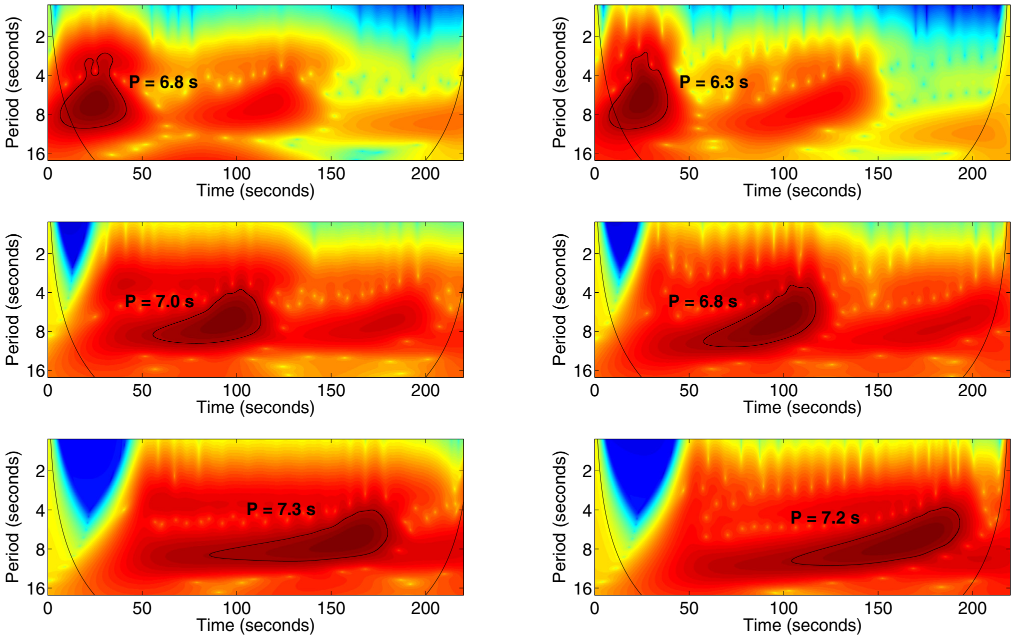

Fig. 11. The "time evolutions" and comparison of tadpole shapes in three different detection points $L_\mathrm{D} = L/4, L/2, 3L/4$ (*upper, middle, and lower panel*, respectively). In the *left column*, the results for the density slab are shown, whereas the results for Harris current sheet can be seen in the *right column*.

Acknowledgements. This research has been supported by Grant IAA300030701 of Grant Agency of the Academy of Sciences of the Czech Republic and Grant P209/10/1680 of Grant Agency of the Czech Republic. The wavelet analysis was performed using software written by C. Torrence and G. Compo available at URL `http://paos.colorado.edu/research/wavelets`.

References

Aschwanden, M. 2004, Phys. Sol. Corona (Chichester, UK: Springer, Praxis Publ.)
Aschwanden, M., Fletcher, L., Schrijver, C. J., & Alexander, D. 1999, ApJ, 520, 880
Chung, T. J. 2002, Comput. Fluid Dyn. (New York, USA: Cambridge University Press)
De Moortel, I., Ireland, J., Walsh, R. W., & Hood, A. W. 2002, Sol. Phys., 209, 61
Edwin, P. M., & Roberts, B. 1982, Sol. Phys., 76, 239
Edwin, P. M., & Roberts, B. 1983, Sol. Phys., 88, 179
Jelínek, P., & Karlický, M. 2009, Eur. Phys. J. D, 54, 305
Jelínek, P., & Karlický, M. 2010, IEEE Trans. Plasma Sci., 38, 2243
Jiřička, K., Karlický, M., Kepka, O., Tlamicha, A. 1993, Sol. Phys., 147, 203
Karlický, M., Jelínek, P., & Mészárosová H. 2011, A&A, 529, A96
Katsiyannis, A. C., Williams, D. R., McAteer, R. T. J., et al. 2003, A&A, 406, 709
Kliem, B., Karlický, M., & Benz, A. O. 2000, A&A, 360, 715
Mészárosová, H., Sawant, H. S., Cecatto, J. R., et al. 2009a, Adv. Space Res., 43, 1479
Mészárosová, H., Karlický, M., Rybák, J., & Jiřička, K. 2009b, ApJ, 697, L108
Mészárosová, H., Karlický, M., Rybák, J., & Jiřička, K. 2009c, A&A, 502, L13
Murawski, K., & Roberts, B. 1994, Sol. Phys., 151, 305
Nakariakov, V. M., & Roberts, B. 1995, Sol. Phys., 159, 399
Nakariakov, V. M., Arber, T. D., Ault, C. E., et al. 2004, MNRAS, 349, 705
Nakariakov, V. M., Pascoe, D. J., & Arber, T. D. 2005, Space Sci. Rev., 121, 115
Ofman, L., & Wang, T. 2002, ApJ, 580, L85
Priest, E. R. 1982, Solar Magnetohydrod (London, England: D. Reidel Publishing Company)
Roberts, B. 1981a, Sol. Phys., 69, 27
Roberts, B. 1981b, Sol. Phys., 69, 39
Roberts, B., Edwin, P. M., & Benz, A. O. 1983, Nature, 305, 688
Roberts, B., Edwin, P. M., & Benz, A. O. 1984, ApJ, 279, 857
Sankaran, K., Martinelli, L., Jardin, S. C., & Choueiri, E. Y. 2002, Int. J. Numer. Meth. Engng., 53, 1415
Sato, T., & Hayashi, T. 1979, Phys. Fluids, 22, 1189
Selwa, M., & Murawski, K. 2004, A&A, 425, 719
Selwa, M., Murawski, K., & Solanki, S. K. 2005, A&A, 436, 701
Selwa, M., Ofman, L., & Murawski, K. 2007, ApJ, 668, L83
Smith, J. M., Roberts, B., & Oliver, R. 1997, A&A, 327, 377
Wang, T. J., & Solanki, S. K. 2004, A&A, 421, L33
Torrence, Ch., & Compo, G. P. 1998, Bull. Am. Meteor. Soc., 79, 61
Zhukov, V. I. 1989, Astrophys. Space Sci., 154, 247

A&A 546, A49 (2012)
DOI: 10.1051/0004-6361/201219891

Astronomy & Astrophysics

Magnetoacoustic waves in a vertical flare current-sheet in a gravitationally stratified solar atmosphere

P. Jelínek[1], M. Karlický[2], and K. Murawski[3]

[1] University of South Bohemia, Faculty of Science, Institute of Physics and Biophysics, Branišovská 10, 370 05 České Budějovice, Czech Republic
e-mail: `pj@matfyz.cz`
[2] Academy of Sciences of the Czech Republic, v. v. i., Astronomical Institute, Fričova 258, 251 65 Ondřejov, Czech Republic
[3] Maria Curie-Skłodowska University, Institute of Physics, Group of Astrophysics, Radziszewskiego 10, 20 031 Lublin, Poland

Received 26 June 2012 / Accepted 9 August 2012

ABSTRACT

Aims. We numerically studied evolution of impulsively generated magnetoacoustic waves in the vertical flare current-sheet that is embedded in the gravitationally stratified solar atmosphere and compared it with its gravity-free counterpart.

Methods. We adopted a two-dimensional (2D) magnetohydrodynamic (MHD) model, in which we solved a full set of ideal time-dependent MHD equations by means of the FLASH code, using the adaptive mesh refinement (AMR) method. To initiate the fast sausage magnetoacoustic waves, we used axisymmetric Gaussian velocity perturbation. As a diagnostic tool of these magnetoacoustic waves, we used the wavelet analysis method.

Results. We present a model of magnetoacoustic wave propagation with a gravity that is more realistic than that presented in previous studies. We compare our results with those of a gravity-free case. In equilibrium the current-sheet with gravity requires a non-zero horizontal component of the magnetic field, contrary to the gravity-free case. This causes differences in the parameters of the wave signal that propagates along the current sheet. In addition to these differences we find that wave signal variations and their wavelet tadpoles are more complex in the case with gravity than in the gravity-free case. Furthermore, for a shorter scale-height we found a prolongation of the wavelet tadpoles. These differences result from a variation of the dispersive properties and group velocities of the propagating magnetoacoustic waves with height in the solar atmosphere in the gravitational case. We show that these results can affect the diagnostics of physical processes in solar flares.

Key words. Sun: corona – Sun: flares – Sun: oscillations – methods: numerical – magnetohydrodynamics (MHD)

1. Introduction

Magnetohydrodynamic (MHD) waves are recognized as an efficient tool in diagnostics of the solar corona as well as of solar flares, see e.g. Roberts (2000), Nakariakov (2003), and Macnamara & Roberts (2010, 2011). Waves and oscillations are observed by modern imaging and spectral instruments in the visible light, EUV, X-ray and radio bands, and some of them can be interpreted in terms of MHD plasma theory. The magnetically dominated solar plasma can support the propagation of various types of waves. These MHD waves and oscillations have been investigated and analyzed in many theoretical and numerical studies. Among various studied cases we can distinguish propagating (De Moortel et al. 2002), slow magnetoacoustic standing (Ofman & Wang 2002; Nakariakov et al. 2004; Selwa et al. 2005; Zaqarashvili et al. 2005; Jelínek & Karlický 2009, 2010), fast magnetoacoustic: kink (Nakariakov et al. 1999; Aschwanden et al. 2002; Wang & Solanki 2004; Andries et al. 2005; Pascoe et al. 2010) and sausage modes (Pascoe et al. 2007, 2009). These modes have been observed with highly sensitive instruments such as SUMER (SoHO) and TRACE, as well as by other recent solar missions, e.g., EIS/Hinode or EUVI/STEREO. Also, compressible MHD waves (Ofman et al. 1999); De Moortel et al. (2000) and flare-generated global kink oscillations of solar coronal loops (Schrijver et al. 2002) were discovered; for a comprehensive review, see Nakariakov & Verwichte (2005).

The impulsively generated MHD waves and oscillations can be excited by various processes in the solar corona. The impulsive flare process, which provides either single or multiple sources of disturbances, is the most probable one. The impulsively generated magnetoacoustic waves are trapped in regions of higher density, i.e. in regions with a lower Alfvén speed, which act as waveguides. The periodicity of propagating fast sausage waves results from the time evolution of an impulsively generated signal (see Roberts et al. 1983, 1984 and Murawski & Roberts 1994). These waves in a coronal waveguide have three distinct phases: (1) periodic phase (long-period spectral components are fastest and they arrive first at the detection point); (2) quasi-periodic phase (both long and short-period spectral components arrive and interact); (3) decay (or Airy) phase, where the signal passes the detection point (Roberts et al. 1984).

The wavelet analysis of impulsively generated (fast sausage) magnetoacoustic wave trains shows the typical tadpole shape with a narrow-spectrum tail preceding a broadband head. These tadpole signatures (wavelet tadpole) were first observed by the SECIS instrument in the 1999 solar-eclipse data (see Katsiyannis et al. 2003). Similarly, Mészárosová et al. (2009a,b) detected for the first time the tadpoles in the wavelet spectra in some radio sources, which has also been confirmed numerically, see e.g. Nakariakov et al. (2004, 2005).

Owing to their enhanced density, current-sheets are the structures that can guide the MHD waves. Karlický et al. (2011)

found the wavelet tadpoles in sources of the narrowband dm-spikes. These authors concluded that these wavelet tadpoles indicate that the magnetoacoustic waves propagate in the global current-sheet (current layer) in the turbulent reconnection outflows. This paper served as a motivation of a more extended and detailed study of the magnetoacoustic (fast sausage) waves in the current-sheet, see Jelínek & Karlický (2012).

The present paper extends our previous model (Jelínek & Karlický 2012). We study an evolution of the propagating fast sausage magnetoacoustic waves in a vertical flare current-sheet under the influence of gravity, which makes our model more realistic. Then we compare it with the gravity-free case. Because these processes are important for a diagnostics of solar flares, we analyze the computed waves in the same way as those observed, i.e., using the wavelet analysis method.

The structure of the present paper is as follows. Section 2 describes our numerical models, governing equations, initial conditions, and perturbations. In Sect. 3, the numerical results, obtained by means of our computer models, are shown and discussed. Finally, Sect. 4 presents our conclusions.

2. Physical model

2.1. Governing equations

In our numerical model of the vertical flare current-sheet in the gravitationally stratified solar atmosphere, the plasma dynamics is described by the two-dimensional (2D) time-dependent ideal magnetohydrodynamic equations, see e.g. Priest (1982):

$$\frac{\mathrm{D}\varrho}{\mathrm{D}t} = -\varrho\nabla\boldsymbol{v}, \tag{1}$$

$$\varrho\frac{\mathrm{D}\boldsymbol{v}}{\mathrm{D}t} = -\nabla p + \boldsymbol{j}\times\boldsymbol{B} + \varrho\boldsymbol{g}, \tag{2}$$

$$\frac{\mathrm{D}\boldsymbol{B}}{\mathrm{D}t} = (\boldsymbol{B}\cdot\nabla)\boldsymbol{v}, \tag{3}$$

$$\frac{\mathrm{D}e}{\mathrm{D}t} = -\gamma e\nabla\cdot\boldsymbol{v}, \tag{4}$$

$$\nabla\cdot\boldsymbol{B} = 0. \tag{5}$$

Here $\mathrm{D}/\mathrm{D}t \equiv \partial/\partial t + \boldsymbol{v}\cdot\nabla$ is the total time derivative, ϱ is the mass density, $\boldsymbol{v}$ is the flow velocity, $\boldsymbol{B}$ is the magnetic field, and $\boldsymbol{g} = [0, -g_\odot, 0]$ is the gravitational acceleration with $g_\odot = 274\ \mathrm{m\,s^{-2}}$. The current density $\boldsymbol{j}$ in Eq. (2) is expressed as

$$\boldsymbol{j} = \frac{1}{\mu_0}\nabla\times\boldsymbol{B}, \tag{6}$$

where $\mu_0 = 1.26\times10^{-6}\ \mathrm{H\,m^{-1}}$ is the magnetic permeability of free space. The specific internal energy, e, in Eq. (4) is given by

$$e = \frac{p}{(\gamma-1)\varrho}, \tag{7}$$

with the adiabatic coefficient, which we set and hold fixed as $\gamma = 5/3$.

2.2. Equilibrium

For a still ($\boldsymbol{v} = \boldsymbol{0}$) equilibrium, the Lorentz and gravity forces have to be balanced by the pressure gradient in the entire physical domain

$$-\nabla p + \boldsymbol{j}\times\boldsymbol{B} + \varrho\boldsymbol{g} = \boldsymbol{0}. \tag{8}$$

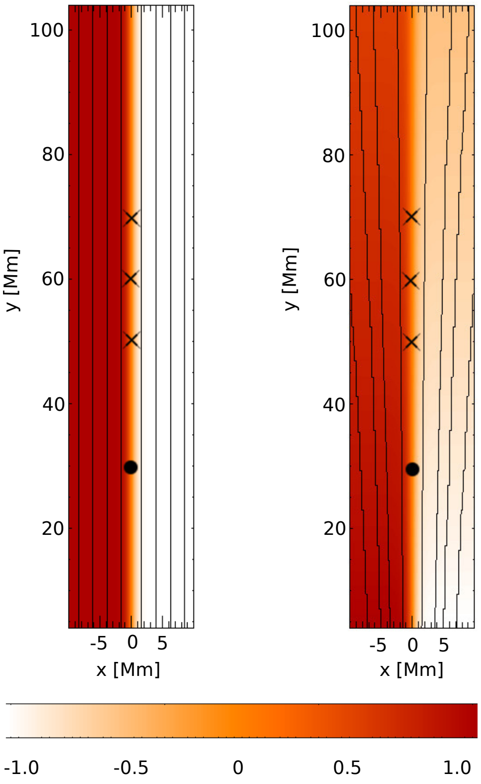

Fig. 1. Vertical magnetic field component, B_y, (color map) for the gravity-free medium (*left*) and gravitationally stratified solar atmosphere (*right*). The magnetic field lines are displayed by solid lines. The full circles denote the location of the initial perturbation and crosses correspond to locations of detection points.

The solenoidal condition, $\nabla\cdot\boldsymbol{B} = 0$, is identically satisfied by the magnetic flux function, $\boldsymbol{A}$,

$$\boldsymbol{B} = \nabla\times\boldsymbol{A}. \tag{9}$$

For calculating the magnetic field in the vertical flare current-sheet we use the magnetic flux function $\boldsymbol{A} = [0, 0, A_z]$ in general form

$$A_z = -B_\mathrm{o} w_\mathrm{cs}\log\left\{\left|\cosh\left(\frac{x}{w_\mathrm{cs}}\right)\right|\right\}\exp\left(-\frac{y}{\lambda}\right). \tag{10}$$

Here the coefficient λ denotes the magnetic scale-height. For the limit case of $\lambda \to \infty$ the exponent becomes unity for a gravity-free medium. The symbol B_o is used for the magnetic field at $x \to \infty$, and w_cs is the half-width of the current-sheet. Here we set and hold fixed $w_\mathrm{cs} = 1.0$ Mm.

Figure 1 displays the vertical component of the magnetic field, B_y, for the gravity-free case (left panel) and for the gravitationally stratified solar corona (right panel). The magnetic field lines are expressed by full lines. Note that at $x = 0$ the vertical magnetic field component, B_y, experiences a sudden jump from negative (for $x < 0$) to positive values (for $x > 0$).

2.2.1. Gravity-free medium

In the gravity-free case, $\boldsymbol{g} = [0, 0, 0]$, we find that the magnetic field is

$$\boldsymbol{B} = \left[0, B_{\mathrm{o}} \tanh\left(\frac{x}{w_{\mathrm{cs}}}\right), 0\right]. \tag{11}$$

This magnetic field corresponds to the Harris current-sheet. It changes from B_0 for high positive values of x to $-B_0$ for high negative values of x, passing through zero at $x = 0$ (Fig. 1).

From the equation of static equilibrium, Eq. (8), we obtain the formula for the gas pressure distribution in the following form, see e.g. (Smith et al. 1997)

$$p(x, y) = p_{\mathrm{CS}} \cdot \mathrm{sech}^2\left(\frac{x}{w_{\mathrm{CS}}}\right), \tag{12}$$

where p_{CS} is the gas pressure at the center of the Harris current-sheet, expressed as

$$p_{\mathrm{CS}} = n_{\mathrm{CS}} k_{\mathrm{B}} T. \tag{13}$$

We assumed that in the equilibrium the plasma is isothermal with a temperature $T = 10.0 \times 10^6$ K (for the first studied case) or $T = 5.0 \times 10^6$ K (for the second studied case). The particle density in the center of the Harris current-sheet is $n_{\mathrm{CS}} = 4.0 \times 10^{16}$ kg m^{-3} and $k_{\mathrm{B}} = 1.38 \times 10^{-23}$ J K^{-1} is the Boltzmann constant. After specifying gas pressure and temperature, we find the mass density distribution from the ideal gas law,

$$\varrho = \frac{mp}{k_{\mathrm{B}} T}. \tag{14}$$

2.2.2. Gravitationally stratified medium

To satisfy the solenoidal condition given by Eq. (5), combining it with Eq. (9) and using the gravitational acceleration that is oriented in the negative y-direction, $\boldsymbol{g} = [0, -g_{\odot}, 0]$, we obtain the equations for the magnetic field in the x-y plane as

$$B_x(x, y) = B_{\mathrm{o}} \frac{w_{\mathrm{cs}}}{\lambda} \ln\left[\cosh\left(\frac{x}{w_{\mathrm{cs}}}\right)\right] \exp\left(-\frac{y}{\lambda}\right), \tag{15}$$

$$B_y(x, y) = B_{\mathrm{o}} \tanh\left(\frac{x}{w_{\mathrm{cs}}}\right) \exp\left(-\frac{y}{\lambda}\right). \tag{16}$$

For details see Galsgaard & Roussev (2002).

In our 2D model without and with the gravity, Eq. (8) attains the following form:

$$\frac{\partial p(x, y)}{\partial x} + j_z B_y(x, y) = 0, \tag{17}$$

$$\frac{\partial p(x, y)}{\partial y} - j_z B_x(x, y) + \varrho g(x, y) = 0. \tag{18}$$

Here j_z is the only non-zero component of the electric current density $\boldsymbol{j}$ (see Eq. (6)), given by $j_z = \frac{1}{\mu_0}(\nabla \times \boldsymbol{B})_z$.

The condition of integrability of the above equations leads to

$$\mu_0 g \frac{\partial \varrho(x, y)}{\partial x} = \nabla \cdot (\mu_0 j_z \boldsymbol{B}), \tag{19}$$

from which we can derive the formulae for the distribution of the mass density

$$\begin{aligned}\varrho(x, y) \; = \; & \left\{ \frac{B_{\mathrm{o}}^2}{\mu_0 g \lambda} \left\{ 1 + \ln\left[\cosh\left(\frac{x}{w_{\mathrm{cs}}}\right)\right]\right\} \mathrm{sech}^2\left(\frac{x}{w_{\mathrm{cs}}}\right) \right. \\ & \left. + \varrho_0 \right\} \exp\left(-2\frac{y}{\lambda}\right), \end{aligned} \tag{20}$$

and gas pressure

$$\begin{aligned} p(x, y) \; = \; & \left\{ \frac{B_{\mathrm{o}}^2}{2\mu_0} \mathrm{sech}^2\left(\frac{x}{w_{\mathrm{cs}}}\right) + \frac{B_{\mathrm{o}}^2 w_{\mathrm{cs}}^2}{2\mu_0 \lambda^2} \ln^2\left[\cosh\left(\frac{x}{w_{\mathrm{cs}}}\right)\right] \right. \\ & \left. + \frac{\varrho_0 g \lambda}{2} \right\} \exp\left(-2\frac{y}{\lambda}\right) + p_0. \end{aligned} \tag{21}$$

Here ϱ_0 and p_0 are arbitrary integration constants. The corresponding plasma temperature is determined by Eq. (14).

2.3. Perturbations

At the start of the numerical simulation ($t = 0$ s), the equilibrium is perturbed by the Gaussian pulse in the x-component of velocity and has the following form (e.g. Nakariakov et al. 2004, 2005):

$$v_x = -A_0 \frac{x}{\lambda_y} \exp\left[-\frac{(x - L_{\mathrm{P}})}{\lambda_x}\right]^2 \exp\left[-\frac{y}{\lambda_y}\right]^2, \tag{22}$$

where A_0 is the initial amplitude of the pulse, and $\lambda_x = \lambda_y = 1.0$ Mm are the widths of the velocity pulse in the longitudinal and transverse directions, respectively. This pulse triggers preferentially fast magnetoacoustic sausage waves.

The perturbation point, L_{P}, in both the cases, is located on the axis of the current-sheet, at a distance of 30 Mm from the bottom boundary of the simulation region. The detection points, L_{P}, are also on the current-sheet axis and the distance between the perturbation and detection points is $\Delta \equiv |L_{\mathrm{D}} - L_{\mathrm{P}}| = 20, 30,$ and 40 Mm, respectively. See full black circles and crosses in Fig. 1.

3. Numerical model

The 2D time-dependent ideal MHD Eqs. (1)–(4) were solved numerically with the FLASH code. This code was initially developed to model nuclear flashes on the surfaces of neutron stars and white dwarfs, and the interior of white dwarfs; but it has since been applied to model a wide variety of astrophysical processes, see e.g. Fryxell et al. (2000). Currently, it is a well tested, fully modular, parallel, multiphysics, open science, simulation code that implements second- and third-order unsplit Godunov solvers and adaptive mesh refinement (AMR), see e.g. Chung (2002) and Murawski (2002). The Godunov solver combines the corner transport upwind method for multidimensional integration and the constrained transport algorithm for preserving the divergence-free constraint on the magnetic field (Lee & Deane 2009). In our case, the AMR strategy is based on controlling the numerical errors in a gradient of mass density that leads to reducing the numerical diffusion within the entire simulation region.

For our numerical simulations we used a 2D Eulerian box with the height and width of the simulation region; for all the studied cases, $H = 100$ Mm and $W = 20$ Mm, respectively (see Fig. 1). The spatial resolution of the numerical grid was determined with the AMR method and we used the AMR grid with the minimum (maximum) level of the refinement blocks set to 3 (7). Note that a spatial grid size has to be less than the typical width of the current-sheet along the x-direction and the typical wavelength of the magnetoacoustic waves along the y-direction, respectively. We found $\min(\Delta x) = 0.31$ Mm and $\min(\Delta y) = 0.26$ Mm, which satisfies the above mentioned condition (semi-width of the current-sheet is $w_{\rm CS} = 1.0$ Mm and the estimated minimal wavelength is approximately 5.0 Mm). As a consequence of the real plasma medium extension we applied free-boundary conditions at the boundaries of the simulation region, so that the waves could freely leave the simulation box without any significant reflection.

4. Numerical results

We present the numerical results of evolution of fast magnetoacoustic sausage waves in the vertical current-sheet embedded in the gravitationally stratified solar atmosphere. Simultaneously, we compare these results with those obtained for the gravity-free case. Furthermore, we compare the numerical results in the gravitationally stratified solar atmosphere calculated for two different scale-heights. From wave signals detected at the three detection points we also compute the wavelet spectra and wave periods of obtained wavelet tadpoles.

For the wavelet analysis we used the Morlet wavelet, which consists of a plane wave modulated by a Gaussian,

$$\Psi(t) = \pi^{-1/4} \exp^{(i\sigma t)} \exp^{-(t^2/2)}, \tag{23}$$

where the parameter σ allows trade between time and frequency resolutions. Here we assumed the value of parameter $\sigma = 6$, as recommended by Farge (1992). The wave periods are estimated from the global wavelet spectrum as the most dominant period in this spectrum. More details about the wavelet method and its implementation can be found e.g. in Farge (1992) and Torrence & Compo (1998).

4.1. Gravity-free vs. gravitationally stratified solar atmosphere

In the following, in addition to the gravity-free current-sheet we consider the vertical current-sheet including gravity with two different scale-heights: the longer and shorter ones corresponding in the 1D gravity model to that with the temperature $T = 10.0 \times 10^6$ K and $T = 5.0 \times 10^6$ K, respectively. In the case with the longer scale-height we also study two cases with two different widths of the current-sheet.

First, we compare the profiles of the normalized mass densities along the vertical axis of the current-sheet in the gravity-free case and gravitationally stratified plasma for a longer scale-height (Figs. 2 and 3). In Fig. 2 the normalized mass density in a gravity-free medium for times 10 s, 50 s, and 100 s is shown, while in Fig. 3 similar results are presented for the gravitationally stratified case for two widths of the current-sheet (in the left part for $w_{\rm CS} = 1.0$ Mm and $w_{\rm CS} = 1.5$ Mm in the right-hand side of the figure).

At the very early stage of the wave evolution, e.g. at $t = 10$ s (solid line), the wave has a very simple form in both cases. For longer times, $t = 50$ s and $t = 100$ s (dashed and dotted lines, respectively), some differences appear. The wave in the case of the gravitationally stratified solar atmosphere is slightly undulated and more irregular than in the gravity-free case. This effect seems to be caused by different wave dispersion in these two cases. Furthermore, in Fig. 3 one would expect that the wave amplitude will grow while the wave propagates toward lower mass densities, which occur at higher altitudes of the solar atmosphere. However, as can be seen here, the maximum amplitude decreases with height. This is caused by a relatively strong spatial dispersion of the wave pulse energy into larger and larger volume. Namely, different wave components of the initial wave pulse propagate with different group velocities and the wave pulse becomes longer in the vertical direction. Moreover, in this direction also the width of the current-sheet and thus the wave pulse becomes wider with an increase of y.

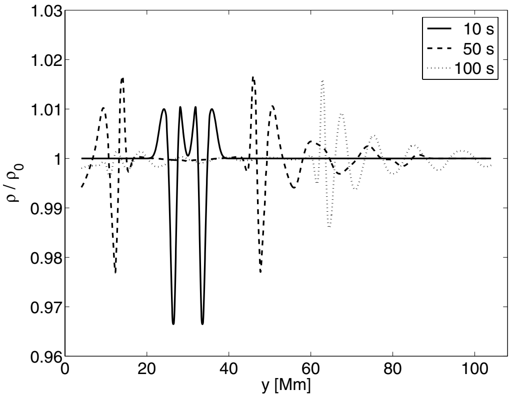

Fig. 2. Profiles of the normalized mass density along the vertical axis ($x = 0$) of the current-sheet at times $t = 10$ s (solid line), 50 s (dashed line) and 100 s (dotted line) for the gravity-free case. The semi-width of the current-sheet is $w_{\rm CS} = 1.0$ Mm.

We compare here also the incoming wave signals (expressed in relative plasma density variations) to the three selected detection points (Fig. 4) as well as the corresponding wavelet tadpoles (Fig. 5). In the left panels of both figures the results for the gravity-free current-sheet are shown. These results (wave periods as well as the wavelet tadpole shapes) look similar to those published by Jelínek & Karlický (2012). For comparison purposes, in the right columns we show the numerical results for the current-sheet that is embedded in the gravitationally stratified solar atmosphere.

If we compare the numerical results displayed in Fig. 4, we can see that the wave signals propagating in the gravitationally stratified solar corona (right) have more irregular shapes than in the gravity-free case (left), which results from stronger wave dispersion in the former case. The arrival time of the "leading signal" is very similar in both cases because the mass density and the magnetic field in the vertical y-direction decreases in the same way, and thereforep the corresponding Alfvén speeds are approximately of the same magnitude.

As a result of the above mentioned irregularities in the incoming wave signals, which propagate in the gravitationally stratified solar atmosphere, we observe altered shapes of the wavelet tadpoles compared to the gravity-free case (Fig. 5).

The slightly different wave periods can also be discernible by comparing these two cases, as well as the different lengths of wavelet tadpoles. Nakariakov et al. (2005) found that narrower longitudinal drivers produce a broader k-spectrum above the cutoff for wave propagation in the waveguide, and accordingly, a broader interval of wave periods is detected. In our previous work (Jelínek & Karlický 2012) we verified these results for the Harris current-sheet by varying the current-sheet width.

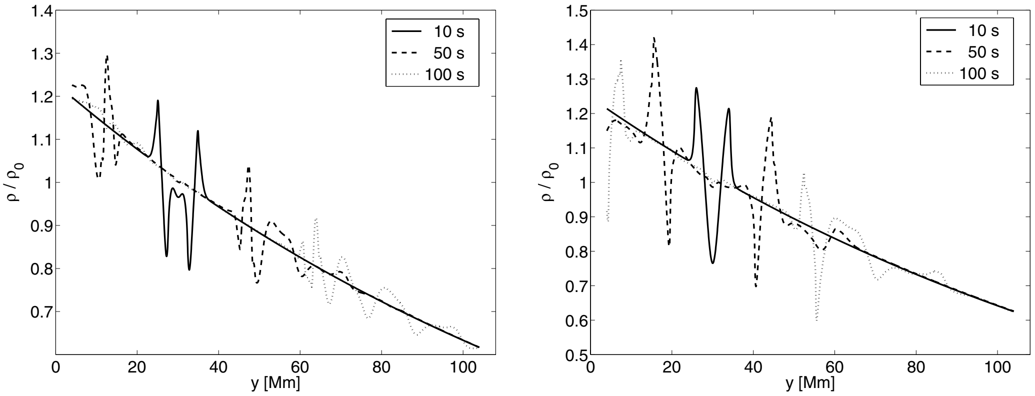

Fig. 3. Profiles of the normalized mass density along the vertical axis of the current-sheet ($x = 0$) at times $t = 10$ s (solid line), 50 s (dashed line) and 100 s (dotted line) for the case of the gravity, longer scale-height and two semi-widths of the current-sheet $w_{\rm CS} = 1.0$ Mm (*left*) and $w_{\rm CS} = 1.5$ Mm (*right*).

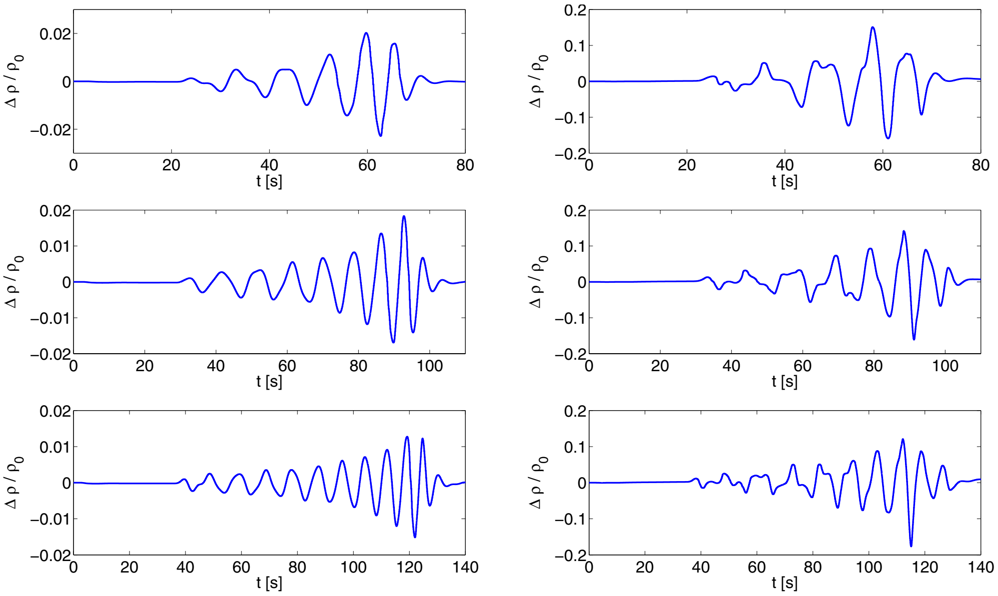

Fig. 4. Incoming wave signals (expressed in relative plasma density variations) at the detection points $L_{\rm D} = 50$ Mm, 60 Mm, and 70 Mm (*upper*, *middle*, and *lower panel*, respectively). In the *left column*, the signals for the gravity-free case are shown; the signals detected in the gravitationally stratified solar atmosphere are presented in the *right panel*. The semi-width of the current-sheet is $w_{\rm CS} = 1.0$ Mm.

Therefore we conclude that the prolongation of the wave periods in the case of the gravitationally stratified solar corona results from the width of the current-sheet, which grows with heights (Fig. 1, right). This conclusion is also supported by the calculations performed for the two widths of the current-sheet, see Fig. 3, left part (narrower width) and right part (wider width of the current-sheet), where we verified that the wave period is directly proportional to the semi-width of the current-sheet in accordance with the relation provided by Roberts et al. (1984)

$$P \approx \frac{w}{v_{\rm Alf}}\cdot \qquad (24)$$

4.2. Gravitationally stratified solar atmosphere

Figure 6 illustrates the same numerical results as Fig. 3, but for the shorter scale-height, corresponding in the 1D gravity model to the plasma temperature, $T = 5.0 \times 10^6$ K. The slope of the mass density in this case is steeper and the wave moves more slowly than in the case with the longer scale-height (Fig. 3). This corresponds to the fact that in this case the external Alfvén speed is slower than for the longer scale-height. Again at the very early stages $t = 10$ s (solid line) the wave has a simple form and later (50 and 100 s, dashed and dotted lines, respectively) it becomes undulated and irregular due to the wave dispersion.

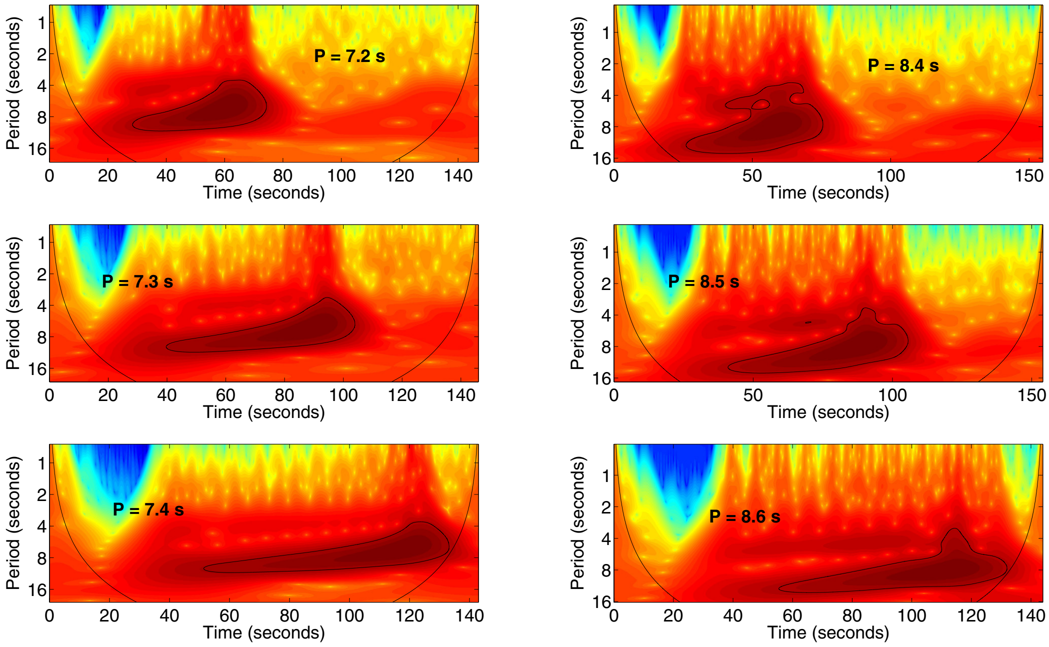

Fig. 5. Temporal evolution of wavelet tadpoles for the three detection points: $L_\mathrm{D} = 50$ Mm, 60 Mm, and 70 Mm (*upper, middle, and lower panel*, respectively) for the gravity-free (*left panels*) and gravitationally stratified (*right panels*) solar atmosphere. The semi-width of the current-sheet is $w_\mathrm{CS} = 1.0$ Mm.

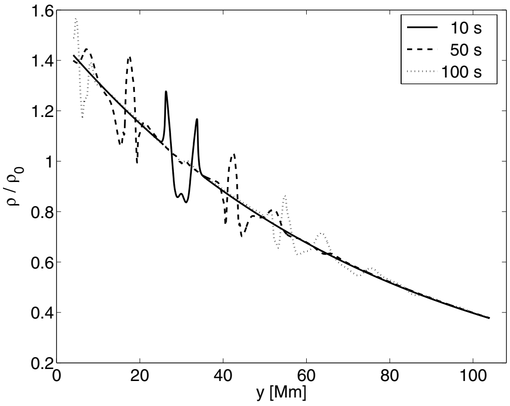

Fig. 6. Profiles of the normalized mass density along the vertical axis of the current-sheet for ($x = 0$) at times $t = 10$ s (solid line), 50 s (dashed line) and 100 s (dotted line) for the gravitationally stratified plasma with the shorter scale-height. The semi-width of the current-sheet is $w_\mathrm{CS} = 1.0$ Mm.

Figure 7 displays incoming wave signals and corresponding wavelet tadpoles for the shorter scale-height to the three detection points. Comparing these signals with those in Fig. 4, we observe delays in the arrival times of the "leading signals", which results from the lower value of the external Alfvén speed in this case, as mentioned in the previous paragraph. The estimated values of the arrival times of the "leading signals" to the detection points are presented in Table 1.

The forms of the wave signals are very similar and therefore there are no essential differences between the shapes of the wavelet tadpoles. On the other hand, if we compare the wave periods for both studied cases, we find that the wave period becomes longer for the shorter scale-height. This effect results from a lower value of the Alfvén speed and the ratios between the wave periods are approximately $\sqrt{2}$.

Figures 4 and 7 show that the wave signal is more strongly attenuated in the case of the shorter scale-height. This is because the initial perturbation (which has the same initial amplitude in velocity) propagates in a denser environment than in the case of the longer scale-height. The denser environment here is due to the same value of the magnetic field in both studied cases, and consequently, according to Eq. (13), for the same pressure inside the current-sheet the shorter scale-height leads to the higher mass density.

Comparing Figs. 5 and 7 (right panels), we infer that the wavelet tadpoles become longer in the case of the shorter scale-height. Because we already verified the calculations given by Roberts et al. (1984) in our previous work for the Harris current-sheet, the time duration of the wavelet tadpole can be calculated as $t_\mathrm{dp} - t_\mathrm{ls}$, where $t_\mathrm{dp} = |L_\mathrm{D} - L_\mathrm{P}|/v_\mathrm{A}$ and $t_\mathrm{ls} = |L_\mathrm{D} - L_\mathrm{P}|/v_\mathrm{gr}^\mathrm{min}$ is the time of the decay phase and the arrival time of the "leading signal", respectively (Jelínek & Karlický 2012). Hence, we conclude that longer lasting wavelet tadpoles result from a decrease in the group velocity. The group velocity in the case of the shorter scale-height is lower as a consequence of the higher mass density in the Harris current-sheet. As a result, the decay

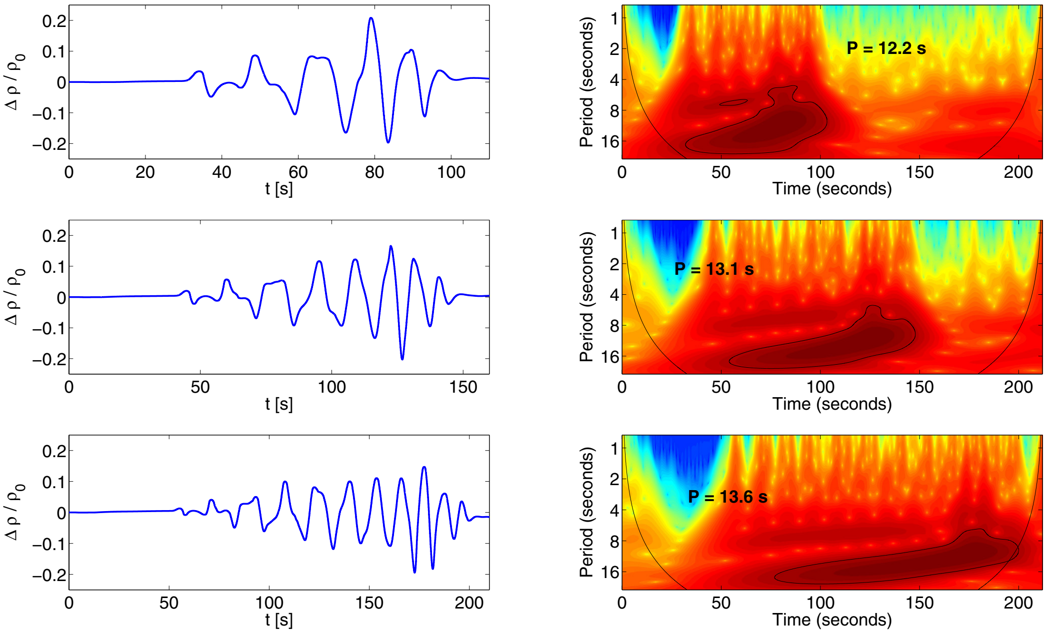

Fig. 7. Comparison of the incoming signals (relative plasma density variations) and corresponding wavelet tadpoles at the three different detection points L_D = 50 Mm, 60 Mm, and 70 Mm (*upper*, *middle*, and *lower panel*, respectively) in the case of the gravity and the shorter scale-height. The semi-width of the current-sheet is w_{CS} = 1.0 Mm.

Table 1. Arrival times of "leading signals" to the detection points L_D.

L_D[Mm]	Case #1	Case #2	Case #3
50	≈19 s	≈19 s	≈28 s
60	≈28 s	≈28 s	≈39 s
70	≈35 s	≈35 s	≈50 s

Notes. Cases #1 and #2 correspond to the arrival times presented in the left and right part of Fig. 4, while case #3 corresponds to the arrival times in the left part of Fig. 7.

phase of the wave signal comes later than in the case of longer scale-height.

Figure 8 shows the contours of mass density for the longer and shorter scale-heights close to the area of the detection points (left parts of subfigures (a) and (b), respectively). In the right parts of these subfigures the selected zoomed parts of the mass densities are displayed. We also represent the vectors of the total velocity as black arrows. The results in Figs. 8a and b are displayed at time t = 100 s.

The initial Gaussian pulse in the horizontal component of the velocity generates the magnetoacoustic waves that perturb the equilibrium in the mass density. As a result, we observe the characteristic "sausage" structures after a sufficiently long time. In the case of the longer scale-height we see the structure with a longer wavelength than in the case with the shorter scale-height. These figures also show that the wave propagates faster in the case of the longer scale-height, as shown in Figs. 3 and 6, which display slices of these structures along the axes of the vertical flare current-sheet.

In the zoomed-in views of the mass density contours (right parts of Figs. 8a and b) the maxima and minima of wave amplitudes are displayed. They also show the vectors of the plasma flow velocities. We can see that there are inflows of the plasma in front of the propagating wave amplitude maxima, whereas on the rear side of these maxima the plasma is outflowing. As a result, the current-sheet is periodically narrowed and broadened according to the sausage wave structure.

5. Conclusions

By including gravity in our model, we made it more realistic than the previous models. We solved 2D time-dependent ideal MHD equations using the FLASH numerical code, implementing AMR (Lee & Deane 2009). We studied the propagation of magnetoacoustic waves in the vertical flare current-sheet in a gravitationally stratified solar atmosphere and for a gravity-free case. We compared the numerical results for two different scale-heights in the gravitationally stratified solar atmosphere.

We found several important differences between the studied cases. First, for the gravitationally stratified current-sheet it is necessary to implement additional horizontal component of the magnetic field, contrary to the gravity-free case. As a consequence of this modification, properties of the current-sheet such as the waveguide are changed. At the bottom part of the numerical box the parameters of the current-sheets are the same in both cases. However, in the gravity case the width of the current-sheet grows with height. This explains the longer wave periods of propagating magnetoacoustic waves in the gravitationally stratified solar atmosphere compared to the gravity-free case. Namely, the wave period is directly proportional to the width

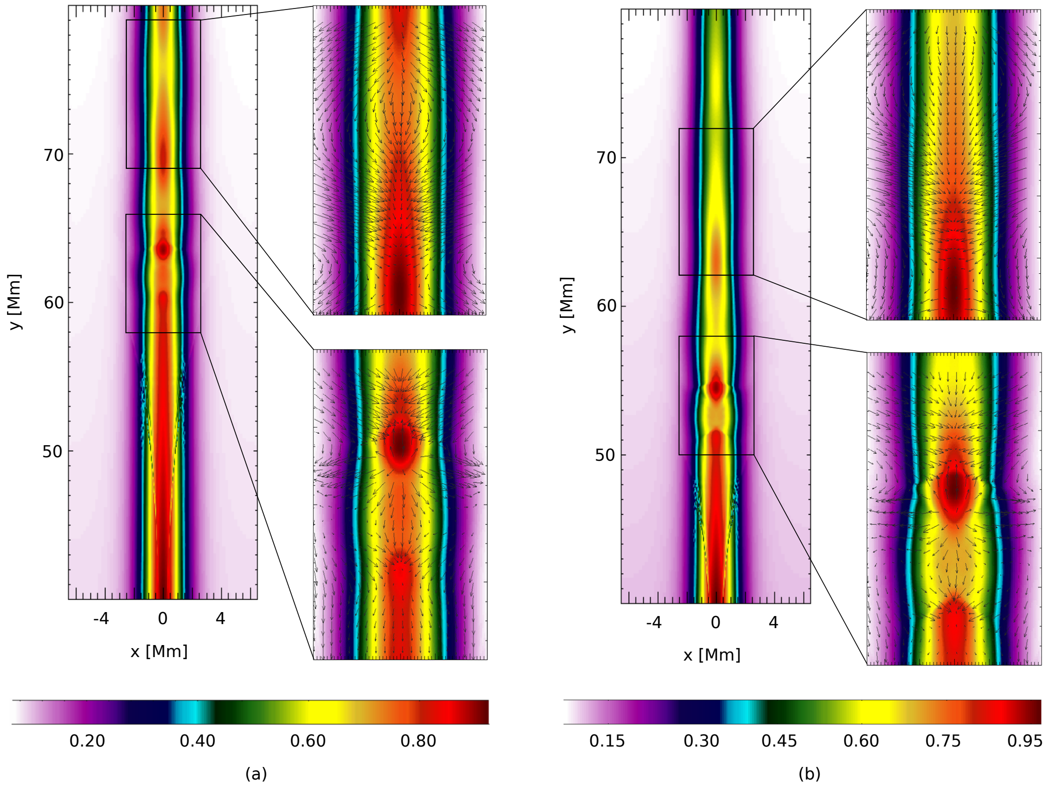

Fig. 8. Spatial profiles of the mass density close to the area of the detection points with zoomed areas at t = 100 s for the case of the gravitationally stratified solar corona. The left part **a)** corresponds to the longer scale-height whereas the right part **b)** of the figure shows the area for the shorter scale-height. The black arrows represent the plasma velocity vectors. The mass density is expressed by colors which correspond to the ratio of the local mass density to that in the perturbation point, L_P, in the initial time.

of the waveguide (current-sheet). The period is furthermore inversely proportional to the Alfvén speed, but this change is less important in this case.

By comparing the numerical results in the gravitationally stratified solar atmosphere we also found differences in the wave periods for the two different scale-heights. For the shorter scale-height case we found an even longer period, but here it is caused mainly by higher mass densities, i.e. by a lower Alfvén speed inside the waveguide. In this case also the minimal value of the group velocity is lower than in the case with longer scale-height. This explains the longer duration of the wavelet tadpoles.

However, these differences are mainly caused by the principal differences in the equilibrium current-sheet in the case with and without gravity. In addition to these differences we found that variations of the wave signal and their wavelet tadpoles are more irregular in the case with gravity than in the gravity-free case. We propose that these differences result from variations with height of the dispersive properties and group velocities of the propagating magnetoacoustic waves in the gravitational case.

The question arises how these results can be used for solar flare diagnostics. Obviously, the model of propagating fast magnetoacoustic sausage waves in the gravitationally stratified atmosphere is more realistic than that for the gravity-free case. The gravitationally stratified case allows us to make a direct comparison with observational data. The most frequently measurable parameters of these waves in solar events are periods and their temporal changes. For some events we can even compute the corresponding wavelet spectra with characteristic tadpoles. Combining these data with the possible determination of the wave types and their wavelengths (from positional measurements) together with independent estimates of the Alfvén speed at these locations (e.g. by the magnetic field extrapolation and UV and optical spectroscopy methods), we can directly compare the results of the present numerical modeling with the observational findings.

Furthermore, an improved description of the propagation of the fast sausage magnetoacoustic waves in waveguides (current-sheets or density enhancement regions) in the gravitationally stratified solar atmosphere can contribute to solving of the long-standing discussion about the origin of the so-called fiber (intermediate) bursts, (Young et al. 1961; Slottje 1981). Namely, there are several models of these bursts based on the whistler, Alfvén, and sausage magnetoacoustic waves (e.g. Bernold & Treumann 1983; Aurass et al. 1987; Mann et al. 1987; Kuznetsov 2006). However, there is still no clear evidence which types of waves are really present in radio sources of these bursts.

Acknowledgements. The authors P.J. and M.K. acknowledge support from the research project RVO:67985815 of the Astronomical Institute AS and Grants P209/10/1680 and P209/12/0103 of the Grant Agency of the Czech Republic. The author P. J. expresses his cordial thanks to Dr. J. Blažek for a discussion. This work has been supported by a Marie Curie International Research Staff Exchange Scheme Fellowship within the 7th European Community Framework Program (P. J. and K. M.). The FLASH code used in this work was in part developed by the DOE-supported ASC/Alliances Center for Astrophysical Thermonuclear Flashes at the University of Chicago. The wavelet analysis was performed using the software written by C. Torrence and G. Compo available at URL `http://paos.colorado.edu/research/wavelets`.

References

Andries, J., Goossens, M., Hollweg, J. V., Arregui, I., & Van Doorsselaere, T. 2005, A&A, 430, 1109
Aschwanden, M. J., De Pontieu, B., Schrijver, C. J., & Alexander, D. 1999, ApJ, 520, 880
Aurass, H., Chernov, G. P., Karlický, M., Kurths, J., & Mann, G. 1987, Sol. Phys., 112, 347
Bernold, T. E. X., & Treumann, R. 1983, A&A, 264, 677
Chung, T. J. 2002, Computational Fluid Dynamics (New York, USA: Cambridge University Press)
De Moortel, I., Ireland, J., & Walsh, R. W. 2000, A&A, 355, L23
De Moortel, I., Ireland, J., Walsh, R. W., & Hood, A. W. 2002, Sol. Phys., 209, 61
Farge, M. 1992, Annu. Rev. Fluid Mech., 24, 395
Fryxell, B., Olson, K., Ricker, P., et al. 2000, ApJS, 131, 273
Galsgaard, K., & Roussev, I. 2002, A&A, 383, 685
Jelínek, P., & Karlický, M. 2009, Eur. Phys. J. D, 54, 305
Jelínek, P., & Karlický, M. 2010, IEEE Trans. Plasma Sci., 38, 2243
Jelínek, P., & Karlický, M. 2012, A&A, 537, A46
Karlický, M., Jelínek, P., & Mészárosová H. 2011, A&A, 529, A96
Katsiyannis, A. C., Williams, D. R., McAteer, R. T. J., et al. 2003, A&A, 406, 709
Kuznetsov, A. A. 2006, Sol. Phys., 237, 153
Lee, D., & Deane, A. E. 2009, J. Comput. Phys., 228, 952
Macnamara, C. K., & Roberts, B. 2010, A&A, 515, A41
Macnamara, C. K., & Roberts, B. 2011, A&A, 526, A75
Mann, G., Karlický, M., & Moschmann, U. 1987, Sol. Phys., 110, 381
Mészárosová, H., Sawant, H. S., Cecatto, J. R., et al. 2009a, Adv. Space Res., 43, 1479
Mészárosová, H., Karlický, M., Rybák, J., & Jiřička, K. 2009b, ApJ, 697, L108.
Murawski, K. 2002, Analytical and Numerical Methods for Wave Propagation in Fluid Media (Singapore: World Scientific)
Murawski, K., & Roberts, B. 1994, Sol. Phys., 151, 305
Nakariakov, V. M. 2003, in Dynamic Sun, ed. B. Dwiwedi (CUP)
Nakariakov, V. M., & Verwichte, E. 2005, Liv. Rev. Sol. Phys., 2, 3
Nakariakov, V. M., Ofman, L., Deluca, E. E., Roberts, B., & Davilla, J. M. 1999, Science, 285, 862
Nakariakov, V. M., Arber, T. D., Ault, C. E., et al. 2004, Mon. Not. R. Astron. Soc., 349, 705
Nakariakov, V. M., Pascoe, D. J., & Arber, T. D. 2005, Space Sci. Rev., 121, 115
Ofman, L., & Wang, T. 2002, ApJ, 580, L85
Ofman, L., Nakariakov, V. M., & DeForest, C. E. 1999, ApJ, 541, 441
Pascoe, D. J., Nakariakov, V. M., & Arber, T. D. 2007, A&A, 461, 1149
Pascoe, D. J., Nakariakov, V. M., Arber, T. D., & Murawski, K. 2009, A&A, 494, 1119
Pascoe, D. J., Wright, A. N., & De Moortel, I. 2010, ApJ, 711, 990
Priest, E. R. 1982, Solar Magnetohydrodynamics (London, England: D. Reidel Publishing Company)
Roberts, B., Edwin, P. M., & Benz, A. O. 1983, Nature, 305, 688
Roberts, B., Edwin, P. M., & Benz, A. O. 1984, ApJ, 279, 857
Roberts, B. 2000, Sol. Phys., 193, 139
Schrijver, C. J., Aschwanden, M. J., & Title, A. M. 2002, Sol. Phys., 206, 69
Selwa, M., Murawski, K., & Solanki, S. K. 2005, A&A, 436, 701
Slottje, C. 1981, Atlas of Fine Structures of Dynamic Spectra of Solar Type-IV-dm and Some Type-II Radio Bursts (Dwingeloo, The Netherlands)
Smith, J. M., Roberts, B., & Oliver, R. 1997, A&A, 327, 377
Thompson, B. J., Plunkett, S. P., Gurman, J. B., et al. 1998, Geophys. Res. Lett., 25, 2465
Torrence, Ch., & Compo, G. P. 1998, Bull. Am. Meteor. Soc., 79, 61
Wang, T. J., & Solanki, S. K. 2004, A&A, 421, L33
Young, C. W., Spencer, C. L., Moreton, G. E., & Roberts, J. A. 1961, ApJ, 133, 243
Zaqarashvili, T. V., Oliver, R., & Ballester, J. L. 2005, A&A, 456, L13

A&A 550, A1 (2013)
DOI: 10.1051/0004-6361/201220296

Astronomy
&
Astrophysics

Radio fiber bursts and fast magnetoacoustic wave trains

M. Karlický[1], H. Mészárosová[1], and P. Jelínek[2]

[1] Astronomical Institute of the Academy of Sciences of the Czech Republic, 25165 Ondřejov, Czech Republic
e-mail: `karlicky@asu.cas.cz`
[2] University of South Bohemia, Faculty of Science, Institute of Physics and Biophysics, Branišovská 10, 370 05 České Budějovice, Czech Republic

Received 28 August 2012 / Accepted 28 November 2012

ABSTRACT

Aims. We present a model for dm-fiber bursts that is based on assuming fast sausage magnetoacoustic wave trains that propagate along a dense vertical filament or current sheet.

Methods. Eight groups of dm-fiber bursts that were observed during solar flares were selected and analyzed by the wavelet analysis method. To model these fiber bursts we built a semi-empirical model. We also did magnetohydrodynamic simulations of a propagation of the magnetoacoustic wave train in a vertical and gravitationally stratified current sheet.

Results. In the wavelet spectra of the fiber bursts computed at different radio frequencies we found the wavelet tadpoles, whose head maxima have the same frequency drift as the drift of fiber bursts. It indicates that the drift of these fiber bursts can be explained by the propagating fast sausage magnetoacoustic wave train. Using new semi-empirical and magnetohydrodynamic models with a simple radio emission model we generated the artificial radio spectra of the fiber bursts, which are similar to the observed ones.

Key words. Sun: flares – Sun: corona – Sun: radio radiation – Sun: oscillations

1. Introduction

Fiber bursts are considered to be a fine structure of the broadband type IV radio bursts. In the dynamic spectrum, they occur in groups of many single fibers, which are narrowband and have almost the same frequency drift. Because this frequency drift is between those of types II and III bursts, the fiber bursts are also called the intermediate-drift bursts (Bernold & Treumann 1983; Aurass et al. 1987; Benz & Mann 1998; Jiřička et al. 2001).

There are two types of models of these bursts: a) one based on the whistler waves (Kuijpers 1975; Chernov 1976; Mann et al. 1987) and b) one based on the Alfvén waves or solitons (Treumann et al. 1990). Both these types of models can be used for estimating the coronal magnetic fields (Benz & Mann 1998; Rausche et al. 2007), which is otherwise very difficult to determine. For this reason the theory and interpretation of fiber bursts are very important. However, these two types of models give different values for the magnetic field strength, and there is still a debate about which models are correct.

Besides these models, Kuznetsov (2006) proposes a model in which the fiber bursts are generated by a modulation of the radio emission by magnetohydrodynamic waves. He also proposes that these waves could be magnetoacoustic waves of a sausage mode type that propagates along the dense coronal loop.

It is known that the structures with higher plasma density (like dense loops or current sheets) act as waveguides, where the fast magnetoacoustic waves are trapped (Roberts et al. 1984). If these waves are impulsively triggered at some location in such a dense structure, then at some distance from the initiation site along this structure, these propagating waves form the wave trains owing to their dispersion properties. The trains exhibit three phases: (1) periodic phase (long-period spectral components arrive as the first ones at the observation point); (2) quasi-periodic phase (both long- and short-period spectral components arrive and interact); and finally (3) decay phase (Roberts et al. 1983, and 1984). As shown by Nakariakov et al. (2004), wavelet spectra of these trains correspond to the wavelet tadpoles (tail plus head). Detailed numerical simulations of these magnetoacoustic (fast sausage) wave trains and corresponding tadpoles in the density slab, as well as in the current sheet, were performed by Jelínek & Karlický (2012).

Mészárosová et al. (2009a,b) analyzed several radio events. In the first paper we found the wavelet tadpoles in the gyro-synchrotron radio burst, where all the tadpoles were detected at the same time in the whole frequency range. In second paper, analyzing the 2005 July 11 radio burst (generated by the plasma emission processes), we found the wavelet tadpoles that slowly drifted with the frequency drift corresponding to the drift of the whole group of the fiber bursts. Furthermore, Mészárosová et al. (2011) repeated the wavelet analysis of the 2005 July 11 radio event, considering a much broader range of time periods, as well as longer time intervals than in the previous paper. Thus, we found the tadpoles with the period of $P \approx 1.9$ s and with the fast frequency drift corresponding to the drift of individual fiber bursts. Based on this, we proposed that the fiber bursts are generated by a modulation of the type IV radio emission by the magnetoacoustic wave trains. Karlický et al. (2011) also found the wavelet tadpoles in sources of the narrowband dm-spikes.

In the present paper, we firstly verify the above-mentioned statement about the similarity of the frequency drifts of individual fiber bursts to head maxima of the corresponding tadpoles by the wavelet analysis of more observed groups of fibers. Then we simulate fibers in a newly developed semi-empirical model. Due to limitations of this model we also made a first attempt to simulate the fiber bursts in a full magnetohydrodynamic (MHD) model with the fast sausage magnetoacoustic wave train propagating in a vertical and gravitationally stratified current sheet.

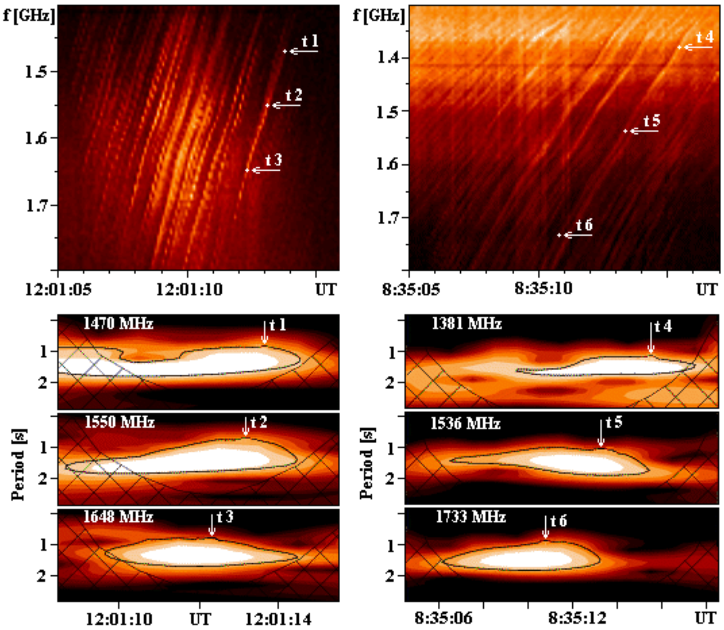

Fig. 1. *Upper panels*: examples of the fiber bursts at 12:01:05–12:01:16 UT (November 23, 1998, *left panel*) and 8:35:05–8:35:17 UT (November 18, 2003, *right panel*). *Bottom part*: corresponding wavelet power spectra showing the tadpoles with the period $P = 1.4$ s (Table 2). In both spectra, at selected frequencies the times of the tadpoles' head maxima were determined ($t1$–$t6$) and also shown in the upper dynamic radio spectra (*upper panels*). The tadpole head maxima drift as the fiber bursts.

Using a simple radio emission model we produce artificial radio spectra of the fiber bursts, which are similar to those observed.

The paper is organized as follows: Sect. 2 describes the set of observed fiber bursts and their wavelet analysis. In Sect. 3, we present our semi-empirical model of fiber bursts and their simulations. Section 4 shows a simulation of the fiber bursts using the MHD model. Finally, in Sect. 5 the results are discussed.

2. Fiber bursts observation and its waletet analysis

We selected eight decimetric radio events with the fiber bursts recorded during the years 1998–2005 by the Ondřejov radiospectrograph (Jiřička et al. 1993). The times of their observations, the GOES X-ray and Hα characteristics of associated flares are presented in Table 1. Examples of the characteristic radio dynamic spectra that show two typical groups of fiber bursts are presented in upper panels of Fig. 1 (1998 November 23, 12:01:05–12:01:16 UT – left panel, and 2003 November 18, 8:35:05–8:35:17 UT – right panel). The parameters of all fiber events are summarized in Table 2. The fiber bursts were observed in the frequency range 1000−2000 MHz, and their frequency drift FD_F ranges from $-73\,\mathrm{MHz\,s^{-1}}$ to $-154\,\mathrm{MHz\,s^{-1}}$.

The selected groups of fibers (Table 1) were analyzed using the wavelet method as described by Mészárosová et al. (2009a,b). We searched for tadpoles in the wavelet power spectra of radio flux time series and selected only dominant tadpoles corresponding to the 99% confidence level. The confidence level implies a test against a certain background level. If a peak in the wavelet power spectrum is significantly above background spectrum, then it can be assumed to be a true feature with a certain percent of the confidence (Farge 1992). In the present paper the background spectrum is modeled by the red noise, and a computation of the confidence level is performed as described by Torrence & Compo (1998). The detected wavelet tadpoles and their parameters are summarized in Table 2. Their period P ranges from 1.1 to 2.3 s, and the drift of their head maxima FD_T is in the range from $-61\,\mathrm{MHz\,s^{-1}}$ to $-152\,\mathrm{MHz\,s^{-1}}$. Comparing the frequency drifts of all fiber bursts in Table 2, we can see that the drift of fiber bursts is very similar to that of the head maxima of the corresponding tadpoles (compare values in Cols. 3 and 5 in Table 2). This can be also seen in Fig. 1: see the times $t1$ = 12:01:13.7, $t2$ = 12:01:13.1, $t3$ = 12:01:12.3, $t4$ = 8:35:15.5, $t5$ = 8:35:13.3, $t6$ = 8:35:10.8 UT at the selected frequencies 1470, 1550, 1648, 1381, 1536, and 1733 MHz, respectively.

Because the wavelet tadpoles are interpreted as signatures of the fast sausage magnetoacoustic wave trains (e.g. Nakariakov et al. 2004), the similarity of both the drifts indicates that the fiber bursts are physically connected with these magnetoacoustic wave trains. Based on these results we propose that the analyzed dm-fiber bursts are generated by the fast sausage magnetoacoustic wave which modulates the radio emission of superthermal electrons trapped in a flare loop or in current sheet.

3. Semi-empirical model

This model is similar to the one presented by Kuznetsov (2006). However, it differs in one aspect: for the fast sausage magnetoacoustic waves considered here, the magnetic and density wave perturbations (b_z and ρ_1) are in phase (Erdelyi, priv. comm., 2012), contrary to Kuznetsov (2006), where these perturbations are in anti-phase.

We assume that the magnetoacoustic wave is triggered by a flare and propagates upwards along a dense vertical flare loop. The plasma density and magnetic field in the loop are taken according to the models by Aschwanden (2002, 2004), where the magnetic field is expressed as $B(h) = B_{00}\,(1 + h/h_D)^{-3}$ (h is the height in the solar atmosphere, $h_D = 75$ Mm, and B_{00} is the footpoint magnetic field taken in the following runs Nos. 1 and 2

Table 1. Basic characteristics of the selected events with fiber bursts.

No.	Flare	Radio Start [UT]	 End [UT]	GOES Start [UT]	 Max [UT]	 End [UT]	 X-ray Imp.	Hα Optic. Imp.	 Position	 NOAA AR #
1	Nov. 23, 1998a	11:51	11:52	10:59	11:21	13:25	M3.1	1N	S23 E58	8392
2	Nov. 23, 1998b	11:58	11:59	10:59	11:21	13:25	M3.1	1N	S23 E58	8392
3	Nov. 23, 1998c	12:00	12:02	10:59	11:21	13:25	M3.1	1N	S23 E58	8392
4	Mar. 05, 2000	10:03	10:04				C6.8	SF	S13 E43	8898
5	Apr. 26, 2001a	11:30	11:31	11:26	13:12	13:19	M7.8	2B	N17 W31	9433
6	Apr. 26, 2001b	11:41	11:44	11:26	13:12	13:19	M7.8	2B	N17 W31	9433
7	Nov. 18, 2003	08:34	08:36	08:12	08:31	08:59	M3.9	1F	N00 E19	10501
8	Jul. 11, 2005	16:31	16:43	16:30	16:38	16:50	C1.1	SF	N09 W52	10786

Table 2. Parameters of the fiber bursts and associated wavelet tadpoles.

No.	Fiber bursts Frequency range [MHz]	 $FD_{\rm F}$ [MHz s^{-1}]	Wavelet tadpoles Period [s]	 $FD_{\rm T}$ [MHz s^{-1}]
1	1456–2000	−154	1.5	−152
2	1370–1800	−130	1.5	−122
3	1370–1800	−128	1.4	−127
4	1000–1330	−144	1.1	−136
5	1050–1600	−92	2.0	−87
6	1000–1600	−76	2.3	−61
7	1100–2000	−73	1.4	−75
8	1100–1800	−78	1.9	−86

as B_{00} = 65 G). The plasma density and magnetic field profiles used in the model are shown in Fig. 2.

Although a real wave evolution is complex (see Roberts et al. 1984; Nakariakov et al. 2004, and also the following MHD model), for a simplification we take the velocity of this wave perturbation as the Alfvén speed $v_{\rm A}$ computed along the loop. The ratios of wave perturbations is taken as $b_z/B_0 = \rho_1/\rho_0 \ll 1$, where B_0 and ρ_0 mean the local magnetic field and density in the Aschwanden's models.

We took a wave in the form of the wave packet as

$$F(h,t) = F_0 C_0 \exp\left[-\left(\frac{h - v_{\rm A}(h)t - h_0}{d_{\rm s}}\right)^2\right] \times \cos\left[\frac{2\pi(h - v_{\rm A}(h)t - h_0)}{d_{\rm L}}\right], \quad (1)$$

$$C_0 = \exp\left[-\left(\frac{t - t_{\rm Amax}}{d_{\rm t}}\right)^2\right], \quad (2)$$

where $F(h,t)$ means the density ρ_1 or magnetic field b_z wave perturbation, F_0 is the wave amplitude, h the height in the loop, t the time, $v_{\rm A}$ the local Alfvén speed, h_0 the wave initiation height, $d_{\rm s}$ the spatial width of the wave packet, and $d_{\rm L}$ the wavelength. By changing $d_{\rm s}$ for a fixed $d_{\rm L}$ we can generate the wave for a single fiber or group of fibers. We also added a factor C_0 that limits radio emission to our chosen frequency interval 1300–1700 MHz (see the following): $t_{\rm Amax}$ is thus the time of the maximum wave amplitude, and d_t the corresponding characteristic time. In our computations the time t changes from 0 to 5 s, $t_{\rm Amax}$ = 2.5 s, $d_{\rm t}$ = 1.5 s, and h_0 = 16.9 Mm. The other parameters are presented in Table 3. This propagating wave packet is then superimposed on the density and magnetic field profiles presented in Fig. 2.

In agreement with Kuznetsov (2006), we assume that the radio emission is produced at the double (harmonic) upper hybrid frequency as a result of a coalescence of two upper hybrid waves, generated by the loss-cone instability of superthermal electrons. Furthermore, we assume that the radio emission is generated with a constant intensity in the whole interval of considered heights. It means that every unit of the volume along the flaring loop (or current sheet) generates the same radio emission. Thus, the intensity of the radio emission at some specific frequency depends only on the gradients of $n_{\rm e}$ and B in the radio source; i.e., the wave perturbation modulates the radio emission as proposed by Treumann et al. (1990). Then, the resulting radio

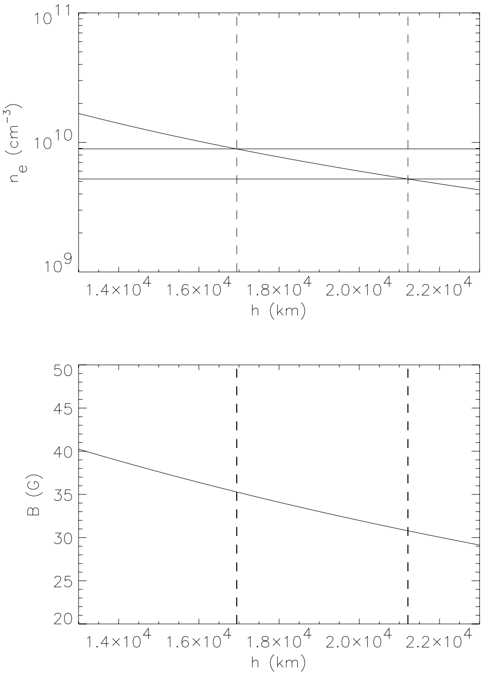

Fig. 2. Plasma density and magnetic field profiles in dependence on the height in the modeled loop. The horizontal full lines in the density plot mean the plasma densities corresponding to the maximum and minimum of frequencies considered in the radio spectra. The vertical dashed lines limit this density interval.

Table 3. Computation parameters.

Run No.	ρ_1/ρ_0	b_z/B_0	$d_{\rm s}$ (km)	$d_{\rm L}$ (km)
1	0.01	0.01	200	800
2	0.01	0.01	800	800

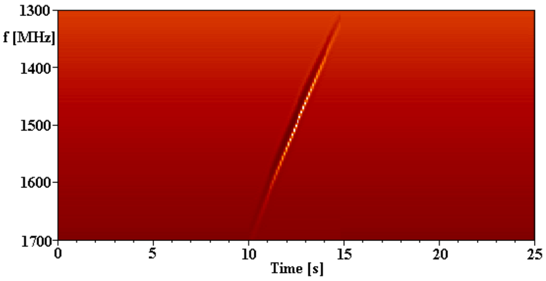

Fig. 3. Computed radio spectrum with the fiber modeled in the semi-empirical model for run No. 1.

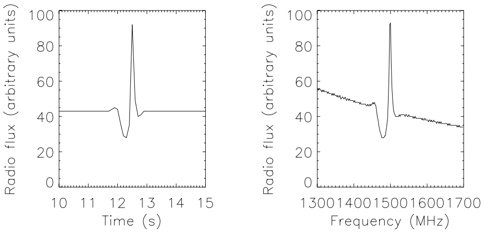

Fig. 4. Example of the time and frequency profiles of the fiber burst modeled in the semi-empirical model for run No. 1. The time profile is plotted at the 1500 MHz frequency and the frequency profile at the time 12.5 s; compare with the spectrum in Fig. 3.

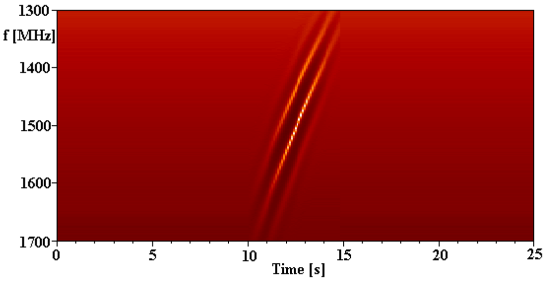

Fig. 5. Computed radio spectrum with the fibers modeled in the semi-empirical model for run No. 2.

flux at the specific frequency f can be expressed as a sum of emissions from plasma volumes having the upper hybrid frequency $f_{\rm up}$ close to $f/2$.

First, we made two runs with the parameters shown in Table 3. The first run was performed for a single perturbation pulse and the second one for the wave train. The computed radio spectrum is in Fig. 3. (Remark: for better presentation of all computed spectra at their beginning we added the 10-second radio spectrum of the unperturbed state.) An example of the time and frequency profiles of the resulting fiber for run No. 1 (cuts in the spectrum shown in Fig. 3) is presented in Fig. 4. Besides the emission peak the emission depression on the low-frequency side of the fiber, as observed, is also clearly visible. The radio spectrum and time and frequency profiles for run No. 2, i.e. for the magnetoacoustic wave train, are shown in Figs. 5 and 6. As can be seen here, the wave train generates a series of fiber bursts.

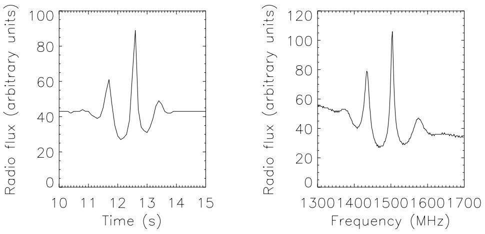

Fig. 6. Example of the time and frequency profiles of the fiber bursts modeled in the semi-empirical model for the run No. 2. The time profile is plotted at 1500 MHz frequency and the frequency profile at time 12.5 s; compare with the spectrum in Fig. 5.

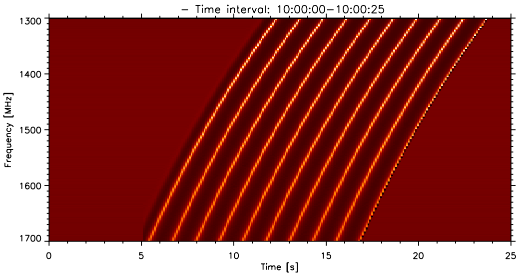

Fig. 7. Computed radio spectrum with the 10 fiber bursts modeled by the semi-empirical model.

Furthermore, as an example, we simulated a group of ten fiber bursts. We consider the wave which is spatially limited to ten wavelengths (wavelength $d_{\rm L}$ = 800 km). It propagates upwards in the solar atmosphere as in runs 1 and 2. However, the magnetic field B_{00} in the used magnetic-field model is B_{00} = 48 G. The constant C_0 (see Eq. (2)) is taken as $C_0 = 1$, which means no global frequency modulation of the radio flux. The computed spectrum with ten fiber bursts is shown in Fig. 7.

Comparing this figure with the radio spectrum in the right-hand panel of Fig. 1, we can see some similarities as well as some deviations. Generally, using this semi-empirical model, we can simulate the frequency drift and repetition period of the fiber bursts by varying the Alfvén speed (through the magnetic field B_{00}) and wavelength of the magnetoacoustic wave ($d_{\rm L}$). On the other hand, deviations are caused by limited information about conditions in the real radio source and also by limitations in the semi-empirical model used. One of the main problem of this semi-empirical model is that dispersive properties of the magnetoacoustic waves are neglected. Therefore, in the following we describe a first attempt to simulate the fiber bursts in a full MHD model, where these properties are implicitly included.

4. MHD model

The main problem of any such model is an initiation of the sufficiently good waveguide for the fast sausage magnetoacoustic waves, which is in equilibrium in the gravitationally stratified solar atmosphere. For a waveguide we can use the dense loop or current sheet, see Jelínek & Karlický (2012). In an analytical form, the model of the vertical current sheet in the gravitationally stratified atmosphere proposed by Galsgaard & Roussev (2002) is an appropriate one for initiating the equilibrium waveguide.

In our case the vertical current sheet (it would be better to call it the current layer) is only a prototype of the waveguide guiding the magnetoacoustic waves. We did not consider any reconnection and fragmentation processes in this current sheet as discussed in Bárta et al. (2011a,b), Karlický et al. (2012), and Cargill et al. (2012), among others. Although the fragmentation is real in these current sheets, we think that such vertical current sheets can exist; see, e.g., the observed current sheet and its width on the order of 1000 km in Fig. 3 in the paper by Lin et al. (2005).

In our model we use the ideal 2D magnetohydrodynamic (MHD) equations:

$$\frac{\mathrm{D}\varrho}{\mathrm{D}t} = -\varrho\nabla\boldsymbol{v}, \tag{3}$$

$$\varrho\frac{\mathrm{D}\boldsymbol{v}}{\mathrm{D}t} = -\nabla p + \boldsymbol{j}\times\boldsymbol{B} + \varrho\boldsymbol{g}, \tag{4}$$

$$\frac{\mathrm{D}\boldsymbol{B}}{\mathrm{D}t} = (\boldsymbol{B}\cdot\nabla)\boldsymbol{v}, \tag{5}$$

$$\frac{\mathrm{D}e}{\mathrm{D}t} = -\gamma e\nabla\cdot\boldsymbol{v}, \tag{6}$$

$$\nabla\cdot\boldsymbol{B} = 0, \tag{7}$$

where $\mathrm{D}/\mathrm{D}t \equiv \partial/\partial t + \boldsymbol{v}\cdot\nabla$ is the total time derivative, ϱ is a mass density, $\boldsymbol{v}$ flow velocity, $\boldsymbol{B}$ the magnetic field, and $\boldsymbol{g} = [0, -g_{\odot}, 0]$ is the gravitational acceleration with $g_{\odot} = 274\ \mathrm{m\,s^{-2}}$. The current density $\boldsymbol{j}$ in Eq. (4) is expressed as

$$\boldsymbol{j} = \frac{1}{\mu_0}\nabla\times\boldsymbol{B}, \tag{8}$$

where $\mu_0 = 1.26\times10^{-6}\ \mathrm{H\,m^{-1}}$ is the magnetic permeability of free space. The specific internal energy e in Eq. (6) is given by

$$e = \frac{p}{(\gamma-1)\varrho}, \tag{9}$$

with the adiabatic coefficient $\gamma = 5/3$.

Equations (3)–(6) are solved numerically by the FLASH code (Fryxell et al. 2000; Lee & Deane 2009). This code implements second- and third-order unsplit Godunov solvers and adaptive mesh refinement (AMR) (see e.g. Chung 2002; Murawski 2002). Spatial resolution of the numerical grid is determined by the AMR method, and we use the AMR grid with a minimum (maximum) level of refinement blocks set to 3 (6). The total number of computational cells covering a whole simulation plane is 267 456. A spatial cell size has to be much smaller than the width of the current sheet in the x-direction and the minimal wavelength of the magnetoacoustic waves in the h-direction. In our model the minimal cell sizes are $\Delta x = 0.0175$ Mm and $\Delta h = 0.005$ Mm (compared with the half width of the current sheet $w_{\mathrm{CS}} = 0.35$ Mm and the minimal wavelength of about 1.0 Mm).

At the start of our numerical calculations we set a refinement procedure in the region covering the current sheet. During the calculations, the FLASH code automatically controlled in each time step the gradient of mass density, which value is then used for refining the grids. For our numerical simulations we used the two-dimensional (2-D) Eulerian box $(-2.25, 2.25)$ Mm $\times$ $(13.0, 23.0)$ Mm in the x- and h- (height) directions, respectively. As a consequence of an extension of the real plasma medium we apply free-boundary conditions at the boundaries of the simulation region, so that the waves can freely leave the simulation box without any significant reflection.

For the description of magnetic field in the vertical current sheet in gravitationally stratified solar atmosphere in the $x-h$ plane we use following expressions:

$$B_x(x,h) = B_{\mathrm{o}}\frac{w_{\mathrm{cs}}}{\lambda}\ln\left[\cosh\left(\frac{x}{w_{\mathrm{cs}}}\right)\right]\exp\left(-\frac{h}{\lambda}\right), \tag{10}$$

$$B_h(x,h) = B_{\mathrm{o}}\tanh\left(\frac{x}{w_{\mathrm{cs}}}\right)\exp\left(-\frac{h}{\lambda}\right), \tag{11}$$

where B_{o} is a magnetic field at $x\to\infty$, w_{CS} is the half width of the current sheet, and λ denotes the magnetic scale-height. For an equilibrium ($\boldsymbol{v} = \boldsymbol{0}$), the Lorentz and gravity forces have to be balanced by the pressure gradient in the entire physical domain

$$-\nabla p + \boldsymbol{j}\times\boldsymbol{B} + \varrho\boldsymbol{g} = \boldsymbol{0}. \tag{12}$$

From this condition we can derive the formulae for distribution of the mass density and gas pressure. For the details see Galsgaard & Roussev (2002) and Jelínek et al. (2012).

In the initial state, we generate the vertical current sheet with the density profile along its axis according to the Aschwanden model (2002). The half width of the current sheet at the height $h = 16.9$ Mm is taken as $w_{\mathrm{CS}} = 0.35$ Mm. In the paper by Jelínek & Karlický (2012), we found that the neutral current sheet serves as the same waveguide as the dense slab if the Alfvén speed at the half width of the current sheet is the same as in the slab. Therefore, in the present current sheet we took this Alfvén speed as 690 $\mathrm{km\,s^{-1}}$. The change of this speed in the studied interval of heights in the current sheet is small.

At the start of the numerical simulation, the initial equilibrium state is perturbed by the Gaussian pulse in the x-component of velocity and has the following form (e.g. Nakariakov et al. 2004, 2005):

$$v_x = -A_0\frac{x}{\lambda_h}\exp\left[-\frac{(x-h_{\mathrm{P}})^2}{\lambda_x^2}\right]\exp\left[-\frac{h^2}{\lambda_h^2}\right], \tag{13}$$

where A_0 is the initial amplitude of the pulse, and $\lambda_x = \lambda_h = 0.35$ Mm are the widths of the velocity pulse in the longitudinal and transverse directions. This pulse tends to trigger fast sausage magnetoacoustic waves. The initial perturbation is located at the height $h_{\mathrm{P}} = 15$ Mm.

Using this MHD model, we computed an evolution of the density profiles along the axis of the vertical current sheet (see examples in Fig. 8). These density profiles were then used in computations of the artificial radio spectrum, as well as the time and frequency profiles shown in Figs. 9 and 10. We used the same simple radio emission model as in the case of the semi-empirical model. As seen in Fig. 9 the frequency drift of these fiber bursts partly changes. It is caused by the wave dispersive effects (included in this MHD model), which change the density wave profile during the wave propagation. Compare this with the semi-empirical model, where the perturbation profile is rigid. The maximum of fiber bursts are produced at the locations with minimal density gradients and these gradients evolve in time. Similarly, the emission depressions, corresponding to the maximal density gradients, evolve in time.

The detailed analysis of these results shows that the model used for the vertical current-sheet is not the best waveguide for the studied magnetoacoustic waves. The change in the magnetic field gradient across the current sheet is not sharp enough. Therefore, some wave energy escapes from this waveguide. This wave energy leakage limits the wave train length and thus also the number and duration of computed fibers. We hope that in a future model we will generate a better waveguide, in which

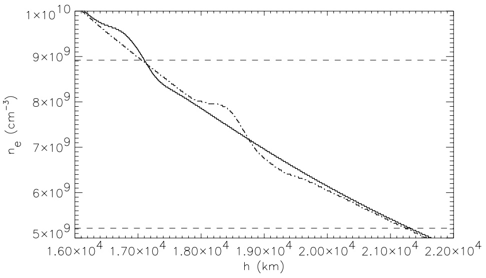

Fig. 8. The density profiles in the MHD model at 11 s (full line) and 14 s (dash-dotted line). The times correspond to times in the spectrum in Fig. 9.

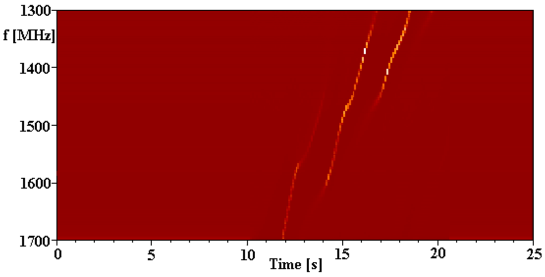

Fig. 9. The computed radio spectrum with the fibers modeled in the MHD model.

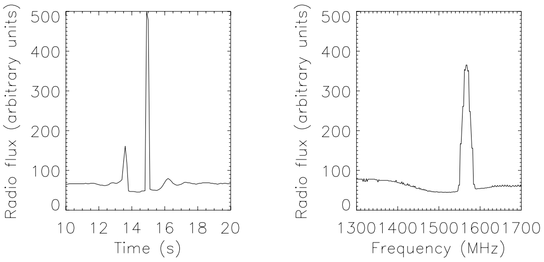

Fig. 10. An example of the time and frequency profiles of the fiber bursts modeled in the MHD model. The time profile is plotted at the 1500 MHz frequency and the frequency profile at the time 14.5 s; compare with the spectrum in Fig. 9.

a longer wave train and thus more fiber bursts will be generated by a single perturbation. On the other hand, more fiber bursts can be generated by a time repetition of the initial perturbation because this is also possible in real conditions. Furthermore, some real radio spectra might show a superposition of the fiber bursts generated in several nearby waveguides.

5. Discussion and conclusions

After analyzing eight groups of observed fiber bursts by the wavelet technique, we found a connection between the dm-fiber bursts and fast sausage magnetoacoustic waves. Based on this connection, we developed the model of the dm-fiber bursts with the fast sausage magnetoacoustic wave propagating in the waveguide of the enhanced plasma density: (a) in the dense loop according to the Aschwanden's density and magnetic field models (semi-empirical model) and (b) in the vertical and gravitationally stratified current-sheet (MHD) model. In both of these models, using the simple emission model according to Treumann et al. (1990), we computed the artificial radio spectra with the fiber bursts that resembles to the observed ones.

We assumed that every unit of the volume along the flaring loop (or current sheet) generates the same radio emission. The intensity of the radio emission at some specific frequency depends only on the density gradient in the radio source. However, the wave perturbation (with weak local magnetic mirrors) can also modulate the growth rate of the upper hybrid waves through change in the loss-cone angle of superthermal electrons (Winglee & Dulk 1986; Yasnov & Karlický 2004) and thus change local emissions. For this purpose, the weighting function $w_e(h(t))$ that expresses these variations can be included in future models.

In all studied decimetric fiber bursts, the frequency drift of the wavelet tadpoles corresponds to the drift of individual fiber bursts. It speaks in favor of the present model with the magnetoacoustic waves in comparison to the model with whistler waves, which is usually considered in the metric frequency range. We propose to do similar wavelet analysis of the metric fiber bursts and to check the validity of their models.

While in the semi-empirical model the form of the wave perturbation is rigid, the MHD model describes perturbations including dispersive properties of the magnetoacoustic waves. It leads to a wavy character of the fiber bursts, which can even be seen in some observed fiber bursts (see e.g. the fibers in the upper-left part of Fig. 1).

The semi-empirical model is very similar to that of Kuznetsov (2006), except that the density and magnetic field perturbations are in phase. The phase relation presented in Kuznetsov (2006) is not correct for the fast sausage magnetoacoustic waves. However, this difference in both the models leads to only small differences in the radio spectrum, because the electron-cyclotron frequency $\omega_{\rm ce}$ is much lower than the plasma frequency $\omega_{\rm pe}$, and thus the upper-hybrid frequency roughly equals the plasma frequency and the magnetic field can be neglected in this case. However, the variation of the magnetic field in the magnetoacoustic wave train can influence the growth rate of the upper hybrid waves owing to the loss-cone instability of superthermal electrons. It can modify the radio emission at some locations along the wave train and thus change the fiber burst profiles. This effect is not considered in the present paper.

Comparing both these models, the semi-empirical is easy to use, however, with a limited description of physical processes under study. The MHD model is much more complicated. One of the main problems is to generate the appropriate initial equilibrium state. The MHD model includes the dispersive effects of the propagating magnetoacoustic waves, so it describes the fiber burst generation in a more realistic way. However, the present MHD vertical and gravitationally stratified waveguide (the current sheet according to the Galsgaard & Roussev model 2002) is not ideal. Owing to its relatively smooth boundaries, the energy of the magnetoacoustic waves escape from this wave guide. The energy of wave decreases, and it is therefore difficult to make long-lasting wave train. This means that we can only simulate a few fiber bursts per one perturbation instead of the long series as in the semi-empirical model. This problem is connected to a solution of the initial equilibrium waveguide. Therefore, to make this MHD model of the fiber bursts more realistic, a better initial waveguide needs to be found. On the other hand, the series of fiber bursts can be generated in the present MHD model using time series of perturbations. Furthermore, some of real radio spectra might show a superposition of the fiber bursts generated in several nearby waveguides.

Considering our simple emission model, we plan to solve the inverse problem to the presented solution: i.e., we plan to determine the density profiles of the propagating magnetoacoustic wave from the fiber burst profiles measured along the radio frequency at some specific times.

Acknowledgements. The authors thank an anonymous referee for comments that improved the paper. This research was supported by grants P209/12/0103 (GA CR), P209/10/1680 (GA CR), the research project RVO:67985815 of the Astronomical Institute AS, and the Marie Curie PIRSES-GA-2011-295272 RadioSun project. The wavelet analysis was performed with software based on tools provided by C. Torrence and G. P. Compo at `http://paos.colorado.edu/research/wavelets`.

References

Aschwanden, M. J. 2002, Space Sci. Rev., 101, 188
Aschwanden, M. J. 2004, Physics of Solar Corona (Germany Berlin: Springer-Verlag), 202
Aurass, H., Chernov, G. P., Karlický, M., Kurths, J., & Mann, G. 1987, Sol. Phys., 112, 347
Bárta, M., Buechner, J., Karlický, M., & Skála, J. 2011a, ApJ, 737, 24
Bárta, M., Buechner, J., Karlický, M., & Kotrč, P. 2011b, ApJ, 730, 47
Benz, A. O., & Mann, G. 1998, A&A, 333, 1034
Bernold, T. E. X., & Treumann, R. 1983, A&A, 264, 677
Cargill, P. J., Vlahos, L., Baumann, G., Drake, J. F., & Nordlund, A. 2012, Space Sci. Rev., 173, 223
Chernov, G. P. 1976, Sov. Astron., 20, 449
Chung, T. J. 2002, Computational Fluid Dynamics (New York, USA: Cambridge University Press)
Farge, M. 1992, Annu. Rev. Fluid Mech., 24, 395
Fryxell, B., Olson, K., Ricker, P., et al. 2000, ApJSS, 131, 273
Galsgaard, K., & Roussev, I. 2002, A&A, 383, 685
Jelínek, P., & Karlický, M. 2012, A&A, 537, A46
Jelínek, P., Karlický, M., & Murawski, K. 2012, A&A, 546, A49
Jiřička, K., Karlický, M., Kepka, O., & Tlamicha, A. 1993, Sol. Phys., 147, 203
Jiřička, K., Karlický, M., Mészárosová, H., & Snížek, V. 2001, A&A, 375, 243
Karlický, M., Jelínek, P., & Mészárosová, H. 2011, A&A, 529, A96
Karlický, M., Bárta, M., & Nickeler, D. 2012, A&A, 541, A86
Kuijpers, J. 1975, Sol. Phys., 44, 143
Kuznetsov, A. A. 2006, Sol. Phys., 237, 153
Lee, D., & Deane, A. E. 2009, J. Comput. Phys., 228, 952
Lin, J., Ko, Y.-K., Sui, L., et al. 2005, ApJ, 622, 1251
Mann, G., Karlický, M., & Moschmann, U. 1987, Sol. Phys., 110, 381
Mészárosová, H., Karlický, M., Rybák, J., & Jiřička, K. 2009a, ApJ, 697, L108
Mészárosová, H., Karlický, M., Rybák, J., & Jiřička, K. 2009b, A&A, 502, L13
Mészárosová, H., Karlický, M., & Rybák, J. 2011, Sol. Phys., 273, 393
Murawski, K. 2002, Analytical and Numerical Methods for Wave Propagation in Fluid Media (Singapore: World Scientific)
Nakariakov, V. M., Arber, T. D., Ault, C. E., et al. 2004, MNRAS, 349, 705
Rausche, G., Aurass, H., Mann, G., Karlický, M., & Vocks, C. 2007, Sol. Phys., 245, 327
Roberts, B., Edwin, P. M., & Benz, A. O. 1983, Nature, 305, 688
Roberts, B., Edwin, P. M., & Benz, A. O. 1984, ApJ, 279, 865
Torrence, C., & Compo, G. P. 1998, Bull. Am. Meteor. Soc., 79, 61
Treumann, R. A., Güdel, M., & Benz, A. O. 1990, A&A, 236, 242
Winglee, R. M., & Dulk, G. A. 1986, ApJ, 307, 808
Yasnov, L. V., & Karlický, M. 2004, Sol. Phys., 219, 289

Monthly Notices of the ROYAL ASTRONOMICAL SOCIETY

MNRAS **434,** 2347–2354 (2013) doi:10.1093/mnras/stt1178
Advance Access publication 2013 July 24

Numerical simulations of magnetoacoustic–gravity waves in the solar coronal curved magnetic field lines structure

P. Jelínek[1]⋆ and K. Murawski[2]

[1]*Institute of Physics and Biophysics, Faculty of Science, University of South Bohemia, Branišovská 10, CZ – 370 05 České Budějovice, Czech Republic*
[2]*Faculty of Mathematics, Physics and Informatics, Maria Curie-Skłodowska University, Radziszewskiego 10, PL-20-031 Lublin, Poland*

Accepted 2013 June 24. Received 2013 June 22; in original form 2013 April 25

ABSTRACT

We present a two-dimensional (2D) magnetohydrodynamic (MHD) model of magnetoacoustic–gravity waves in the gravitationally stratified solar corona that is shaped by a realistic (VAL-C, Vernazza Avrett Loeser model C) temperature profile and curved magnetic field lines. These waves are triggered by an initial Gaussian pulse in the horizontal component of velocity, that is, launched either just below or above the transition region. The time-dependent ideal MHD equations are solved numerically with the use of the FLASH code. The numerical results reveal conversion of a horizontal flow into its vertical counterpart, oscillations of the transition region and vertical jets of cold plasma penetrating the solar corona. The wavelet analysis of the mass-density variations at a fixed detection point leads to the oscillation period of about 180 s, which corresponds to 3-min oscillations observed in solar active regions.

Key words: MHD – methods: numerical – Sun: atmosphere – Sun: oscillations.

1 INTRODUCTION

Waves and oscillations are observed in the solar corona by modern imaging and spectral instruments in the visible light, EUV, X-ray and radio bands. Some of these waves and oscillations can be interpreted in terms of the magnetohydrodynamic (MHD) plasma theory. MHD waves are recognized as an efficient tool in diagnostics of the solar corona and solar flares, see e.g. Roberts (2000), Nakariakov (2003) and Macnamara & Roberts (2010, 2011). The magnetically dominated solar plasma can support the propagation of various types of MHD waves. These waves were investigated and analysed in many theoretical and numerical studies. Among considered cases, we can distinguish propagating slow magnetoacoustic (e.g. De Moortel, Ireland & Walsh 2000), standing slow magnetoacoustic (e.g. Ofman & Wang 2002; Nakariakov et al. 2004; Selwa, Murawski & Solanki 2005; Zaqarashvili, Oliver & Ballester 2005; Jelínek & Karlický 2009, 2010), and standing and propagating fast magnetoacoustic waves of the kink symmetry (e.g. Aschwanden et al. 1999; Nakariakov et al. 1999; Wang & Solanki 2004; Andries et al. 2005; Pascoe, Wright & De Moortel 2010) and of the sausage symmetry (e.g. Pascoe, Nakariakov & Arber 2007; Pascoe et al. 2009; Karlický, Jelínek & Mészárosová 2011; Jelínek & Karlický 2012; Jelínek, Karlický & Murawski 2012; Karlický, Mészárosová & Jelínek 2013). These modes were detected by highly sensitive instruments such as SUMER/*SOHO*, *TRACE* or EIS/*Hinode* and EUVI/*STEREO* (where SUMER is Solar Ultraviolet Measurement of Emitted Radiation, EIS is EUV Imaging Spectrometer, EUVI is Extreme UltraViolet Imager). For a comprehensive review of MHD waves see Nakariakov & Verwichte (2005) and De Moortel & Nakariakov (2012).

Magnetoacoustic–gravity waves were already discussed in the literature. Among others, the impulsive excitation of chromospheric and coronal periodic waves was studied. Some authors demonstrated the formation of a quasi-periodic wave train of a 3-min period in response to an impulsive excitation. For example, Suematsu et al. (1982) devised the 1D hydrodynamic spicule model in which the shock wave was generated. Later on, Shibata (1983), Sterling & Hollweg (1988) and Botha et al. (2011) adopted 2D MHD with a uniform vertical magnetic field to explore the waves generated by a pulse in vertical velocity. We generalize the models described in the above mentioned papers by studying the magnetoacoustic waves generated by a localized symmetric Gaussian pulse in the horizontal component of velocity in the simple magnetic curved structure. Daniłko, Murawski & Erdélyi (2012) and Murawski et al. (2013) studied impulsively generated magnetoacoustic waves in the solar atmosphere permeated by three different configurations of straight magnetic field lines. Depending on the background magnetic field orientation they found the wave periods within the range 150–300 s. Konkol, Murawski & Zaqarashvili (2012) extended this model to the case of curved magnetic field lines, but they considered the slow magnetoacoustic–gravity waves excited by vertical velocity pulse launched from various altitudes of the solar atmosphere. As a result there is a need to generalize these studies for the case of fast magnetoacoustic–gravity waves.

The main aim of this paper is to extend the above mentioned models on a more realistic 2D model of a magnetic cavity for fast magnetoacoustic waves and to compare obtained numerical results

---

⋆ E-mail: pjelinek@prf.jcu.cz

Published by Oxford University Press on behalf of the Royal Astronomical Society

with former findings. In spite of simplicity of the studied structure, it has real application in the solar atmosphere. We can find such or similar structures above active regions and supergranule cells in a quiet region of the solar chromosphere and corona (Priest 1982). These structures, similarly to the structures with straight magnetic field lines, are believed to be ideal waveguides of various types of MHD waves. Moreover, the MHD waves observed in active regions or sunspots are believed to play a significant role in the energy balance of the solar atmosphere and are supposed to contribute to heating of the chromosphere and corona (Khomenko, Collados & Bellot Rubio 2003; Felipe, Khomenko & Collados 2010).

The structure of this paper is as follows. In Section 2, we describe the physical model with governing equations, equilibrium and initial perturbation. In Sections 3 and 4, we develop the numerical model and present the numerical results, respectively. We complete this paper by discussion and conclusions.

2 PHYSICAL MODEL

2.1 Governing equations

In our numerical model, we consider the gravitationally stratified solar atmosphere in which the plasma dynamics is described by the two-dimensional (2D), time-dependent, ideal MHD equations (Priest 1982; Chung 2002):

$$\frac{\mathrm{D}\varrho}{\mathrm{D}t} = -\varrho\nabla\boldsymbol{v}, \tag{1}$$

$$\varrho\frac{\mathrm{D}\boldsymbol{v}}{\mathrm{D}t} = -\nabla p + \boldsymbol{j}\times\boldsymbol{B} + \varrho\boldsymbol{g}, \tag{2}$$

$$\frac{\mathrm{D}\boldsymbol{B}}{\mathrm{D}t} = (\boldsymbol{B}\cdot\nabla)\boldsymbol{v}, \tag{3}$$

$$\frac{\mathrm{D}U}{\mathrm{D}t} = -U(\gamma-1)\nabla\cdot\boldsymbol{v}, \tag{4}$$

$$\nabla\cdot\boldsymbol{B} = 0. \tag{5}$$

Here, $\mathrm{D}/\mathrm{D}t \equiv \partial/\partial t + \boldsymbol{v}\cdot\nabla$ is the material (or convective) time derivative, ϱ is mass density, $\boldsymbol{v}$ is flow velocity, $\boldsymbol{B}$ is the magnetic field, $\boldsymbol{g} = [0, -g_\odot, 0]$ is the gravitational acceleration with $g_\odot = 274\,\mathrm{m\,s^{-2}}$ and the adiabatic coefficient $\gamma = 5/3$. The current density, $\boldsymbol{j}$, in equation (2) is expressed as

$$\boldsymbol{j} = \frac{1}{\mu_0}\nabla\times\boldsymbol{B} \tag{6}$$

with $\mu_0 = 1.26\times10^{-6}\,\mathrm{H\,m^{-1}}$ being the magnetic permeability of free space. The specific internal energy, U, in equation (4) is given by

$$U = \frac{p}{(\gamma-1)\varrho}. \tag{7}$$

2.2 Initial equilibrium

For a still ($\boldsymbol{v} = \boldsymbol{0}$) equilibrium, the Lorentz and gravity forces have to be balanced by the pressure gradient in the entire physical domain,

$$-\nabla p + \boldsymbol{j}\times\boldsymbol{B} + \varrho\boldsymbol{g} = \boldsymbol{0}. \tag{8}$$

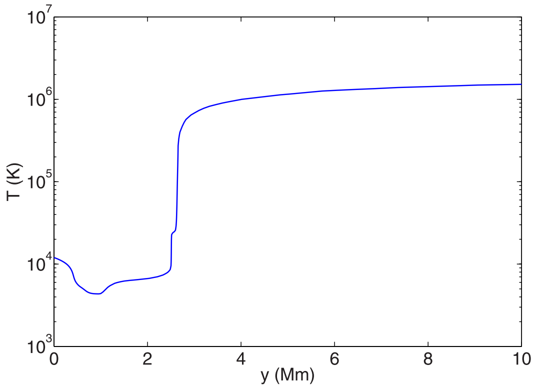

Figure 1. The temperature profile, $T(y)$, in logarithmic scale as a function of height in the solar atmosphere.

Assuming a force-free (Beltrami) magnetic field, $\boldsymbol{j}\times\boldsymbol{B} = \boldsymbol{0}$, the solution of the remaining hydrostatic equation yields

$$p(y) = p_0 \exp\left[-\int_{y_0}^{y}\frac{1}{\Lambda(\tilde{y})}\mathrm{d}\tilde{y}\right], \tag{9}$$

$$\varrho(y) = \frac{p(y)}{g_\odot\Lambda(y)}. \tag{10}$$

Here,

$$\Lambda(y) = \frac{k_B T(y)}{m g_\odot} \tag{11}$$

is the pressure scaleheight which in the case of isothermal atmosphere represents the vertical distance over which the gas pressure falls off by the factor of e, $k_\mathrm{B} = 1.38\times10^{-23}\,\mathrm{J\,K^{-1}}$ is the Boltzmann constant and $m = 0.5m_\mathrm{p}$ is the mean particle mass ($m_\mathrm{p} = 1.672\times10^{-27}$ kg is the proton mass), p_0 in equation (9) denotes the gas pressure at the reference level y_0. In our calculations, we set and hold fixed $y_0 = 10$ Mm.

For the solar atmosphere, the temperature profile $T(y)$ (see Fig. 1), was derived by Vernazza, Avrett & Loeser (1981). At the top of the photosphere, which corresponds to height $y = 0.5$ Mm, the temperature is $T(y) = 5700$ K. At higher altitudes, the temperature falls down to its minimal value $T(y) = 4350$ K at $y \approx 0.95$ Mm. Higher up the temperature rises quite slowly to the height about $y = 2.7$ Mm, where the transition region (TR) is located. Here, the temperature grows up abruptly to the value $T(y) = 1.5$ MK, at the altitude $y = 10$ Mm, which is typical for the solar corona.

The solenoidal condition, $\nabla\cdot\boldsymbol{B} = 0$, is identically satisfied with the implementation of the magnetic flux function, $\boldsymbol{A}$, such as

$$\boldsymbol{B} = \nabla\times\boldsymbol{A}. \tag{12}$$

For the calculation of a 2D magnetic field, we use $\boldsymbol{A} = [0, 0, A]$ with (Konkol et al. 2012)

$$A(x, y) = \frac{sx}{(x-a)^2 + (y-b)^2}. \tag{13}$$

Here, s is a strength of the magnetic moment and coefficients $a = 0.0$ Mm and $b = -2.5$ Mm denote its spatial position. We choose

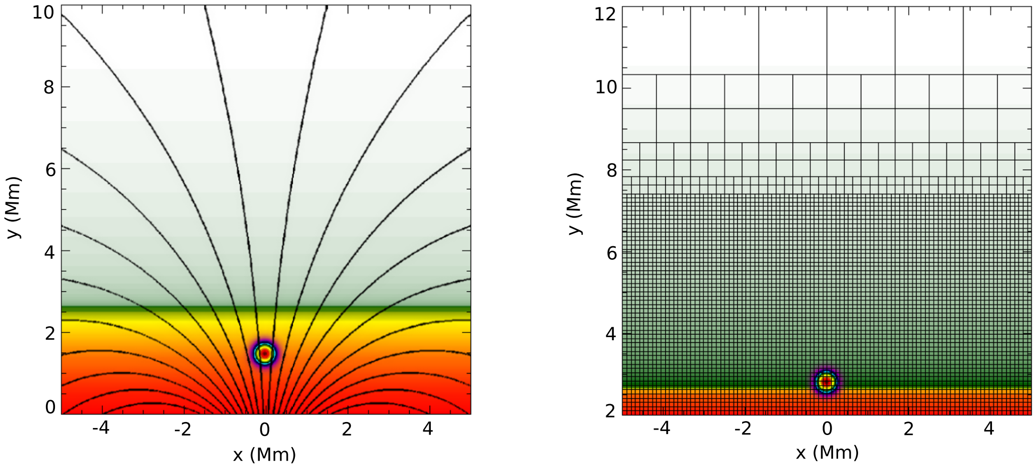

Figure 2. Equilibrium mass density in logarithmic scale, magnetic field lines (solid black lines) and initial Gaussian pulse in the horizontal component of velocity, launched below the TR (thick green line) – left-hand panel. Initial blocks and equilibrium gas pressure in logarithmic scale with the initial pulse launched above the TR – right-hand panel.

s by requiring that at the reference level, $y_0 = 10\,\mathrm{Mm}$, the ratio between Alfvén, c_A, and sound, c_s, speeds is

$$\frac{c_\mathrm{A}(x, y_0)}{c_\mathrm{s}(y_0)} = \sqrt{\frac{B(x, y_0)}{\gamma \mu_0 p(y_0)}} = 10. \tag{14}$$

The initial magnetic field lines are displayed in Fig. 2, left-hand panel, which clearly exhibits their curved nature. The plasma β is defined as

$$\beta(x, y) = \frac{p}{p_\mathrm{mag}} = \frac{2}{\gamma}\left(\frac{c_\mathrm{s}}{c_\mathrm{A}}\right)^2. \tag{15}$$

At $x = 0\,\mathrm{Mm}$, $y = 10\,\mathrm{Mm}$, the plasma $\beta = 0.012$, which is a typical value for the solar corona, e.g. Aschwanden (2004).

2.3 Perturbation

At the start of the numerical simulation ($t = 0\,\mathrm{s}$), the static plasma equilibrium, described in Section 2.2, is perturbed by the Gaussian pulse in the x-component of velocity, i.e.

$$v_x(x, y, t = 0) = A_\mathrm{v} \exp\left[-\frac{x^2}{\lambda_x^2}\right] \exp\left[-\frac{(y - y_\mathrm{P})^2}{\lambda_y^2}\right], \tag{16}$$

where A_v is the amplitude of the initial pulse, y_P is the position of the perturbation and $\lambda_x = \lambda_y = 0.25\,\mathrm{Mm}$ are the widths of the pulse in the horizontal and vertical directions, respectively.

3 NUMERICAL RESULTS

The 2D time-dependent ideal MHD equations (1)–(4) are solved numerically with the adaptation of the FLASH code (Fryxell et al. 2000; Lee & Deane 2009; Lee 2013). This code was originally developed to model nuclear flashes on the surfaces of neutron stars and white dwarfs, and the interior of white dwarfs; but it has since then been applied to model a wide variety of astrophysical processes. Currently, it is a well-tested, fully modular, parallel, multiphysics, open science simulation code that implements second- and third-order unsplit Godunov solvers and adaptive mesh refinement (AMR), see e.g. Chung (2002) and Murawski (2002). The Godunov solver combines the corner transport upwind method for multidimensional integration and the constrained transport algorithm for preserving the divergence-free constraint on the magnetic field (Lee & Deane 2009). In our case, the AMR strategy is based on controlling the numerical errors in a gradient of mass density that leads to reduction of the numerical diffusion within the entire simulation region.

For the wavelet analysis of wave signal, we used the Morlet wavelet, which consists of a plane wave modulated by a Gaussian, i.e.

$$\Psi(t) = \pi^{-1/4} \exp^{(\mathrm{i}\sigma t)} \exp^{-(t^2/2)}, \tag{17}$$

where the parameter σ allows trade between time and frequency resolutions. Here, we assumed the value of parameter $\sigma = 6$, as recommended by Farge (1992). The waveperiods are estimated from the global wavelet spectrum as the most dominant period in this spectrum. More details about the wavelet method and its implementation can be found in Farge (1992) and Torrence & Compo (1998).

We consider two cases of initial pulse launched: (i) below the TR, at $y = y_{\mathrm{p(i)}} = 1.5\,\mathrm{Mm}$ and (ii) above the TR, at $y = y_{\mathrm{p(ii)}} = 2.9\,\mathrm{Mm}$.

For our numerical simulations, we use a 2D Eulerian computation box of $(-5, 5)\,\mathrm{Mm} \times (0, 10)\,\mathrm{Mm}$ and $(-5, 5)\,\mathrm{Mm} \times (2, 12)\,\mathrm{Mm}$ for the cases (i) and (ii), respectively. The spatial resolution of the numerical grid is determined with the AMR method and we used the AMR grid with the minimum (maximum) level of the refinement blocks set to 2 (6). At the start of the numerical simulation ($t = 0\,\mathrm{s}$) the whole simulation region is covered by: (i) 9117 and (ii) 6885 blocks. As each block consists of 8×8 cells, the total number of 583 488 and 440 640 cells is used for the case (i) and (ii), respectively. This results in the maximum (minimum) spatial resolution of $\Delta x_\mathrm{max} = \Delta y_\mathrm{max} = 0.21\,\mathrm{Mm}$ ($\Delta x_\mathrm{min} = \Delta y_\mathrm{min} = 0.01\,\mathrm{Mm}$) above (below) the altitude of $y = 7\,\mathrm{Mm}$ and in all dynamically refined regions, respectively. The initial block system for the case (ii) is illustrated in Fig. 2 (right). As a consequence of the real plasma medium extension at all numerical boundaries, we fix all plasma quantities to their equilibrium values.

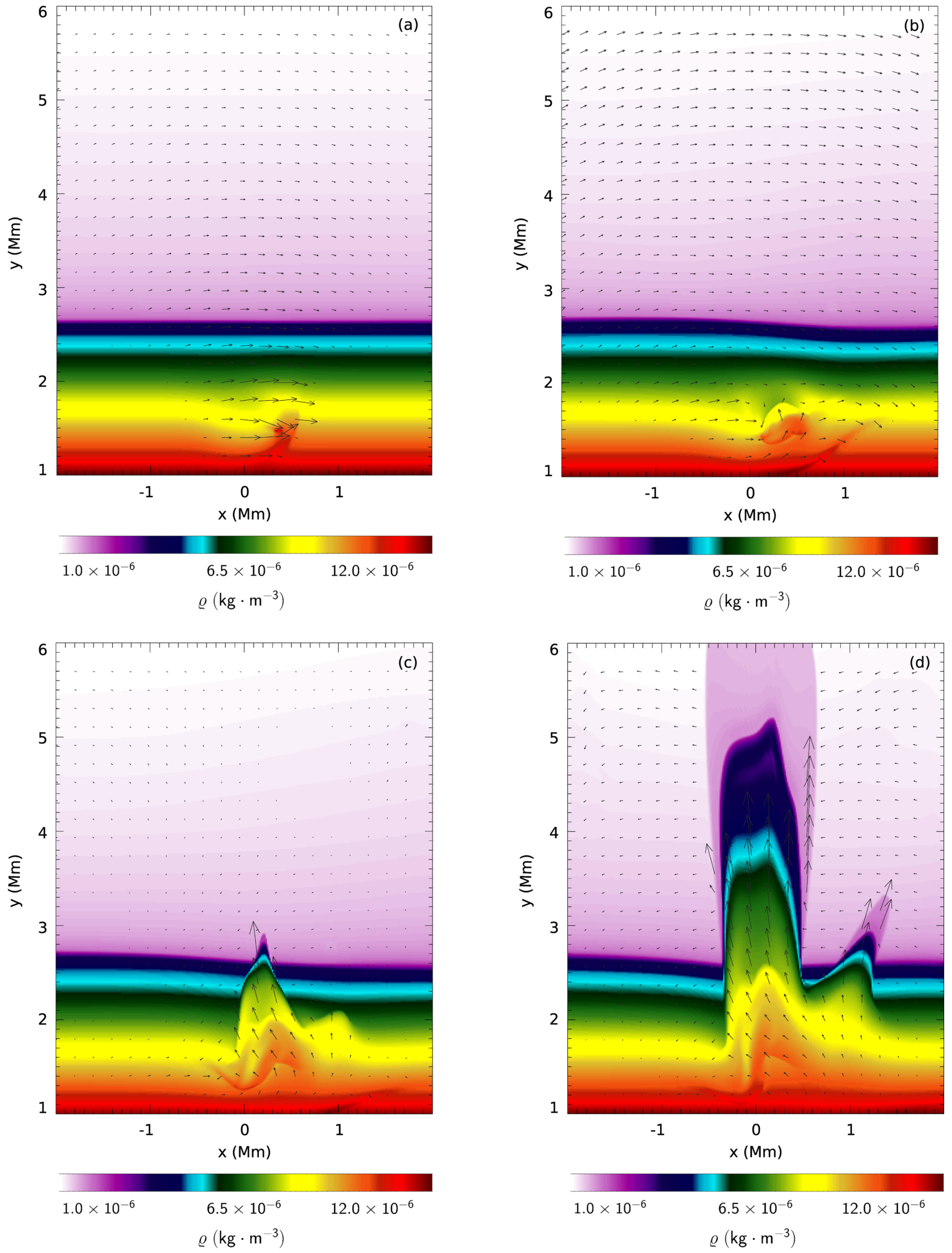

Figure 3. The mass-density profiles, showing the plasma flow conversion, shock wave and velocity vectors (displayed as black arrows) at times: (a) $t = 5.0$ s, (b) $t = 15.0$ s, (c) $t = 30.0$ s and (d) $t = 50.0$ s. The initial velocity pulse was launched below the TR, at $y_{\mathrm{P(i)}} = 1.5$ Mm. The corresponding movie is available in the online version as fig3.avi.

We present the numerical results, obtained for the model described above. Although the numerical simulations were performed for the size of the numerical box mentioned above, we show only the regions where the numerical results are in the range of our interest.

3.1 The pulse below the TR

Here, we present the numerical results for the case of the initial pulse launched below the TR. We choose initial velocity pulse amplitude $A_{\mathrm{v}} = 0.1\, c_{\mathrm{A}}(x = 0,\, y = y_{\mathrm{p(i)}}) = 0.1 \times 10^3\ \mathrm{km\, s^{-1}}$.

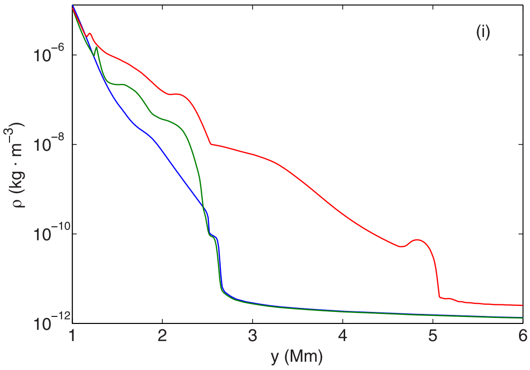

Figure 4. Detailed view to time evolution of vertical slices (for $x = 0$ Mm) of the mass density, resulting from the initial velocity pulse, shown in the logarithmic scale for three simulation times for case (i): $t = 5$, 30 and 50 (blue, green and red line, respectively).

In Figs 3(a)–(d), we display the mass-density profiles for the selected simulation times (5, 15, 30 and 50 s, respectively) and velocity vectors, respectively.

At $t = 5$ s (top left) the initial velocity pulse resulted in plasma compression (rarefaction) at around $x \approx 0.5$ Mm, $y = y_{\mathrm{P}}$ ($x < 0.1$ Mm, $y = y_{\mathrm{p(i)}}$). Later on, at $t = 15$ s, as a result of flow conversion this plasma starts to propagate upwards, generating a shock (top right). This upwardly propagating shock strengthens in time while reaching less-dense plasma altitudes (bottom left). Behind this shock, cold plasma is sucked up into the coronal regions, leading to a system of jets, well seen at $t = 50$ s (bottom right).

In Fig. 4, we present the vertical slices (along the y-axis for $x = 0$ Mm) of the mass density in logarithmic scale for three selected simulation times: $t = 5$, 30 and 50 s. These slices correspond to the results presented in Fig. 3. Shortly after the start of the numerical simulation (blue line), we see that the profile of mass density is not far from the equilibrium state. After the flow conversion, the plasma propagates upwards and perturbs the initial equilibrium (green line). At later time the plasma shock wave is observed at the altitude about 5 Mm in the solar atmosphere (red line).

3.2 The pulse above the TR

In this part of the paper, we show the numerical results for the case (ii) and initial velocity pulse amplitude $A_{\mathrm{v}} = 0.5\, c_{\mathrm{A}}(x = 0, y = y_{\mathrm{p(ii)}}) = 0.5 \times 10^3\ \mathrm{km\,s^{-1}}$.

In Figs 5(a)–(d), we illustrate the mass-density profiles and velocity vectors for selected simulation times (0.5, 2.5, 5.0 and 25.0 s). Shortly after the start of our simulation the initial horizontal velocity pulse triggers the oscillations, transverse to the magnetic field background, in the low-mass-density regions of the solar atmosphere ($t = 0.5$ s, top left). At time $t = 2.5$ s, the plasma above the TR moves upwards to the higher altitudes of the solar atmosphere (positive part of the x-axis), whereas the hotter plasma moves downwards to the TR (negative part of the x-axis), where it experiences reflection back towards higher layers of the solar atmosphere (top right). As a result of that the TR starts to oscillate. At a later time, after the reflection from the TR ($t = 5.0$ s; bottom left) the reflected material moves upwards and pushes up the material located at higher altitudes of the solar atmosphere. At $t = 25$ s (bottom right), we observe practically only the reflected plasma from the TR and as a consequence the bump of plasma sucked up from the TR.

In Fig. 6, we show the vertical slices of mass density (along the y-axis for $x = 0$ Mm) in logarithmic scale for three selected simulation times: $t = 0.5$, 5.0 and 25.0 s. Note that the mass-density profiles do not change so dramatically as in the (i) case. This is because of the fact that above the TR, where the initial velocity pulse is generated, there is not so huge slope in the mass density as it takes place below the TR. By this reason, this pulse is not able to generate any shock wave which would perturb the initial mass-density equilibrium so markedly as in case (i). The blue line corresponds almost to the initial equilibrium (compare with the upper-left panel of Fig. 3). The green and red lines vary slowly with x, representing the plasma being sucked up from the TR to the higher altitudes of the solar atmosphere.

3.3 Oscillation period of the TR

The important phenomenon observed in both above studied cases is the oscillating TR whose waveperiods we are going to estimate. For easier comparison of the excited waveperiods, we placed the detection point, L_{D}, in both cases at the same position in the solar atmosphere, i.e. at $L_{\mathrm{D}}(x_{\mathrm{D}} = 0.5\ \mathrm{Mm}, y_{\mathrm{D}} = 2.7\ \mathrm{Mm})$. Such location of the detection point ensures that we measure pure oscillations of the TR, which does not directly affect magnetoacoustic–gravity waves, triggered by the initial velocity pulse. At the detection point, the incoming signal in the form of variations of the mass density was recorded and subsequently analysed using the wavelet method.

In Figs 7 and 8, we present, for both studied cases (i) and (ii), the time signatures of mass density collected at the detection point, L_{D} (left), and the corresponding global wavelet spectra (right, full blue line), revealing the dominant waveperiod P (right-hand panel). The green dashed line in both figures represents the 99 per cent significance level (Torrence & Compo 1998). By comparing these time signatures, we infer that in case (i) the signal is not attenuated as much as it is in case (ii). From this reason, we tried to estimate the attenuation coefficient. This coefficient can be calculated from the equation of amplitude attenuation:

$$\lambda = \frac{A_{i+1}}{A_i} = \frac{1}{\mathrm{e}^{-(bT_{\mathrm{d}})}}, \tag{18}$$

where A_i and A_{i+1} are two arbitrary successive amplitudes, T_{d} is the attenuated period and b is the attenuation coefficient. To obtain b, we can rewrite equation (18) as follows:

$$b = \frac{1}{T_{\mathrm{d}}} \ln\left(\frac{A_2}{A_1}\right). \tag{19}$$

We found that this coefficient has almost the same value for both studied cases, i.e. $b \approx -0.003$, which means that the oscillations of the TR are similarly attenuated.

For a more accurate estimation of the TR oscillation waveperiod, we run the simulations in case (i) for a longer time, up to $t = 1000$ s, than in case (ii), for which we execute the code up to $t = 500$ s. By using the wavelet method, we find the most dominant periods of the TR oscillation for case (i) as $P_{\mathrm{(i)}} = 199.9$ s and $P_{\mathrm{(ii)}} = 163.1$ s for the second studied case (ii). The average value of both periods gives us the period of about 180.5 s ≈ 3 min, which is very similar to the waveperiods observed above the active regions in sunspots, e.g. by the Solar Dynamics Observatory (SDO)/Atmospheric Imaging Assembly (AIA) and by the Nobeyama Radioheliograph (NoRH; Reznikova et al. 2012).

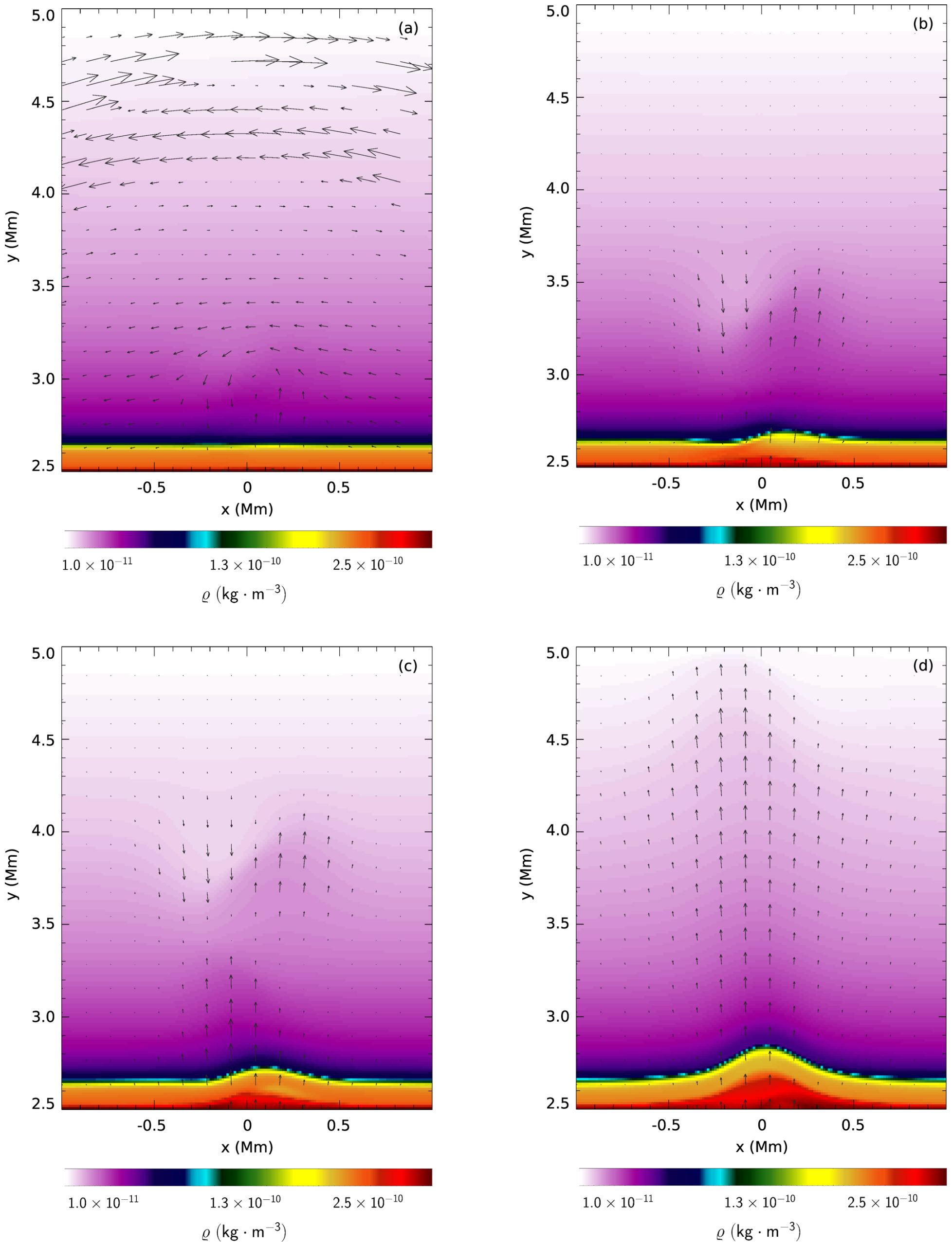

Figure 5. The mass-density profiles showing wave reflection and plasma flow, complemented by velocity vectors (displayed as black arrows) at times: (a) $t =$ 0.5 s, (b) $t = 2.5$ s, (c) $t = 5.0$ s and (d) $t = 25.0$ s. The initial pulse was launched above the TR at $y_{\mathrm{p(ii)}} = 2.9$ Mm. The corresponding movie is available in the online version as fig5.avi.

Comparing Figs 7 and 8, we infer that while in case (i) the mass density converges essentially back to its initial value, it is not so in case (ii), for which some offset is seen. This effect is caused by the fact that the detection point, L_{D}, is placed at the position below the initial pulse. Once the initial velocity pulse is generated, the plasma around is underpressed and as a consequence, from the reason of the huge mass-density difference, the denser plasma from the TR is sucked up to the region of the detection point. Then, we observe

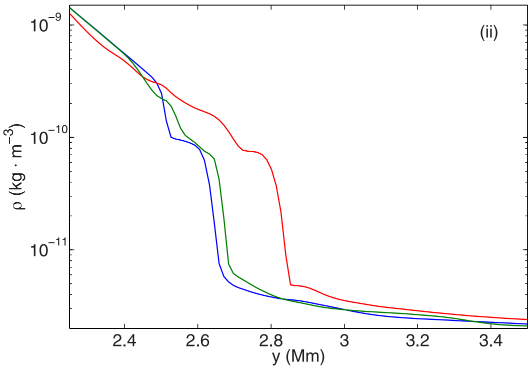

Figure 6. Detailed view to time evolution of vertical slices (for $x = 0$ Mm) of the mass density, resulting from the initial velocity pulse, shown in the logarithmic scale for three simulation times for case (ii): $t = 0.5$, 5.0, and 25.0 s (blue, green and red line, respectively).

just the oscillations of the dense plasma. This effect can be also discernible in case (i), for which slight increase of the mass density up to the time about 100 s from the start of the simulations is seen. Nevertheless, this increase is not so striking as in case (ii) because of relatively small difference in mass densities between the place where the detection, L_D, and perturbation, y_P, points are located.

4 SUMMARY AND CONCLUSIONS

In this paper, we numerically studied propagation of magnetoacoustic–gravity waves in the solar coronal curved magnetic field lines structure. These waves are triggered by the initial Gaussian pulse launched in the horizontal component of velocity either below or above the TR. We also consider a realistic initial (VAL-C) temperature profile in gravitationally stratified solar atmosphere. From our numerical simulations, we reveal the oscillations of the TR for both studied cases – the velocity pulse generated either above or below the TR. We also estimated the oscillation periods which are both very similar to each other and correspond

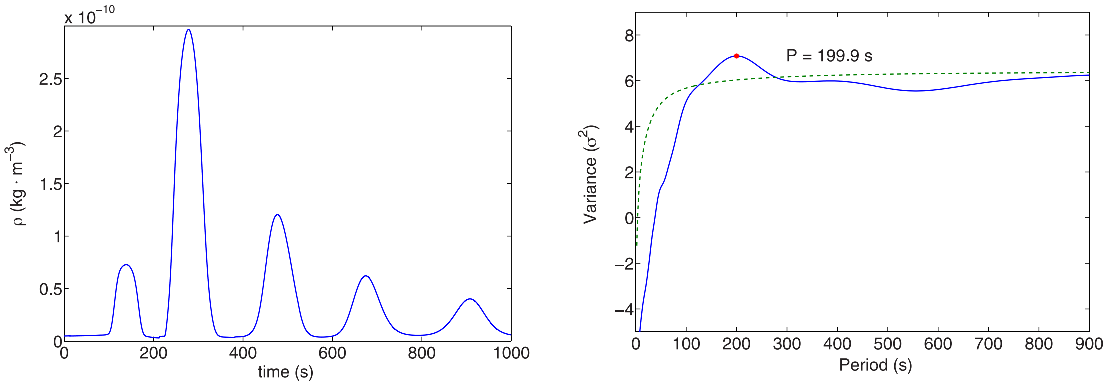

Figure 7. The time signature of mass density collected at the detection point, $L_D(x_D = 0.5, y_D = 2.7)$ Mm, during the simulation (left) and its global wavelet spectrum with calculated period P (right) in the case of the initial pulse generated below the TR. The green dashed line represents 99 per cent significance level.

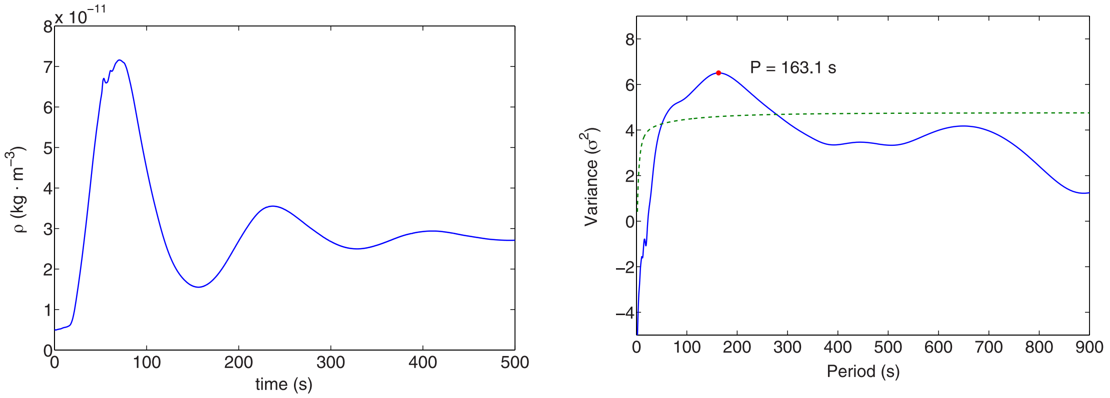

Figure 8. The time signature of mass density collected at the detection point, $L_D(x_D = 0.5, y_D = 2.7$ Mm), during the simulation (left) and its global wavelet spectrum with calculated period P (right) in the case of the initial pulse generated above the TR. The green dashed line represents 99 per cent significance level.

roughly to the 3-min oscillations, observed above the sunspots, e.g. in UV/EUV emission by the SDO/AIA and in the radio emission by the NoRH. We found that the TR oscillations exhibit shorter waveperiod and they are attenuated more strongly in the case of the initial pulse generated above the TR.

The results of our numerical simulations can be summarized as follows. Initial horizontal velocity perturbations launched either below or above the TR are able to trigger vertical flow penetrating higher altitudes of the solar corona. As a consequence of this phenomena, we observe in both cases the oscillations of the TR with the waveperiod close to the 3-min oscillations. The oscillations of TR are attenuated in essentially the same way regardless on the place where the initial velocity pulse was generated.

We should note that our 2D MHD model exhibits shortcomings in the sense that it does not include thermal conduction and radiative transfer along the magnetic field lines. The magnetic field configuration presented in this study is simple, but despite its simplicity, it has real application to active regions of the real solar atmosphere. These shortcomings and simplicity of the presented model require additional studies which we are going to perform in close future.

ACKNOWLEDGEMENTS

PJ acknowledges support of Grants P209/10/1680 and P209/12/0103 of the Grant Agency of the Czech Republic. This work has been done in the frame of a Marie Curie International Research Staff Exchange Scheme Fellowship within the 7th European Community Framework Programme. Authors also thank the Marie Curie FP7-PIRSES-GA-2011-295272 Radiophysics of the Sun project. The authors would also like to express their cordial thanks to Professor V. M. Nakariakov, Dr. M. Karlický and the unknown referee for their comments. The FLASH code used in this work was in part developed by the DOE-supported ASC/Alliances Center for Astrophysical Thermonuclear Flashes at the University of Chicago. The wavelet analysis was performed using the software written by C. Torrence and G. Compo available at URL http://paos.colorado.edu/research/wavelets.

REFERENCES

Andries J., Goossens M., Hollweg J. V., Arregui I., Van Doorsselaere T., 2005, A&A, 430, 1109
Aschwanden M., 2004, Physics of the Solar Corona. Springer, Praxis Publishing, Chichester, UK
Aschwanden M. J., Fletcher L., Schrijver C. J., Alexander D., 1999, ApJ, 520, 880
Botha G. J. J., Arber T. D., Nakariakov V. M., Zhugzhda Y. D., 2011, ApJ, 728, 84
Chung T. J., 2002, Computational Fluid Dynamics. Cambridge Univ. Press, New York, USA
Daniłko D., Murawski K., Erdélyi R., 2012, Acta Phys. Pol., 43, 6
De Moortel I., Nakariakov V. M., 2012, Phil. Trans. R. Soc. A, 370, 3193
De Moortel I., Ireland J., Walsh R. W., 2000, A&A, 355, L23
Farge M., 1992, Annu. Rev. Fluid Mech., 24, 395
Felipe T., Khomenko E., Collados M., 2010, ApJ, 719, 357
Fryxell B. et al., 2000, ApJS, 131, 273
Jelínek P., Karlický M., 2009, Eur. Phys. J. D, 54, 305
Jelínek P., Karlický M., 2010, IEEE Trans. Plasma Sci., 38, 2243
Jelínek P., Karlický M., 2012, A&A, 537, A46
Jelínek P., Karlický M., Murawski K., 2012, A&A, 546, A49
Karlický M., Jelínek P., Mészárosová H., 2011, A&A, 529, A96
Karlický M., Mészárosová H., Jelínek P., 2013, A&A, 550, A1
Khomenko E. V., Collados M., Bellot Rubio L. R., 2003, ApJ, 588, 606
Konkol P., Murawski P., Zaqarashvili T. V., 2012, A&A, 537, A96
Lee D., 2013, J. Comput. Phys., 243, 269
Lee D., Deane A. E., 2009, J. Comput. Phys., 228, 952
Macnamara C. K., Roberts B., 2010, A&A, 515, A41
Macnamara C. K., Roberts B., 2011, A&A, 526, A75
Murawski K., 2002, Analytical and Numerical Methods for Wave Propagation in Fluid Media. World Scientific Press, Singapore
Murawski K., Srivastava A. K., McLaughlin J. A., Oliver R., 2013, Sol. Phys., 283, 383
Nakariakov V. M., 2003, in Dwiwedi B., ed., Dynamic Sun. Cambridge Univ. Press, Cambridge
Nakariakov V. M., Verwichte E., 2005, Living Rev. Sol. Phys., 2, 3
Nakariakov V. M., Ofman L., Deluca E. E., Roberts B., Davilla J. M., 1999, Sci, 285, 862
Nakariakov V. M., Arber T. D., Ault C. E., Katsiyannis A. C., Williams D. R., Keenan F. P., 2004, MNRAS, 349, 705
Ofman L., Wang T., 2002, ApJ, 580, L85
Pascoe D. J., Nakariakov V. M., Arber T. D., 2007, A&A, 461, 1149
Pascoe D. J., Nakariakov V. M., Arber T. D., Murawski K., 2009, A&A, 494, 1119
Pascoe D. J., Wright A. N., De Moortel I., 2010, ApJ, 711, 990
Priest E. R., 1982, Solar Magnetohydrodynamics. Reidel, London, UK
Reznikova V. E., Shibasaki K., Sych R. A., Nakariakov V. M., 2012, ApJ, 746, 119
Roberts B., 2000, Sol. Phys., 193, 139
Selwa M., Murawski K., Solanki S. K., 2005, A&A, 436, 701
Shibata K., 1983, PASJ, 35, 263
Sterling A. C., Hollweg J. V., 1988, ApJ, 327, 950
Suematsu Y., Shibata K., Nishikawa T., Kitai R., 1982, Sol. Phys., 75, 99
Torrence Ch., Compo G. P., 1998, Bull. Am. Meteorol. Soc., 79, 61
Vernazza J. E., Avrett E. H., Loeser R., 1981, ApJ, 45, 635
Wang T. J., Solanki S. K., 2004, A&A, 421, L33
Zaqarashvili T. V., Oliver R., Ballester J. L., 2005, A&A, 456, L13

SUPPORTING INFORMATION

Additional Supporting Information may be found in the online version of this article:

Figure 3. The mass-density profiles, showing the plasma flow conversion, shock wave and velocity vectors (displayed as black arrows) at times: (a) $t = 5.0$ s, (b) $t = 15.0$ s, (c) $t = 30.0$ s and (d) $t = 50.0$ s.
Figure 5. The mass-density profiles showing wave reflection and plasma flow, complemented by velocity vectors (displayed as black arrows) at times: (a) $t = 0.5$ s, (b) $t = 2.5$ s, (c) $t = 5.0$ s and (d) $t = 25.0$ s (http://mnras.oxfordjournals.org/lookup/suppl/doi:10.1093/mnras/stt1178/-/DC1).

This paper has been typeset from a TEX/LATEX file prepared by the author.

The Astrophysical Journal, 788:44 (10pp), 2014 June 10 doi:10.1088/0004-637X/788/1/44

MAGNETOACOUSTIC WAVES PROPAGATING ALONG A DENSE SLAB AND HARRIS CURRENT SHEET AND THEIR WAVELET SPECTRA

Hana Mészárosová[1], Marian Karlický[1], Petr Jelínek[1,2], and Ján Rybák[3]
[1] Astronomical Institute of the Academy of Sciences of the Czech Republic, CZ–25165 Ondřejov, Czech Republic; hana@asu.cas.cz
[2] Faculty of Science, University of South Bohemia, CZ–37005 České Budějovice, Czech Republic
[3] Astronomical Institute of the Slovak Academy of Sciences, SK–05960 Tatranská Lomnica, Slovak Republic

Received 2014 March 12; accepted 2014 April 22; published 2014 May 20

ABSTRACT

Currently, there is a common endeavor to detect magnetoacoustic waves in solar flares. This paper contributes to this topic using an approach of numerical simulations. We studied a spatial and temporal evolution of impulsively generated fast and slow magnetoacoustic waves propagating along the dense slab and Harris current sheet using two-dimensional magnetohydrodynamic numerical models. Wave signals computed in numerical models were used for computations of the temporal and spatial wavelet spectra for their possible comparison with those obtained from observations. It is shown that these wavelet spectra allow us to estimate basic parameters of waveguides and perturbations. It was found that the wavelet spectra of waves in the dense slab and current sheet differ in additional wavelet components that appear in association with the main tadpole structure. These additional components are new details in the wavelet spectrum of the signal. While in the dense slab this additional component is always delayed after the tadpole head, in the current sheet this component always precedes the tadpole head. It could help distinguish a type of the waveguide in observed data. We present a technique based on wavelets that separates wave structures according to their spatial scales. This technique shows not only how to separate the magnetoacoustic waves and waveguide structure in observed data, where the waveguide structure is not known, but also how propagating magnetoacoustic waves would appear in observations with limited spatial resolutions. The possibilities detecting these waves in observed data are mentioned.

Key words: magnetohydrodynamics (MHD) – methods: numerical – Sun: corona – Sun: flares

Online-only material: color figures

1. INTRODUCTION

Oscillations and magnetohydrodynamic (MHD) plasma waves play a very important role in many phenomena observed in the solar and stellar atmosphere (e.g., Aschwanden 2004, Stepanov et al. 2012). These waves and oscillations have been analyzed theoretically as well as numerically. The impulsively generated MHD waves and oscillations can be excited by various processes in the solar corona (e.g., by impulsive flare processes). These flare processes can provide either single or multiple sources of perturbations. It has been theoretically predicted (Roberts et al. 1983, 1984) that impulsively generated propagating fast magnetoacoustic waves can be guided by solar coronal structures with enhanced plasma density (e.g., coronal loops) that is acting as the waveguides. These waves form wave trains propagating along their waveguide. The wave train triggered at the initiation site (perturbation point) can be detected at some distance from this site along the waveguide. Time series measured at the detecting point exhibit periodic, quasiperiodic, and decay phases (Roberts et al. 1984). The quasiperiodic phase is generally much stronger in amplitude and shorter in "periodicity" than the earlier periodic phase. This is caused by a dispersion of these waves.

Nakariakov et al. (2004) studied numerically the evolution of the fast magnetoacoustic waves in the dense slab and their wavelet spectra. They found that the wavelet spectra of these waves have the form of "tadpoles" with a narrow tail that precedes a broadband head. The periodic and quasiperiodic phases, pointed out by Roberts et al. (1984), correspond to the tadpole tail and head, respectively, and the start of decay phase corresponds to the tadpole head maximum.

In observations, the wavelet tadpoles were recognized for the first time in the 1999 solar eclipse data (Katsiyannis et al. 2003). Mészárosová et al. (2009a) found the wavelet tadpoles in the gyrosynchrotron radio burst, where all the tadpoles were detected at the same time over the whole frequency range. In subsequent papers Mészárosová et al. (2009b, 2011b) analyzed dm-radio fiber bursts generated by the plasma emission processes. In this case, the wavelet tadpoles slowly drifted with the frequency drift corresponding to the drift of the whole group of fiber bursts. They also found tadpoles with shorter periods and with faster frequency drift that correspond to the drift of individual fiber bursts. More such cases were shown in the paper by Karlický et al. (2013), where a model of the fiber bursts, based on a modulation of the type IV radio burst emission by the fast magnetoacoustic wave trains, was also presented. The wavelet tadpoles were also found in the 15 sources of narrowband dm-radio spikes (Karlický et al. 2011). Using a two-dimensional (2D) MHD model with the Harris current sheet, they concluded that these wavelet tadpoles indicate the fast magnetoacoustic waves propagating in the reconnection plasma outflows. These studies were supported by numerical simulations made by Jelínek & Karlický (2010, 2012), where they compared the evolution of the fast magnetoacoustic waves in a dense slab and Harris current sheet depending on the plasma beta parameter and width of the waveguide. They found that an increase in the distance between the initial perturbation and the detection point increases the length of the tadpole tail. Besides individual solar coronal loops and the current sheet, there are other possible structures that may act as a waveguide. Mészárosová et al. (2013) found wavelet tadpoles indicating the presence of fast magnetoacoustic waves which propagate in the fan structure of the coronal magnetic null point. Yuan et al. (2013) studied large-scale fast waves in the EUV emission intensity *Solar Dynamics Observatory* (*SDO*)/Atmospheric Imaging Assembly (AIA), where they recognized distinct wave trains with varying periods and wavelengths. Pascoe et al. (2013) used a 2D numerical simulation model of the magnetoacoustic waveguide to consider the effects of an expanding magnetic field. They found that funnel geometry leads to the generation of additional wave trains (formed by the leakage of transverse perturbations) that propagate outside the density structure.

Propagating slow magnetoacoustic waves were observed in coronal loops, e.g., by Hinode/Extreme-ultraviolet Imaging Spectrometer (EIS; Wang et al. 2009a, 2009b) and *Solar and Heliospheric Observatory* (*SOHO*)/EIT and Transition Region and Coronal Explorer (TRACE; Robbrecht et al. 2001), and in two-ribbon flares (Nakariakov & Zimovets 2011) and were also modeled (e.g., Nakariakov et al. 2000).

In our previous studies, researching the wavelet spectra of the solar radio emission, we recognized, besides "normal" tadpoles corresponding to the fast magnetoacoustic waves, some strange tadpoles with additional features, which occurred several times. These additional features are superimposed on the wavelet spectrum of the normal tadpoles. Although some of these features could be formed by chance or by some kind of signal superpositions or, in some cases, by a high level of artificial noise, their relatively frequent occurrence (observed by independent instruments) leads to a question about their real meaning. Therefore, in the present study we carried out an extended parametric investigation of wave processes in waveguides in order to understand better the link between impulsively generated fast and slow magnetoacoustic waves and the parameters and properties of waveguides and forms of their wavelet spectra. We believe that this study will help in the recognition of magnetoacoustic waves in the solar flare atmosphere and in the determination of waveguide (loop or current sheet) parameters.

This paper is organized as follows. In Section 2, the 2DMHD models and wavelet methods that we used are described. Section 3 presents typical examples of the magnetoacoustic waves in the dense slab and Harris current sheet. Then, in Section 4 we show examples of computed time-varying signals, selected from the parametric investigation of these processes, and their wavelet spectra. Section 5 presents a technique that separates wave structures according to their spatial scales and its application. Finally, the results are summarized in Section 6.

2. TWO-DIMENSIONAL MHD NUMERICAL MODEL AND WAVELET METHODS

2.1. *Governing Equations and Numerical Solutions*

We used the 2D MHD numerical model presented in Jelínek & Karlický (2010, 2012) and Jelínek et al. (2012) where the plasma dynamics is described by a full set of ideal time-dependent MHD equations (see, e.g., Priest 1982, Chung 2002):

$$\frac{\mathrm{D}\varrho}{\mathrm{D}t} = -\varrho\nabla\boldsymbol{v}, \tag{1}$$

$$\varrho\frac{\mathrm{D}\boldsymbol{v}}{\mathrm{D}t} = -\nabla p + \boldsymbol{j}\times\boldsymbol{B}, \tag{2}$$

$$\frac{\mathrm{D}\boldsymbol{B}}{\mathrm{D}t} = (\boldsymbol{B}\times\nabla)\boldsymbol{v}, \tag{3}$$

$$\frac{\mathrm{D}U}{\mathrm{D}t} = -U(\gamma-1)\nabla\times\boldsymbol{v}, \tag{4}$$

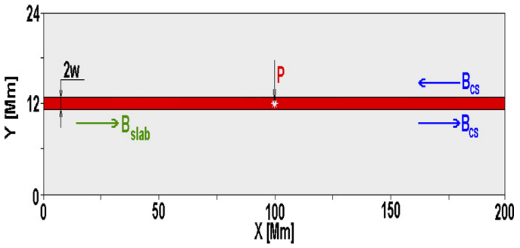

Figure 1. Scheme of a 2D numerical box with a waveguide (in dark) in its center. The length$X$ of the numerical box and waveguide is 200 Mm. The width Y of the numerical box is 24 Mm, and w indicates the half-width of the waveguide. The initial perturbation P is located in the center of the waveguide ($X = 100$ Mm). Arrows show the magnetic field orientation in the dense slab B_{slab} and in the Harris current sheet B_{cs}.

(A color version of this figure is available in the online journal.)

$$\nabla\times\boldsymbol{B} = 0, \tag{5}$$

where $\mathrm{D}/\mathrm{D}t \equiv \partial/\partial t + \boldsymbol{v}\times\nabla$ is the convective time derivative, ϱ is a mass density, $\boldsymbol{v}$ is flow velocity, $\boldsymbol{B}$ is the magnetic field, and the adiabatic coefficient $\gamma = 5/3$. The current density, $\boldsymbol{j}$, in Equation (2) is expressed as

$$\boldsymbol{j} = \frac{1}{\mu_0}(\nabla\times\boldsymbol{B}), \tag{6}$$

where μ_0 is the magnetic permeability of free space. The specific internal energy, U, in Equation (4) is given by

$$U = \frac{p}{(\gamma-1)\varrho}, \tag{7}$$

where p is the pressure.

The magnetohydrodynamic equations (1)–(4) were transformed into a flux-conserving form (Chung 2002) and solved numerically. We used two types of numerical codes. The first one is based on a modified two-step Lax–Wendroff algorithm (Kliem et al. 2000). In this code the simulation box (see Figure 1) was covered by a uniform grid with 2500× 300 cells. The cell size in both the X and Y directions was equal to 0.08 Mm, and the numerical time step was $\Delta t = 0.044$ s. This code was used for all computations in this parametric study. To verify these computations in selected cases, we used the FLASH code (Fryxell et al. 2000; Lee & Deane 2009; Lee 2013), which implements second- and third-order unsplit Godunov solvers and adaptive mesh refinement (AMR; see, e.g., Chung 2002; Murawski 2002). As we used AMR, the minimal grid sizes are found to be $\min(\Delta x) = \min(\Delta y) = 0.03$ Mm. In both codes the open boundary conditions were applied. The waveguide half-widths in both waveguides (dense slab and current sheet) were chosen as $w = 0.5$, 1.0, and 2.0 Mm.

2.1.1. *Initial Conditions and Equilibrium*

Initial conditions were selected according to solar flare conditions and perturbations that generate sausage magnetoacoustic waves. Moreover, to see the differences between magnetoacoustic waves in the dense slab and Harris current sheet, we tried to make both waveguides as similar as possible.

2.1.2. *Dense Slab*

The dense slab is embedded in a magnetic environment with a magnetic field given by the plasma beta parameter

$$\beta = \frac{p}{p_{\mathrm{mag}}} = \frac{2\mu_0 p}{B^2}, \tag{8}$$

where β is assumed to be 0.1. The magnetic field B_{slab} is parallel to the X axis (arrow in Figure 1) and is assumed to be constant in the entire simulation region ($B_{\mathrm{slab}} = 3.5 \times 10^{-3}$ T). The dense slab is considered in equilibrium; therefore, for constant magnetic field the kinetic pressure is also constant everywhere. This also means that the temperature profile across the slab is inverse to the profile of the density.

The mass density profile is considered to be constant along the X axis and is expressed along the Y axis by the formula (Nakariakov & Roberts 1995)

$$\varrho(X, Y) = \varrho_0 + (\varrho_{\mathrm{slab}} - \varrho_0) \times \mathrm{sech}^2\left\{\left[\frac{(Y - Y_P)}{w}\right]^{\alpha}\right\}, \tag{9}$$

where the power index $\alpha = 8$ determines the steepness of the profile, $Y_P = 12$ Mm is the dense slab center in the Y direction, and w is the half-width of the dense slab.

We selected the parameters in and out of the dense slab as follows: the mass density $\varrho_{\mathrm{in}} = 6.69 \times 10^{-11}$ kg m^{-3} (electron density $n_e = 10^{16}$ m^{-3}) and $\varrho_{\mathrm{out}} = 6.08 \times 10^{-12}$ kg m^{-3}, temperature $T_{\mathrm{in}} = 0.45$ MK and $T_{\mathrm{out}} = 5$ MK, the Alfvén velocity $v_{\mathrm{A-in}} = 0.39$ Mm s^{-1} and $v_{\mathrm{A-out}} = 1.28$ Mm s^{-1}, and the sound velocity $c_{\mathrm{s-in}} = 0.11$ Mm s^{-1} and $c_{\mathrm{s-out}} = 0.37$ Mm s^{-1}.

2.1.3. *Harris Current Sheet*

The magnetic field in the Harris current sheet is given by

$$\mathbf{B} = B_{\mathrm{out}} \tanh\left[\frac{(Y - Y_P)}{w}\right]\hat{\mathbf{e}}_X, \tag{10}$$

where B_{out} is the magnetic field at $Y \to \infty$ and w is the half-width of the current sheet (see also Figure 1). Magnetic field B_{out} is determined from (Jelínek & Karlický 2012)

$$B_{\mathrm{out}} = \sqrt{\frac{2\mu_0 p_{\mathrm{cs}}}{1 + \beta}}. \tag{11}$$

The kinetic pressure at the center of the current sheet p_{cs} is calculated from the plasma density at the center of the current sheet ϱ_{cs}. The plasma beta parameter β outside of the current sheet is assumed to be 0.1.

Because of the zero magnetic field at the center of the current sheet $B_{\mathrm{cs}} = 0$, one can calculate, from the condition of equilibrium

$$p + \frac{B^2}{2\mu_0} = \mathrm{const}, \tag{12}$$

that the distribution of the mass density in the simulation box is

$$\varrho(x, y) = \varrho_{\mathrm{cs}} - \frac{m B_x^2(y)}{2\mu_0 k_{\mathrm{B}} T}, \tag{13}$$

where m is the proton mass and k_{B} is the Boltzmann constant.

In our computations the magnetic field B_{out} is chosen as $B_{\mathrm{out}} = 3.5 \times 10^{-3}$ T. The parameters in the center, at the $Y = w$, and out of the current sheet are as follows: mass density $\varrho_{\mathrm{c}} = 6.69 \times 10^{-11}$ kg m^{-3}, $\varrho_w = 3.32 \times 10^{-11}$ kg m^{-3}, and $\varrho_{\mathrm{out}} = 6.08 \times 10^{-12}$ kg m^{-3}; the temperature and sound speed are constant in the whole numerical box $T = 5$ MK and $c_{\mathrm{s}} = 0.37$ Mm s^{-1}; the Alfvén velocity $v_{\mathrm{A-c}} = 0$, $v_{\mathrm{A-w}} = 0.40$ Mm s^{-1}, and $v_{\mathrm{A-out}} = 1.28$ Mm s^{-1}; and the plasma beta parameter $\beta_{\mathrm{c}} = \infty$ and $\beta_{\mathrm{w}} = 0.96$.

2.1.4. *Perturbation*

We perturbed the initial equilibrium (with $\boldsymbol{v} = 0$) by the Gaussian pulse in the Y component of the velocity. The perturbation point P (Figure 1), where the velocity is perturbed, was located at the center ($X_P = 100$ Mm, $Y_P = 12$ Mm) of the numerical box. This initial velocity pulse v_Y followed a profile (e.g., Nakariakov et al. 2004, 2005)

$$v_Y = A_0 \frac{Y}{\lambda_X} \exp\left[-\frac{(X - X_P)^2}{\lambda_X^2}\right] \exp\left[-\frac{(Y - Y_P)^2}{\lambda_Y^2}\right], \tag{14}$$

where $A_0 = 1.5 \times 10^4$ m s^{-1} is the initial amplitude of the pulse and λ_X and λ_Y are the half-widths of the velocity pulse in the X and Y directions, respectively. We used the size of the perturbation half-widths $\lambda_X = 1.5$ Mm and $\lambda_Y = 0.5$ Mm in our whole study (except Section 4.1).

2.2. *Wavelet Methods*

We used wavelet power spectra for an analysis of time series collected in selected points along the waveguide at different distances from the initial perturbation point P. These power spectra in our entire study are based on the wavelet analysis technique (Torrence & Compo, 1998) with the Morlet mother function with the parameter $\omega = 6$.

In this study we used wavelet power spectra where both the cone of influence (COI; edge effects become important due to finite-length time series) and the confidence level (CL) relative to red noise were taken into account. In each time series, only the regions outside the COI with CL above 99% are considered significant. Thus, we studied only the most dominant characteristic wavelet signatures.

3. TYPICAL EXAMPLES OF PROPAGATING MAGNETOACOUSTIC WAVES IN THE DENSE SLAB AND HARRIS CURRENT SHEET

Figure 2 shows a time evolution of the density perturbations propagating along the dense slab (left part) and Harris current sheet (right part) at four times: 0.5, 50, 100, and 150 s after they were triggered by the initial perturbation in the center of the waveguide (marked by P). The half-width of both waveguides is $w = 1$ Mm. (Note that there are also negative perturbation peaks similar to the positive ones, but they are only partly visible in the figure.) Analyzing the properties of these perturbations (propagation velocities, dispersions, and the phases between the density and magnetic field perturbations) for all computed variables and comparing them to theoretical studies (e.g., Roberts et al. 1984), we recognized here three types of waves: the fast magnetoacoustic waves (marked by F), the slow magnetoacoustic waves (marked by S), and the nonpropagating wave at the location of the initial perturbation (marked by I). Both the fast and slow magnetoacoustic waves propagate from the center of the waveguide (location of the initial perturbation) in opposite directions toward the ends of the waveguide ($X = 0$ and 200 Mm). While the fast magnetoacoustic waves F consist of

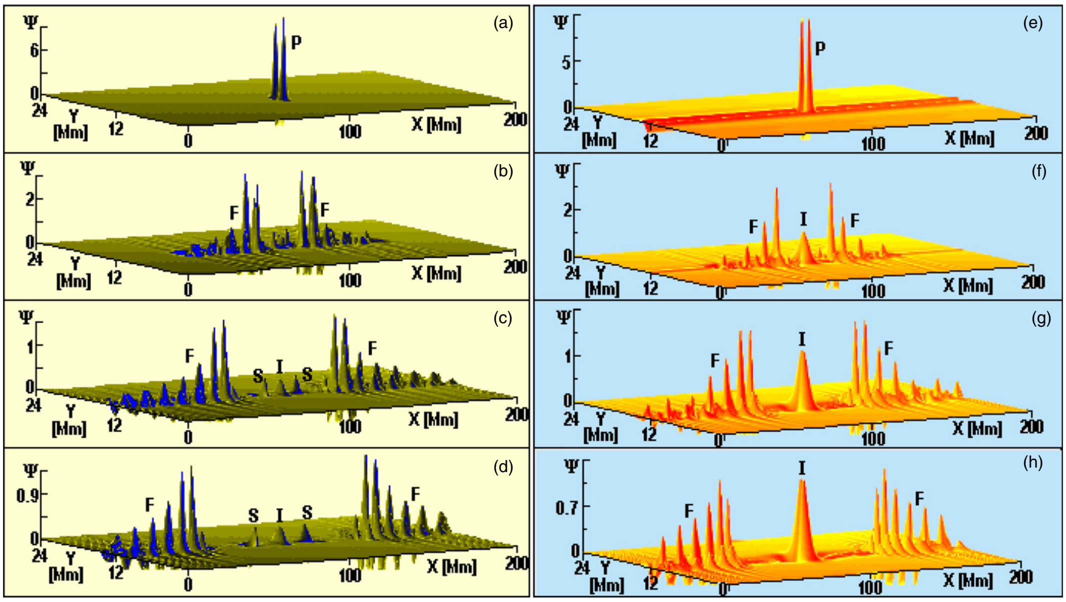

Figure 2. Spatial evolution of the fast *F* and slow *S* magnetoacoustic waves propagating in the dense slab (panels (a)–(d)) and the Harris current sheet (panels (e)–(h)) expressed as $\Psi = 10^{-3}(\varrho - \varrho_0)/\varrho_0$, where ϱ is the density and ϱ_0 is the initial density. In both cases, the waveguide half-width w is 1 Mm. The initial perturbation *P* is generated in the center of waveguide ($X = 100$ Mm, $Y = 12$ Mm). Panels in both columns show propagating waves at times 0.5 s (panels (a) and (e)), 50 s (panels (b) and (f)), 100 s (panels (c) and (g)), and 150 s (panels (d) and (h)) after their generation by the initial perturbation. The peak *I* remains at the site of the initial perturbation.

(A color version of this figure is available in the online journal.)

many peaks (wave train), where the smallest peaks propagate as the first ones along the waveguide with the highest speed, the slow magnetoacoustic waves *S* occur only as single peaks during the entire evolution process. Such behavior is a natural effect of the dispersive and nearly nondispersive properties of the fast and slow magnetoacoustic waves, respectively.

The nonpropagating peak *I* differs for the slab and current sheet. In the dense slab this peak *I* (e.g., Figure 2(d)) is a single peak with small amplitude (comparable to the amplitudes of slow waves) and is seen only in density perturbation records. On the other hand, in the current sheet the peak *I* is relatively strong and has a double-peak structure (e.g., Figure 2(h)). It appears in all physical variables, but with different structural complexities. Both these peaks *I* remain at the site of the initial perturbation *P* during the entire simulation, and one initial perturbation causes one nonpropagating peak *I*.

4. TEMPORAL EVOLUTION OF THE FAST MAGNETOACOUSTIC WAVES AND THEIR WAVELET SPECTRA

Time series of all physical variables were collected at detection points with a distance of 5 Mm from each other along the whole waveguide, where a wave train of the fast magnetoacoustic wave propagates. For the purpose of this paper, we selected time series of a ratio of the density perturbation $(\varrho - \varrho_0)$ and the initial density ϱ_0, i.e., $\Psi = 10^{-3}(\varrho - \varrho_0)/\varrho_0$. From these series we computed the wavelet power spectra at all detection points. Typical examples are summarized in Figure 3, where the time series and their wavelet spectra with tadpole patterns for the dense slab (panels (a)–(c)) and Harris current sheet (panels (d)–(f)) are shown. The transverse half-width of the initial perturbation is in all cases $\lambda_Y = 0.5$ Mm. The wavelet spectra were computed for three values of the half-width of the waveguide, $w = 0.5$ Mm (panels (a) and (d)), $w = 1.0$ Mm (panels (b) and (e)), and $w = 2.0$ Mm (panels (c) and (f)), and at three detection points located 10 Mm (panels (a1)–(f1)), 30 Mm (panels (a2)–(f2)), and 50 Mm (panels (a3)–(f3)) from the initial perturbation site. Here, we can see that characteristic time periods of guided waves t_p increase with an increase of the width of the dense slab, in agreement with the relation $t_p = 2.6w/v_{\mathrm{A-in}}$ (Roberts et al. 1984, Jelínek & Karlický 2012). However, here, we found that for the Harris current sheet this period is $t_p \approx 2.6w/v_{\mathrm{A-w}}$, where $v_{\mathrm{A-w}}$ is the Alfvén velocity at the half-width w of the current sheet. The wavelet spectra also confirm that tadpole tails become longer, increasing the distance between the initial perturbation and detection points.

In addition to these known facts, there are new details concerning a form of the main tadpole and also additional structures. For example, in the wavelet spectra corresponding to the narrow waveguide ($w = 0.5$ Mm) the tadpole heads are suppressed for both the dense slab and current sheet. This is consistent with the results of modeling presented in Nakariakov et al. (2005). The situation differs for the wavelet spectra with a broader waveguide ($w = 1.0$ Mm), where the tadpole heads are more distinctly expressed for both the slab and current sheet. The additional structures are small (arrow 1 in Figure 3) for the slab and more significant for the current sheet (arrows 6 and 8). Furthermore, for the broad waveguide ($w = 2.0$ Mm) all tadpole heads are accompanied by additional structures (arrows 2–5, 7, and 9). There is a significant difference between additional structures for the dense slab and current sheet. While in the slab

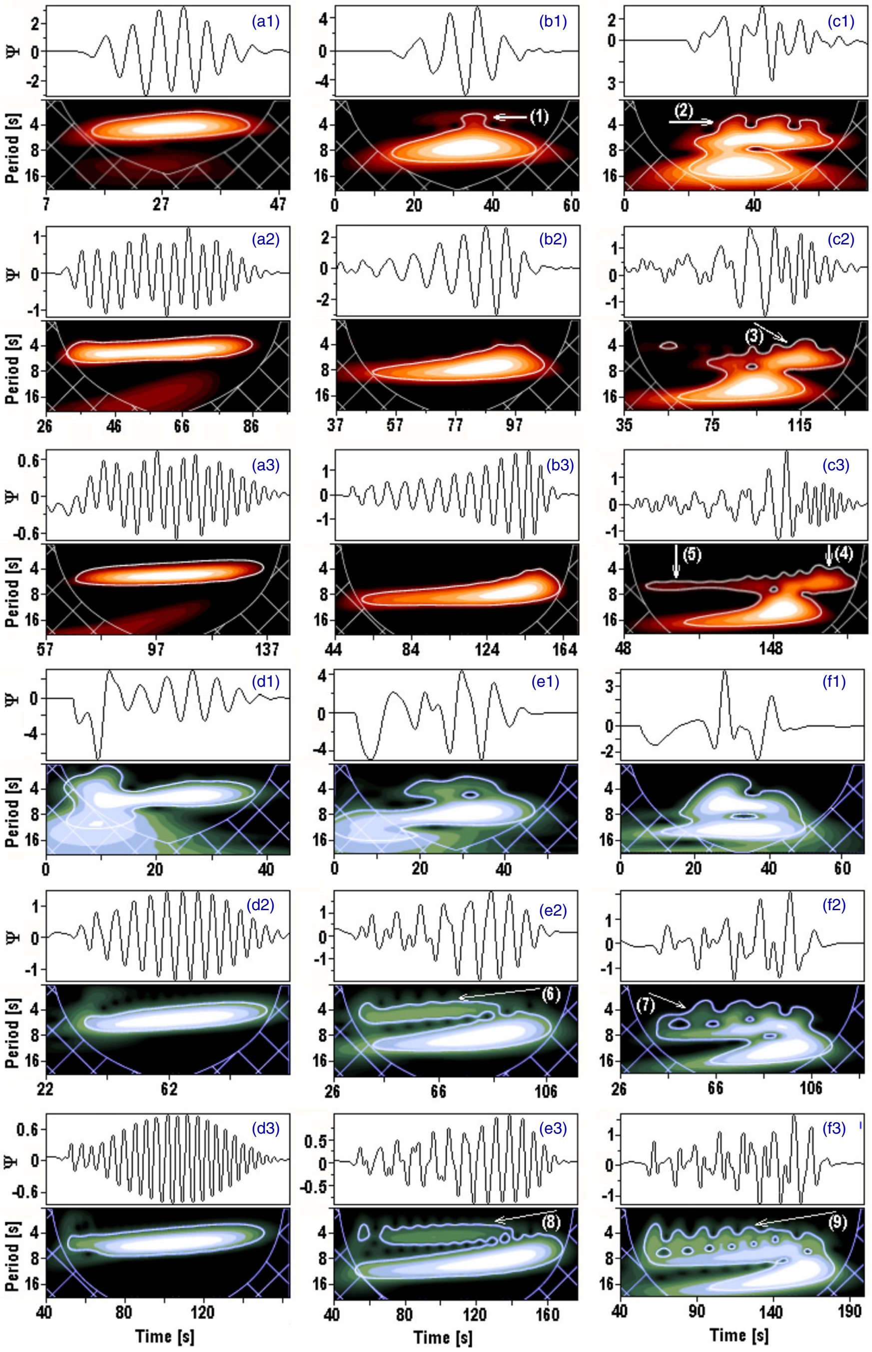

Figure 3. Time series of $\Psi = 10^{-3}(\varrho - \varrho_0)/\varrho_0$ and their wavelet spectra in the dense slab (panels (a)–(c)) and Harris current sheet (panels (d)–(f)) depending on the half-width of the waveguide $w = 0.5$ Mm (panels (a) and (d)), $w = 1.0$ Mm (panels (b) and (e)), and $w = 2.0$ Mm (panels (c) and (f)) and for detection points located 10 Mm (panels (a1)-(c1) and (d1)–(f1)), 30 Mm (panels (a2)–(c2) and (d2)–(f2)), and 50 Mm (panels (a3)–(c3) and (d3)–(f3)) from the initial perturbation. Some wavelet tadpole patterns show various types of additional structures (arrows 1–9).

(A color version of this figure is available in the online journal.)

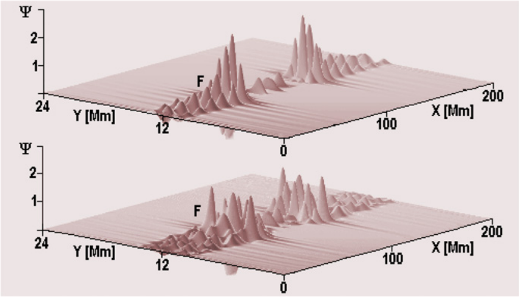

Figure 4. Spatial distribution of $\Psi = 10^{-3}(\varrho - \varrho_0)/\varrho_0$ along the dense slab at a time of 100 s after the initial perturbation, where F means the fast magnetoacoustic wave train. Top and bottom panels are for half-widths $w = 1.0$ Mm and $w = 2.0$ Mm, respectively.

(A color version of this figure is available in the online journal.)

case the additional structures (arrows 2–4) are always delayed after the tadpole head maximum, in the current sheet case the additional structures (arrows 6–9) always precede the tadpole head maximum. Sometimes, we can see the preceding additional structures also in the slab case (arrow 5), but they are always accompanied by the delayed ones. The additional structures (arrows 1–9) have shorter periods than the period of the main tadpole. They are connected to an appearance of additional wave trains in the waveguide, as shown in Figure 4. While the case with the waveguide half-width $w = 1$ Mm (top panel) shows a rather simple wave train, the case with the waveguide half-width $w = 2$ Mm (bottom panel) displays several mixed wave trains. In such a case, the main wave train at the waveguide center ($Y \approx 12$ Mm) causes the main tadpole, and the additional wave trains cause the additional structures in the wavelet spectrum. Note that the same results as presented in Figures 2 and 3 were also obtained using the FLASH code (see Section 2).

The slow magnetoacoustic waves are expressed as a simple "blob" on the wavelet spectrum. Because their amplitude is much smaller than that of the fast magnetoacoustic waves, they appear on the wavelet spectrum only at low confidence levels.

4.1. *Effects of Different Half-widths of Perturbations*

There is a question of whether a form of the wavelet tadpoles can be affected by different types of initial perturbation, e.g., by a change in the ratio between the transverse half-width of perturbation λ_Y and the half-width of waveguide w. Therefore, we computed time series of $\Psi = 10^{-3}(\varrho - \varrho_0)/\varrho_0$ and their wavelet spectra (see Figure 5) for the dense slab (panels (a) and (b)) and Harris current sheet (panels (c) and (d)), where the perturbation half-width λ_Y was selected as $\lambda_Y = 0.5w$ (panels (a1)–(d1)), $\lambda_Y = w$ (panels (a2)–(d2)), and $\lambda_Y = 2w$ (panels (a3)–(d3)). The wavelet tadpoles were computed for the waveguide half-widths $w = 1.0$ Mm (panels (a1)–(a3) and (c1)–(c3)) and $w = 2.0$ Mm (panels (b1)–(b3) and (d1)–(d3)). All time series are collected at the detection point located 30 Mm from the initial perturbation point.

As seen in Figure 5, when the waveguide half-width is $w = 1.0$ Mm, there are no significant additional structures for

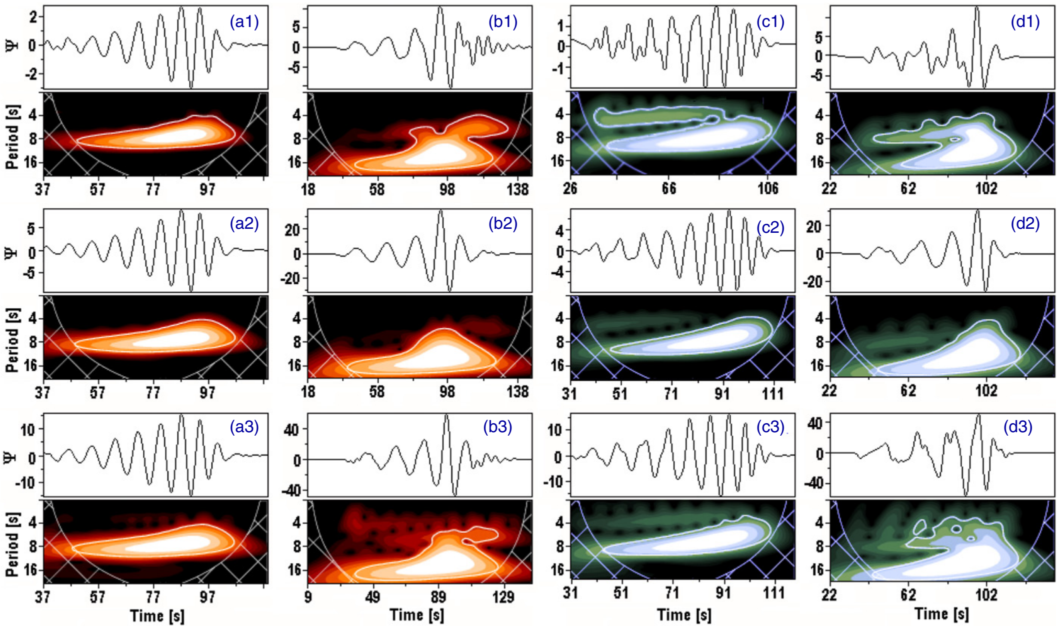

Figure 5. Time series of $\Psi = 10^{-3}(\varrho - \varrho_0)/\varrho_0$ and their wavelet spectra depending on the ratio between the transverse half-width of the perturbation λ_Y and the half-width of the waveguide w: $\lambda_Y = 0.5w$ (panels (a1)–(d1)), $\lambda_Y = w$ (panels (a2)–(d2)), and $\lambda_Y = 2w$ (panels (a3)–(d3)). Wavelet spectra for the dense slab (panels (a) and (b)) and the Harris current sheet (panels (c) and (d)) are computed for $w = 1.0$ Mm (panels (a) and (c)) and $w = 2.0$ Mm (panels (b) and (d)). All time series are collected in the detection point located 30 Mm from the initial perturbation.

(A color version of this figure is available in the online journal.)

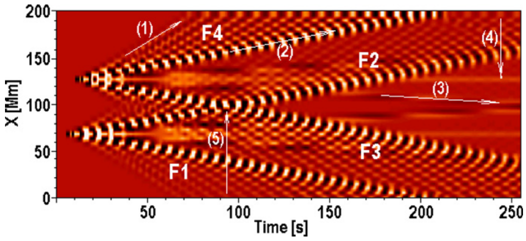

Figure 6. Dynamic spectrum of time series of $\Psi = 10^{-3}(\varrho - \varrho_0)/\varrho_0$ collected at all points along the density slab, i.e., for $X = 0$–200 Mm with a grid distance of 5 Mm. The first and second perturbations are generated 5 and 10 s after the start of computation, and they are located at the points with $X = 70$ and 130 Mm ($Y = 12$ Mm), respectively. Both perturbations generate four fast ($F1$–$F4$) and four slow magnetoacoustic waves. Waves $F2$ and $F3$ propagate toward the waveguide center ($X = 100$ Mm), and they interact at a time of 93 s (arrow 5). The fastest and slowest spectral components of wave $F4$ are shown by arrows 1 and 2, respectively. Arrow3 shows one of the slow magnetoacoustic waves. Arrow4 displays the nonpropagating peak I seen, e.g., in Figure 2.

(A color version of this figure is available in the online journal.)

the dense slab (panels (a1)–(a3)). In case of the current sheet, there are additional structures only if the perturbation half-width is smaller than that of the waveguide (panel (c1)). When the waveguide half-width is $w = 2.0$ Mm (panels (b1)–(b3) and (d1)–(d3)), then the additional structures appear in all cases, except the case where the perturbation and waveguide half-widths are the same. In such a case, the tadpole head is extended toward shorter periods (see panels (b2) and (d2)).

We also made computations for the dense slab and Harris current sheet with the waveguide half-widths $w = 0.5$ Mm for all values of λ_Y as in Figure 5. In these cases none of the tadpoles have any additional structures, and all have suppressed heads regardless of the half-width of the perturbation.

4.2. *Mutual Interactions of Propagating Magnetoacoustic Waves*

We also studied wavelet spectra for the case with two perturbations in one waveguide, which generate several interacting waves. We considered the same numerical box as in Figure 1, with the dense slab having a half-width of 1.0 Mm.

An example of such wave interactions is shown in Figure 6, where the density perturbation $\Psi = 10^{-3}(\varrho - \varrho_0)/\varrho_0$ is excited. This dynamic spectrum is computed from time series collected at detection points along the waveguide at locations $X = 0$–200 Mm and $Y = 12$ Mm. The spatial step between detection points along the X coordinate is 5 Mm. The first and second perturbations were initiated at locations $X = 70$ and 130 Mm, 5 and 10 s after the simulation starting time, respectively. The initial amplitude of both perturbations is the same, i.e., $A_0 = 1.5 \times 10^4$ m s^{-1}. Both perturbations generate two pairs of fast ($F1$–$F4$) wave trains and two pairs of slow waves. As presented in Figure 6, fast waves $F1$ and $F4$ propagate toward the waveguide ends $X = 0$ and 200 Mm, respectively. On the other hand, fast waves $F2$ and $F3$ propagate to the waveguide center ($X = 100$ Mm), where they interact. First, we can see an interaction of the fastest components of these waves, corresponding to the periodic parts of the wave trains and also to tadpole tails in the wavelet spectra. In the following times, slower and slower wave components start to interact. The velocities of the fastest and slowest components of wave $F4$, which are marked by arrows 1 and 2, are 1.0 and 0.35 Mm s^{-1}, respectively. Note that the most distinct and slowest components of waves $F2$ and $F3$, which correspond to the quasiperiodic parts of the wave trains and also to tadpole heads in the wavelet spectrum, interact at a time of 93 s (arrow 5). Arrow3 shows one of the slow waves propagating at a speed of 0.1 Mm s^{-1}. This slow wave has only one component. Arrow4 displays one of the peaks I (see Figure 2), which remains at the location of the initial perturbation ($X = 130$ Mm) during the whole simulation.

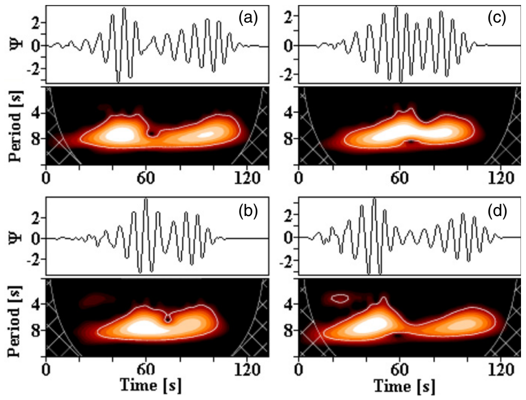

Figure 7. Wavelet spectra corresponding to a mutual interaction between two fast magnetoacoustic waves in the dense slab. Panels (a), (b), (c), and (d) present the wavelet spectra of time series of $\Psi = 10^{-3}(\varrho - \varrho_0)/\varrho_0$ collected at points with $X = 90$, 95, 105, and 110 Mm, respectively.

(A color version of this figure is available in the online journal.)

Comparing the velocities found for these waves with the assumed Alfvén velocities in and out of the dense slab ($v_{\mathrm{A-in}}$ and $v_{\mathrm{A-out}}$) and the sound velocity in the dense slab ($c_{\mathrm{s-in}}$; see Section 2), we can see that the computed velocities agree with those theoretically predicted by Roberts et al. (1984). Namely, the velocities of the fastest and slowest components of the fast wave train should correspond to $v_{\mathrm{A-out}} = 1.28$ Mm s^{-1} and $v_{\mathrm{A-in}} = 0.39$ Mm s^{-1}, respectively, and the velocity of the slow magnetoacoustic wave should correspond to the sound velocity $c_{\mathrm{s-in}} = 0.11$ Mm s^{-1}. Note that a determination of the fastest component of the fast wave train is not very precise because of its very low signal at the arrival time at the detection point.

For the Harris current sheet with the same half-width w, the dynamical spectrum is very similar to that of the dense slab (Figure 6).

The wavelet spectra of an interaction between fast magnetoacoustic waves $F2$ and $F3$ in the dense slab are displayed in Figure 7. Panels (a), (b), (c), and (d) present time series of $\Psi = (\varrho - \varrho_0)/\varrho_0$ collected *near* their interaction region, i.e., at the detection points $X = 90$, 95, 105, and 110 Mm, and their wavelet spectra. The wavelet patterns look like they are composed of two tadpoles. The first tadpole corresponds to the wave train before the interaction of waves, and the second one corresponds to the wave train after the wave interaction. Because waves $F2$ and $F3$ were not initiated at the same time (they are separated by a small delay of 5 s), the interacting wave trains at the interaction site are similar but not the same (not in the same state of evolution). This difference is also found between the wavelet patterns in Figures 7(a) and (d) (and Figures 7(b) and (c)). The wavelet spectrum of this interaction at $X = 100$ Mm is similar to that in panel (b2) of Figure 3.

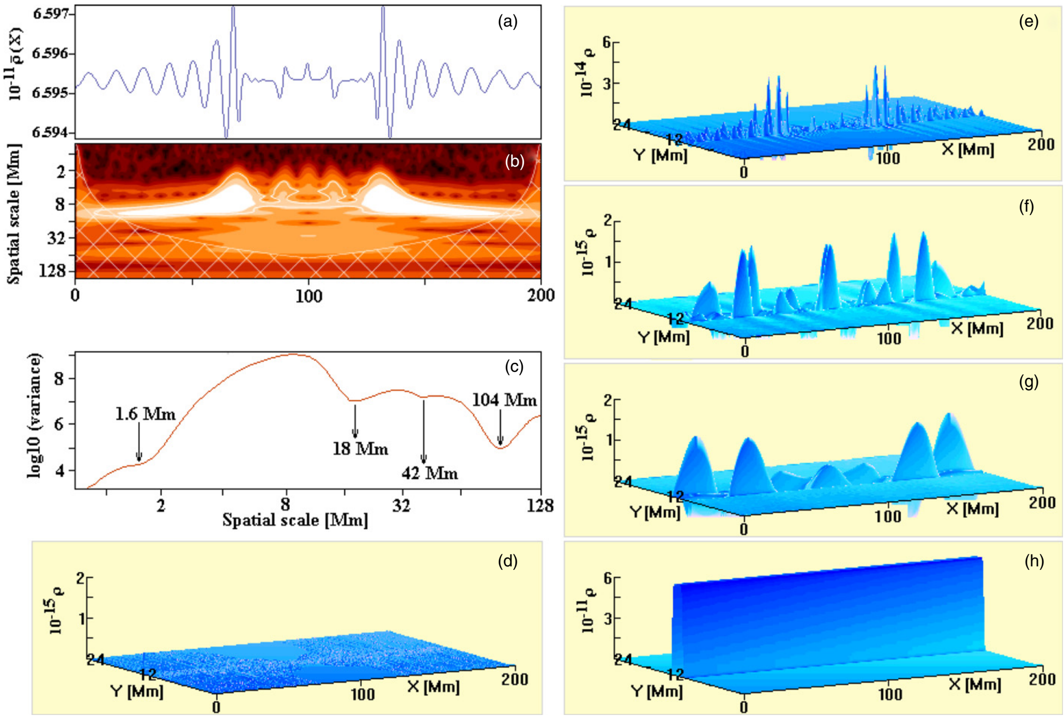

Figure 8. Separation of density variations according to their characteristic spatial scales. Panel (a) shows variations of the averaged density $\bar{\varrho}(X)$ depending on the spatial coordinate X. Panel (b) shows the wavelet power spectrum of the variable $\bar{\varrho}(X)$. Panel (c) presents the global wavelet spectrum with individual minima at 1.6, 18, 42, and 104 Mm. Panel (d) shows the filtered spatial structure for spatial scales <1.6 Mm corresponding to a numerical noise. Panel (e) presents the filtered spatial structure for spatial scales in the range of 1.6–18 Mm, showing both fast and slow magnetoacoustic waves. Panels (f) and (g) present filtered spatial structures with spatial scales in the ranges 18–42 and 42–104 Mm, respectively, showing long spatial components of the waves. Panel (h) presents the filtered spatial structure with spatial scales >104 Mm, showing the original density profile.

(A color version of this figure is available in the online journal.)

(Note that in the ideal case where both waves (with the same A_0) are initiated at the same time, the interacting wave trains at the interaction site will be the same.) Far away from the interaction site (distances >10 Mm) the time series and their wavelet power spectra show two separate tadpoles. In summary, the wavelet spectra of mutual interactions of the fast magnetoacoustic waves depend on the evolution states of the wave trains of both waves at the time of their interaction.

5. MAGNETOACOUSTIC WAVES SEPARATED INTO SEVERAL SPATIAL SPECTRAL COMPONENTS

Generally, perturbations of magnetoacoustic waves are superimposed on an initial waveguide profile. Thus, to display these waves (which have relatively small amplitudes) distinctly, we subtract the initial profile, e.g., the initial density profile ϱ_0. However, we can only make this subtraction in the case of numerical simulations, where the profile ϱ_0 is known. Such a subtraction is impossible to make in observed data, where these initial profiles of the waveguides are not generally known. To mimic a situation with observed data, we analyzed data obtained from our numerical simulations directly, i.e., without any subtractions.

Note that the effect of the line-of-sight (LOS) angle can significantly affect an observed signal. The importance of this effect in the observational manifestation of MHD waves in the optically thin regime was demonstrated in Gruszecki et al. (2012) and Antolin & Van Doorsselaere (2013). The LOS effect is not included in numerical simulations presented in this study.

We used the method based on wavelets as described by Mészárosová et al. (2011a). Generally, this method enables us to separate spatial or time structures according to their spatial or time scales. In the present case, we use this method to separate (filter) the magnetoacoustic waves from computed densities in the dense slab at one selected instant according to characteristic spatial scales.

An example of such a separation is presented in Figure 8, where we analyzed the magnetoacoustic waves at 100 s after the initial perturbation, the same case as shown in Figure 2(c). First, we computed the averaged density $\bar{\varrho}(X)$ (averaged in the dense slab along the Y coordinate, i.e., between $Y_{\mathrm{min}} = 11$ Mm and $Y_{\mathrm{max}} = 13$ Mm), which is dependent on the spatial coordinate X. This averaged density, its spatial wavelet power spectrum, and its global wavelet spectrum are shown in Figures 8(a), (b), and (c), respectively. The wavelet power spectrum displays tadpoles at spatial scales of 1.6–18 Mm. These tadpoles are spatial equivalents of the tadpoles found in time series (Section 4). The global wavelet spectrum shows individual minima at 1.6, 18, 42, and 104 Mm. They enable us to determine the most characteristic spatial variations of the averaged density $\bar{\varrho}(X)$ (for more details, see Mészárosová et al. 2011a).

We used the determined characteristic spatial scales to divide the spatial variations $\bar{\varrho}(X)$ into five spatial scale intervals: <1.6 Mm, 1.6–18 Mm, 18–42 Mm, 42–104 Mm, and >104 Mm. After an inversion procedure for the wavelet spectra in the entire numerical box in the selected spatial scale ranges, we obtained spatial structures as shown in Figures 8(d)–(h). While the spatial structure shown in the panel (e) (spatial scales 1.6–18 Mm) corresponds to the main spatial components of both the fast and slow magnetoacoustic waves, the structure in panel (h) (spatial scales >104 Mm) corresponds to the initial dense slab. The structure in panel (d) (spatial scales <1.6 Mm) is numerical noise. Besides these structures, in panels (f) and (g) we can see the structures expressing very long spatial components of the magnetoacoustic waves at spatial scales of 18–42 and 42–104 Mm, respectively. These components are interesting because they show how the propagating magnetoacoustic waves would appear in observations with limited spatial resolutions.

6. CONCLUSIONS

Motivated by our previous studies, in which we tried to interpret various forms of the wavelet spectra of observed data, in the present paper we made an extended parametric study of the properties of impulsively generated fast and slow magnetoacoustic waves propagating in the dense slab and Harris current sheet.

The following results were obtained.

1. Both the dense slab and Harris current sheet are good waveguides of magnetoacoustic waves. The dense slab and Harris current sheet with the presented parameters guide the fast magnetoacoustic waves in a similar way. They differ in guiding the slow magnetoacoustic waves. The difference comes from the different magnetic fields and temperature structures of these waveguides.
2. The characteristic period of the fast magnetoacoustic waves is given by $t_p = 2.6w/v_{\mathrm{A-in}}$ in the dense slab and by $t_p \approx 2.6w/v_{\mathrm{A-w}}$ in the Harris current sheet, where $v_{\mathrm{A-in}}$ is the Alfvén velocity inside the dense slab and $v_{\mathrm{A-w}}$ is the Alfvén velocity at the half-width w of the current sheet. Because in our models $v_{\mathrm{A-in}}$ and $v_{\mathrm{A-w}}$ are similar, for the same w in both waveguides, we obtain similar periods and also similar tadpoles in the wavelet spectra. Therefore, from only tadpole forms in an analysis of the observed data, the dense slab and Harris current sheet cases cannot be distinguished.
3. Each fast magnetoacoustic wave forms a wave train where the components with the smallest and largest amplitudes propagate at the highest and lowest speeds, respectively. The slow magnetoacoustic wave propagates as a single peak. It is a natural effect of the dispersive and nearly nondispersive properties of the fast and slow magnetoacoustic waves, respectively.
4. We found a nonpropagating wave at the site of the initial perturbation in both the dense slab and current sheet cases. In the dense slab, this wave had a single structure, with a small amplitude, and was detected only in density perturbation records. In the current sheet this wave was relatively strong and had a double structure. It appeared in all physical variables, but with different structural complexities. This stationary structure is known as the entropy mode (see, e.g., Murawski et al. 2011). We showed that this nonpropagating wave can be detected in spatially resolved data.
5. Comparing the wavelet spectra for the dense slab and current sheet cases, computed for their different half-widths, we found significant differences. For cases with the narrow waveguide ($w = 0.5$ Mm) the tadpole heads were suppressed. For the broader waveguide with $w \approx 1.0$ Mm, the additional structures on wavelet tadpole heads were significant only for the current sheet. For the waveguide with $w \approx 2.0$ Mm, the wavelet tadpole heads were extended by the additional structures. In the dense slab case these additional structures were always delayed after the tadpole head maximum. The current sheet case is the opposite. The additional structures can be explained by additional magnetoacoustic wave trains, which appeared in broader waveguides. Comparing the periods of these features and that of the main tadpole, it looks like these features could be the third harmonics of the main wave train. The tadpoles with additional structures had already been found in observed data. For example, in the paper by Mészárosová et al. (2013), the right panel of Figure 8 shows a wavelet structure similar to the one presented here in panel (b1) of Figure 3.
6. The different half-widths of perturbation can affect the occurrence of the additional structures in broader waveguides $\gtrsim$1.0 Mm. When the perturbation half-width is smaller than that of the waveguide, the additional structures are always significant in the current sheet, while in the dense slab they are only significant for the waveguide half-width ≈2 Mm. When the perturbation half-width is greater than that of the waveguide, the additional structures only occur for the waveguide half-width ≈2 Mm in both waveguide types. In this case, these structures are suppressed comparing with the previous case. The additional structures vanish if the perturbation half-width is equal or similar to that of the waveguide. Then the tadpole head is extended toward shorter periods, especially for the broad waveguide ≈2 Mm. In observed data such wavelet structures have already been observed, e.g., in Figure 3 of Mészárosová et al. (2009b).
7. We studied tadpole patterns corresponding to mutual interactions of waves generated by two perturbations. The dynamical spectrum of these processes revealed (1) two pairs of fast and slow magnetoacoustic waves, (2) many fast wave train components, and (3) the propagating speed of the slow waves as well as the speeds of the components of the fast wave train that belong to the periodic and quasiperiodic wave phases, i.e., to the wavelet tadpole tail and head, respectively. The velocities of the fastest and slowest components of the fast wave train and the slow magnetoacoustic waves agree with those theoretically predicted. The dynamic spectrum of the current sheet is similar to the dynamical spectrum for the dense slab.
8. It was shown that the wavelet spectra of a mutual interaction of the fast magnetoacoustic waves depends on the evolution states of the wave trains of both waves at the time of their interaction.
9. We presented a method based on a wavelet technique that separates the spatial components at one instance that correspond to the magnetoacoustic waves and spatial structure of the waveguide. This method is proposed to search for magnetoacoustic waves in observed spatial imaging data where the waveguide structure is not generally known, where the observing cadence is not sufficient for time series gathering, and when the data space resolution is rather poor.

We hope that all these results help in the correct interpretation of the wavelet spectra of processes connected to magnetoacoustic waves, especially the fast magnetoacoustic waves.

H.M., M.K., and P.J. acknowledge support from grant P209/12/0103 (GA CR), research project RVO:67985815 of the Astronomical Institute AS, and the Marie Curie PIRSES-GA-2011-295272 RadioSun project. The work of J.R. was supported by the Slovak Research and Development Agency under contract APVV-0816-11 and by the Science Grant Agency, project VEGA 2/0108/12. The program of mobility between the academies of the Czech Republic and Slovakia is also acknowledged. The FLASH code used in this work was in part developed by the DOE-supported ASC/Alliances Center for Astrophysical Thermonuclear Flashes at the University of Chicago. The wavelet analysis was performed using software based on tools provided by C. Torrence and G. P. Compo at http://paos.colorado.edu/research/wavelets.

REFERENCES

Antolin, P., & Van Doorsselaere, T. 2013, A&A, 555, A74
Aschwanden, M. 2004, Physics of the Solar Corona: An Introduction (Chichester: Praxis)
Chung, T. J. 2002, Computational Fluid Dynamics (New York: Cambridge Univ. Press)
Fryxell, B., Olson, K., Ricker, P., et al. 2000, ApJS, 131, 273
Gruszecki, M., Nakariakov, V. M., & Van Doorsselaere, T. 2012, A&A, 543, A12
Jelínek, P., & Karlický, M. 2010, IEEE Trans. Plasma Sci., 38, 2243
Jelínek, P., & Karlický, M. 2012, A&A, 537, A46
Jelínek, P., Karlický, M., & Murawski, K. 2012, A&A, 546, A49
Karlický, M., Jelínek, P., & Mészárosová, H. 2011, A&A, 529, A96
Karlický, M., Mészárosová, H., & Jelínek, P. 2013, A&A, 550, A1
Katsiyannis, A. C., Williams, D. R., McAteer, R. T. J., et al. 2003, A&A, 406, 709
Kliem, B., Karlický, M., & Benz, A. O. 2000, A&A, 360, 715
Lee, D. 2013, JCoPh, 243, 269
Lee, D., & Deane, A. E. 2009, JCoPh, 228, 952
Mészárosová, H., Karlický, M., Rybák, J., & Jiřička, K. 2009a, ApJL, 697, L108
Mészárosová, H., Karlický, M., Rybák, J., & Jiřička, K. 2009b, A&A, 502, L13
Mészárosová, H., Rybák, J., & Karlický, M. 2011a, A&A, 525, A88
Mészárosová, H., Karlický, M., & Rybák, J. 2011b, SoPh, 273, 393
Mészárosová, H., Dudík, J., Karlický, M., et al. 2013, SoPh, 283, 473
Murawski, K. 2002, Analytical and Numerical Methods for Wave Propagation in Fluid Media (Singapore: World Scientific)
Murawski, K., Zaqarashvili, T. V., & Nakariakov, V. M. 2011, A&A, 533, A18
Nakariakov, V. M., Arber, T. D., Ault, C. E., et al. 2004, MNRAS, 349, 705
Nakariakov, V. M., Pascoe, D. J., & Arber, T. D. 2005, SSRv, 121, 115
Nakariakov, V. M., & Roberts, B. 1995, SoPh, 159, 399
Nakariakov, V. M., Verwichte, E., Berghmans, D., & Robbrecht, E. 2000, A&A, 362, 1151
Nakariakov, V. M., & Zimovets, I. V. 2011, ApJL, 730, L27
Pascoe, D. J., Nakariakov, V. M., & Kupriyanova, E. G. 2013, A&A, 560, A97
Priest, E. R. 1982, Solar Magnetohydrodynamics (Dordrecht: Riedel)
Robbrecht, E., Verwichte, E., Berghmans, D., et al. 2001, A&A, 370, 591
Roberts, B., Edwin, P. M., & Benz, A. O. 1983, Natur, 305, 688
Roberts, B., Edwin, P. M., & Benz, A. O. 1984, ApJ, 279, 857
Stepanov, A. V., Zaitsev, V. V., & Nakariakov, V. M. 2012, Coronal Seismology1st (Weinheim: Wiley-VCH)
Torrence, C., & Compo, G. P. 1998, BAMS, 79, 61
Wang, T. J., Ofman, L., & Davila, J. M. 2009a, ApJ, 696, 1448
Wang, T. J., Ofman, L., Davila, J. M., & Mariska, J. T. 2009b, A&A, 503, L25
Yuan, D., Shen, Y., Liu, Y., et al. 2013, A&A, 554, A144

A&A 581, A131 (2015)
DOI: 10.1051/0004-6361/201424234

Astronomy & Astrophysics

Spectroscopic observations and modelling of impulsive Alfvén waves along a polar coronal jet

P. Jelínek[1], A. K. Srivastava[2], K. Murawski[3], P. Kayshap[4], and B. N. Dwivedi[2]

[1] University of South Bohemia, Faculty of Science, Institute of Physics and Biophysics, Branišovská 10, 370 05 České Budějovice, Czech Republic
e-mail: `pjelinek@prf.jcu.cz`
[2] Department of Physics, Indian Institute of Technology (Banaras Hindu University), 221005 Varanasi, India
[3] Group of Astrophysics, UMCS, ul. Radziszewskiego 10, 20-031 Lublin, Poland
[4] Inter University Centre for Astronomy and Astrophysics, Ganeshkhind, 411007 Pune, India

Received 19 May 2014 / Accepted 12 July 2015

ABSTRACT

Context. The magnetic reconnection in the solar corona results in impulsively generated Alfvén waves, which drive a polar jet.

Aims. Using the Hinode/EIS 2″ spectroscopic observations, we study the intensity, velocity, and full width at half maximum (FWHM) variations of the strongest Fe XII 195.12 Å line along the jet to find the signature of Alfvén waves. We numerically simulate the impulsively generated Alfvén waves within the vertical Harris current sheet, forming the jet plasma flows, and mimicking their observational signatures.

Methods. Using the FLASH code and an atmospheric model with an embedded, weakly expanding magnetic field configuration within a vertical Harris current sheet, we solve the 2.5-dimensional (2.5D) ideal magnetohydrodynamic (MHD) equations to study the evolution of Alfvén waves and vertical flows forming the plasma jet.

Results. At a height of ~5 Mm from the base of the jet, the red-shifted velocity component of Fe XII 195.12 Å line attains its maximum (5 $\mathrm{km\,s^{-1}}$), which converts into a blue-shifted velocity component between the altitude of 5−10 Mm. The spectral intensity continuously increases up to 10 Mm, while the FWHM still exhibits low values with an almost constant trend. This indicates that the reconnection point within the jet's magnetic field topology lies in the corona 5−10 Mm from its footpoint anchored in the Sun's surface. Beyond this height, the FWHM shows a growing trend. This may be the signature of Alfvén waves that impulsively evolve, due to reconnection, and propagate along the jet. From our numerical data, we evaluate space- and time- averaged Alfvén waves velocity amplitudes at different heights in the jet's current sheet, which contribute to the non-thermal motions and spectral line broadening. The synthetic width of Fe XII 195.12 Å line exhibits a similar trend of increment as in the observational data, possibly proving the existence of Alfvén waves, impulsively generated by reconnection, that propagate along the jet.

Conclusions. The numerical simulations show that the impulsive perturbations in the transversal component of velocity at the reconnection point can excite the Alfvén waves. These waves can power the plasma jet higher into the polar coronal hole, as vertical plasma flows are also associated with these waves due to pondermotive force. The simulated Alfvén waves match well with the observed non-thermal broadening along the jet, which may provide direct spectroscopic evidence of the impulsively excited Alfvén waves within the polar jet.

Key words. magnetohydrodynamics (MHD) – Sun: atmosphere – Sun: corona – waves – methods: numerical

1. Introduction

Polar coronal jets are well-observed, large-scale, and confined plasma transients in the solar atmosphere (see Nisticò et al. 2009; Nisticò & Zimbardo 2012). They can significantly contribute to the energy transport and the formation of nascent supersonic wind. The exact driving mechanisms of these kinds of jets are still debated. Broadly speaking, the two candidates, namely magnetic reconnection and magnetohydrodynamic (MHD) waves, are known to trigger these jets (e.g. Shibata 1982; Yokoyama & Shibata 1995; Cirtain et al. 2007; Nishizuka et al. 2008; Filippov et al. 2009; Pariat et al. 2009, 2015; Srivastava & Murawski 2011; Kayshap et al. 2013a,b, and references cited therein). The observations of Alfvén waves associated with the polar coronal jets are either related to the imaging observations of photospherically driven waves propagating along the jet (Cirtain et al. 2007) or some transversal perturbations evolved during the reconnection at the base of the jet (Nishizuka et al. 2008). These Alfvén waves are also ubiquitous in the localized magnetic structures (e.g. spicules, prominences, small-scale chromospheric flux tubes) as well as in the large-scale corona (e.g. De Pontieu et al. 2007; Okamoto et al. 2007; Tomczyk et al. 2007; Jess et al. 2009; Mathioudakis et al. 2013, and references cited therein).

Detection of Alfvén wave in solar magnetic structures is not yet well established, as these waves are incompressible. In the polar coronal plasma, these waves are observed in the form of spectral line profile variations (Banerjee et al. 1998; Harrison et al. 2002). Narrowing of the spectral line-width is attributed to the dissipation of small-amplitude Alfvén waves (Harrison et al. 2002; O'Shea et al. 2005; Bempord & Abbo 2012; Dwivedi et al. 2014, and references cited therein). The growth and dissipation of Alfvén waves have been modelled in the corona, which also explain the observed line-width variations (e.g. Pekenulu et al. 2002; Dwivedi & Srivastava 2006; Chmielewski et al. 2013, 2014). In particular, Chmielewski et al. (2013) reported that the observed line broadening, particularly in the polar corona, can be explained in terms of impulsively generated non-linear Alfvén waves. Non-linear Alfvén waves may be the likely candidates for transporting energy in the solar corona (Murawski et al. 2015a). These waves can also power the large-scale, as well as confined plasma transients, e.g. solar jets, nascent wind, and plasma flows (Murawski et al. 2015b).

It has been reported that the Alfvén waves power various jets (e.g. X-ray jets, spicules) and exist in a variety of coronal magnetic structures, however, they are identified as kink waves (Van Doorsselaere et al. 2008a,b). The existence of mixed radial and azimuthal waves are also reported in theory and observations (Goossens et al. 2009, 2012; Tian et al. 2012; Srivastava & Goossens 2013, and references cited therein). Numerical simulations support the general interpretation of the observed oscillations as a coupling of the kink and Alfvén waves (see e.g. Pascoe et al. 2010, 2011). Kamio et al. (2010) reported the spectroscopic observations of a rotating coronal jet and interpreted it as an evolution of kink waves and instability. The solar jets are found to be driven by various physical processes, e.g. the direct magnetic reconnection generated Lorentz force (Nishizuka et al. 2008), the reconnection generated pulse (Srivastava & Murawski 2011), the emergence and internal reconnection in small-scale kinked fluxtubes (Kayshap et al. 2013a,b), etc. However, the pure Alfvén waves driven coronal jets are difficult to detect because of observational constraints and the dynamic nature of the jet's typical magnetic field and plasma configuration.

In the present paper, we study the Hinode/EIS spectroscopic observations of a polar jet. We find the spectroscopic signatures of impulsively generated Alfvén waves and associated plasma flows within the jet. We model the observed physical processes (waves and flows) in the jet as a natural consequence of reconnection generated velocity pulse in the vertical and gravitationally stratified Harris current sheet lying in the appropriate model atmosphere with VAL-III C temperature (Vernazza et al. 1981). The structure of the present paper is as follows. In Sect. 2, we present the observational results. Section 3 describes numerical model, governing equations, initial conditions, perturbations, and numerical solutions. In Sect. 4, the numerical results are shown. The discussion and conclusions are outlined in the last section.

2. Hinode/EIS observations of a polar coronal jet

2.1. Spectroscopic data and observational analyses

A polar jet is observed using 2″ slit scan by EUV Imaging Spectrometer (Culhane et al. 2006) onboard Hinode on 22 April, 2009. It is an established fact that the 40″ and 266″ slots observe the temporal image data, while 1″ and 2″ slits are appropriate for the spectroscopic observations of the solar corona and transition region (TR). The EIS observes high-resolution spectra in two wavelength intervals, i.e. 170–211 and 246–292 Å, using its short-wavelength (SW) and long-wavelength (LW) CCDs, respectively. The observed data contain spectral line profiles of Fe XIII 202.04 Å, Fe XI 188.23 Å, Fe XV 284.16 Å, Fe XII 195.12 Å, Fe X 184.54 Å, Si VII 275.35 Å, O V 192.9 Å and He II 256.32 Å. The scanning started at 05:31:43 UT and ended at 06:33:29 UT. The exposure time on each scanning step was 31 s. The polar jet and related plasma column, which were moving off the limb, are scanned fully in a single spatio-temporal step at 06:29 UT because they went straight into the corona. This provides us with an opportunity to understand the wave activity along the jet, which already reached up to a certain height in the polar corona. The 2″ slit started scanning steps over the polar coronal hole with (Xcen, Ycen) ~ (30″, 939″). The observation window on the CCDs is 400 pixels high along the slit with a width of 40 pixels in the horizontal direction. The Y-direction covers the solar atmosphere from 740″ to 1139″ (400 pixels with 1″/pxiel). The direction of dispersion has the spectral resolution of 0.02.

We apply standard EIS data reduction procedures and calibration files to the data acquired at the EUV-telescope, which is the raw (zeroth-level) data. The subroutines can be found in the sswidl software tree[1]. These standard subroutines correct for dark-current subtraction, cosmic-ray removal, flat-field correction, hot pixels, warm pixels, and bad or missing pixels. The data are saved in the level-1 data file, while associated errors are saved in the error file. We choose the strong line Fe XII 195.12 Å to examine the spatial variations of the intensity, Doppler velocity, and full width at half maximum along the jet from its base get the clues of transversal waves. We co-align the Fe XII 195.12 Å map w.r.t. the long-wavelength CCD observations of He II 256.32 Å by considering it as a reference image and by estimating the offset. The orbital and slit-tilt are also corrected for data using the standard method described in the EIS software notes. We perform the double Gaussian fitting for the removal of the weak blend of Fe XII 195.18 Å line that affects the line profile of Fe XII 195.12 Å. The fitting function is a Gaussian for the line profile (see gauss_.pro in SolarSoft), and a straight line for background continuum (see line_.pro in SolarSoft). The fitting of the observed spectral line profile gives peak intensity, centroid (measure of flows), and Gaussian width (measure of thermal and non-thermal motions). We apply the procedure described by Young et al. (2009) in this context, which is also available in the EIS Software Note 17. We constrain Fe XII 195.18 Åline to have the same width as the Fe XII 195.12 Å line. We search for the blend line Fe XII 195.18 Å within the range of +0.06 Å w.r.t. the centroid of the main line Fe XII 195.12 Å. We assume and require that the contribution of the blended line is searched within maximum 28% limit compared to the peak intensity of the main Fe XII 195.12 Å line. We perform the fitting over binned data of 2 pixel × 6 pixel to increase the signal-to-noise ratio and to obtain the reasonable fitting and estimated parameters (cf. Figs. 1 and 2). The example of the Fe XII 195.12 Å fitted spectra at 14 points along the chosen slit along jet are shown in Fig. 2. These fitted profiles of Fe XII 195.12 Å are free from any contribution of the weak blend of Fe XII 195.18 Å. The 14 spatial points along the jet correspond to various heights for which the spectral parameters are derived (Fig. 3).

The wavelength calibration and estimation of the reference wavelength of Fe XII 195.12 Å line is performed using the limb method (Peter & Judge 1999). The box is chosen at the north pole limb from where the integrated spectra is derived (cf. Fig. 1, intensity map). It is likely that in and outwards motions near the limb almost cancel each other out. Therefore, the centroid of the line profile represents the rest wavelength of particular emission line. The Gaussian fitting gives the estimate of the reference wavelength as 195.128 Å. This reference wavelength is used in deriving the Doppler velocities in the region of our interest (cf. Figs. 1 and 3).

---

[1] http://www.darts.isas.jaxa.jp/pub/solar/ssw/hinode/eis/

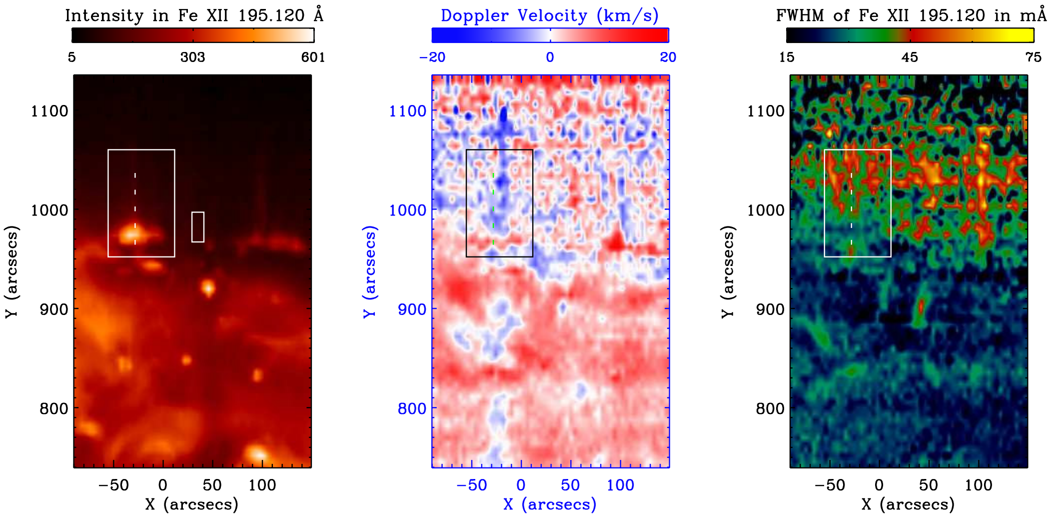

Fig. 1. Intensity, Doppler velocity, and FWHM maps of Fe XII 195.12 Å line, showing the polar jet moving off the limb outwards. The white line is the position of the slit along the jet upon which the spectral parameters are estimated. The footpoint of the jet where the slit's lowest part lies, has the coordinates of (−28″, 964″). The white rectangular box is chosen at the limb of the north polar corona from where the integrated line profile of Fe XII 195.12 Å is derived and fitted to obtain its rest wavelength.

2.2. Observational results

Figure 1 displays the intensity (left), Doppler-velocity (middle), FWHM (right) maps of the polar coronal hole where the straight coronal jet has already moved off the limb. The maps are related with spectral measurements over 2 pixel × 6 pixel binned data with good signal-to-noise ratio. The jet is visible in the left-most part of the intensity map, and it has a typical inverted Y-shape structure (cf. within the box in the intensity map). At the same place, in the Doppler velocity map we see the red-shifted base of the jet while the plasma moves outwards (blue shift) in the higher plasma column of the jet (cf. within the box in the Doppler velocity map). The blue shift and red shift measured in the off-limb jet correspond to the line-of-sight component of velocity variations. It seems that the jet is slightly tilted towards us. Therefore, at a certain height, the jet plasma that is outflowing towards us provides a blue shift signature, while the downflowing plasma towards the Sun within the jet gives the red shift. In the FWHM map, we find the increased contribution of the line width in the jet plasma column (cf. within the box in the line-width map). Also, the jet is not visible in Si VII 275.35 line (Log $T_f \approx 5.0$), thereby confirming that it is not formed by cool transition region plasma. The jet is also not evident at higher temperatures. It is found that mostly its plasma is maintained at the inner coronal temperature of 1.0 MK. Therefore, the jet is best observed in Fe XII 195.12 Å line. We do not conjecture that it is made up of a single temperature plasma. In the given observational baseline, its plasma temperature can on average be around the formation temperature of Fe XII line, i.e. Log $T_f \approx 6.1$.

We choose a straight slit from the base of the jet in the outwards direction along the jet plasma column (cf. Fig. 1). We measure the variation of intensity (left panel), Doppler velocity (middle panel), and FWHM (right panel) of Fe XII 195.12 Å line along this chosen path (cf. Fig. 3). The first position at the bottom of the slit is the base of the jet, which is referenced as "zero Mm". The rest of the slit represents the progressive height along the jet scaled in Mm. The total height of the slit along the jet is 56 Mm (cf. Fig. 3). We consider the estimations of these spectral parameters along the jet up to only those heights (≈55 Mm) where spectral fitting is reasonable with fewer fitting errors (cf. Fig. 2). It is clear from these panels that intensity is continuously enhanced up to 10 Mm, and decreases thereafter Doppler velocity changes from its maximum value of red shift about +5 km s^{-1} from the base of the jet to the blue shift (outflows) at a height between 5−10 Mm. We find the variation of FWHM along the same path. It is almost constant without much variation up to 10–15 Mm (cf. Fig. 3, right panel). Above this height, the FWHM increases from 30 mÅ to 55 Å with a significant positive gradient (cf. red-fitted line in the right panel of Fig. 3). The red line shows second order polynomial fit on the FWHM data.

2.3. Physical interpretations of the observational results

The small-scale and low-lying bright-point loops form the wide base of the jet. They reconnect with pre-existing open field lines and propel the jets' plasma. This scenario is in accordance with the model given by Yokoyama & Shibata (1995) about the coronal jet formation. The red shift is maximum (+5 km s^{-1}) at 5 Mm height, which means the plasma is downflowing at this location. Above this height between 5−10 Mm, this red shift is transformed into blue shift. This vertical region acts as a reconnection region where plasma flows in both directions: the downflows in small-scale loops forming the base of the jet and upflows along open field lines of the jet forming its plasma motion higher into the corona. The region where downflows (red shift) convert into outflows (blue shift) and intensity (thus density) tends towards its maximization indicates that reconnection already drove the energy release below this location near the base of the jet. The reconnection propels the plasma outwards along the open field lines of the jet. The maximum observed blue shift is 7.5 km s^{-1} along the jet, however, the jet is projected

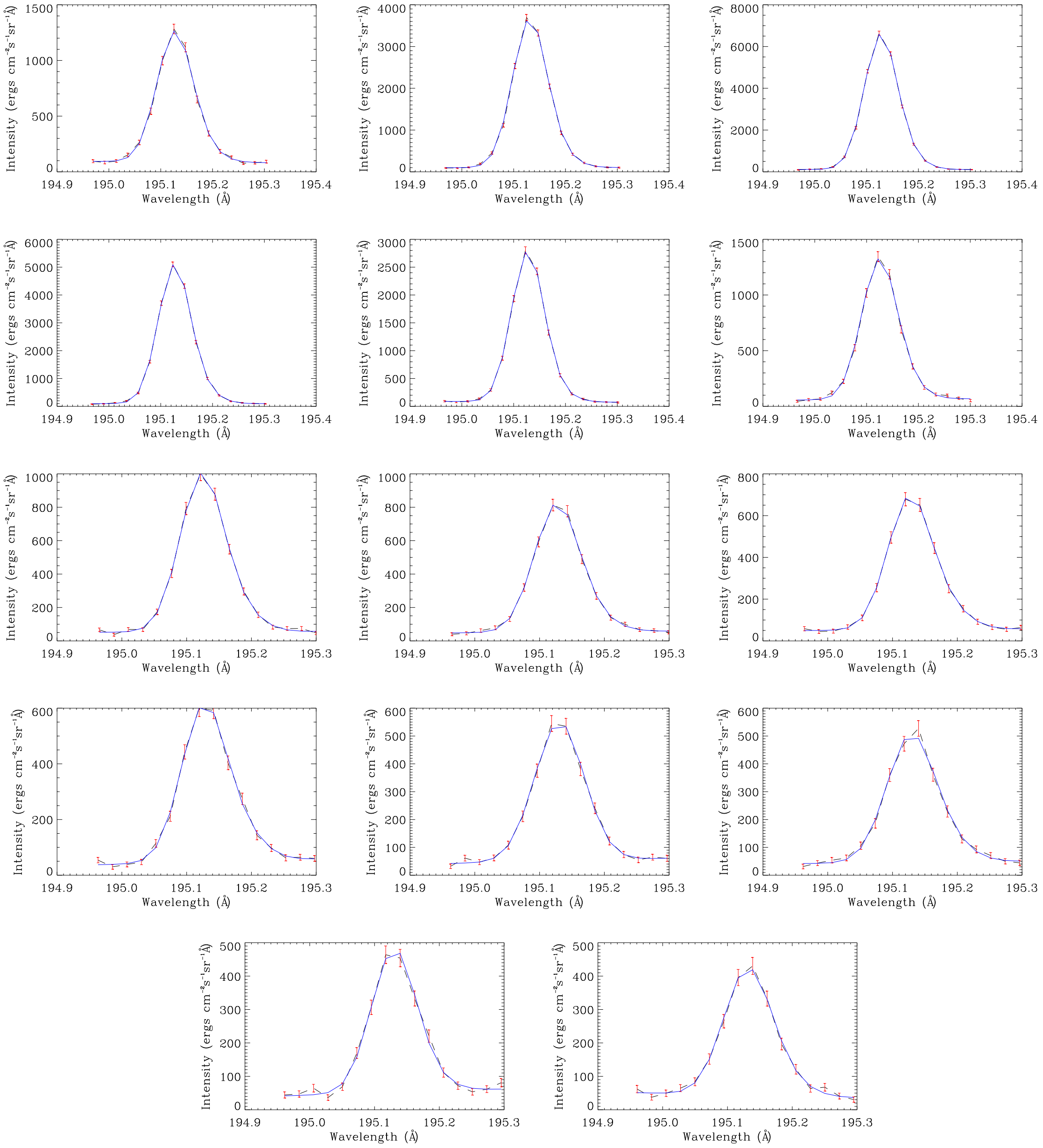

Fig. 2. Gaussian fit to the spectra derived on the chosen path along the jet. The white slit on the jet (cf. Fig. 1) is divided into 14 super pixels, each of the size of 2 × 6 pixel square. The line profile is derived from each super pixel (dotted blue), and the corresponding estimation of plasma parameters are made by fitting the double Gaussian (solid blue).

off the limb at the north pole. The plasma motions along the jet may have minimum contribution to the line-of-sight (LOS) Doppler shift. Therefore, the estimated Doppler velocity should be considered an apparent lower-bound velocity, which is not the actual speed of the jet. This simply provides the signature of the outflowing plasma along the jet. The FWHM also shows the increasing trend beyond 10−15 Mm height. The FWHM value exactly at the base of the jet at the north polar limb is somewhat higher, i.e. 40 mÅ. We can discard it because of the limb effects. The contribution of stray light from continuum near the limb

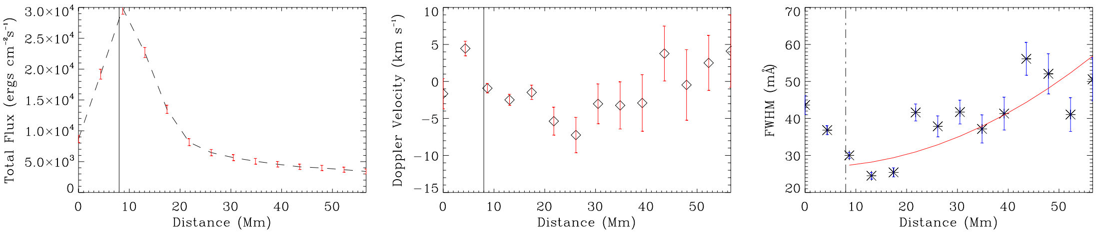

Fig. 3. Variation of intensity, Doppler velocity, and FWHM of Fe XII 195.12 Å line along the path chosen on the polar jet from its base outwards. The red line shows second order polynomial fit to the FWHM data.

may affect the line profile and its width. The second point of estimated FWHM lies even higher around 36 mÅ at 5 Mm where the highest red shift (downflow) is observed. At 5.0 Mm height, the energy release is likely to be present as downflow is maximum at this location. The energy release may cause the line-width broadening of the spectral line (Somov 1994). Therefore, the spatial points that lie in the lower segment of the jet closer to the energy release site in the spatial range 5−15 Mm from Jet's footpoint, possess comparatively higher values of FWHM. As we move away from the energy release site at higher heights, the jet's temperature is uniform near the formation temperature of optically thin Fe XII 195.12 Å line. Therefore, the contribution to the FWHM increment may be mainly due to the increment in non-thermal motions.

The reconnection generates the outflowing plasma along jet's open magnetic field lines, as well as the downflowing plasma along the small-scale loops forming its base. This region (0−15 Mm), therefore, may be the most likely place in the lower segment of the jet around which the reconnection and related physical processes occurred. Beyond this region, the FWHM of the observed spectral line increases significantly because of non-thermal motions, as evident in the observational baseline. This FWHM broadening may be associated with the evolution and growth of the non-linear and impulsively generated Alfvén waves propagating along the open field lines of the jet away from the reconnection site higher into the corona. In theory as well as observations, Alfvén waves are found to be excited in the large-scale polar coronal holes (Banerjee et al. 1998; Chmielewski et al. 2013).

The FWHM also shows varying trends in and around the observed jet, however, these trends are not so systematic and closely correlated with intensity and Doppler velocity variations with height as we observed within the jet. We do not present these plots. However, we have examined the region outside the jet's plasma column and its inverted Y-shape base in its western side. The intensity decreases rapidly as we move outside the limb, which is an obvious trend. However, there is no trend in the Doppler velocity. Doppler velocity only shows weak downflows. The FWHM also does not show any trend in its variation with height. In conclusion, present observations demonstrate the signature of impulsive Alfvén waves along the jet above the energy release site near its footpoint. In the next section, we describe our model of impulsive Alfvén waves in the 2D vertical current sheet to match with some observed properties of these wave modes.

3. Numerical model of impulsive Alfvén waves in 2D vertical Harris current sheet

Keeping in mind the impulsive generation of Alfvén waves due to energy release within the observed jet, we model the propagation of a transverse pulse in a 2D vertical Harris current sheet. Above the reconnection point, perturbations may evolve in the form of Alfvén waves propagating at various higher heights as well as the driven coupled plasma flows. We consider the height of 5 Mm in our model to launch the reconnection generated velocity pulse in a 2D vertical current sheet.

3.1. Governing equations

In our numerical model of a Harris current sheet, embedded in a gravitationally stratified solar atmosphere, the plasma dynamics is described by the following 2.5-dimensional (2.5D) time-dependent ideal MHD equations (cf. Priest 1982; Chung 2002):

$$\frac{\mathrm{D}\varrho}{\mathrm{D}t} = -\varrho\nabla\cdot\boldsymbol{v}, \tag{1}$$

$$\varrho\frac{\mathrm{D}\boldsymbol{v}}{\mathrm{D}t} = -\nabla p + \boldsymbol{j}\times\boldsymbol{B} + \varrho\boldsymbol{g}, \tag{2}$$

$$\frac{\mathrm{D}\boldsymbol{B}}{\mathrm{D}t} = (\boldsymbol{B}\cdot\nabla)\boldsymbol{v}, \tag{3}$$

$$\frac{\mathrm{D}e}{\mathrm{D}t} = -\gamma e\nabla\cdot\boldsymbol{v}, \tag{4}$$

$$\nabla\cdot\boldsymbol{B} = 0. \tag{5}$$

Here $\mathrm{D}/\mathrm{D}t \equiv \partial/\partial t + \boldsymbol{v}\cdot\nabla$ is the total time derivative, ϱ is the mass density, $\boldsymbol{v}$ is the flow velocity, $\boldsymbol{B}$ is the magnetic field, and $\boldsymbol{g} = [0, -g_\odot, 0]$ is the gravitational acceleration, which is oriented in the negative y-direction, with $g_\odot = 274\ \mathrm{m\,s^{-2}}$. Our model does not include the radiative and thermal conductive losses. This model may not fully describe the reconnection generated heating and related additional plasma evolution within the jet as we do not invoke the non-classical thermodynamical terms (e.g. radiative and thermal losses) in the governing energy equation. We only aim to understand the non-linear wave dynamics and associated vertical flows along the jet.

The current density $\boldsymbol{j}$ in Eq. (2) is expressed as

$$\boldsymbol{j} = \frac{1}{\mu_0}(\nabla\times\boldsymbol{B}), \tag{6}$$

where $\mu_0 = 1.26\times10^{-6}\ \mathrm{H\,m^{-1}}$ is the magnetic permeability of free space.

The internal energy density, e, in Eq. (4) is given by

$$e = \frac{p}{\gamma-1}, \tag{7}$$

with the adiabatic coefficient, which we set and hold fixed as $\gamma = 5/3$.

3.2. Gravitationally stratified Harris current sheet

For a static ($\boldsymbol{v} = \boldsymbol{0}$) equilibrium, the Lorentz and gravity forces must be balanced by the pressure gradient in the entire physical domain

$$-\nabla p + \boldsymbol{j} \times \boldsymbol{B} + \varrho \boldsymbol{g} = \boldsymbol{0}. \tag{8}$$

The solenoidal condition, $\nabla \cdot \boldsymbol{B} = 0$, is identically satisfied by the magnetic flux function, $\boldsymbol{A}$,

$$\boldsymbol{B} = \nabla \times \boldsymbol{A}. \tag{9}$$

For calculating the magnetic field in the vertically oriented Harris current sheet, we use the magnetic flux function $\boldsymbol{A} = [0, 0, A_z]$ as (Galsgaard & Roussev 2002; Jelínek et al. 2012)

$$A_z = -B_0 w_{\mathrm{cs}} \ln\left\{\left|\cosh\left(\frac{x}{w_{\mathrm{cs}}}\right)\right|\right\} \exp\left(-\frac{y}{\lambda}\right) \cdot \tag{10}$$

Here the coefficient λ denotes the magnetic scale height. The symbol B_0 is used for the external magnetic field and w_{cs} is the half-width of the current sheet. We set and hold fixed $w_{\mathrm{cs}} = 1.0$ Mm. Substituting Eq. (10) into Eq. (9) we obtain the equations for the magnetic field in the x–y plane as (Galsgaard & Roussev 2002; Jelínek et al. 2012)

$$B_x(x, y) = B_0 \frac{w_{\mathrm{cs}}}{\lambda} \ln\left[\cosh\left(\frac{x}{w_{\mathrm{cs}}}\right)\right] \exp\left(-\frac{y}{\lambda}\right), \tag{11}$$

$$B_y(x, y) = B_0 \tanh\left(\frac{x}{w_{\mathrm{cs}}}\right) \exp\left(-\frac{y}{\lambda}\right) \cdot \tag{12}$$

Equation (8), while written in terms of its components, attains the following form:

$$\frac{\partial p(x, y)}{\partial x} + j_z B_y(x, y) = 0, \tag{13}$$

$$\frac{\partial p(x, y)}{\partial y} - j_z B_x(x, y) + \varrho g(x, y) = 0. \tag{14}$$

Here j_z is the only non-zero component of the electric current density $\boldsymbol{j}$, see Eq. (6), given by $j_z = \frac{1}{\mu_0}(\nabla \times \boldsymbol{B})_z$. The condition of integrability of the above equations leads to

$$\mu_0 g \frac{\partial \varrho(x, y)}{\partial x} = \nabla \cdot (\mu_0 j_z \boldsymbol{B}), \tag{15}$$

from which we can derive the formulae for the distribution of the mass density (cf. Galsgaard & Roussev 2002; Jelínek et al. 2012)

$$\varrho(x, y) = \left\{\frac{B_0^2}{\mu_0 g \lambda}\left\{1 + \ln\left[\cosh\left(\frac{x}{w_{\mathrm{cs}}}\right)\right]\right\} \mathrm{sech}^2\left(\frac{x}{w_{\mathrm{cs}}}\right)\right.$$
$$\left. + \varrho_0\right\} \cdot \exp\left(-2\frac{y}{\lambda}\right), \tag{16}$$

and the gas pressure,

$$p(x, y) = \left\{\frac{B_0^2}{2\mu_0} \mathrm{sech}^2\left(\frac{x}{w_{\mathrm{cs}}}\right) + \frac{B_0^2 w_{\mathrm{cs}}^2}{2\mu_0 \lambda^2} \ln^2\left[\cosh\left(\frac{x}{w_{\mathrm{cs}}}\right)\right]\right.$$
$$\left. + \frac{\varrho_0 g \lambda}{2}\right\} \cdot \exp\left(-2\frac{y}{\lambda}\right) + p_0. \tag{17}$$

Here ϱ_0 and p_0 are integration constants. The corresponding plasma temperature is assumed to be $T = 1.25 \times 10^6$ K.

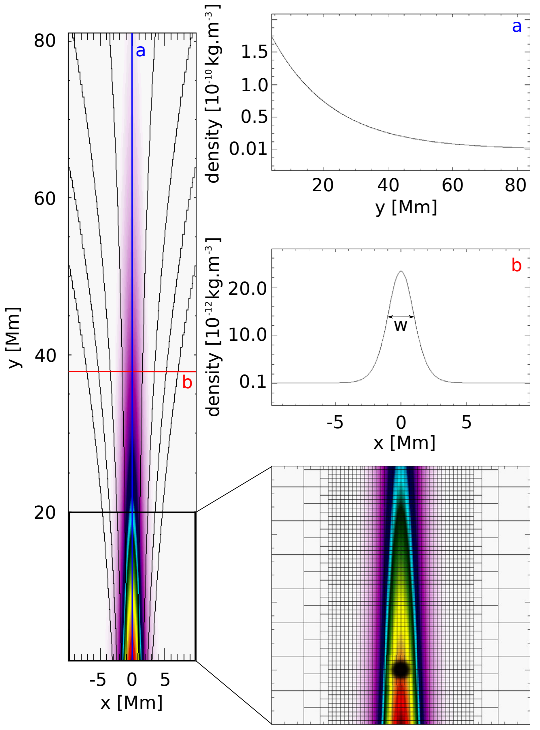

Fig. 4. Mass density distribution in the Harris current sheet, where the black contours represent the structure of magnetic field. On the right-hand side of the figure both **a)** vertical (for $x = 0$ Mm) and **b)** horizontal (for $y = 37.65$ Mm, which is magnetic scale height) slices in mass density are shown, as well as the details of the part of the simulation region illustrating the computational grid, with adaptive mesh refinement (AMR). At the altitude $y = 5$ Mm the perturbation point, L_{P}, is marked by full black circle.

3.3. Initial perturbation

At the start of the numerical simulation ($t = 0$ s), the equilibrium is perturbed by the Gaussian pulse in the z-component of velocity and has the following form (e.g. Nakariakov et al. 2004, 2005):

$$V_z(x, y, t = 0) = -A_0 \cdot \frac{x}{\lambda} \cdot \exp\left[-\frac{x^2 + (y - L_{\mathrm{P}})^2}{\lambda^2}\right], \tag{18}$$

where A_0 is the amplitude of the initial pulse and $\lambda = 4$ Mm is its width. This pulse preferentially triggers Alfvén waves. The perturbation point, L_{P}, is located on the axis of the Harris current sheet, at a distance of 5 Mm from the bottom boundary of the simulation region (see full black circle in Fig. 4). We set the detection points, L_{D}, on the current-sheet axis, at the distance between the perturbation and detection points $\Delta \equiv |L_{\mathrm{D}} - L_{\mathrm{P}}| = 10, 15, 20, 25, 30, 35, 40, 45, 50,$ and 55 Mm.

In the 2.5D model, the Alfvén waves decouple from magnetoacoustic waves. They can be described solely by $V_z(x, y, t)$. As a result, the initial pulse of Eq. (18) triggers Alfvén waves, which are approximately described in the linear case by the wave equation

$$\frac{\partial^2 V_z(x, y, t)}{\partial t^2} = c_{\mathrm{A}}^2(x, y) \frac{\partial^2 V_z(x, y, t)}{\partial s^2}, \tag{19}$$

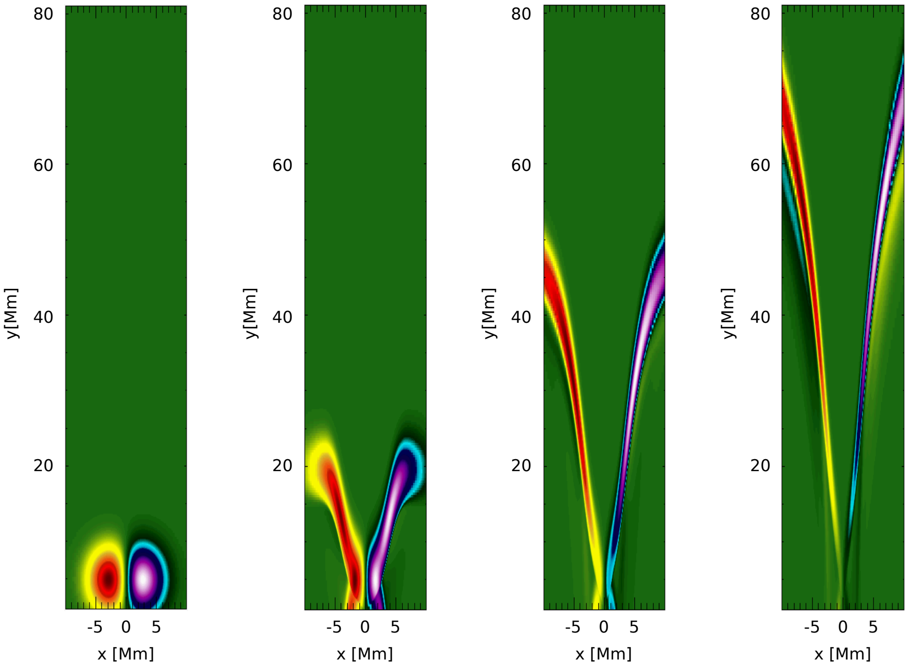

Fig. 5. Time evolution of velocity component V_z, corresponding to Alfvén waves, at $t = 0, 10, 30$, and 70 s *from left to right*.

where s is the coordinate along the magnetic line and the Alfvén speed, c_A, is defined as

$$c_A(x, y) = \sqrt{\frac{B_x^2(x, y) + B_y^2(x, y)}{\mu_0 \varrho(x, y)}}. \tag{20}$$

Here $\varrho(x, y)$ is given by Eq. (16).

3.4. Numerical solutions

We solve the 2.5D time-dependent, ideal MHD Eqs. (1)–(4) numerically, making use of the FLASH code (Fryxell et al. 2000; Lee & Deane 2009; Lee 2013). It is now well tested, fully modular, parallel, multiphysics, open science, simulation code that implements second- and third-order unsplit Godunov solvers with various slope limiters and Riemann solvers as well as adaptive mesh refinement (AMR; see e.g. Chung 2002). The Godunov solver combines the corner transport upwind method for multidimensional integration and the constrained transport algorithm for preserving the divergence-free constraint on the magnetic field (Lee & Deane 2009). We have used the minmod slope limiter and the Riemann solver (e.g. Murawski 2002; Toro 2006). The main advantage of using AMR technique is to refine a numerical grid at steep spatial profiles while keeping a grid coarse at the places where fine spatial resolution is not essential. In our case, the AMR strategy is based on controlling the numerical errors in a gradient of mass density that leads to reduction of the numerical diffusion within the entire simulation region.

For our numerical simulations, we use a 2D Eulerian box of its height $H = 80$ Mm and width $W = 20$ Mm. The spatial resolution of the numerical grid is determined with the AMR method. We use the AMR grid with the minimum (maximum) level of the refinement blocks set to 3 (7). The whole simulation region is covered by 12 884 blocks. Since every block consists 8×8 numerical cells, this number of blocks corresponds to 824 576 numerical cells.

A spatial grid size has to be less than the typical width of the current sheet along the x-direction and the typical wavelength of the Alfvén waves along the y-direction, respectively. We find $\min(\Delta x) = \min(\Delta y) = 0.04$ Mm, which satisfies the above-mentioned condition (semi-width of the current sheet is $w_{CS} = 1.0$ Mm and the estimated minimal wavelength is approximately 10.0 Mm). At all boundaries, we fix all plasma quantities to their equilibrium values using fixed-in-time boundary conditions, which lead only to negligibly small numerical reflections of incident wave signals.

4. Results

4.1. Numerical results

In a current sheet, a velocity perturbation is generated most likely due to reconnection at a height of 5 Mm (cf. Fig. 4), which evolves with height in the stratified solar atmosphere. The initial pulse excites the Alfvén waves. These waves, which are associated with the perturbations in V_z, propagate along the open magnetic field lines to higher altitudes (y-direction): see the time evolution of V_z at $t = 0, 10, 30$, and 70 s (Fig. 5). The initial pulse (left) spreads into upward and downward propagating waves, which are very well seen at $t = 10$ s (second left). Since these waves follow magnetic field lines, which are diverging with height, the left and right profiles of the Alfvén waves move apart with y (see the right most panel).

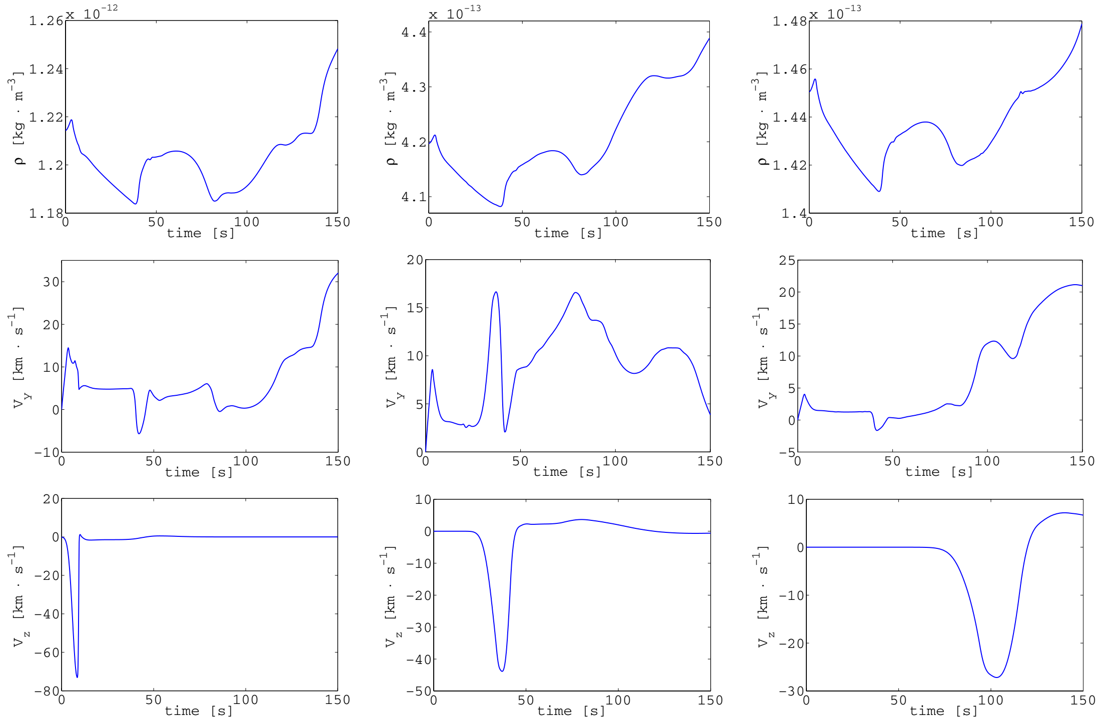

Fig. 6. *Top, middle, and bottom panels*: spatio-temporal averaged mass density ϱ, velocity components V_y , and V_z at three different heights 15, 35, and 55 Mm above the solar surface, respectively.

The associated magnetoacoustic waves produce the mass density perturbations at various heights and also create the vertical plasma dynamics. Some instantaneous mass density, V_y and V_z velocity variations at 15, 35, and 55 Mm heights along the current sheet above the solar surface are shown in Fig. 6. At each height, we have the temporal signatures of the perturbations of these parameters due to the evolution of waves.

4.2. Synthetic line-width increment due to Alfvén waves

In the numerical domain, we have the evolution of Alfvén waves in the Harris current sheet, which propagate along open magnetic field lines in its stratified atmosphere. These Alfvén waves are described by the perturbations in the transverse velocity component (V_z). They result in the magneto-plasma as unresolved non-thermal motions (Banerjee et al. 1998; Chmielewski et al. 2013). The non-thermal motions due to Alfvén waves leave their signature in the line profiles at each height in terms of their broadening. The increment in the line width, therefore, provide the signature of Alfvén wave amplification (Banerjee et al. 1998; O'Shea et al. 2005). As mentioned above, the broadening of line profiles due to Alfvén waves basically lead to the unresolved motions. This contribution to the spectrum, at any particular height in the solar atmosphere, can be due to various wave trains already passed through that detection point. However, these motions are not resolved by the spectrometer though inherent within the spectrum in terms of line broadening. Therefore, we average over the space (entire pulse width) and time (500 s) of various V_z signals to know the resultant contribution of the unresolved non-thermal motions. The detailed discussions can be found in Chmielewski et al. (2013). In this subsection, we describe the procedure that we adopt to convert the simulated velocity signals (V_z) into synthetic line width of Fe XII 195.12 Å. At any particular height in the model atmosphere, we average the wave velocity amplitude (V_z) over the entire pulse width between $t_\mathrm{a}-250$ and $t_\mathrm{a}+250$ s, where t_a is the arrival time of a wave signal to that particular height (Chmielewski et al. 2013). Therefore, the averaged transverse motions contribute to the non-thermal unresolved motions at a particular height in the model atmosphere as observed in the form of spectral line profile variation due to Alfvén waves. The averaged wave velocity amplitude is scaled in terms of non-thermal speed as $\xi^2 = 0.5\,V_z^2$ taking the polarization and the direction of the propagation of Alfvén waves with respect to the line-of-sight into consideration(Banerjee et al. 1998). It should be noted that this scaling can be applicable for longer exposures. Our spatio-temporal averaging of velocity signal satisfies this requirement. Using the following formula (Mariska 1992):

$$\sigma^2 = \left[4\ln 2\left(\frac{\lambda}{c}\right)^2\left(\frac{2k_\mathrm{B}T}{m_\mathrm{i}}+\xi^2\right)+\sigma_\mathrm{I}^2\right], \tag{21}$$

we estimate the synthetic line width (FWHM) of Fe XII (λ = 195.12 Å; $T_f = 1.2\times10^6$ K) as a function of height in the model current sheet where Alfvén waves are present. Here, σ_I is the instrumental width associated with the Hinode/EIS spectrometer slit. The observed line width is converted into FWHM and subtracted from the instrumental width. While we derive the synthetic line width of Fe XII 195.12 Å from the numerical data,

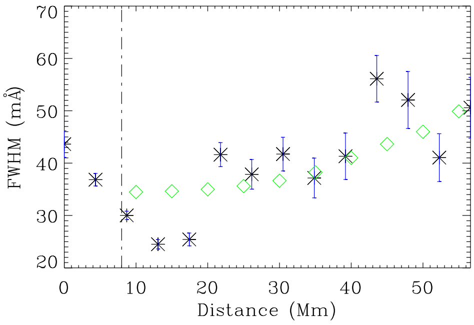

Fig. 7. Variation of synthetic line width with height (diamonds) of Fe XII 195.12 Å as derived by considering the contribution of propagating Alfvén waves in the Harris current sheet, and the observed line-width broadening along the polar jet (asterisks).

we ignore this factor as it only contains the physical information of thermal and non-thermal motions. It is clear from Fig. 7 (diamonds) that the synthetic line width resulting from the contribution of Alfvén waves grows with height, and its trend matches the variation of the observed line width (cf. Fig. 2, bottom panel; beyond 10 Mm).

We conclude that the Alfvén waves excited impulsively in our model atmosphere play a similar role like the transverse waves excited within the observed polar jet. Therefore, we precisely constrain the physical mechanisms, i.e. reconnection generated Alfvén waves, which also play a role in triggering the observed jet. The detailed comparison is given in the next subsection. The width of the formed line profile depends both on the thermal and non-thermal contributions in the emitted plasma. It is shown that the heating plays a crucial role in the formation of spectral lines and its equivalent width (e.g. Peter et al. 2006). In the present observational baseline, we have found that our less intense jet does not show much temperature variation along its extended part in the corona as observed by Hinode/EIS. It is only clearly visible in Fe XII 195.12 Å line, while it is not evident in cooler (Si VII 275.35 Å, $\log T_f = 5.0$ MK) as well as hot (Fe XV 284.16 Å, $\log T_f = 6.4$ MK) lines. This means that the heating episode quickly subsides after the reconnection generated origin of the jet. When it is scanned through Hinode/EIS 2″-slit, it has already reached its maximum height in the polar corona with the plasma maintained around inner coronal temperature of 1.0 MK. Therefore, the thermal width in the formed line profiles of Fe XII 195.12 Å (both observed and spectral) can be considered as a constant width equivalent to the formation temperature of Fe XII line, i.e. $T_f = 1.2 \times 10^6$ K. The non-thermal contribution and resultant line broadening, therefore, result from the Alfvén wave amplification along the jet in its stratified atmosphere.

4.3. Comparison with the observational data

The observed jet is triggered by the reconnection between low-lying bipolar loops at its base, and pre-existing open field lines of the polar corona. This forms the typical inverted Y-shape configuration of the jet, and a vertical Harris current sheet along the jet body. The X-type reconnection point can be created somewhere at coronal heights above the inverted Y-shape base of the jet. We model this vertical Harris current sheet as an upper part of the jet where waves and plasma perturbations occur. We assume that the magnetic reconnection generates a velocity pulse, which results in Alfvén waves propagation along the coronal jet.

In the observations, we find the reconnection point at a height 5−10 Mm from the base of the jet where maximum downflow speed is converted into blue shift at higher heights along the jet. Up to this height, the measured FWHM is almost constant. It grows significantly beyond this height, and maximizes up to 50 Mm height along the jet. As noted in Sect. 2, this provides the most likely signature of Alfvén wave growth along the jet body beyond the reconnection point.

In our model, the transverse velocity perturbations are generated due to the reconnection in the lower part of the Harris current sheet, which correspond to Alfvén waves. Although, we only include the reconnection generated velocity pulse in the vertical current sheet of the jet. We obtain the time signatures of Alfvén waves at each height, and convert them into the unresolved non-thermal velocity. Since mass density decreases with height along the open field lines, Alfvén waves are amplified, contributing more to the non-thermal motions at higher altitudes. This results in the line width growth with height of any observed line profile in the stratified solar atmosphere. The synthesized FWHM (line width) due to the contribution of Alfvén waves propagating in the current sheet along the jet body. The synthetic FWHM also shows a similar increasing trend up to $y = 55$ Mm (cf. Fig. 7). It is constant up to $y = 15$ Mm above the reconnection point. Beyond the reconnection point, the observed FWHM profile along the polar jet (Fig. 3, right panel) increases. This confirms that the Alfvén waves are impulsively excited within the typical jet morphology due to magnetic reconnection. Alfvén waves propagate along the jet's open magnetic field lines, and further leave their signatures in the form of the observed line width variation. Moreover, the excited slow magnetoaoustic waves perturb the plasma and result in the vertical flows along the magnetic field lines, which cause the jet plasma dynamics. In conclusion, our model supports the scenario of the evolution of non-linear Alfvén waves in the polar coronal jet, and the associated flows that may contribute to its plasma evolution. However, it should be noted that we do not consider the jet's plasma evolution due to heating or direct $\boldsymbol{j} \times \boldsymbol{B}$ force, which may also contribute initially in its formation.

5. Discussions and conclusion

Using the Hinode/EIS data, we observe that the magnetic reconnection takes place at the coronal height within a polar jet. Above and below the reconnection point, the plasma shows upflows (-7 km s^{-1}) and downflows ($+5$ km s^{-1}), respectively. This confirms the formation of a typical reconnection-generated coronal jet. We also find the line-width increment (Fe XII 195.12 Å) along the jet body beyond the reconnection point as a likely signature of the impulsively generated Alfvén waves. The observed line width increment with height matches with its theoretically estimated values, obtained by considering the contribution of Alfvén waves amplitude in the unresolved non-thermal motions of the plasma jet. The inference of this matching provides the physics of Alfvén waves, which are driven within the coronal jets. The reconnection within the vertical Harris current sheet along the jet's body trigger the longitudinal and transverse perturbation, which are associated with fast magnetoacoustic and Alfvén waves. The Alfvén waves leave their signatures collectively in the form of spectral line broadening with height, while the fast magnetoacoustic waves form the plasma flows in the jet. Linear and non-linear Alfvén waves can also be generated at the photosphere by granular motions. The region between the photosphere and the transition region acts as an Alfvénic resonator (e.g. Matsumoto & Shibata 2010). In the present case, we do not find any observational signature of Alfvén waves below 10 Mm within the jet. Therefore, we conjecture that the Alfvén waves are impulsively triggered above the reconnection site lying between 5−10 Mm above the footpoint of the jet. The photospheric Alfvén waves generated by granular motions have typical initial amplitude of a few km s^{-1}. When they propagate higher into the stratified atmosphere, they do amplify. However, in the present case, the Alfvén waves are triggered in situ at coronal height and possess the larger instantaneous amplitudes (>10 km s^{-1}). Therefore, we abbreviate them as impulsively generated nonlinear Alfvén waves propagating along the polar jet.

The underlying reconnection can drive Alfvén waves, which excite the vertical plasma flow. We did not aim to understand the temporal evolution of jet plasma and its heating as previously explored by various models (e.g. Moreno-Insertis et al. 2013). Instead, we aim to understand the signature of Alfvén wave dynamics and associated vertical flows along the jet. We find the clues of both in the form of line-width increment and Doppler velocity distribution (blue shift) along the jet at various heights. For this purpose, we select the Hinode/EIS scanning spectral observations to understand the spatial variation of emission (flux) and plasma properties (flows and width) along the jet. The jet was initially launched due to the reconnection, which may also liberate the heat. The heat flux may be subsided during the whole half-life time of the jet when it has already reached a maximum altitude in the polar corona. The impulsive launch of the jet might leave other physical processes for rest of the time in space along with the jet, i.e. Alfvén waves and associated vertical flows. We observed these two physical processes through EIS spectroscopic scan data, which also confirm the model. Our model is simple in the sense that it does not include the radiative or thermal conductive losses. As a result, this model may not fully describe the reconnection generated heating and related additional plasma evolution within the jet as we do not include the thermodynamical losses in the governing energy equation. In general, the non-consideration of these terms may not affect the properties of Alfvén waves that evolved along the jet. However, they do affect the mass density and temperature evolution of the jet plasma. In our case, the jet is visible in the inner coronal temperature of 1.0 MK, and it is not a very hot evolution of the jet. Moreover, weak EUV emissions also suggest that plasma is not well evolved along the jet spine and it is not a bulky jet as is the case for X-ray jets and surges. To understand and compare the properties of the triggered Alfvén waves, we consider the simplified ideal situation in our model by ignoring the losses. These thermodynamical losses will be considered in our future works in which we will examine their effects on the evolution of temperature and density within the jet.

There is only one report in the imaging X-ray observations from Hinode/XRT, which shows that the small amplitude Alfvén waves propagating from photosphere into the corona can drive the X-ray jets (Cirtain et al. 2007). These important detections are debated by Van Doorsselaere et al. (2008a,b). There are several attempts to model the polar jets in terms of the evolution of Alfvén waves (Kaghashvili 2009; Pariat et al. 2009, 2015; Hollweg & Kaghashvili 2012, and references cited therein). These models are purely analytical/numerical without any observational support. Nevertheless, they typically reveal the physics of the jet-forming regions as to how these waves can be excited within the typical magnetic field configurations of these jets. Nishizuka et al. (2008) proposed a model of the coronal jets by extending the model of Yokoyama & Shibata (1995) and found that direct reconnection generated forces can drive both the plasma jet and Alfvén waves at its base. Recently, Kayshap et al. (2013a,b) reported that the reconnection in the lower atmosphere can generate the pulse train and associated slow shocks to drive the surge plasma. Shibata et al. (2007) also suggested three types of the processes for the jet formation caused by the reconnection at different heights. Depending upon the height of magnetic reconnection in the pre-existing magnetic field configuration of the jet, the hot X-ray, EUV, and cool jets as well as H$_\alpha$ surges can be triggered in the coronal, transition region, and chromospheric reconnection, respectively. Therefore, reconnection can be an efficient mechanism to drive the waves/pulses within the confined magneto-plasma system (i.e. various jets), which can also play a role to power them. Alfvén waves are well studied both in theory and observations in driving the small-scale chromospheric jets (e.g. spicules; Kudoh & Shibata 1999; McIntosh et al. 2011).

In the present work, we have specifically made an effort to find the signatures of reconnction within a jet at a certain height from where the impulsively excited Alfvén waves and plasma motions are evident. We find a good match between the observed scenario and the given physical model of impulsive excitation of Alfvén waves within the vertical Harris current sheet. Our model has the appropriate temperature conditions as well as stratified atmosphere in 2.5D framework, along with a consideration of the transition region, which plays an important role in reflecting the Alfvén waves. The transition region has an important implication for contribution in non-thermal motions of the corona and in the formation of spectral lines provided they are excited below the transition region. In the present case, the site for impulsive energy release lies in the inner corona. Therefore, the excited Alfvén waves propagating in the outwards direction do not have any influence on the transition region. Moreover, the appropriate temperature conditions also set the stratification within the model atmosphere, which result in the appropriate growth of the Alfvén waves. Therefore, its contribution to the non-thermal motions and corresponding synthetic line broadening are adequately examined and studied. They also match the observed line width variation along the polar jet.

In conclusion, the numerical simulations show that the perturbations in the transversal component of velocity above the reconnection point within the current sheet (the upper part of the jet and its reconnection site) can impulsively excite Alfvén waves. This can also trigger the plasma jet higher in the polar coronal hole as vertical plasma flows associated with magnetoacoustic waves. The inferred contribution of simulated Alfvén waves and their synthetic line widths match the observed nonthermal line broadening along the jet. This provides a direct spectroscopic signature of the reconnection generated Alfvén waves within the polar jet in its typical magnetic field configuration (i.e. the Harris current sheet and its X-type reconnection site).

Acknowledgements. The authors thank the anonymous referee for constructive comments. A.K.S. thanks the visiting scientist travel grant from Prof. K. Murawski, UMCS, Lublin, Poland during September−October 2014 where this work was initiated, and he also acknowledges Shobhna for all her support. We acknowledge the use of Hinode/EIS observations in the present study. This work has granted an access to the HPC resources of CINES under the allocation 2012 D0 046331 & 2013 D0046331 made by GENCI (Grand Equipement National de Calcul Intensif). P.J. acknowledges support from the Grant P209/12/0103 of the Grant Agency of the Czech Republic. P.J. and K.M. also thank the Marie Curie FP7-PIRSES-GA-2011-295272 Radiophysics of the Sun project. The authors also express their thanks to Piotr Chmielewski for his help with numerical data processing. The FLASH code used in this work was in part developed by the

DOE-supported ASC/Alliances Center for Astrophysical Thermonuclear Flashes at the University of Chicago.

References

Banerjee, D., Teriaca, L., Doyle, J. G., & Wilhelm, K. 1998, A&A, 339, 208
Bemporad, A., & Abbo, L. 2012, ApJ, 751, 110
Chmielewski, P., Srivastava, A. K., Murawski, K., & Musielak, Z. E. 2013, MNRAS, 428, 40
Chmielewski, P., Srivastava, A. K., Murawski, K., & Musielak, Z. E. 2014, Acta Physica Polonica A, 125, 158
Chung, T. J. 2002, Computational Fluid Dynamics (Cambridge University Press)
Cirtain, J. W., Golub, L., Lundquist, L., et al. 2007, Science, 318, 1580
Culhane, J. L., Doschek, G. A., Watanabe, T., et al. 2006, Proc. SPIE, 6266, 62660
De Pontieu, B., McIntosh, S. W., Carlsson, M., et al. 2007, Science, 318, 1574
Dwivedi, B. N., & Srivastava, A. K. 2006, Sol. Phys., 237, 143
Dwivedi, B. N., Srivastava, A. K., & Mohan, A. 2014, PASJ, 66, S13
Filippov, B., Golub, L., & Koutchmy, S. 2009, Sol. Phys., 254, 259
Fryxell, B., Olson, K., Ricker, P., et al. 2000, ApJS, 131, 273
Galsgaard, K., & Roussev, I. 2002, A&A, 383, 685
Goossens, M., Terradas, J., Andries, J., Arregui, I., & Ballester, J. L. 2009, A&A, 503, 213
Goossens, M., Andries, J., Soler, R., et al. 2012, ApJ, 753, 111
Harrison, R. A., Hood, A. W., & Pike, C. D. 2002, A&A, 392, 319
Hollweg, J. V., & Kaghashvili, E. K. 2012, ApJ, 744, 114
Jess, D. B., Mathioudakis, M., Erdélyi, R., et al. 2009, Science, 323, 1582
Jelínek, P., Karlický, M., & Murawski, K. 2012, A&A, 546, A49
Kaghashvili, E. K., Quinn, R. A., & Hollweg, J. V. 2009, ApJ, 703, 1318
Kayshap, P., Srivastava, A. K., Murawski, K., & Tripathi, D. 2013a, ApJ, 770, L3
Kayshap, P., Srivastava, A. K., & Murawski, K. 2013b, ApJ, 763, 24
Kudoh, T., & Shibata, K. 1999, ApJ, 514, 493
Lee, D. 2013, J. Comput. Phys., 243, 269
Lee, D., & Deane, A. E. 2009, J. Comput. Phys., 228, 952
Mariska, J. T. 1992, Cambridge Astrophysics Series (New York: Cambridge University Press)
Mathioudakis, M., Jess, D. B., & Erdélyi, R. 2013, Space Sci. Rev., 175, 1
Matsumoto, T., & Shibata, K. 2010, ApJ, 710, 1857
McIntosh, S. W., de Pontieu, B., Carlsson, M., et al. 2011, Nature, 475, 477
Moreno-Insertis, F., & Galsgaard, K. 2013, ApJ, 771, 20
Murawski, K. 2002, Analytical and Numerical Methods for Wave Propagation in Fluid Media (Singapore: World Scientific)
Murawski, K., Solov'ev, A., Musielak, Z. E., Srivastava, A. K., & Kraśkiewicz, J. 2015a, A&A, 577, A126
Murawski, K., Srivastava, A. K., Musielak, Z. E., & Dwivedi, B. N. 2015b, ArXiv e-prints [`arXiv:1505.03793`]
Nakariakov, V. M., Arber, T. D., Ault, C. E., et al. 2004, MNRAS, 349, 705
Nakariakov, V. M., Pascoe, D. J., & Arber, T. D. 2005, Space Sci. Rev., 121, 115
Nishizuka, N., Shimizu, M., Nakamura, T., et al. 2008, ApJ, 683, L83
Nisticò, G., & Zimbardo, G. 2012, Adv. Sp. Res., 49, 408
Nisticò, G., Bothmer, V., Patsourakos, S., & Zimbardo, G. 2009, Sol. Phys., 259, 87
Okamoto, T. J., Tsuneta, S., Berger, T. E., et al. 2007, Science, 318, 1577
O'Shea, E., Banerjee, D., & Doyle, J. G. 2005, A&A, 436, L35
Pariat, E., Antiochos, S. K., & DeVore, C. R. 2009, ApJ, 691, 61
Pariat, E., Dalmasse, K., DeVore, C. R., Antiochos, S. K., & Karpen, J. T. 2015, A&A, 573, A130
Pascoe, D. J., Wright, A. N., & De Moortel, I. 2010, ApJ, 711, 990
Pascoe, D. J., Wright, A. N., & De Moortel, I. 2011, ApJ, 731, 73
Peter, H., & Judge, P. G. 1999, ApJ, 522, 1148
Peter, H., Gudiksen, B. V., & Nordlund, Å. 2006, ApJ, 638, 1086
Priest, E. R. 1982, Solar Magnetohydrodynamics (London, England: D. Reidel Publishing Company)
Shibata, K. 1982, Sol. Phys., 81, 9
Shibata, K., Nakamura, T., Matsumoto, T., et al. 2007, Science, 318, 1591
Somov, B. V. 1994, Space Sci. Rev., 70, 161
Srivastava, A. K., & Murawski, K. 2011, A&A, 534, A62
Srivastava, A. K., & Goossens, M. 2013, ApJ, 777, 17
Tomczyk, S., McIntosh, S. W., Keil, S. L., et al. 2007, Science, 317, 1192
Toro, E. F. 2006, Int. J. Num. Meth. Fluids, 52, 433
Van Doorsselaere, T., Brady, C. S., Verwichte, E., & Nakariakov, V. M. 2008a, A&A, 491, L9
Van Doorsselaere, T., Nakariakov, V. M., & Verwichte, E. 2008b, ApJ, 676, L73
Vernazza, J. E., Avrett, E. H., & Loeser, R. 1981, ApJ, 45, 635
Yokoyama, T., & Shibata, K. 1995, Nature, 375, 42
Young, P. R., Watanabe, T., Hara, H., & Mariska, J. T. 2009, A&A, 495, 587

The Astrophysical Journal, 812:105 (9pp), 2015 October 20 doi:10.1088/0004-637X/812/2/105

ELECTRIC CURRENT FILAMENTATION AT A NON-POTENTIAL MAGNETIC NULL-POINT DUE TO PRESSURE PERTURBATION

P. Jelínek[1], M. Karlický[2], and K. Murawski[3]

[1] University of South Bohemia, Faculty of Science, Institute of Physics and Biophysics, Branišovská 10, CZ-37005 České Budějovice, Czech Republic; pjelinek@prf.jcu.cz

[2] Academy of Sciences of the Czech Republic, v. v. i., Astronomical Institute, Fričova 258, CZ-25165 Ondřejov, Czech Republic

[3] Maria Curie-Skłodowska University, Institute of Physics, Group of Astrophysics, Radziszewskiego 10, PL-20031 Lublin, Poland

Received 2015 June 19; accepted 2015 September 11; published 2015 October 13

ABSTRACT

An increase of electric current densities due to filamentation is an important process in any flare. We show that the pressure perturbation, followed by an entropy wave, triggers such a filamentation in the non-potential magnetic null-point. In the two-dimensional (2D), non-potential magnetic null-point, we generate the entropy wave by a negative or positive pressure pulse that is launched initially. Then, we study its evolution under the influence of the gravity field. We solve the full set of 2D time dependent, ideal magnetohydrodynamic equations numerically, making use of the FLASH code. The negative pulse leads to an entropy wave with a plasma density greater than in the ambient atmosphere and thus this wave falls down in the solar atmosphere, attracted by the gravity force. In the case of the positive pressure pulse, the plasma becomes evacuated and the entropy wave propagates upward. However, in both cases, owing to the Rayleigh–Taylor instability, the electric current in a non-potential magnetic null-point is rapidly filamented and at some locations the electric current density is strongly enhanced in comparison to its initial value. Using numerical simulations, we find that entropy waves initiated either by positive or negative pulses result in an increase of electric current densities close to the magnetic null-point and thus the energy accumulated here can be released as nanoflares or even flares.

Key words: magnetohydrodynamics (MHD) – methods: numerical – Sun: corona – Sun: flares – waves

1. INTRODUCTION

Magnetohydrodynamic (MHD) waves are omnipresent in the solar atmosphere. Their study is one of the most rapidly developing branches of solar physics; see the recent review by De Moortel & Nakariakov (2012). The diversity of MHD waves is studied in various structures, e.g., in simple density slabs and Harris current-sheets (Jelínek & Karlický 2012; Jelínek et al. 2012; Mészárosová et al. 2014), and in magnetic funnels and open magnetic structures (Jelínek & Murawski 2013; Pascoe et al. 2013, 2014). Recent numerical results are summarized by Pascoe (2014) and are also confirmed by observations, e.g., by Nisticò et al. (2013, 2014).

Among these MHD waves is the so-called entropy wave, (Goedbloed & Poedts 2004). Similarly to slow and fast MHD waves, the entropy wave is the solution for the dispersion relation in MHD equations. In this wave, the plasma velocity, magnetic field, and gas pressure remain undisturbed. The only disturbed quantities are the plasma density, and, as a result of that, the temperature and entropy. In a still and gravity-free medium, this wave is non-propagating, i.e., the phase-velocity (or frequency) of this wave is zero with respect to the medium. In the case of non-ideal plasma, the entropy wave has an equivalent, which is called the thermal mode (Field 1965; De Moortel & Hood 2003; Macnamara & Roberts 2010). This wave has been considered in the problem of reconnecting current sheets; see Somov (2012) and references therein. However, this wave is generally believed to be rapidly damped (De Moortel & Hood 2003; Murawski et al. 2011) and usually neglected (Somov 2012). However, in the paper by Murawski et al. (2011) it was proposed that the entropy wave at magnetic null-points can consist of indirect observational evidence of nanoflares in the solar corona. In the present paper, we follow this idea, and instead of the potential magnetic null-point studied by Murawski et al. (2011), we consider the more general case of the non-potential magnetic null-point. In such a null-point, there is a free energy that can be released in the form of nanoflares or even flares. Similarly to the paper by Murawski et al. (2011) we assume that the entropy wave is generated by a sudden pressure pulse: (a) the negative pressure pulse that may result from the thermal instability or (b) the positive pressure pulse that mimics thermal energy release.

In this paper, we show that during an evolution of the entropy wave in the non-potential null-point the electric current is rapidly filamentated and at some locations the current densities are strongly enhanced. The filamentation of the electric current is an essential process in any flare as is shown by, e.g., Bárta et al. (2011) and Nickeler et al. (2013). At locations with the enhanced electric current densities, when their values become greater than the thresholds for some plasma instabilities (e.g., the ion-sound or Buneman instability), plasma waves can be generated and the anomalous resistivity is produced (Foullon et al. 2005; Nakariakov et al. 2006). These processes release the magnetic field energy through Ohmic dissipation.

This paper is structured as follows. In Section 2, we describe our numerical model with the initial equilibrium and perturbations implemented. The results of numerical simulations and their interpretation are summarized in Section 3. Finally, we complete the paper by concluding in Section 4.

2. MODEL

In this section, we describe physical and numerical models of the null-point and adopt them to study entropy waves that are triggered by pressure pulses that are launched at the null-point.

2.1. Governing Equations

Our numerical model describes the gravitationally stratified solar atmosphere, in which the plasma dynamics is described by the two-dimensional (2D), time-dependent, ideal MHD equations (see, e.g., Priest 1982; Chung 2002):

$$\frac{D\varrho}{Dt} = -\varrho\nabla\boldsymbol{v}, \tag{1}$$

$$\varrho\frac{D\boldsymbol{v}}{Dt} = -\nabla p + \boldsymbol{j}\times\boldsymbol{B} + \varrho\boldsymbol{g}, \tag{2}$$

$$\frac{D}{Dt}\left(\frac{\boldsymbol{B}}{\varrho}\right) = \left(\frac{\boldsymbol{B}}{\varrho}\cdot\nabla\right)\boldsymbol{v}, \tag{3}$$

$$\frac{D(\varrho U)}{Dt} = -\varrho U(\gamma - 1)\nabla\cdot\boldsymbol{v}, \tag{4}$$

$$\nabla\cdot\boldsymbol{B} = 0. \tag{5}$$

Here $D/Dt \equiv \partial/\partial t + \boldsymbol{v}\cdot\nabla$ is the material (or convective) time derivative, ϱ is a mass density, $\boldsymbol{v}$ flow velocity, $\boldsymbol{B}$ the magnetic field, $\boldsymbol{g} = [0, -g_\odot, 0]$ the gravitational acceleration with $g_\odot = 274\ \mathrm{m\ s^{-2}}$, and the adiabatic coefficient $\gamma = 5/3$. Current density $\boldsymbol{j}$ in Equation (2) is expressed as

$$\boldsymbol{j} = \frac{1}{\mu_0}\nabla\times\boldsymbol{B}, \tag{6}$$

where $\mu_0 = 1.26\times10^{-6}\ \mathrm{H\ m^{-1}}$ is the magnetic permeability of free space. The specific internal energy, U, in Equation (4) is given by

$$U = \frac{p}{(\gamma - 1)\varrho}. \tag{7}$$

Similarly to Murawski et al. (2011), we neglect the radiative losses and thermal conduction.

2.2. Initial Equilibrium

For a still ($\boldsymbol{v} = 0$) equilibrium, the Lorentz and gravity forces have to be balanced by the pressure gradient in the entire physical domain,

$$-\nabla p + \boldsymbol{j}\times\boldsymbol{B} + \varrho\boldsymbol{g} = \boldsymbol{0}. \tag{8}$$

Assuming a force-free magnetic field, $\boldsymbol{j}\times\boldsymbol{B} = 0$, in the null-point, the solution of the remaining hydrostatic equation yields

$$p_{\mathrm{h}}(y) = p_0\exp\left[-\int_{y_0}^{y}\frac{1}{\Lambda(\tilde{y})}d\tilde{y}\right], \tag{9}$$

$$\varrho(y) = \frac{p(y)}{g_\odot\Lambda(y)}. \tag{10}$$

Here

$$\Lambda(y) = \frac{k_{\mathrm{B}}T(y)}{\overline{m}g_\odot} \tag{11}$$

is the pressure scale-height, which, in the case of isothermal atmosphere, represents the vertical distance over which the gas pressure decreases by a factor of $e \approx 2.7$, $k_{\mathrm{B}} = 1.38\times10^{-23}\ \mathrm{J\ K^{-1}}$ is the Boltzmann constant and $\overline{m} = 0.6\,m_{\mathrm{p}}$ is the mean particle mass ($m_{\mathrm{p}} = 1.672\times10^{-27}$ kg is the proton mass), and $p_0 \approx 10^{-2}$ Pa in Equation (9) denotes the gas pressure at the reference level y_0. In our calculations, we set and hold fixed at $y_0 = 10$ Mm.

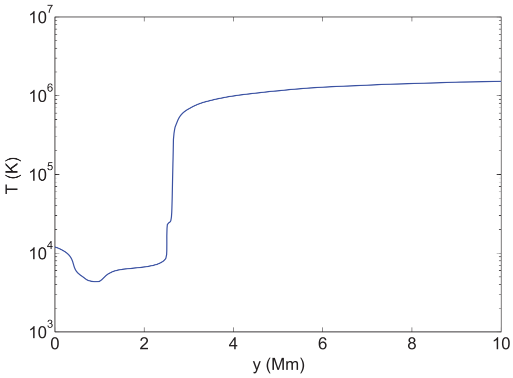

Figure 1. Temperature profile, $T(y)$, in logarithmic scale as a function of height y in the solar atmosphere.

For the solar atmosphere, the temperature profile $T(y)$ (see Figure 1) was derived by Vernazza et al. (1981). At the top of the photosphere, which corresponds to the height $y = 0.5$ Mm, and the temperature is $T(y) = 5700$ K. At higher altitudes, the temperature falls down to its minimal value $T(y) = 4350$ K at $y \approx 0.95$ Mm. Higher up, the temperature rises slowly to the height of about $y = 2.7$ Mm, where the transition region is located. Here the temperature grows up abruptly to the value, $T(y) = 1.5$ MK, at the altitude $y = 10$ Mm, which is typical for the solar corona.

The solenoidal condition, $\nabla\cdot\boldsymbol{B} = 0$, is identically satisfied with the use of the magnetic flux function, $\boldsymbol{A}$, such as

$$\boldsymbol{B} = \nabla\times\boldsymbol{A}. \tag{12}$$

Specifically, to represent the non-potential null-point, we use

$$\boldsymbol{A} = [0, 0, A_z]$$

with (Parnell et al. 1997)

$$A_z = \frac{1}{4}B_0\left[(\mathcal{J}_t - \mathcal{J}_z)y^2 - (\mathcal{J}_t + \mathcal{J}_z)x^2\right], \tag{13}$$

where $\mathcal{J}_t$ is the threshold current, which only depends on the parameters associated with the potential part of the field and it is assumed to be a constant in our calculations. The parameter $\mathcal{J}_z$ is the magnitude of the current perpendicular to the plane of the null-point. Both $\mathcal{J}_t$ and $\mathcal{J}_z$ are free parameters that govern the magnetic field configuration. For $\mathcal{J}_z = 0$, we get a potential null-point, for $|\mathcal{J}_z| < \mathcal{J}_t$ a non-potential null-point, anti-parallel magnetic field lines $|\mathcal{J}_z| = \mathcal{J}_t$, and an elliptical null for $|\mathcal{J}_z| > \mathcal{J}_t$. See Parnell et al. (1997) for more details. The magnetic field at the reference level is set and held fixed as $B_0 = 10$ G.

The equilibrium gas pressure and mass density are computed according to the following equations; see, e.g., Solov'ev (2010) and Kuźma et al. (2015):

$$p(x, y) = p_{\mathrm{h}} - \frac{1}{\mu_0}\left[\int_{-\infty}^{x}\frac{\partial^2 A}{\partial y^2}\frac{\partial A}{\partial x}dx + \frac{1}{2}\left(\frac{\partial A}{\partial x}\right)^2\right], \tag{14}$$

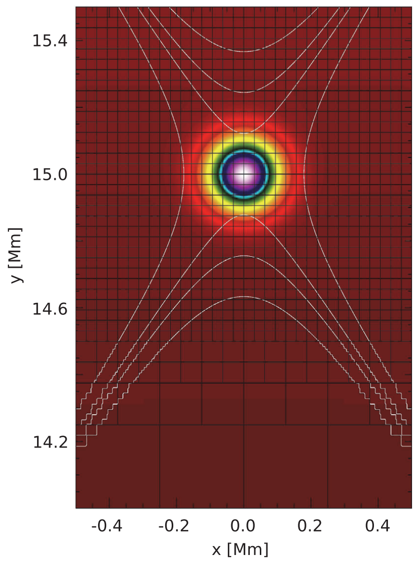

Figure 2. Simulation region for the negative pressure pulse ($A_p = -0.75$) launched in the center of the magnetic null-point. The white solid lines represent magnetic field lines which the typical X-shape in the center. As a complement, the computational blocks are also shown by thin, black, solid boxes.

$$\varrho(x, y) = \varrho_{\mathrm{h}}(y) + \frac{1}{\mu_0 g_\odot}\left\{\frac{\partial}{\partial y}\left[\int_{-\infty}^{x}\frac{\partial^2 A}{\partial y^2}\frac{\partial A}{\partial x}dx + \frac{1}{2}\left(\frac{\partial A}{\partial x}\right)^2\right] - \frac{\partial A}{\partial y}\nabla^2 A\right\}. \tag{15}$$

With the use of Equation (13) in these general formulas, we obtain the expressions for the equilibrium gas pressure

$$p(x, y) = p_{\mathrm{h}}(y) - \frac{B_0^2}{4\mu_0}\mathcal{J}_z(\mathcal{J}_t + \mathcal{J}_z)x^2 \tag{16}$$

and mass density

$$\varrho(x, y) = \varrho_{\mathrm{h}}(y) + \frac{B_0^2}{2\mu_0 g}\mathcal{J}_z(\mathcal{J}_t - \mathcal{J}_z)y. \tag{17}$$

2.3. Perturbations

At the start of the numerical simulation ($t = 0$ s), the equilibrium with the magnetic null-point is perturbed, similarly to Murawski et al. (2011), by a Gaussian pulse of the following form:

$$p(x, y, t = 0) = p_0\left\{1 + A_{\mathrm{p}}\exp\left[-\frac{x^2 + (y - y_{\mathrm{P}})^2}{w^2}\right]\right\}, \tag{18}$$

where p_0 is the initial gas pressure, A_p denotes the initial amplitude of the pulse, $y_{\mathrm{P}} = 15$ Mm is the position of the perturbation point, and $w = 0.1$ Mm is the width of the pressure pulse; see Figure 2. The negative pressure pulse corresponds to $A_p < 0$ and it mimics plasma cooling, while the pressure pulse is represented by $A_p > 0$ and it indicates plasma heating, which is implemented near the magnetic null-point. Note that, despite the negative pressure pulse, the total pressure $p(x, y, t = 0)$ in Equation (18) remains positive.

2.4. Numerical Code

We solve the 2D time-dependent, ideal MHD Equations (1)–(4) numerically, making use of the FLASH code (Fryxell et al. 2000; Lee & Deane 2009). It is now a well tested, fully modular, parallel, multi-physics, open science, simulation code that implements second- and third-order unsplit Godunov solvers with various slope limiters and Riemann solvers as well as adaptive mesh refinement (AMR; e.g., Chung 2002). The Godunov solver combines the corner transport upwind method for multi-dimensional integration and the constrained transport algorithm for preserving the divergence-free constraint on the magnetic field (Lee & Deane 2009). We use the minmod slope limiter and the Riemann solver (e.g., Toro 2006). The main advantage of using the AMR technique is to refine a numerical grid at steep spatial profiles while keeping the grid coarse at the places where fine spatial resolution is not essential. In our case, the AMR strategy is based on controlling the numerical errors in a gradient of mass density that leads to the reduction of the numerical diffusion within the entire simulation region.

For our numerical simulations, we use a 2D Eulerian box of its height $H = 2$ Mm; see Figure 2. Note that in this figure the simulation region is zoomed in to display the null-point including the initial perturbation in more detail. The spatial resolution of the numerical grid is determined by the AMR method. We use the AMR grid with the minimum (maximum) level of the refinement blocks set to 3 (6). The whole simulation region is covered by 1434 blocks. Since every block consists of 8×8 numerical cells, this number of blocks corresponds to 91,776 numerical cells, and the smallest spatial resolution is $\Delta x = \Delta y = 3.9$ km.

At all boundaries, we fix all plasma quantities to their equilibrium values, which lead only to negligibly small numerical reflections of incident wave signals.

3. NUMERICAL RESULTS

Prior to performing numerical simulations, by making the simulation test, we verify that for the adopted grid resolution the system remains in numerical equilibrium, while not being perturbed by any gas pressure pulse. After this basic numerical test, we start to simulate the system dynamics by launching either negative and positive initial gas pressure pulses. Because we study the non-potential magnetic neutral point, we assume in all considered cases that ($|\mathcal{J}_z| < \mathcal{J}_t$); see Parnell et al. (1997). We perform numerical simulations for the following cases: (a) $\mathcal{J}_t/\mathcal{J}_z = 1.25$; (b) $\mathcal{J}_t/\mathcal{J}_z = 2.5$; (c) $\mathcal{J}_t/\mathcal{J}_z = 5.0$. However, we show here the preferential results for $\mathcal{J}_t/\mathcal{J}_z = 2.5$, while the results for cases (a) and (c) are simply compared with those obtained for case (b).

3.1. Null-point with the Negative Pressure Pulse

We assume here the negative amplitude of the initial pressure pulse, $A_p = -0.75$. In Figure 3, we present the evolution of the mass density. At $t = 1$ s, we see that the initial pressure pulse triggered fast and slow magnetoacoustic waves

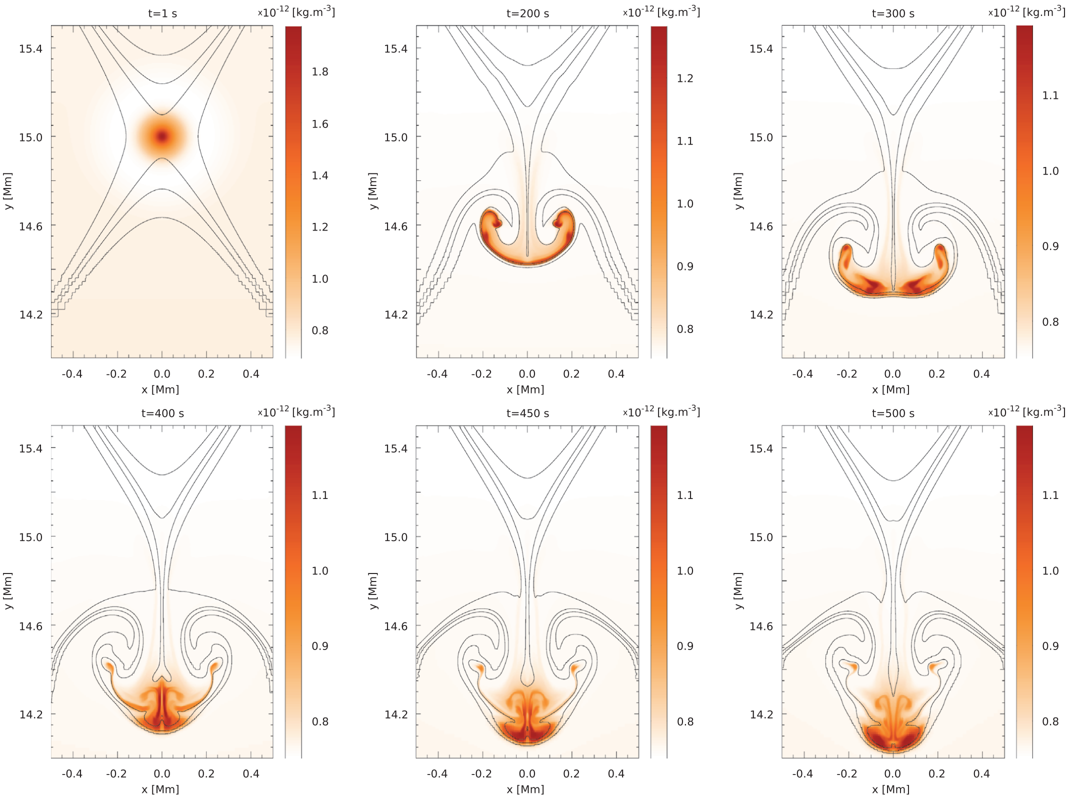

Figure 3. Time evolution of mass density for $A_p = -0.75$, with a clear development of Rayleigh–Taylor instability. The black solid lines show representative magnetic field lines.

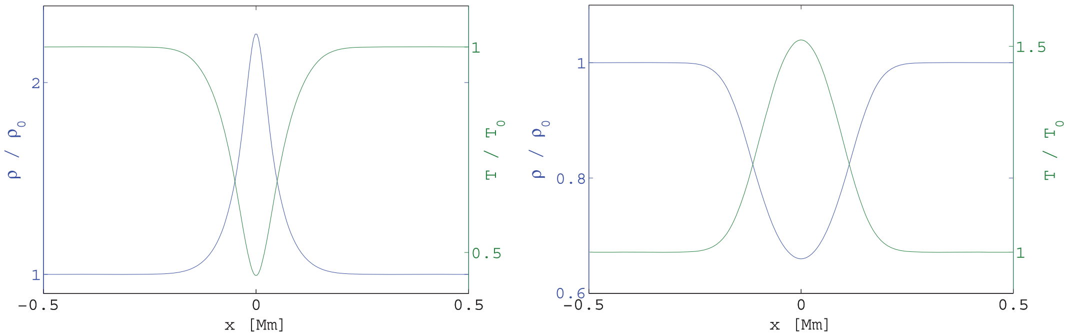

Figure 4. Entropy mode at $t = 10$ s, represented by rarefied and hot plasma regions in the case of the negative initial pressure pulse (left panel) and the positive pressure pulse (right panel).

that propagate quasi-isotropically out of the null-point (see the expanding circular feature at $t = 1$ s).

Later on, as a result of the initial negative pressure pulse, the entropy wave with the enhanced mass density and decreased temperature is formed; see their profiles in Figure 4, left panel. Very shortly after the initial pressure pulse (≈15 s), the entropy wave, represented by the dense blob, starts to move down, along the direction of the gravity action force. Because this blob falls down to an environment with higher density, after some time (≈100–150 s) the Rayleigh–Taylor (RT) instability develops. At $t \approx 350$ s, the blob starts to move up because it is reflected from high density layers and also due to the action of magnetic tension force, and then at $t \approx 400$ s it moves down again.

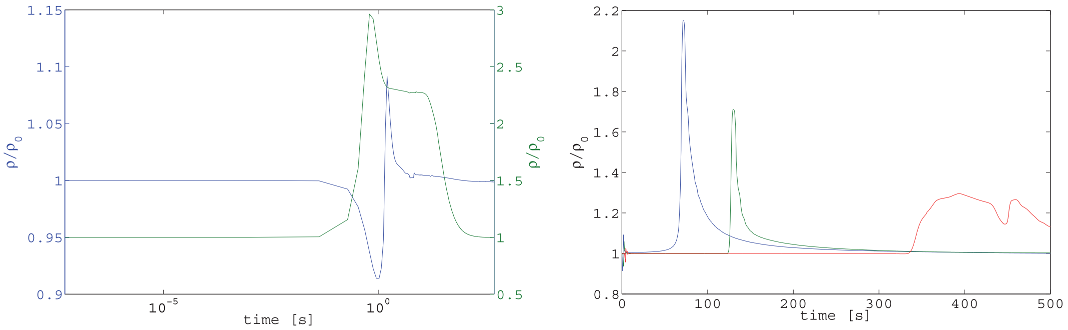

Figure 5. Time evolution of mass density in the case of $A_p = -0.75$, collected at the detection points placed at $x = 0$ Mm along the y axis in positions $y = 15.2$ Mm (left blue line) and $y = 15.0$ Mm (left green line) and $y = 14.8$, $y = 14.6$, and $y = 14.2$ Mm (right red, green, and blue line, respectively). Note that the time axis on the left-hand side is in the logarithmic scale, showing the very beginning of the process.

In Figure 5, we present the time evolution of the mass density computed at different detection points. In the left panel, we show the mass density in two detection points ((0, 15.2) Mm (blue) and (0, 15.0) Mm (green)). The initial pressure pulse triggers large amplitude magnetoacoustic waves. After the initial phase which lasts until $t \approx 10$ s, and during which fast and slow magnetoacoustic waves pass the detection point, the mass density starts to saturate slowly to its equilibrium value (Figure 5, left panel, blue line). This fits the theory of entropy waves perfectly, according to which the entropy waves affect the mass density; for a negative pressure pulse, the mass density ϱ should increase as is indeed observed in the numerical experiments.

In the right panel of Figure 5, we see the evolution of the mass density in three detection points located below the perturbation point ($y = 14.8$, $y = 14.6$, and $y = 14.2$ Mm, red, green, and blue colored lines, respectively). At the very beginning (within the order of seconds) we can again observe the propagating fast magnetoacoustic waves. After the passage of magnetoacoustic waves, the system slowly relaxes to its equilibrium state followed, after some time, by a steep increase in mass density, depending on the position of a detection point. Because the blob descends to the denser layers of the solar atmosphere, the amplitude of these waves decreases, which is clearly seen by comparing all of the lines in this plot. Furthermore, the blue line shows how the blob is reflected from layers at lower altitudes with higher densities.

Figure 6 consists of four panels. The upper left panel shows the current density distribution at time $t^{\max} = 242$ s, i.e., at the time when its maximum value has been reached. From this figure, one can see that the maximum value of the current density is located in the vicinity of the vertical axis of the null-point. As the mass density at this time slowly relaxes to the equilibrium value (see Figure 5 right part), the electron velocity, according to the relation for electric current density, $\boldsymbol{j} = -ne\boldsymbol{v}$, attains its maximum as well.

In the upper right panel of Figure 6, we present the time evolution of the maximal current density detected along the vertical axis of the null point. Note that the vertical axis is in logarithmic scale to show the time evolution in more detail. In this figure, there are two maxima. The first one appears very shortly after the initial perturbation (units of seconds). This is very likely related to the rapid increase of mass density in the null-point. Then, the current density rapidly decreases simultaneously with the mass density decrease. After ≈10–15 s, the current density starts to grow slowly again, but now as the result of the electron velocity increase.

Finally, the two bottom panels of Figure 6 illustrate the horizontal (left) and vertical slices (right) of the current density. The horizontal slice is taken at the point of the maximal value of the electric current density, i.e., at ($x = \langle -0.5, 0.5\rangle$ and $y = 14.65$). The vertical slice is displayed along the axis of the null-point, i.e., at ($x = 0$ and $y = \langle 13.5, 15.5\rangle$). From both of these panels and also from the upper right panel, we can find that the maximal value of the current density is 138× higher than its initial value; see Table 1.

3.2. Null-point with the Positive Pressure Pulse

In this section, we consider the positive amplitude of the initial pressure pulse, $A_p = +1$. In Figure 7, we present the evolution of mass density and compare it to the already discussed case of $A_p = -0.75$. At the beginning phase of the system evolution, we see that fast and slow magnetoacoustic waves are triggered by the initial pressure pulse. After their escape from the launching place, the entropy wave is formed similarly as in the case of $A_p < 0$. However, contrary to the case of $A_p = -0.75$, its mass density is decreased and temperature enhanced; see Figure 4, right panel. Thus, the positive pressure pulse results in the entropy wave (blob) moving up from (≈20 s), owing to its mass density which is lower than that in the ambient medium. Between (100–200 s) we can observe again the growth of RT instability, similarly as in the previous case. Note that at $t \approx 370$ s the central part of the mass density blob starts to move down due to the gravity and magnetic tension force. The latter plays a role as the magnetic field lines are frozen in the plasma.

Figure 8 shows the time evolution of the mass density in different detection points. In the left panel of this figure, the results for two detection points (center of magnetic null-point, $y = 15.0$ Mm, green line and ($y = 14.8$ Mm), blue line) are presented. Here we can see that in the center of the magnetic null-point the mass density abruptly falls off due to the initial pressure pulse. After a few seconds (1–10 s) the mass density starts to increase in agreement with the theory of the entropy wave. In the meantime, the mass density represented by the blue line starts to relax to its initial equilibrium value. In the right panel of this figure, we show the mass density evolution

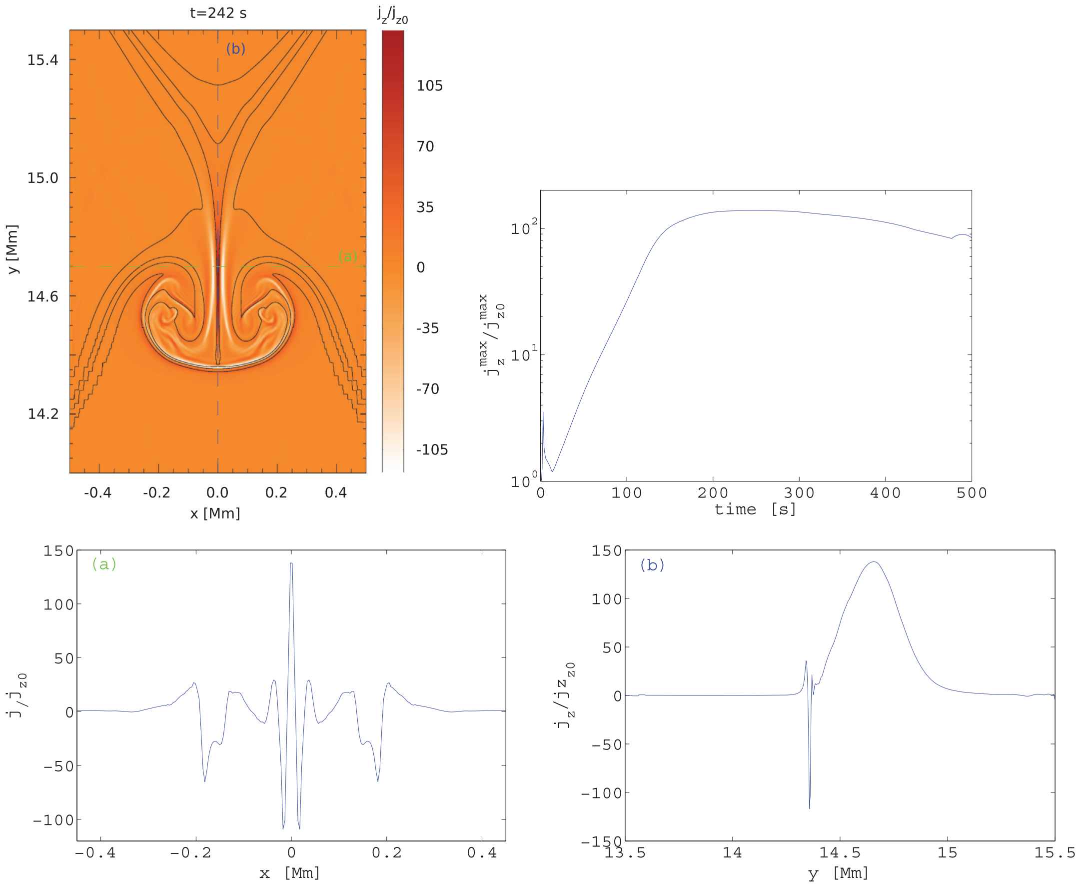

Figure 6. Current density for the negative amplitude of the pressure pulse, $A_p = -0.75$, at the time when the current density reached its maximum value, $t^{\max} = 242$ s (upper left). The black solid lines show the representative magnetic field lines. The light-green and light-blue dashed lines represent the positions of horizontal and vertical slices (shown in the bottom panels of the figure), respectively. The time evolution of maximum values of the current density (upper right); note that the vertical axis is in the logarithmic scale. The horizontal ($y = 14.65$ Mm) and vertical ($x = 0$ Mm) slices for the maximal current density at $t^{\max}$ are shown in the lower left and lower right panels, respectively.

Table 1

Relative Ratios of Initial Current Densities with Respect to Initial Current Density in Case (b)—Third Column and Relative Ratios of Maximum Current Density with Respect to Their Initial Values—Fourth Column

Studied Case	A_p	$j_z^0/j_z^0(b)$	$j_z^{\max}/j_z^0$
(a): $\mathcal{J}_t/\mathcal{J}_z = 1.25$	−0.75	1.98	106.39
	+1.00		213.76
(b): $\mathcal{J}_t/\mathcal{J}_z = 2.50$	−0.75	1.00	137.88
	+1.00		246.26
(c): $\mathcal{J}_t/\mathcal{J}_z = 5.00$	−0.75	0.51	163.13
	+1.00		286.82

in three detection points located above the perturbation point ($y = 15.2$, $y = 15.4$ and $y = 15.6$ Mm; red, green, and blue color, respectively). Similarly to the case of the negative pressure pulse, the mass density oscillates as a result of the fast magnetoacoustic waves propagating through the detection points. Later on (depending on the position of the detection point), the large amplitude waves pass and mass density starts to increase to its equilibrium value. We see that after a certain time (again depending on the detection point position) the mass density tends to decrease—this is well represented by the green line, which results from the gravitational force, as the blob starts to move down at time ≈370 s, as described in the previous paragraph.

Figure 9 consists of four panels, similar to Figure 6. The upper-left panel shows the current density at the time when the current density has reached its maximal value, at $t^{\max} = 273$ s. From this figure, we can again clearly see that the maximum value of the current density takes place in the vicinity of the vertical axis of the null-point. For the same reason as in the case of $A_p = -0.75$, the plasma velocity also attains its maximum at this time.

The upper right panel of Figure 9 presents the same quantity using the same scale as in the previous case of the negative pressure pulse. In this figure are two similarly discernible

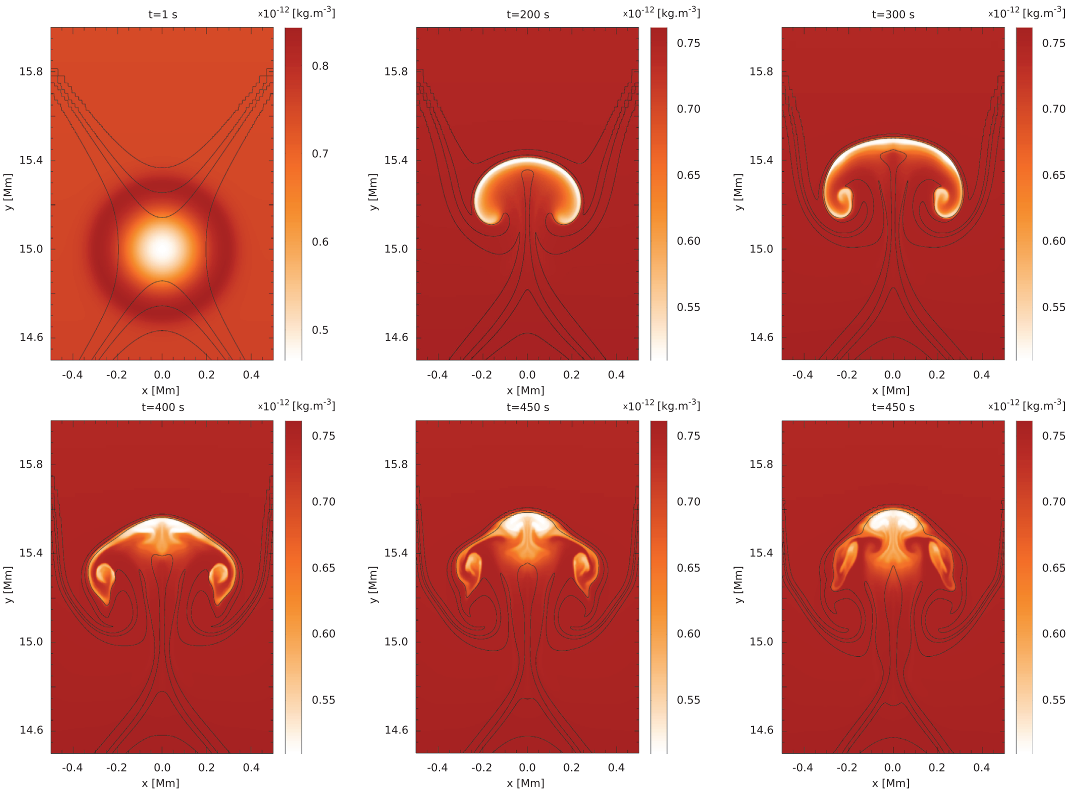

Figure 7. Time evolution of mass density for the positive pressure pulse, $A_p = +1$, with a clear development of Rayleigh–Taylor instability. The black solid lines show representative magnetic field lines.

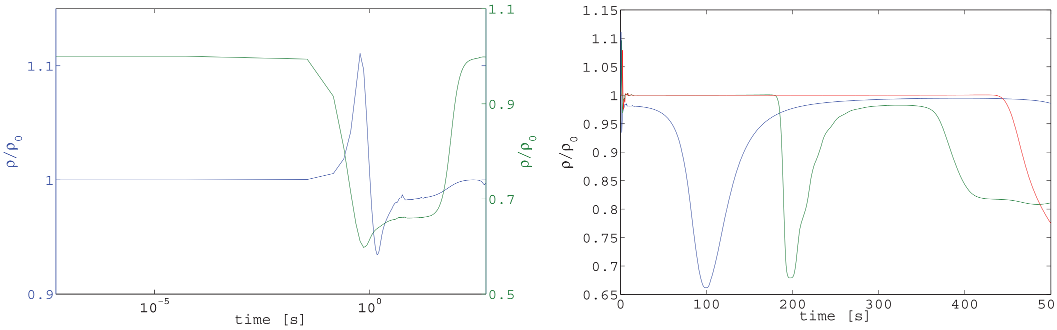

Figure 8. Time evolution of mass density, for the positive amplitude of the pressure pulse, $A_p = +1$, in the detection points placed along the y axis, for $x = 0$ Mm, at $y = 14.8$ (left blue line) and $y = 15.0$ Mm (left green line) and $y = 15.2$, $y = 15.4$ and $y = 15.6$ Mm (right red, green and blue line, respectively). Note that the time axis in the left panel is in the logarithmic scale, showing the initial phase of the process.

maxima. However, comparing the results to the first studied case, some differences can be spotted. The first maximum is not related to the increased mass density in the center of the null-point due to the initial pressure pulse. Because the pressure pulse is positive, the mass density in the launching point (center of the magnetic null-point) decreases very quickly. On the other hand, in the vicinity of the perturbation point the mass density increases, as can be seen from Figure 8. After this first maximum, the current density starts to decrease, to the time (30–40 s), when, by the same reason as in the previous case, its growth in time is again evident.

Finally, the two bottom panels of Figure 9 (left and right) show the horizontal and vertical slices, respectively. The horizontal slice has been taken at the point of the maximal

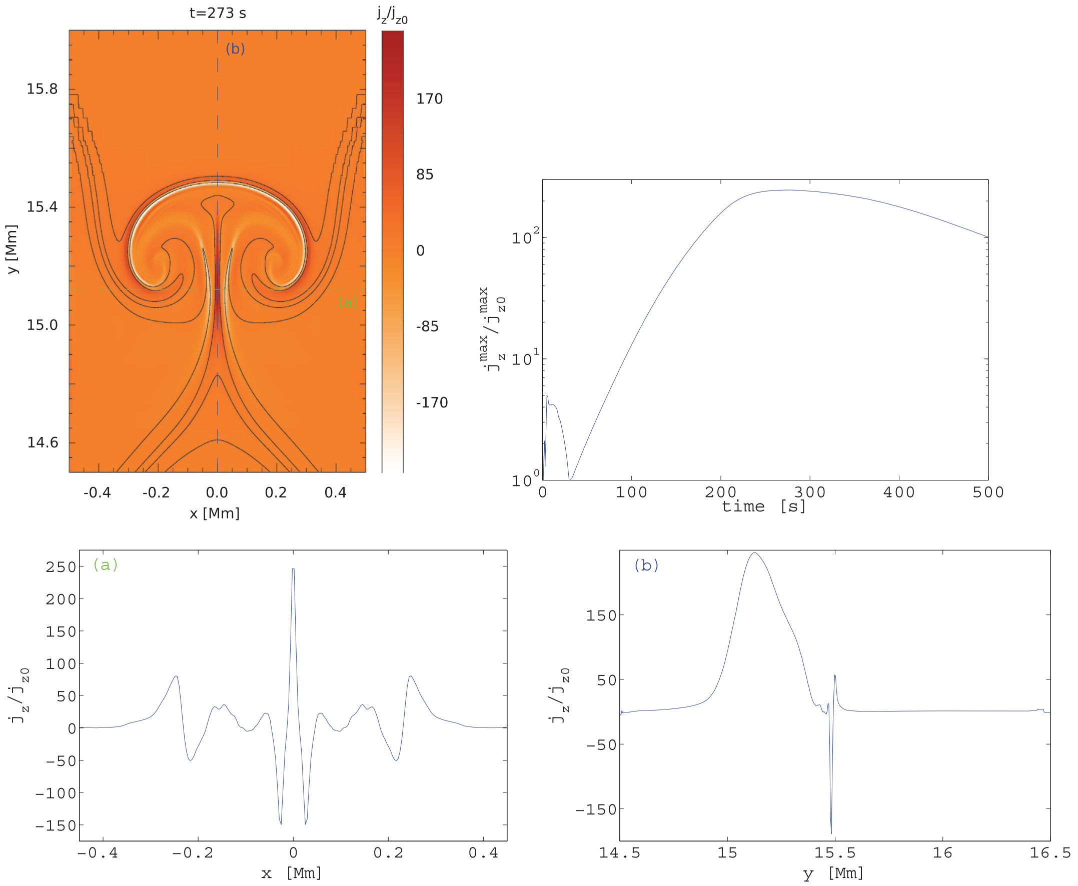

Figure 9. Current density for the positive amplitude of the pressure pulse, $A_p = +1$, at the time when the current density reached its maximum $t^{\max} = 273$ s (upper left). The black solid lines show the representative magnetic field lines. The light-green and light-blue dashed lines represent the positions of horizontal and vertical slices (shown in the lower panels of the figure), respectively. The time evolution of maximum values of the current density (upper right); note that the vertical axis is in the logarithmic scale. The horizontal ($y = 15.12$ Mm) and vertical ($x = 0$ Mm) slices for the maximal current density at $t^{\max}$ are shown in the lower left and lower right panels, respectively.

value of the electric current density, i.e., ($x = \langle -0.5, 0.5\rangle$ and $y = 15.12$). The vertical slice is shown along the axis of the null-point, i.e., ($x = 0$ and $y = \langle 14.5, 16.5\rangle$). From both panels, and finally also from the upper right panel, we can see that the maximal value of the current density is 246× higher compared with the initial value; see Table 1.

3.3. Comparison of Results for Different Ratios of $\mathcal{J}_t$ and $\mathcal{J}_z$

As we mentioned above, we also numerically studied the following two cases: (a) $\mathcal{J}_t/\mathcal{J}_z = 1.25$ and (c) $\mathcal{J}_t/\mathcal{J}_z = 5.0$. Here we compare these results with case (b): $\mathcal{J}_t/\mathcal{J}_z = 2.5$, described above in more detail.

We found that the evolution of mass density for the cases (a) and (c) exhibits essentially the same behavior as in the case of (b)—corresponding Figures 3 and 7. For this reason, the mass density evolution in the selected detection points (corresponding to Figures 5 and 8) also exhibits practically non-essential changes.

On the other hand, we find interesting changes in current densities for all studied cases; see Table 1. Here we present the relative ratios of initial current densities with respect to the initial current density in case (b)—third column, and relative ratios of maximum current density with respect to their initial values—fourth column. This table reveals that by increasing the parameter $\mathcal{J}_t/\mathcal{J}_z$, the initial current density in the non-potential null point increases. It is expected that if we combine Equations (6) and (12), we can find that the current density is directly proportional to $\mathcal{J}_z$ as

$$j_z = \frac{B_0}{2\mu_0}\mathcal{J}_z. \tag{19}$$

On the other hand, if we compare the values of maximal current densities, we observe that with increasing $\mathcal{J}_t/\mathcal{J}_z$, the maximal current density also increases, for both amplitudes of initial pressure pulses. It is also clearly visible that for the positive pressure pulse ($A_p = +1.0$), the maximum current density is higher than for the negative pressure pulse ($A_p = -0.75$).

Table 2
The Times When the Current Density Reached a Maximum Value

Studied Case	A_p	$t\,(j_z^{\max})$(s)
(a): $\mathcal{J}_t/\mathcal{J}_z = 1.25$	-0.75	242.0
	$+1.00$	301.0
(b): $\mathcal{J}_t/\mathcal{J}_z = 2.50$	-0.75	242.0
	$+1.00$	273.0
(c): $\mathcal{J}_t/\mathcal{J}_z = 5.00$	-0.75	244.0
	$+1.00$	259.0

In Table 2, we present the times at which the current density for all of the studied cases reaches its maximum. We can see that, whereas for the negative initial pulse ($A_p = -0.75$) the time remains practically the same, in the case of the positive pressure pulse ($A_p = +1$), the maximum is reached earlier for a higher value of $\mathcal{J}_t/\mathcal{J}_z$. It is also evident that the time is higher for the positive pressure pulse in all of the studied cases.

4. SUMMARY

We performed numerical simulations of evolution of the entropy wave generated by the pressure pulse in the non-potential magnetic null-point. We solved 2D, time-dependent, ideal MHD equations using the FLASH numerical code, which implements AMR. To make the numerical model more realistic, we considered the initial (VAL-C) temperature profile in the gravitationally stratified solar atmosphere. Numerical calculations are performed for three different initial cases. We described here only one case in detail, whereas the remaining two are only quantitatively compared with the first one.

Our results can be summarized as follows. The initial negative or positive pressure pulse, which mimics a sudden cooling, e.g., produced by the thermal instability or sudden heating caused by some energy release, leads, respectively, to the accumulation or evacuation of plasma at the null-point. In our case, this accumulation or evacuation forms the entropy wave, which evolves due to gravity. The entropy wave, produced by the initial pressure pulse of its negative amplitude, leads to a mass density that is greater than in the ambient atmosphere and thus it falls down, being attracted by the gravity. In the case of the positive pressure pulse, the entropy wave propagates upward. These entropy wave motions in both cases are limited by the magnetic tension force.

We found that during an evolution of the entropy wave the electric current is strongly filamented owing to the Rayleigh–Taylor instability. At some locations, the electric current density increases up to 138 times (negative initial pressure pulse) and 246 times (positive pressure pulse) its initial value.

When the current density exceeds the corresponding thresholds for some plasma instabilities (e.g., the ion-acoustic or Buneman instability), then plasma waves can be generated and anomalous resistivity is produced. These processes can release the magnetic field energy through the Ohmic dissipation.

Comparing the numerical results in all of the studied cases, we found that the maximum of the current density ($j_z^{\max}/j_z^0$), reached in the filamentation process, grows with the parameter $\mathcal{J}_t/\mathcal{J}_z$. We also found that for the positive pressure pulses, the current density reached values higher than for the negative pressure pulses.

Based on these results, the following sequence of processes can be proposed. The thermal instability in the non-potential magnetic null-point produces the “catastrophic” cooling, i.e., the negative pressure pulse. This pulse generates the entropy wave and then after its evolution and filamentation process, at locations with highly enhanced electric current densities, the magnetic-energy release (nanoflare) takes place. For example, the bright points in coronal EUV lines (Madjarska et al. 2003; Tian et al. 2008) could be explained by this.

The authors thank the anonymous referee for constructive comments that improved the paper. The authors also acknowledge the Marie Curie FP7-PIRSES-GA-2011-295272 RadioSun project. P.J. and M.K. acknowledge support from grants P209/12/0103 of the Grant Agency of the Czech Republic, and the European grant FP7-SPACE-2013–1 F-CHROMA (No. 606862). P.J. thanks Dr. Tom Van Doorsselaere for support of his scientific stay at the Faculty of Science, Catholic University in Leuven, Belgium, during March–May 2015, where P.J. almost finished this work. This work has been supported by a Marie Curie International Research Staff Exchange Scheme Fellowship within the 7th European Community Framework Program and by the Polish National Foundation grant No. 2014/15/B/ST9/00106. The FLASH code used in this work was developed by the DOE-supported ASC/Alliances Center for Astrophysical Thermonuclear Flashes at the University of Chicago.

REFERENCES

Bárta, M., Büchner, J., Karlický, M., & Skála, J. 2011, ApJ, 737, 24
Chung, T. J. 2002, Computational Fluid Dynamics (New York: Cambridge Univ. Press)
De Moortel, I., & Hood, A. W. 2003, A&A, 408, 755
De Moortel, I., & Nakariakov, V. M. 2012, RSPTA, 370, 3193
Field, G. B. 1965, ApJ, 142, 531
Foullon, C., Verwichte, E., Nakariakov, V. M., & Fletcher, L. 2005, A&A, 440, L59
Fryxell, B., Olson, K., Ricker, P., et al. 2000, ApJS, 131, 273
Goedbloed, J. P. H., & Poedts, S. 2004, Principles of Magnetohydrodynamics (New York: Cambridge Univ. Press)
Jelínek, P., & Karlický, M. 2012, A&A, 537, A46
Jelínek, P., Karlický, M., & Murawski, K. 2012, A&A, 546, A49
Jelínek, P., & Murawski, K. 2013, MNRAS, 434, 2347
Kuźma, B., Murawski, K., & Solov’ev, A. 2015, A&A, 577, A138
Lee, D., & Deane, A. E. 2009, JCoPh, 228, 952
Macnamara, C. K., & Roberts, B. 2010, A&A, 515, A41
Madjarska, M. S., Doyle, J. G., Teriaca, L., & Banerjee, D. 2003, A&A, 398, 775
Mészárosová, H., Karlický, M., Jelínek, P., & Rybák, J. 2014, ApJ, 788, 44
Murawski, K., Zaqarashvili, T. V., & Nakariakov, V. M. 2011, A&A, 533, A18
Nakariakov, V. M., Foullon, C., Verwichte, E., & Young, N. P. 2006, A&A, 452, 343
Nickeler, D. H., Karlický, M., Wiegelmann, T., & Kraus, M. 2013, A&A, 556, A61
Nisticò, G., Nakariakov, V. M., & Verwichte, E. 2013, A&A, 552, A57
Nisticò, G., Pascoe, D. J., & Nakariakov, V. M. 2014, A&A, 569, A12
Parnell, C. E., Neukirch, T., Smith, J. M., & Priest, E. R. 1997, GApFD, 84, 245
Pascoe, D. J. 2014, RAA, 14, 805
Pascoe, D. J., Nakariakov, V. M., & Kupriyanova, E. G. 2013, A&A, 560, A97
Pascoe, D. J., Nakariakov, V. M., & Kupriyanova, E. G. 2014, A&A, 568, A20
Priest, E. R. 1982, Solar Magneto-hydrodynamics (Dordrecht: Reidel)
Solov’ev, A. A. 2010, ARep, 54, 86
Somov, B. V. 2012, in Plasma Astrophysics, Part I, Fundamentals and Practice, Vol. 391 (New York: Springer)
Tian, H., Curdt, W., Marsch, E., & He, J. 2008, ApJL, 681, L121
Toro, E. F. 2006, IJNMF, 52, 433
Vernazza, J. E., Avrett, E. H., & Loeser, R. 1981, ApJS, 45, 635

ISSN 1845–8319

STRUCTURED MASS DENSITY SLAB AS A WAVEGUIDE OF FAST MAGNETOACOUSTIC WAVES

P. JELÍNEK[1,2] and M. KARLICKÝ[2]

[1]*Institute of Physics and Biophysics, Faculty of Science,*
University of South Bohemia, Branišovská 31, CZ–37005 České Budějovice,
Czech Republic
[2]*Astronomical Institute, Academy of Sciences of the Czech Republic,*
Fričova 258, CZ–25165 Ondřejov, Czech Republic

Abstract. Coronal loops are waveguides for magnetohydrodynamic (MHD) waves. These loops are expected to be structured. Therefore, in the present paper, we numerically studied the propagation of the fast MHD waves in the structured density slab (composed from a broad density slab with one axisymmetric narrow sub-slab superposed), and analysed the wave signals. Then, this structured slab was divided into its components, i.e., to simple broad and narrow slabs and the same analysis was made. We compared results of both these cases. For the calculations we adopted a two-dimensional (2D) magnetohydrodynamic (MHD) model, in which we solved a full set of ideal time-dependent MHD equations using the FLASH code, applying the adaptive mesh refinement (AMR) method. To initiate the fast sausage magnetoacoustic waves, we used axisymmetric Gaussian velocity perturbation. Wave signals were detected in different locations along the slab and as a diagnostic tool of these waves, the wavelet analysis method has been used. We found that for the structured density slab with sufficiently sharp boundaries, i.e., for good quality waveguides (without an energy leakage), the guided waves in the structured slab behave similarly as in its separated (simple slab) components.

Key words: magnetohydrodynamics - flares - waves - oscillations - numerical methods

1. Introduction

The magnetically dominated solar plasma supports the propagation of various types of MHD waves. These waves were already observed in the solar corona by modern imaging and spectral instruments in the visible light, EUV, X-ray, and radio bands and investigated and analyzed in many theoretical and numerical studies. Several types of waves were recognized: a) propagating waves (De Moortel *et al.* 2000), b) slow magnetoacoustic standing waves (Nakariakov *et al.* 2004), c) fast kink magnetoacoustic waves (Pascoe *et al.* 2010) and fast sausage magnetoacoustic waves (Pascoe *et al.* 2009;

Karlický *et al.* 2011; Karlický *et al.* 2013 and Jelínek & Murawski 2013). For a comprehensive review of MHD waves, see e.g. De Moortel & Nakariakov (2012).

These waves can be excited by various processes in the solar corona. The impulsive flare process, which provides either single or multiple sources of disturbances, is the most probable one. Then these waves are trapped in regions of higher density, e.g., in coronal loops or current sheets, which serve as waveguides. Due to dispersion properties, the fast sausage magnetoacoustic waves belong to the most interesting ones. Their wavelet spectra show the typical tadpole shape where a narrow-spectrum tail precedes a broadband head. These tadpole signatures (wavelet tadpole) were firstly observed by the SECIS instrument in the 1999 solar-eclipse data (see Katsiyannis *et al.* 2003), and later in radio observations (Meszárosová *et al.* 2009).

In numerical simulations, up to now, the waveguides (loops) for the MHD waves were described only by simple density slabs (see, e.g., Jelínek & Karlický 2012, Meszárosová *et al.* 2014). However, coronal loops can be structured. Therefore, in the present paper, for the first time, we study a propagation of the fast magnetoacoustic waves in a structured density slab.

The paper is organized as follows. In Section 2 we describe the numerical model and simulations, including the equilibrium and perturbations. The numerical results with the description are presented in the Section 3. We complete the paper by conclusions in Section 4.

2. Numerical Model and Simulations

In presented numerical model we describe the plasma dynamics by the two-dimensional (2-D) time dependent ideal magnetohydrodynamic (MHD) equations, in the form which we used in our previous studies, e.g. (Jelínek *et al.* 2012, Jelínek & Murawski 2013). These 2-D MHD equations were solved numerically with the FLASH (parallel, multiphysics code), using the adaptive mesh refinement (AMR) method, see (Lee & Deane 2009, Lee 2013).

For a still ($\mathbf{v} = \mathbf{0}$) equilibrium, we assume that the magnetic field is parallel to the y-axis, see Jelínek & Karlický (2012) and we used the value $B_0 = 40$ G in the whole simulation region. The mass density profile in the slab is considered to be constant along the x-axis and along the y-axis the mass density profile is expressed by the formula given by Nakariakov & Roberts (1995), its graphical form is presented in Fig.1. As we choose the

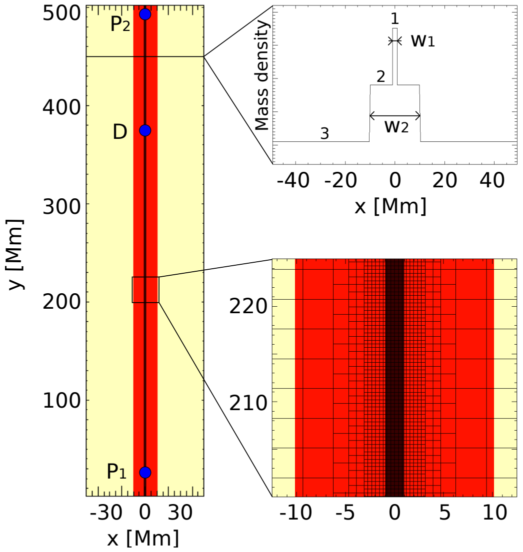

Figure 1: Mass density distribution in modelled structured slab with marked perturbation points, P_i, and detection point, D. On the top of the right side of figure, we present, the horizontal slice with points $1, 2$ and 3 in mass density (see the text for exact values) and also showing the semi-widths of slabs w_1 and w_2. In the bottom part of the figure, the detail of the part of simulation region showing the computational grid in used Adaptive Mesh Refinement (AMR), is presented.

periods of wave signals in the narrow density slab to be $\wp_1 = 3.0$ s and $\wp_2 = 30.0$ s in the broad slab, we can find, from the following formula, the values of mass densities in these sub-slabs and automatically also in the structured slab:

$$\wp_i = \frac{2.6w}{B}\sqrt{\mu_0 \cdot (\varrho_i - \varrho_{i+1})}. \tag{1}$$

The distribution of the gas pressure over the whole simulation region is supposed to be a constant, $p_0 = 0.01$ Pa, and the plasma temperature in the simulation region is then calculated from the ideal gas law.

At the start of the numerical simulation ($t = 0$ s), the equilibrium is perturbed by the Gaussian pulse in the x-component of velocity (e.g. Nakariakov *et al.* 2004). Such type of the pulse triggers preferentially fast magnetoacoustic sausage waves.

The perturbation points, P_i, and the detection point, D, are located on the axis of the structured slab. In Table I the exact positions of these

Table I: Geometrical and physical parameters used in our calculations, indicated for all studied cases.

Parameter	Studied case		
	#1	#2	#3
w_1 [Mm]	1.0	–	1.0
w_2 [Mm]	–	10.0	10.0
P_1 [Mm]	10.0	–	25.0
P_2 [Mm]	–	50.0	492.0
D [Mm]	127.0	430.0	375.0
ϱ_1 [$10^{-12}\mathrm{kg}\cdot\mathrm{m}^{-3}$]	35.2	–	35.2
ϱ_2 [$10^{-12}\mathrm{kg}\cdot\mathrm{m}^{-3}$]	18.1	18.1	8.1
ϱ_3 [$10^{-12}\mathrm{kg}\cdot\mathrm{m}^{-3}$]	–	1.0	1.0
$\mathrm{c}_1^{\mathrm{Alf}}$; c_1^{s} [$\mathrm{Mm}\cdot\mathrm{s}^{-1}$]	0.604; 0.028	–; –	0.604; 0.028
$\mathrm{c}_2^{\mathrm{Alf}}$; c_2^{s} [$\mathrm{Mm}\cdot\mathrm{s}^{-1}$]	0.842; 0.039	0.842; 0.039	0.842; 0.039
$\mathrm{c}_3^{\mathrm{Alf}}$; c_3^{s} [$\mathrm{Mm}\cdot\mathrm{s}^{-1}$]	–; –	3.578; 0.234	3.578; 0.234

points for all studied cases are presented. For the wavelet analysis of wave signal, collected at the detection point, we used the Morlet wavelet, which consists of a plane wave modulated by a Gaussian, see (Farge 1992, Torrence & Compo 1998). The wave periods are estimated from the global wavelet spectrum as the most dominant period in this spectrum.

For our numerical simulations we used a 2-D Eulerian computation box of $(-7.5, 7.5)$ Mm $\times$ $(2.0, 102.0)$ Mm for the case #1 and $(-50.0, 50.0)$ Mm $\times$ $(2.0, 502.0)$ Mm for the cases #2 and #3, respectively. The spatial resolution of the numerical grid was determined with the AMR method and we used the AMR grid with the minimum (maximum) level of the refinement blocks set to 3 (7) in all studied cases. For more details and better understanding of the described situation, see Fig. 1. We used free-boundary conditions in our numerical model, so that the waves could freely leave the simulation box without any significant reflection.

3. Numerical Results

We numerically studied three cases: #1 fast magnetoacoustic waves in the simple narrow and high density slab (sub-slab), initiated by the velocity pulse with a semi-width of $\lambda_1 = 0.5$ Mm, #2 waves in the simple broad

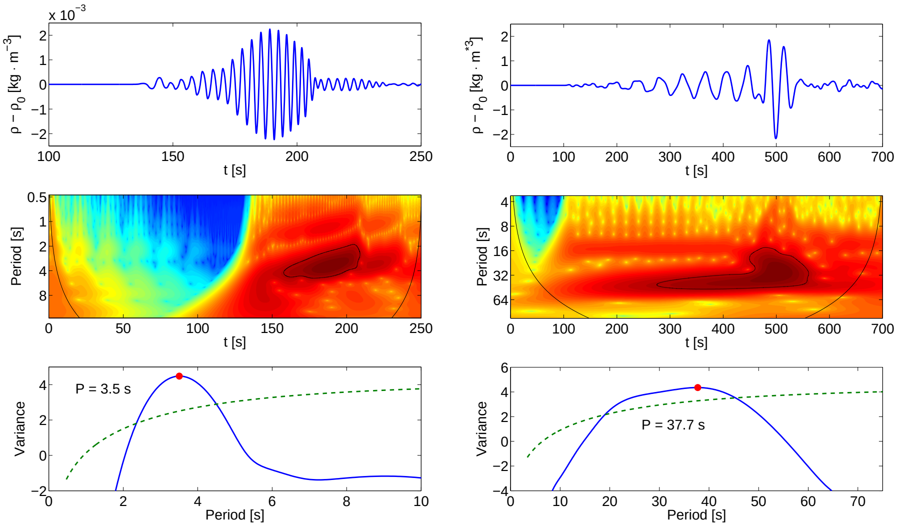

Figure 2: Studied cases #1 and #2 (left and right columns)– time evolution of mass density $\varrho(0;\mathrm{D}) - \varrho_0(0;\mathrm{D})$ (upper panel); corresponding wavelet analysis with typical tadpole shape (middle); bottom panel: the global wavelet spectrum of the incoming signal (full blue line) with dominant wave period (red dot), and the 99% significance level (dash-dotted green line).

and low density slab, initiated by the velocity pulse with a semi-width of $\lambda_2 = 5.0$ Mm, and finally #3 waves in the structured density slab, initiated by both of these pulses. As we found in our previous numerical studies (e.g. Jelínek *et al.* 2012), the quality and the shape of the wavelet tadpole strongly depends on the distance between the perturbation and detection point. The time of the first arrival of wave signal to the detection point is proportional to this distance and indirectly proportional to external Alfén speed (Roberts *et al.* 1984). Because of the fact that in both sub-slabs we have different Alfvén speeds (see Table I) we have to shift both perturbation points to each other in the case of structured mass density slab to allow the wave signal arrive to detection point at the time when both of wave signals can interact.

In the first part of our paper, we studied the fast sausage waves in isolated simple density slabs; in the narrow and high density slab (case #1) and in the broad and low density one (case #2). Obtained results are summarized in Fig. 2, where the time evolution of the wave signals and

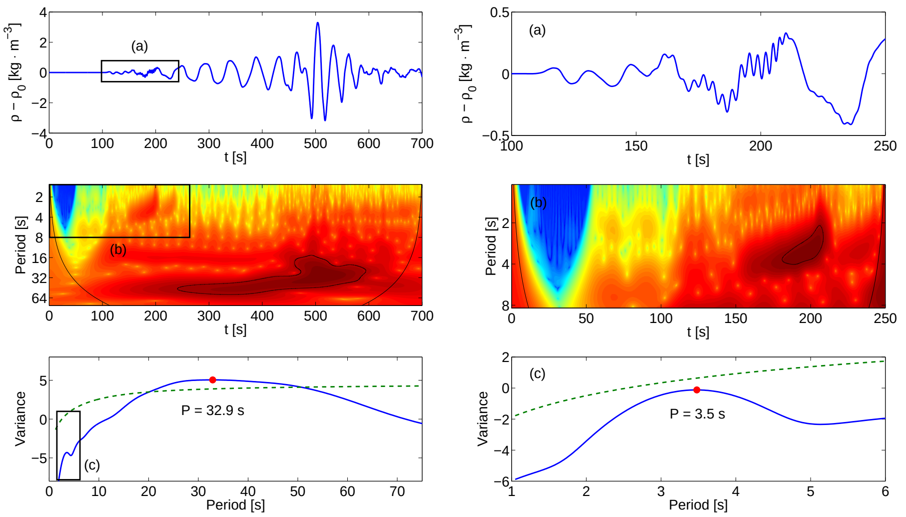

Figure 3: Studied case #3 – left column: the time evolution of mass density $\varrho(0;\mathrm{D}) - \varrho_0(0;\mathrm{D})$ (upper panel); corresponding wavelet analysis with typical tadpole shape (middle); bottom panel: the global wavelet spectrum of the incoming signal (full blue line) with dominant wave period (red dot), and the 99% significance level (dash-dotted green line). Right column: detailed views to the parts displayed as black rectangles in the left column.

corresponding wavelet spectra with estimated wave periods for both studied cases are presented. As follows from the tadpole structures in the cases #1 and #2, we detected the fast sausage magnetoacoustic wave propagating in both of these slabs (waveguides). The periods were estimated as 3.5 s and 37.7 s (see Fig. 1, bottom parts), and their ratio is thus about 10. The periods and its ratio are fully consistent with analytical formulae for calculation of periods in such slabs and agree with the results obtained in our previous studies, see e.g. (Jelínek & Karlický 2012, Jelínek *et al.* 2012 or Meszárosová *et al.* 2014).

Then, in the second part of our study, we studied the propagation of the fast magnetoacoustic waves in the structured density slab (composed from the above mentioned simple slabs). The results are summarized in Fig.3. The left part of this figure describes the global process, and the right part the process in zoomed interval. Once again, the time evolution of the wave signal and its wavelet spectra are shown; together with the estimated periods

(3.5 and 32.9 s). As can be seen here, the structured density slab serves as the waveguide of two fast sausage magnetoacoustic waves. Their periods are close to those detected in the isolated simple slabs. The boundaries in all studied cases were sharp, therefore the slabs are of good quality, i.e. without an energy leakage out of slabs. For smoother boundaries of slabs there is an exchange of the wave energy in the structured slab (between narrow and broad slabs) and therefore there can be observed the mixing of the waves.

4. Conclusions

In this paper we numerically studied propagation of the fast sausage magnetoacoustic waves in the structured density slab with one axisymmetric sub-slab. We also divided the structured density slab into its parts (broad and low density slab and narrow and high density slab) and compared propagating waves and their wavelet spectra in all these cases. We found that for the structured density slab with sufficiently sharp boundaries, i.e., for good quality waveguides (without an energy leakage), the guided waves in the structured slab behave similarly as in its separated (simple slab) components.

Acknowledgements

The authors acknowledge support from the research project RVO:67985815 of the Astronomical Institute AS and Grant P209/12/0103 of the Grant Agency of the Czech Republic. The authors would also like to express their cordial thanks to Professor Kris Murawski for valuable discussions and the unknown referees for their comments. The FLASH code used in this work was in part developed by the DOE-supported ASC/Alliances Center for Astrophysical Thermonuclear Flashes at the University of Chicago. The wavelet analysis was performed using the software written by C. Torrence and G. Compo. `http://paos.colorado.edu/research/wavelets`.

References

De Moortel, I., Ireland, J., and Walsh, R. W.: 2000, *Astron. Astrophys.* **355**, L23.

De Moortel, I. and Nakariakov, V. M.: 2012, *Philos. T. R. Soc. A* **370**, 3193.

Farge, M.: 1992, *Annu. Rev. Fluid Mech.* **24**, 395.

Goossens, M.: 2003, *An Introduction to Plasma Physics and Magnetohydrodynamics*, Kluwer Academic Publishers, Dordrecht, The Netherlands.

Jelínek, P. and Karlický, M.: 2012, *Astron. Astrophys.* **537**, A46.

Jelínek, P., Karlický, M., and Murawski, K.: 2012, *Astron. Astrophys.* **546**, A49.

Jelínek, P. and Murawski, K.: 2013, *Mon. Not. R. Astron. Soc.* **435**, 2347.

Karlický, M., Jelínek, P., and Mészárosová, H.: 2011, *Astron. Astrophys.* **529**, A96.

Karlický, M., Mészárosová, H., and Jelínek, P.: 2013, *Astron. Astrophys.* **550**, A1.

Katsiyannis, A. C., *et al.*: 2003, *Astron. Astrophys.* **406**, 709.

Lee, D. and Deane, A. E.: 2009, *J. Comput. Phys.* **228**, 952.

Lee, D.: 2013, *J. Comput. Phys.* **243**, 269.

Mészárosová, H., Karlický, M., Rybák, J., and Jiřička, K.: 2009, *Astron. Astrophys.* **502**, 13.

Mészárosová H., Karlický, M., Jelínek, P., and Rybák, J.: 2014, *Astrophys. J.* **788**, 44.

Nakariakov, V. M. and Roberts, B.: 1995, *Solar Phys.* **159**, 399.

Nakariakov, V. M., *et al.*: 2004, *Mon. Not. R. Astron. Soc.* **349**, 705.

Nakariakov, V. M., Pascoe, D. J., and Arber, T. D.: 2005, *Space Sci. Rev.* **121**, 115.

Pascoe, D. J., *et al.*: 2009, *Astron. Astrophys.* **494**, 1119.

Pascoe, D. J., Wright, A. N., and De Moortel, I.: 2010, *Astrophys. J.* **711**, 990.

Roberts, B., Edwin, P. M., and Benz, A. O.: 1984, *Astrophys. J.* **279**, 857.

Torrence, Ch. and Compo, G. P.: 1998, *Bull. Amer. Meteor. Soc.* **79**, 61.

Space Sci Rev (2016) 200:75–203
DOI 10.1007/s11214-015-0233-0

Magnetohydrodynamic Oscillations in the Solar Corona and Earth’s Magnetosphere: Towards Consolidated Understanding

V.M. Nakariakov[1,2,3] · V. Pilipenko[4] · B. Heilig[5] · P. Jelínek[6] · M. Karlický[7] · D.Y. Klimushkin[8] · D.Y. Kolotkov[1] · D.-H. Lee[2] · G. Nisticò[1] · T. Van Doorsselaere[9] · G. Verth[10] · I.V. Zimovets[4,11,12]

Received: 4 May 2015 / Accepted: 29 December 2015 / Published online: 2 February 2016

Abstract Magnetohydrodynamic (MHD) oscillatory processes in different plasma systems, such as the corona of the Sun and the Earth’s magnetosphere, show interesting similarities and differences, which so far received little attention and remain under-exploited. The successful commissioning within the past ten years of THEMIS, Hinode, STEREO and SDO spacecraft, in combination with matured analysis of data from earlier spacecraft (Wind, SOHO, ACE, Cluster, TRACE and RHESSI) makes it very timely to survey the breadth of observations giving evidence for MHD oscillatory processes in solar and space plasmas, and state-of-the-art theoretical modelling. The paper reviews several important topics, such as Alfvénic resonances and mode conversion; MHD waveguides, such as the magnetotail,

---

✉ V.M. Nakariakov
V.Nakariakov@warwick.ac.uk

[1] Centre for Fusion, Space and Astrophysics, University of Warwick, Coventry CV4 7AL, UK

[2] School of Space Research, Kyung Hee University, Yongin, 446-701 Gyeonggi, Korea

[3] Central Astronomical Observatory at Pulkovo, St. Petersburg 196140, Russia

[4] Space Research Institute, Moscow 117997, Russia

[5] Tihany Geophysical Observatory, Geological and Geophysical Institute of Hungary, Tihany, Hungary

[6] Faculty of Science, Institute of Physics and Biophysics, University of South Bohemia, 370 05 České Budějovice, Czech Republic

[7] Astronomical Institute of the Academy of Sciences of the Czech Republic, 25165 Ondřejov, Czech Republic

[8] Institute of Solar-Terrestrial Physics, Lermontov St. 126A, Irkutsk 664033, Russia

[9] Department of Mathematics, Centre for Mathematical Plasma Astrophysics, KU Leuven, 3001 Leuven, Belgium

[10] Solar Physics and Space Plasma Research Centre (SP2RC), University of Sheffield, Sheffield S3 7RH, UK

[11] National Space Science Center, Chinese Academy of Sciences, Beijing 100190, China

[12] International Space Science Institute, Beijing 100190, China

coronal loops, coronal streamers; mechanisms for periodicities produced in energy releases during substorms and solar flares, possibility of Alfvénic resonators along open field lines; possible drivers of MHD waves; diagnostics of plasmas with MHD waves; interaction of MHD waves with partly-ionised boundaries (ionosphere and chromosphere). The review is mainly oriented to specialists in magnetospheric physics and solar physics, but not familiar with specifics of the adjacent research fields.

Keywords Magnetohydrodynamic waves (e.g., Alfvén waves) · MHD waves, plasma waves, and instabilities · Magnetic pulsations · Corona · Solar activity · Flares

1 Introduction

The solar corona and the Earth's magnetosphere are undoubtedly the most studied natural plasma systems. Both consist of highly ionised plasmas penetrated by a magnetic field, that plays the decisive role in the structure, short-term dynamics and long-term evolution of these plasmas. The solar corona and the Earth's magnetosphere are the key elements of the solar-terrestrial connections and hence attract growing interest in the context of space weather and climate. Moreover, both the corona and the magnetosphere are natural plasma laboratories, where one can find the combinations of physical conditions of broad interest. In particular, there are conditions directly relevant to the efforts in controlled fusion. Also, the corona and magnetosphere are priceless for the investigation of fundamental physical processes operating in natural and laboratory plasmas (e.g. magnetic reconnection, wave-particle interaction, macroscopic and microscopic instabilities, charged particle acceleration, turbulence). One of these basic physical processes is magnetohydrodynamic (MHD) waves. In both the Earth's magnetosphere and the solar corona MHD waves are well observed with satisfactory time and spatial resolution, mainly because of the recently commissioned new generation of space-borne and ground-based observational tools.

MHD waves are propagating or standing perturbations of macroscopic parameters of the plasma (see Alfvén 1942, who was eventually awarded the Nobel prize in 1970). More specifically, MHD waves can perturb the magnitude and direction of the magnetic field, the plasma mass density and associated concentrations of individual species (e.g. electrons and positive ions), plasma temperature and gas pressure. In addition, MHD waves include perturbations of the electric field, electric current, and macroscopic (or bulk) flows of the plasma. Essentially, the presence of MHD waves is connected with MHD restoring forces associated with the magnetic tension and total (gas plus magnetic) pressure, and with the plasma inertia, caused by the frozen-in condition (perpendicular motions of the plasma lead to the change of the magnetic field geometry, and the other way around). MHD waves have been intensively studied in the Earth's magnetosphere for several decades. In the solar corona, the main interest in MHD waves appeared more recently, in the late 90s, with the first observations of these waves with high-resolution extreme-ultraviolet (EUV) imagers on the space missions SOlar and Heliospheric Observatory (SOHO) and Transition Region and Coronal Explorer (TRACE). Both coronal and magnetospheric observations provide us with abundant information about MHD waves. In both the fields, there is a number of elaborated theoretical models addressing specific observational properties of MHD waves. Responding to the intensive research activity in the MHD wave studies, there are a number of comprehensive reviews of different aspects of the topic, see, e.g. Zaitsev and Stepanov (2008), Petrosyan et al. (2010), Banerjee et al. (2011), Patsourakos and Vourlidas (2012), De Moortel and Nakariakov (2012), Stepanov et al. (2012), Mathioudakis et al. (2013), Liu and Ofman (2014) for most recent "solar" reviews, and Guglielmi and Pokhotelov (1996), Walker

(2005), Alperovich and Fedorov (2007) for "magnetospheric" reviews. Regrettably, in the majority of cases MHD wave phenomena in the solar corona and the Earth's magnetosphere are studied separately. Moreover, cross-talk between these two communities who are studying rather similar plasma environments is complicated by the use of different terminology and different observational techniques.

A comparative study of physical phenomena associated with MHD waves in the corona and magnetosphere provides us with promising basis for deepening our understanding of MHD waves in general. Moreover, the complementarity of the knowledge gained by both these research communities, and exploitation of differences and similarities of MHD wave dynamics in the corona and magnetosphere can bring breakthrough results to both research branches, and is of unequivocal importance for MHD wave studies in other astrophysical, geophysical, space and laboratory plasma systems. The aim of this review is to initiate the mutually beneficial dialogue between the research communities specialising in MHD wave studies in the solar corona and the Earth's magnetosphere. To begin with we shall briefly introduce the basic properties of coronal and magnetospheric plasmas, aiming to establish the common terminology and create the ground for the further discussion. This will be followed by the discussion of specific phenomenology and theoretical modelling. In the end, we describe the similarities and differences between the observed MHD waves. Most notably, in the solar corona the waves are measured through remote-sensing and only the collective oscillation parameters can be measured. On the other hand, in magnetospheric waves in-situ parameters are measured, but often the global picture is lacking and no detailed spatial information is available.

MHD wave processes in the terrestrial magnetosphere are observed as ultra-low frequency (ULF) waves in the frequency band from fractions of mHz to a few Hz. Interestingly, despite very different spatial scales, MHD wave processes observed in the solar corona have frequencies in the same band. We describe both theoretical models and analysis of observational ground and satellite data. We have tried not just to review separately ULF waves in the magnetosphere and solar coronal waves, but to provide, on one hand, observational and theoretical ideas from magnetospheric physics which could be applied in solar physics and the other way around. In addition, we outline unresolved problems, where the experience and expertise gained in the general MHD wave community is of great importance. This review is mainly oriented to specialists in magnetospheric physics and solar physics, but not familiar with specifics of the adjacent research fields. In other words, the solar part is written for magnetospheric physicists, whereas the magnetospheric part—for solar specialists. The comprehensive reference list would be too lengthy and might exceed the review length. Therefore, we have provided references to key papers and reviews only, whereas many important observational studies or historic aspects of a problem have been omitted.

1.1 What Is the Solar Corona?

The corona of the Sun is the upper-most part of the solar atmosphere. It consists of almost fully-ionised hydrogen plasma, with about 20 % (by mass) of alpha particles and much lower fraction (less than 2 % by mass) of ions of heavier chemical elements. The corona lies above the partly-ionised and relatively cool region of the solar atmosphere, the *chromosphere*, where the temperature is a few tens of thousand K, and the mass density drops down with height from about $10^{-8}\ \mathrm{g\,cm^{-3}}$ to $10^{-14}\ \mathrm{g\,cm^{-3}}$ in about 3000 km. In the corona, the mass density keeps decreasing with height, with the typical values of $10^{-16}\ \mathrm{g\,cm^{-3}}$. The corresponding value of the electron concentration is of the order of $10^{8}\ \mathrm{cm^{-3}}$. Typically,

1.2.4 Main Differences Between the Corona and Earth's Magnetosphere

The solar corona and terrestrial magnetosphere are seemingly very different plasmas: plasma of the low corona is collisional (see the estimations in Sect. 1.1, showing that typical collision times much shorter than the observed wave periods), whereas the magnetospheric plasma is collisionless. Nonetheless, MHD approach works well for both those two opposite extreme situations. MHD theory was elaborated to describe motion and waves in a highly-conductive fluid, such as highly-collisional plasma of the solar corona. However, even in a collisionless plasma, such as the near-Earth plasma environment, the single-fluid MHD approach can be applied for large-scale wave processes owing to a nearly-infinite field-aligned conductivity (e.g. Kadomtsev 1982). Only for small-scale processes in the magnetosphere (a relevant scales are given in Sect. 12) the assumption of the infinite field-aligned conductivity, and hence the applicability of the MHD approach, may be violated. These small-scale ULF waves, as well as processes where large-scale wave interaction with a small group of resonant particles are involved, should be described by the kinetic approach, with the use of the Vlasov equation.

Concerning the ion cyclotron frequency, frequencies of both MHD oscillations in the corona and the long-period part of ULF waves in the magnetosphere (e.g., Pc3–5 and Pi2–3 pulsations) are much lower than it. Only high-frequency part of magnetospheric ULF waves (e.g., Pc1 and Pi1 pulsations) has the frequencies approaching the lowest values of the magnetospheric proton cyclotron frequency, near the tops of the magnetic field lines. These pulsations are associated with electromagnetic ion-cyclotron waves.

Another important difference is connected with the minor species, which should be taken into account in the consideration of low-frequency cyclotron resonances (e.g. Cranmer 2002). If in the corona the heavy elements are highly ionised (e.g. Fe IX, He II, O VI), in the magnetosphere the lower ionisation states, e.g. O I and He I are abundant.

Observational approaches in these two plasma environments are very different too. The main difference compared to coronal MHD wave observations is that in the magnetosphere and on the ground, observations are in-situ point observations, while solar observations are obtained from remotely sensed images of the phenomenon as a whole. Thus, coronal observations allow us to study simultaneously the time and spatial evolution of the waves, e.g. resolving both the wavelength and the wave period. However, these observations may be affected by insufficient time and spatial resolution, and are affected by optically-thin effects, i.e. the integration along the line of sight. On the other hand, magnetospheric observations are usually not restricted by the resolution, but may lack the spatial information.

Thus, the similarity between the solar coronal and Earth's magnetospheric plasmas should be exploited with serious caution. There is a number of fundamental physical differences that need to be taken into account. Nevertheless, despite the important differences of these two plasma environments, in the following discussion we attempt to establish the ground for the consolidated understanding of MHD wave processes in the magnetosphere and the corona.

2 Global Propagating Waves in Solar Corona

2.1 Observations of Global Coronal Waves

There is not any observational evidence of global oscillations of the solar corona, similar to the low-degree acoustic oscillations of the solar surface. The largest example of the coronal MHD wave activity is propagating *global coronal waves*. The first detection of global coro-

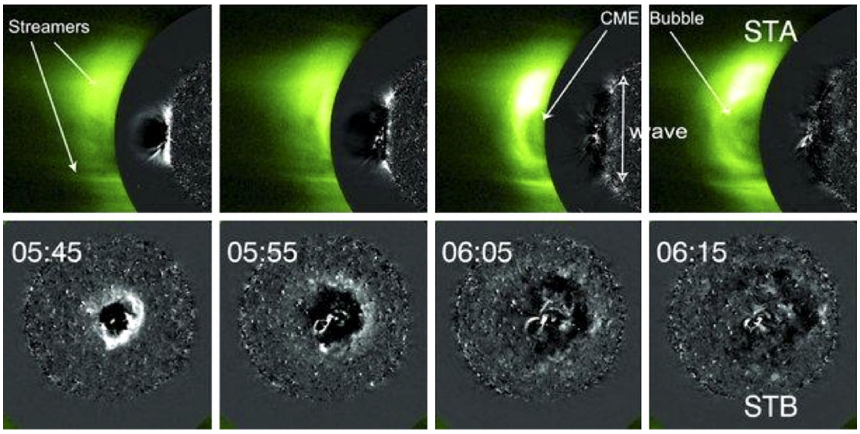

Fig. 3 First quadrature observations from STEREO of a CME-EUV wave event. *Top panel*: temporal sequence of COR1-EUVI 195 Å images from STEREO-A, showing the evolution of the wave on the solar disk and the CME in the coronagraph from a lateral perspective. *Bottom panel*: front view of the wave from STEREO B, with a clear circular wave front. From Patsourakos and Vourlidas (2009)

nal waves was achieved by the Extreme ultraviolet Imaging Telescope (EIT) aboard SoHO, which was launched in 1995. Large-scale coronal disturbances propagating in the form of arc or circular bright fronts were captured in the images at 195 Å (see Fig. 3). These disturbances, also referred to as coronal bright fronts (CBF), are usually generated after strong impulsive releases of energy and cover a significant portion of the solar disk, comparable with the solar disk radius. The perception of a propagating wave is additionally enforced by a trailing and expanding dimming region (signature of the evacuation of the plasma), highlighted using a running difference method. They were named as "EIT waves", in virtue of the instrument that has permitted their discovery (Thompson et al. 1999), and were immediately interpreted as the manifestation of a fast-magnetoacoustic mode, i.e. a compressive wave propagating quasi-perpendicularly to the direction of the local magnetic field (e.g. Wang 2000; Ofman and Thompson 2002). Almost twenty years from their discovery, a great debate about their nature, formation and relationships to flares and CMEs is still ongoing. This debate has been further stimulated by observations from the follow-up and currently operative space missions, e.g. STEREO and SDO. For this reason, EIT waves are now referred with the generic name of "EUV waves" or global coronal waves (Fig. 3). For a detailed perspective on the topic, the reader is invited to refer to the reviews of Gallagher and Long (2011), Patsourakos and Vourlidas (2012) and references therein.

The first possible identification of large-extended disturbances propagating in the solar atmosphere should actually be moved backward of thirty years. Indeed, observations in the Hα channel of the chromosphere, which is the layer just below the corona, led to detecting large-scale arc-shaped fronts propagating away from a flaring region at very high speeds ranging between 500–1500 $\mathrm{km\,s^{-1}}$ (for comparison, chromospheric sound and Alfvén speeds are about one or two orders of magnitude lower). These rapidly-propagating chromospheric disturbances are known as Moreton waves, after the name of the discoverer (Moreton 1960), and they were interpreted and modelled in terms of a fast MHD shock that propagates in the corona and sweeps through the underneath chromosphere. The wave, refracted towards a low Alfvén velocity region, sharpen into an enhanced fast-mode shock wave that could emit type II radio bursts (Uchida 1968) (which are slowly-drifting spectral features that are usually associated with electrons accelerated by the shock front). Thus,

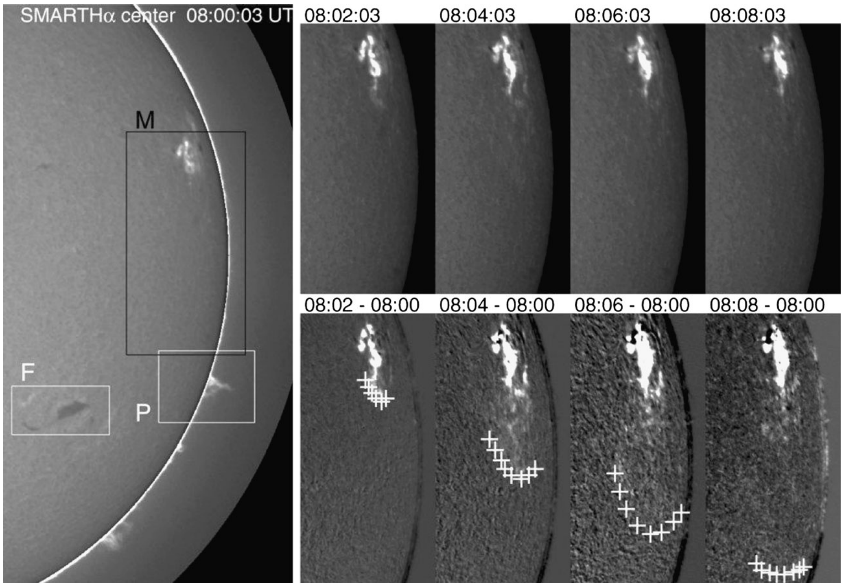

Fig. 4 Example of a Moreton wave observed with the Solar Magnetic Activity Research Telescope (SMART) (http://www.hida.kyoto-u.ac.jp/SMART/). The region "M" in the *left panel* outlines the region of interest from where a sequence of Hα *images* are given in normal intensity (*top-right panel*) and running difference intensity (*top-bottom panel*). The Moreton wave front is marked by white plus signs. From Asai et al. (2012)

the EIT waves detected in the corona have been regarded as the coronal counterpart of chromospheric Moreton waves. However, several studies showed big discrepancies between Moreton and EIT waves, especially in the estimate of the propagation speed. An example is shown in Fig. 4.

The main features of global EUV waves as deduced from the analysis of numerous observations can be summarised as follows:

- Global coronal waves are mainly seen as a single wave front (a solitary wave).
- They appear to be triggered by impulsive energy releases, such as flares or CMEs. Precise statistical studies show that EUV waves are more associated with CMEs rather than flares. Without CMEs, even a powerful flare cannot produce global waves (Biesecker et al. 2002; Chen 2006). Generally, the appearance of a global coronal wave implies an expanding CME although occasionally the white-light coronagraph may not be able to detect it due to sensitivity. Correspondingly some slow CMEs are not accompanied by clear global coronal waves possibly because the intensity enhancement is too weak.
- EUV waves propagate in the form of a circular or large arc-shaped bright front of the EUV emission, with a typical speed in the range of 200–500 $\mathrm{km\,s^{-1}}$, followed by an expanding dimming region. The dimming is associated with the evacuation of the coronal plasma due to the lift-off of the associated CME flux-rope. Few events reveal a dome-like structure, resulting in a 3D expansion (radial and lateral directions) of the EUV wave (Veronig et al. 2010).
- Kinematic analysis of several events (Fig. 5) show that, after being excited, the wave fronts are drastically decelerated (Veronig et al. 2008; Long et al. 2011) and the magnitude of the deceleration is even higher for waves with higher initial speeds (Warmuth and Mann 2011).

- understand better the relationship of EUV waves with powerful flares, type II radio bursts;
- define the 3D evolution of EUV waves and their related CMEs, in particular the physical mechanism for the decoupling of the EUV and CME fronts in the early stages of the evolution;
- the processes occurring during the propagation of EUV in the corona, the response of the coronal medium to the wave transit, quantification of the rate of transmission/reflection through coronal holes, magnetic separatrices and other obstacles;
- deeper understanding of the relationship between global coronal and chromospheric waves;
- determination of the thermal evolution of the EUV waves;
- revealing the effect of fine structuring (the effective dispersion and dissipation) on the wave evolution, including wave scattering and coupling with other modes.

The phenomenon of global coronal waves seems to be similar to impulsive fast magnetoacoustic disturbances propagating in the Earth's magnetosphere, discussed in Sect. 5.4.2. This similarity and its implications need to be studied.

3 Magnetospheric MHD Waveguides and Resonators

Natural MHD resonators and waveguides formed by various plasma non-uniformities play an important role in both coronal and magnetospheric physics. Their occurrence causes the effects of wave dispersion, refraction, mode coupling, and the possibility of significant accumulation of the wave energy in certain regions of outer space, where this wave power can influence dynamics of charged particles. Also, an MHD resonator can form a fine multi-peak structure of MHD wave spectra, which can be used as a tool for "hydromagnetic spectroscopy" of the space environment, known as MHD seismology. In this section we discuss these phenomena in the Earth's magnetosphere.

3.1 MHD Waves in a Cold Plasma

In a cold plasma (i.e. $\beta = 0$, a very good approximation for the majority of the magnetosphere), MHD modes can be described by Maxwell's equations with the dielectric permeability being derived via ideal MHD as $\hat{\varepsilon}_\perp = c^2/V_\mathrm{A}^2$, where c is the speed of light. For curved field lines it is convenient to use a field-aligned orthogonal curvilinear coordinate system $\{x^1, x^2, x^3\}$, in which the field lines play the role of coordinate lines x^3, the stream lines are coordinate lines x^2, and the surfaces of constant pressure P (magnetic shells) are coordinate surfaces $x^1 = \mathrm{const}$ (Fig. 8). Coordinates x^1 and x^2 represent the radial and azimuthal coordinates. The physical length along a field line is expressed in terms of an increment of the corresponding coordinate as $dl_\| = \sqrt{g_3}dx^3$, where g_3 is the component of the metric tensor, and $\sqrt{g_3}$ is the Lamé coefficient denoted as h_3. Similarly, for the transverse direction we have $dl_1 = \sqrt{g_1}dx^1$, and $dl_2 = \sqrt{g_2}dx^2$. The corresponding Lamé coefficients are $h_1 = \sqrt{g_1}$ and $h_2 = \sqrt{g_2}$. The determinant of the metric tensor is $g = g_1 g_2 g_3$.

As any electromagnetic field can be decomposed into the potential and non-potential parts, the MHD wave electric ($\mathbf{e}$) and magnetic ($\mathbf{b}$) fields are decomposed into two modes: the Alfvén mode in which the disturbed magnetic field $\mathbf{b}_\perp$ is perpendicular to the equilibrium field $\mathbf{B}_0$ and divergence-free, $\nabla \cdot \mathbf{b}_\perp = 0$, and thus the longitudinal component vanishes, $b_\| = 0$; and the fast magnetoacoustic mode in which $\mathbf{b}_\perp$ is curl-free, $\nabla \times \mathbf{b}_\perp = 0$, and thus the field-aligned component of the current vanishes, $j_\| = 0$. The electric field $\mathbf{e}$ has only

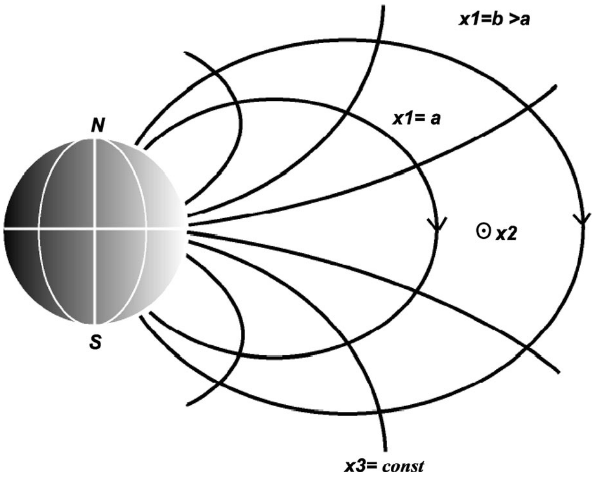

Fig. 8 The field-aligned orthogonal curvilinear coordinate system $\{x^1, x^2, x^3\}$ for the Earth's magnetosphere, in which the field lines play the role of coordinate lines x^3, the stream lines are azimuthal coordinate lines x^2, and the magnetic shells are radial coordinate surfaces $x^1 = \text{const}$. From Mager and Klimushkin (2008)

components transverse to the magnetic field, as $\varepsilon_\parallel \to \infty$. A 2D electric field $\mathbf{e}_\perp$ can be decomposed into the potential (Alfvénic) and solenoidal (magnetoacoustic) parts, characterised by the potentials Φ and Ψ, correspondingly, as

$$\mathbf{e}_\perp = -\nabla_\perp \Phi + \nabla_\perp \times \mathbf{e}_\parallel \Psi. \tag{2}$$

Thus, linearised MHD equations for waves with the frequencies ω and wave vector $\mathbf{k} = (k_1, k_2, k_3)$ (where the indices correspond to the axes of the curvilinear coordinate system shown in Fig. 8) in an inhomogeneous plasma immersed into a curvilinear magnetic field can be reduced to the following set

$$\begin{aligned} &\hat{L}_\mathrm{A}\Phi + \hat{L}_\mathrm{c}\Psi = 0, \\ &\hat{L}_\mathrm{F}\Psi + \hat{L}_\mathrm{c}^{+}\Phi = 0, \end{aligned} \tag{3}$$

where $\hat{L}_\mathrm{F}(\omega)$ is the fast magnetoacoustic operator

$$\hat{L}_\mathrm{F} = -\Delta_\perp \frac{V_\mathrm{s}^2 + V_\mathrm{A}^2}{V_\mathrm{A}^2}\Delta_\perp - \left[\partial_1 \frac{g_2}{\sqrt{g}}\hat{L}_\mathrm{P}\frac{g_2}{\sqrt{g}}\partial_1 - k_2^2\frac{g_1}{\sqrt{g}}\hat{L}_\mathrm{T}\frac{g_1}{\sqrt{g}}\right], \tag{4}$$

with $\Delta_\perp \equiv \partial_1(g_2/\sqrt{g})\partial_1 - k_2^2(g_1/\sqrt{g})$, and V_s is the sound speed and V_A is the Alfvén speed; $\hat{L}_\mathrm{A}$ is the Alfvénic operator that comprises the Alfvénic toroidal $\hat{L}_\mathrm{T}$ and Alfvénic poloidal $\hat{L}_\mathrm{P}$ operators,

$$\hat{L}_\mathrm{A} = \partial_1 \hat{L}_\mathrm{T}\partial_1 - k_2^2\hat{L}_\mathrm{P},$$

with

$$\hat{L}_\mathrm{T} = \partial_3\frac{g_2}{\sqrt{g}}\partial_3 + \frac{\sqrt{g}}{g_1}\frac{\omega^2}{V_\mathrm{A}^2}, \qquad \hat{L}_\mathrm{P} = \partial_3\frac{g_1}{\sqrt{g}}\partial_3 + \frac{\sqrt{g}}{g_2}\frac{\omega^2}{V_\mathrm{A}^2}; \tag{5}$$

and coupling between the modes is determined by the operator $\hat{L}_\mathrm{c}$,

$$\hat{L}_\mathrm{c} = ik_2\left(\partial_1\frac{\omega^2}{V_\mathrm{A}^2}\right) + \left[\partial_1\partial_3\frac{g_2}{\sqrt{g}}\partial_3\frac{g_1}{\sqrt{g}}ik_2 - ik_2\partial_3\frac{g_1}{\sqrt{g}}\partial_3\frac{g_2}{\sqrt{g}}\partial_1\right];$$

contrast is for the lower harmonics ($n = 1$–2). Variations of Q-factor for higher harmonics ($n = 3$–4) are less significant: from about 3–5 during daytime up to about 7 during nighttime.

4 Coronal Plasma Non-uniformities as Magnetoacoustic Waveguides and Resonators

As the plasma of the solar corona is observed to be highly filamented along the magnetic field, the main building block of the coronal wave modelling is the theory of MHD modes of a plasma cylinder. This model is used for the description of dynamical processes in a number of plasma structures of the corona, e.g. loops of active regions and post-flare arcades, various filaments, plumes in coronal holes, etc.

Consider a straight cylindrical magnetic flux tube of radius a, filled in with a plasma with the properties different from the surrounding plasma. The magnetic field is directed along the axis of the cylinder, that coincides with the z-axis. In the simplest case, the equilibrium physical parameters experience a jump at the boundary of the cylinder and are constant elsewhere. Thus, inside the cylinder, the mass density, the plasma temperature and pressure, and the parallel component of the magnetic field are ρ_0, p_0, T_0 and B_0, respectively, while the values of these quantities outside the cylinder are ρ_e, p_e, T_e and B_e. The equilibrium condition is the continuity of the total pressure P_tot, which is the sum of the plasma and magnetic pressures, across the boundary,

$$p_0 + \frac{B_0^2}{2\mu} = p_\mathrm{e} + \frac{B_\mathrm{e}^2}{2\mu}. \tag{23}$$

The characteristic speeds of MHD waves inside and outside the cylinder are the sound speeds V_s0 and V_se, and the Alfvén speeds, V_A0 and V_Ae, respectively. It is also convenient to define the so-called tube (or cusp) speeds, V_T0 and V_Te, namely $V_\mathrm{T0} = V_\mathrm{s0}V_\mathrm{A0}/\sqrt{V_\mathrm{s0}^2 + V_\mathrm{A0}^2}$. The value of the effective adiabatic index γ_0 that is used in the definition of the sound speed, was recently seismologically estimated in the corona as about 1.1 (Van Doorsselaere et al. 2011).

Linear MHD perturbations of this stable equilibrium are described by the dispersion relation

$$\rho_\mathrm{e}\big(\omega^2 - k_z^2 V_\mathrm{Ae}^2\big)\kappa_0 \frac{I_m'(\kappa_0 a)}{I_m(\kappa_0 a)} + \rho_0\big(k_z^2 V_\mathrm{A0}^2 - \omega^2\big)\kappa_\mathrm{e}\frac{K_m'(\kappa_\mathrm{e} a)}{K_m(\kappa_\mathrm{e} a)} = 0, \tag{24}$$

where ω is the angular frequency, k_z is the longitudinal wavenumber, m is the azimuthal wave number, $I_m(x)$ and $K_m(x)$ are modified Bessel functions of order m, the prime denotes the derivative with respect to the argument. The expressions

$$\kappa_0^2 = -\frac{(\omega^2 - V_\mathrm{s0}^2 k_z^2)(\omega^2 - V_\mathrm{A0}^2 k_z^2)}{(V_\mathrm{s0}^2 + V_\mathrm{A0}^2)(\omega^2 - V_\mathrm{T0}^2 k_z^2)}, \qquad \kappa_\mathrm{e}^2 = -\frac{(\omega^2 - V_\mathrm{se}^2 k_z^2)(\omega^2 - V_\mathrm{Ae}^2 k_z^2)}{(V_\mathrm{se}^2 + V_\mathrm{Ae}^2)(\omega^2 - V_\mathrm{Te}^2 k_z^2)}. \tag{25}$$

are the transverse wave numbers in the internal and external media, respectively. They are equivalent to k_r in Eq. (21). Waves that correspond to different solutions to Eq. (24) are referred to as MHD *modes* of the plasma cylinder. For $\kappa_\mathrm{e}^2 > 0$ the perturbations are evanescent outside the cylinder, and are guided along the cylinder. These modes are called *trapped* (Zaitsev and Stepanov 1982; Edwin and Roberts 1983). Modes with $\kappa_\mathrm{e}^2 < 0$ are subject to leakage to the external medium. In this *leaky* regime the wave energy is guided along the

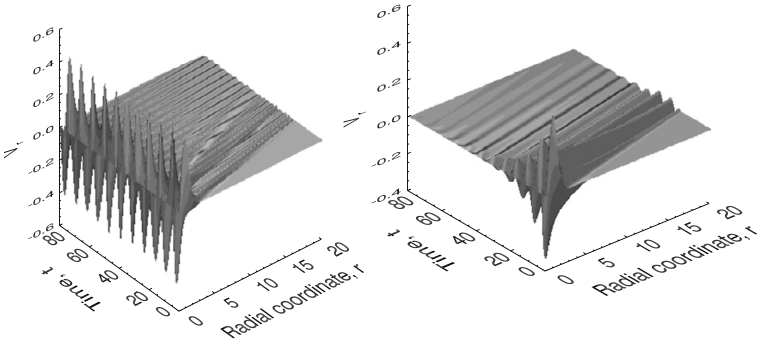

Fig. 15 Variation of the radial velocity in the standing sausage mode of a plasma cylinder, in the trapped (*left panel*) and leaky (*right panel*) regimes. From Nakariakov et al. (2012)

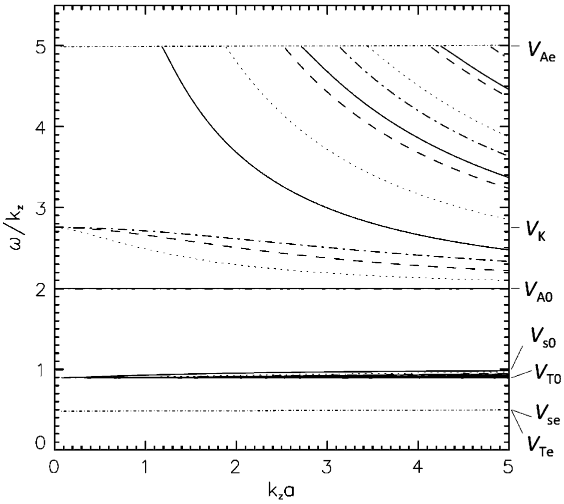

Fig. 16 Phase speeds ω/k_z of MHD modes of a field-aligned plasma cylinder as a function of the longitudinal wave number k_z for the parameters $V_{A0} = 2V_{s0}$, $V_{Ae} = 5V_{s0}$, $V_{se} = 0.5V_{s0}$, $V_{s0} = 1$. The *horizontal dash-dotted lines* indicate the characteristic speeds. The *solid horizontal line* shows the torsional Alfvén waves. The *solid curves* are solutions for $m = 0$, the *dotted lines* for $m = 1$, the *dashed lines* $m = 2$ and the *dash-dotted* for $m = 3$ modes. Figure adapted from Nakariakov and Verwichte (2005)

cylinder too, but the waves are continuously radiated to the external medium. Hence, the amplitude inside the cylinder decreases (Cally 1986; Kopylova et al. 2007) that is accounted for by a complex ω. These two regimes are illustrated in Fig. 15 for a standing mode.

Properties of the modes are determined by the physical parameters of the equilibrium. For example, in a typical coronal loop with $V_{A0} < V_{Ae}$ and $V_{se} < V_{s0}$, phase speeds of the trapped modes lie in two bands, the *fast* band, $[V_{A0}, V_{Ae}]$, and the *slow* band $[V_{T0}, V_{s0}]$. The general solutions to the dispersion relation (Eq. (24)) are displayed in Fig. 16.

The integer azimuthal wavenumber m determines the modal structure with respect to the angle around the axis of the cylinder (see Fig. 17). In the low-β plasma the parameter m is important for the properties of fast modes, and practically does not affect the slow modes. Thus, we consider fast modes of different m only.

Waves with $m = 0$ (perturbations are independent on the azimuthal angle with respect to the cylinder axis) are called *sausage* modes, also known as *radial*, *peristaltic* or simply *fast magnetoacoustic*. A sausage mode is a sequence of axisymmetric expansions and contractions of the cross-section of the cylinder, accompanied by a variation in the plasma density and magnetic field magnitude. Perturbations of the plasma pressure and magnetic field are in phase in this mode. This mode does not perturb the axis of the cylinder. For a fixed wave-

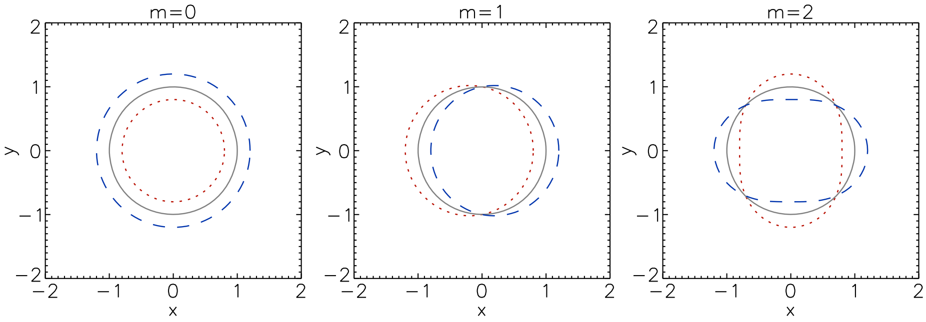

Fig. 17 Diagrams showing the structure of $m = 0$ (sausage) modes (*left panel*), $m = 1$ (kink) modes (*middle panel*), and $m = 2$ (fluting) modes (*right panel*). The *solid line* is the equilibrium position of the flux tube, and the *dotted* and *dashed lines* two extreme phases

length, a sausage mode has the shortest period of all possible modes in a plasma cylinder (see Fig. 16). A sausage mode has a cut-off value of ω dependent on the wavelength, that determines the transition from the leaky regime to the trapped regime. In the low-β plasma the velocity streamlines for a sausage mode are almost radial.

Waves with $m = \pm 1$ are *kink* modes that are non-axisymmetric displacements of the cylinder axis with little or no deformation of the loop cross-section. Kink modes with finite wavelengths are compressive, and hence like sausage modes, they have fast magnetoacoustic properties. In the long wavelength limit kink modes become weakly compressive and are sometimes called *Alfvénic* (Goossens et al. 2012) and related to surface Alfvén waves. In this limit the kink mode phase speed approaches the so-called *kink speed*

$$V_{\mathrm{K}} = \left(\frac{\rho_0 V_{\mathrm{A0}}^2 + \rho_{\mathrm{e}} V_{\mathrm{Ae}}^2}{\rho_0 + \rho_{\mathrm{e}}}\right)^{1/2} \approx \left(\frac{2}{1 + \rho_{\mathrm{e}}/\rho_0}\right)^{1/2} V_{\mathrm{A0}}, \qquad (26)$$

where the second expression corresponds to the low-β plasma. In this regime a kink mode is characterised by periodic radial and azimuthal velocity streamlines. Waves with higher m are referred to as *flute* or *ballooning* modes. They have not been convincingly identified in coronal observations, and hence they are not discussed in this review further.

Longitudinal (or slow) modes are constituted by mainly field-aligned compressive motions. In the short wavelength limit these modes reduce to usual acoustic waves and propagate at the sound speed V_{s0}. Perturbation of the plasma pressure and magnetic field are in anti-phase in this mode. In the long-wavelength limit, longitudinal modes propagate at the tube speed V_{T0}. In this regime the local wave vector is almost perpendicular to the field, while the bulk flows induced by this mode remain mainly field-aligned. As longitudinal modes with different azimuthal wavenumbers m have in a low-β plasma very close dispersion curves, usually, possibly erroneously, they are considered as a single mode. However, higher $|m| > 0$ slow modes should result in oppositely directed parallel velocities in the loop.

In cylinders with smooth radial profiles of the Alfvén speed individual surfaces of constant Alfvén speed support propagation of incompressive Alfvén waves called *torsional* waves. In these waves the plasma moves in the azimuthal direction only, and hence they can be considered as waves of alternate vorticity and electric current density. Torsional waves do not perturb the cylinder boundary radially, i.e. compressively. In the solar context, torsional waves are not considered as modes, as they are not collective: their spectrum is continuous as different surfaces of constant Alfvén speed support waves with different periods and/or wavelengths, that do not interact with each other in an ideal plasma. In contrast, sausage, kink, flute and longitudinal modes are collective, disturbing the whole cylinder. Moreover, in contrast with MHD modes that are subject to geometrical dispersion, torsional waves are dispersionless.

A dispersion relation analogous to Eq. (24) can be written for other plasma configurations, e.g. for a field-aligned slab or a current sheet. Properties of MHD modes of a slab are mainly similar to cylinder modes (see, e.g. Edwin and Roberts 1982). The major difference is that slab kink modes tend to the external Alfvén speed in the long wavelength limit, instead of the kink speed. In a number of theoretical models, the slab geometry is used instead of the cylindrical geometry, because of the analytical simplicity.

Despite its obvious simplicity, the theory of MHD modes of a straight plasma cylinder with a sharp boundary, provides a solid and commonly accepted basis for the study of MHD oscillations and waves in various plasma configurations of the solar corona. The generalisation of this theory on the important case of the smooth boundary is discussed in Sect. 5.5. Another potentially important effect, of the loop curvature, was shown to be not significant for MHD mode periods (Van Doorsselaere et al. 2004b).

5 MHD Mode Conversion

A linear resonant conversion of the fast mode into the Alfvén mode can occur on some distinct magnetic (resonant) shells. In the magnetospheric and coronal physics, this phenomenon plays rather different roles: while in the former it is considered as a generation mechanism for the observed (usually, Alfvén) modes or a way to interpret its observed spatial structure, in the latter it is considered as a mechanism for the absorption of the energy of observed collective modes, i.e. their linear transformation in unresolved small-scale Alfvénic motions, and associated plasma heating. However, the physics behind this phenomenon is similar in both branches of MHD wave physics.

5.1 The Box Model

The simplest model which allows one to take into account the plasma inhomogeneity is the box model, where the field lines are considered to be straight and the Alfvén speed depends only on the perpendicular (e.g. corresponding to the radial direction in the magnetospheric geometry or in coronal flux tubes) coordinate x, across the field directed in the z-direction (see Fig. 18). In this model all perturbed values can be chosen to depend on the e.g. azimuthal (y) and parallel (z) coordinates as $\propto \exp(-i\omega t + ik_y y + ik_\parallel z)$.

The linearised MHD equations describing the structure of coupled Alfvén and fast magnetoacoustic modes in the box model can be combined into a single ordinary differential equation for the wave component b_z

$$b_z'' - 2\frac{\kappa_A'}{\kappa_A} b_z' + \kappa_F^2 b_z = 0, \tag{27}$$

where the prime means differentiation with respect to the radial coordinate (e.g. $\kappa_A' = d\kappa_A/dx$), and

$$\kappa_A^2 = k_A^2 - k_\parallel^2, \qquad \kappa_F^2 = k_A^2 - k_\parallel^2 - k_y^2, \tag{28}$$

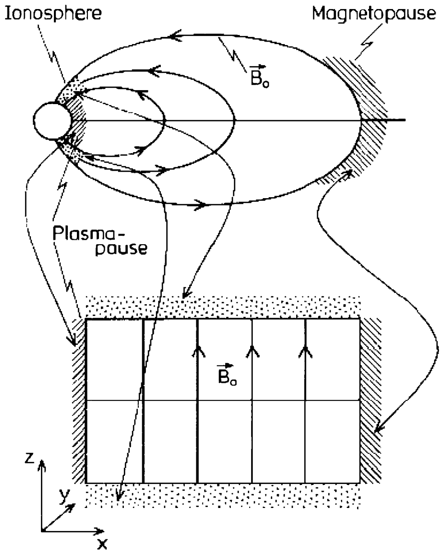

Fig. 18 Schematic illustration of the correspondence between the magnetospheric box model and realistic magnetosphere. From Glassmeier et al. (1999)

where $k_A = \omega / V_A$. For such a 1D inhomogeneity the mathematical structure of the MHD equations is similar (but not identical) to Maxwell's equations for resonant conversion of electromagnetic waves into plasma oscillations.

Equation (27) has two characteristic points:

- the singularity point x_A at $\omega = k_\parallel V_A(x)$, where $\kappa_A = 0$;
- the reflection point x_F at $\omega^2 = (k_y^2 + k_\parallel^2) V_A^2(x)$, where $\kappa_F = 0$ and the effective wave number of WKB solution $k_x = k_F$ tends to zero.

Since the resonant point is situated on the magnetic surface where the Alfvénic dispersion relation $\omega = k_\parallel V_A$ holds, it corresponds to resonant Alfvén mode excitation on the resonant surface (the *field line resonance* in the magnetospheric physics). The Alfvén mode is subject to effective dissipation by small but finite viscosity or resistivity, because of very steep gradients in the radial direction. Thus, the singularity at x_A results in the energy transfer towards the resonant surface, its accumulation in its vicinity, absorption of the wave energy and subsequent plasma heating on the resonant surface.

The reflection point x_F is a signature of the fact that the fast mode propagating from regions of the low Alfvén speed cannot reach the resonant point being reflected back. However, a part of the fast mode energy is tunnelling deeper into the plasma (because of the exponentially evanescent solution). It is that tunnelled energy that generates the Alfvén mode on the resonant magnetic shell. This phenomenon is usually called the *Alfvén resonance*.

The Alfvén resonance and transparency regions for the fast magnetoacoustic mode are spatially separated from one another, so the mode conversion has the character of sub-barrier tunnelling. The distance between the resonant and reflecting shells depends on the azimuthal wave vector value k_y. If k_y is large (azimuthally small-scale waves) compared with the inverse inhomogeneity scale in plasma, then only the exponentially small part of the wave energy can penetrate deep into the magnetosphere. In this case, the resonant mechanism of the Alfvén mode generation is ineffective and one must search for the wave's sources *in situ*. This is why the magnetospheric physicists believe that the Alfvén waves with high azimuthal wave numbers m are generated by some internal processes (see Sect. 9.2 for more detail).

Equation (40) was derived under the assumption that the damping time τ is much greater than the period P. In recent years, the validity of this damping expression (Eq. (40)) has been questioned, since observations (Sect. 6.1) show that the damping time is of the order of the period ($\tau \gtrsim P$, see also Fig. 24). For example, Pascoe et al. (2013b) found in numerical simulations that the damping is initially described by a Gaussian function ($\exp(-t^2/\tau^2)$), rather than exponential damping ($\exp(-t/\tau)$) as expected from Eq. (40). This was confirmed by Hood et al. (2013), who quantified the effect analytically. The presence of Gaussian damping has a potential impact on measuring damping times and therefore on seismology with damping times as well.

The main open questions and challenges for the theory of resonant absorption in the context of the corona lie in the generalisation of the theory to more complicated and realistic plasma systems, and in the observational signatures. A more concrete list would be:

- The observed kink oscillations have a large displacement (compared to the loop radius). How does resonant absorption work in such a non-linear regime? How does it compete against the non-linearly excited Kelvin–Helmholtz instability at the edge of the loop (e.g. Terradas et al. 2008a; Antolin et al. 2014)?
- How does resonant absorption work in bundles of loops? How does the global motion transfer to the individual strands, and how do the individual strands dissipate the transverse motion?
- What are the observational signatures of resonant absorption? Can we directly observe the mechanism of resonant absorption taking place, using spectrometers or imaging telescopes?
- What is the role played by the effect of resonant absorption in the undamped kink oscillations, see Sect. 6.1?

6 Standing Modes of Coronal Plasma Structures

As in the corona there are both open and close plasma configurations, coronal MHD waves ("local", in contrast with the global coronal waves discussed in Sect. 2) occur in both standing and propagating forms. Wavelengths of standing waves are prescribed by the lengths of resonators, e.g. the length of the oscillating coronal loop. There can be a number of standing longitudinal harmonics. The longest wavelength oscillation is called the *global* (or fundamental) mode. Usually only the global mode and its second harmonics are detected in coronal observations. Standing MHD oscillations in the corona are truly local, connected with certain loops or other plasma structures. Their wavelengths are determined by the geometrical parameters of the plasma non-uniformities that are essentially smaller than the solar radius. Also, the transverse scale of these non-uniformities is usually much shorter than the longitudinal scale, i.e. the non-uniformities are caused by field-aligned filamentation. Thus, the longitudinal wavelength of coronal standing waves are typically much longer than their transverse scale.

6.1 Standing Kink Modes

Transverse oscillations of coronal loops were first observed by Aschwanden et al. (1999) and Nakariakov et al. (1999) in the EUV band, inducing a number of observational studies and theoretical modelling. The oscillations are seen as transverse displacements of bright loops, with periods from a few minutes to several tens of minutes. Different loops have different well defined periods, which suggests that the oscillations have natural frequencies of the loop system. The beginning of the oscillation usually coincides with a flare or CME with an epicentre nearby (see Sect. 9.3). The oscillations are almost harmonic. After the excitation, kink oscillations experience a rapid decay, typically fitted with an exponential function with the characteristic decay time equal to 2–4 oscillation periods (although a Gaussian function may be more appropriate, see Sect. 5.5). Hence the quality factor of the oscillations, or the Q-factor, can be defined as $Q = \pi\tau/P$ and is between 6–25. The decay time scales linearly with the period of oscillations (see Ofman and Aschwanden 2002, and also Fig. 24). The strong damping is attributed to the effect of resonant absorption, discussed in Sect. 5.5, however, other mechanisms are possible, such as wave leakage, and phase mixing (see Ofman and Aschwanden 2002, for discussion). The amplitude of the oscillations is typically several Mm, that is several minor radii of the loop (radius of the loop's flux tube cross-section). The typical periods range from a few minutes in short EUV loops to several hours in dense cool filaments of prominences.

The loops of different lengths are observed to have different periods of oscillations. In almost all observed cases only a few periods of oscillations are seen. Occasionally, together with the displacement, periodic variation of the loop brightness is observed. This effect is most likely connected with the periodic variation of the column depth of the oscillating loop segment, caused by its displacement with respect to the LOS (Cooper et al. 2003a; Verwichte et al. 2009).

In the vast majority of cases the oscillations have horizontal polarisation, in other words the loop displacement is parallel to the surface of the Sun. The same polarisation is detected by some occasional quasi-stereoscopic observations (Verwichte et al. 2009). There have not been observational reports of the circular or elliptical polarisation. Usually only the global mode is seen, with the maximum displacement amplitude near the loop top, and only in a few cases higher longitudinal harmonics have been detected (Andries et al. 2009). In all cases, the nodes of the oscillation are observed near the loop footpoints, hence the dense plasma of the chromosphere acts as a rigid wall for the transverse oscillations (c.f. the effect of the ionosphere on the magnetospheric oscillations).

The period of standing kink oscillations is approximately determined as

$$P_{\mathrm{kink}} \approx 2L/n_{\mathrm{L}} V_{\mathrm{K}}, \tag{41}$$

where L is the loop length, and n_{L} is the longitudinal harmonic number that indicates the number of half-wavelengths along the loop (Fig. 26). However, there is a significant deviation, up to 10 %, from the equidistant spectrum, i.e., the ratio of the global mode period to the period of the second harmonics is less than 2. This effect is attributed to the interplay between density stratification and flux tube expansion: the Alfvén speed and hence the kink speed at the loop top and the footpoints are different from each other. The global mode with the maximum at the loop top then samples a lower kink speed than the second harmonics that samples the kink speed in the loop legs (see Andries et al. 2009, for detailed discussion).

Very recently a new regime of standing kink oscillations was discovered (Wang et al. 2012; Nisticò et al. 2013; Anfinogentov et al. 2013). It was found out that in addition to the intensively studied large-amplitude rapidly-decaying regime, there are also low-amplitude undamped oscillations, near the very threshold of the available spatial resolution of the observational instruments. Figure 25 shows both the decaying and decay-less regimes for the same loop. Oscillation periods in this new regime are not different from the large-amplitude kink oscillations in the same loop. The amplitude is lower than one minor radius of the loop. All segments of the loop are seen to oscillate in phase and hence the oscillations are standing. Usually several cycles of the oscillation are well seen, with the amplitude remaining constant

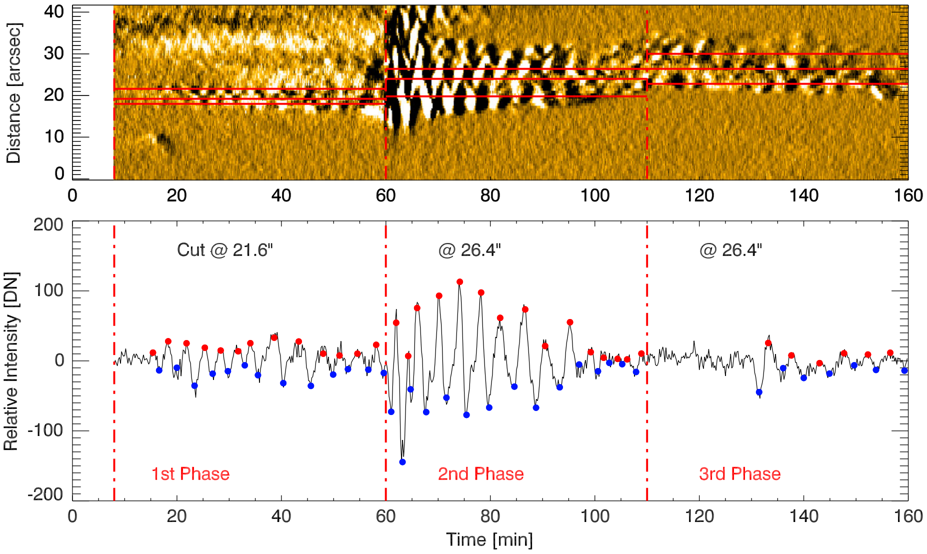

Fig. 25 Kink oscillations of a coronal loop. The *top panel* shows the time-distance plot made for a slit across the loop near its top. The periodic transverse displacements are clearly seen. The *bottom panel* shows the zoomed parts of the time distance maps: the *red* and *blue bullet* are the maxima and minima positions. The *1st* and *3rd phases* correspond to the decay-less low-amplitude oscillations, while the *2nd phase* to the large amplitude decaying oscillations excited by a CME. From Nisticò et al. (2013)

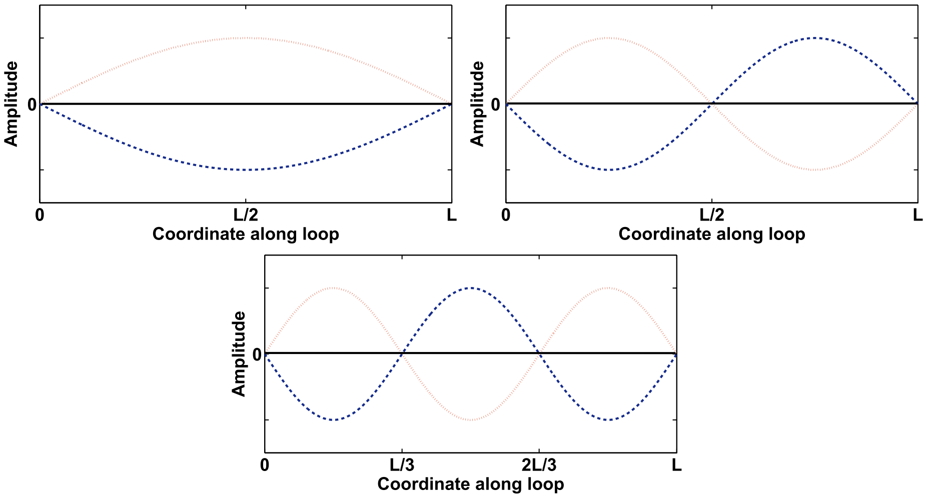

Fig. 26 Displacements of the plasma in the global mode (*top left*), its second harmonic (*top right*), and third harmonic (*bottom*) for a loop of length L. The *black line* shows the position of the undisturbed loop and the red dotted and blue dashed lines indicate the extrema of displacement, corresponding to different phases of the oscillation

or even growing during the observation. There is no observational indication that the oscillation is excited by any bursty energy release. It is very likely that the apparent end of the oscillation is not caused by any decay, but is simply connected with the deterioration of the observation conditions. The physical mechanism for the decay-less oscillations is still subject to discussion, while the constant amplitude may result from some balance between persistent external driving, e.g. by granulation motions, and damping, e.g. by resonant absorption.

Despite intensive study, there are still a number of open questions connected with kink modes. More specifically:

- The excitation mechanism in both decaying and decay-less regimes needs to be revealed.
- In the decaying large-amplitude regime, what is the mechanism for the selectivity of the excitation: why some loops gain the large initial displacement while similar loops situated nearby do not?
- Also, what causes the large initial displacement of the loop in this regime? (See discussion in Sect. 9.3.)
- Why is the horizontal polarisation predominantly excited?
- If the rapid decay of kink oscillations is indeed caused by resonant absorption, the transfer of energy from the kink oscillation to the torsional Alfvénic motions needs to be observed at least indirectly, e.g. via the increase in the non-thermal broadening of coronal emission lines.
- It is also unclear whether what we see as an oscillating loop is the actual loop, or it is a bundle of smaller scale plasma threads. For sharp transverse profiles of the plasma in the oscillating loop, resonant absorption efficiency is suppressed, and oscillations of good quality should be observed. But, they are not: in all observed cases the decay time is not longer than a few oscillation periods.

6.2 Sausage Modes

In the low-β plasma, a sausage ($m = 0$, see Sect. 4) oscillation that is characterised by radial motions of the plasma is difficult to detect. The observations with the line-of-sight perpendicular to the oscillating loop segment give us the same plasma that displaces along the line-of-sight, but does not leave it. Hence, the brightness of the pixel becomes modulated by the oscillations very weakly (Gruszecki et al. 2012). Detection of this mode with imaging telescopes is possible either with the oblique LOS (Antolin and Van Doorsselaere 2013), or in the radio band where the emission may come from a small part of the oscillating volume filled with the non-thermal electrons. Moreover, as sausage modes have periods shorter than the periods of other modes (e.g. 15–20 s), often the required time resolution can be achieved in the radio band only. On the other hand, observations of sausage oscillations in radio impose an additional constraint: the need for the highlighting non-thermal electrons makes it possible only during a solar flare.

The first confident detection of the sausage oscillation was made with NoRH in the microwave band (Nakariakov et al. 2003). Quasi-periodic modulation of the gyrosynchrotron intensity radiation from a flaring loop was found to have the spatial distribution consistent with the theoretically predicted spatial structure of the global sausage mode and its second harmonic. The observed periods were about 16 s for the global mode and 9 s for the second harmonic. The modulation depth reached 30 % of the background gyrosynchrotron emission in the flare. Figure 27 shows the microwave image of a flaring loop, the total signal of the gyrosynchrotron intensity emission of the flare, the signals coming from the legs of the loop and from its top, and power spectra of the signals. The top of the loop oscillates with a period of about 16 s. This periodicity is suppressed in the loop legs, where a shorter period, about 9 s, dominates. The longer periodicity corresponds to the global mode, with the maximum signal at the loop top and nodes near the footpoints. The shorter periodicity corresponds to the second harmonics that has a node at the loop top. The presence of the 9-s

- The apparent recurrence of the oscillation events suggests selectivity of the excitation mechanism, but what is the physical reason for the selectivity?
- What is the effect of the nonlinearity associated with the large oscillation amplitude, and how can it be detected observationally?
- Regarding observations, it is necessary to look for examples of shorter period oscillations, and to study the scaling of the oscillation period and decay time with the loop length and the plasma temperature.
- It is also of interest to search for the resonant excitation of longitudinal oscillations by umbral and penumbral sunspot oscillations in the loops anchored in sunspots.

So far, the majority of theoretical models of longitudinal oscillations were restricted to the infinite-field approximation: only the field-aligned flows were considered. This approach is more suitable to the waves that are plane in the transverse direction. However, in coronal loops and other plasma non-uniformities longitudinal waves are in an entirely different regime. Their transverse wavelength is much shorter than the longitudinal wavelength. This difference results in the longitudinal phase speed being the tube speed, rather than the sound speed, even without any wave-guiding non-uniformity (Roberts 2006). In a low-β plasma this effect does not significantly change the longitudinal speed, justifying the use of the infinite-field approximation for the determination of the resonant properties of plasma loops. However, it may be important for nonlinearity, dissipation and observability, and hence needs to be considered in detail (see, e.g. Afanasyev and Nakariakov 2015). Likewise, identification of the auto-oscillatory regime would be interesting for revealing the plasma heating function.

7 Propagating MHD Waves in Coronal Plasma Structures

There are also various propagating waves detected in the corona. Below we describe several types of propagating waves and their interpretation in terms of MHD wave theory in a plasma cylinder, given in Sect. 4.

7.1 Propagating Longitudinal Waves

One of the first wave phenomena detected in the solar corona with sufficient spatial and time resolution, was the slowly-propagating waves of EUV emission disturbances in polar plumes (Ofman et al. 1997, 1999; DeForest and Gurman 1998), in the inter-plume regions (Banerjee et al. 2001), and near footpoints of long coronal loops and fan-like structures (Berghmans and Clette 1999; Robbrecht et al. 2001). Comprehensive reviews of these phenomena can be found by Nakariakov (2006), De Moortel (2009). Here, we introduce the term "slowly-propagating waves" to highlight their difference from the rapidly propagating waves of EUV emission disturbances, described in Sect. 7.4. The waves are seen as upwardly propagating quasi-periodic intensity variations in EUV and soft X-ray bands. They are well-identified as periodic diagonal stripes in the time-distance map (see Fig. 29). The direction of the wave propagation coincides with the direction of the plasma filamentation and hence with the direction of the magnetic field. Fixing the spatial coordinate, i.e. choosing a certain value at the horizontal axes in panels b or c of Fig. 29, one gets a time signal and can determine its periodicity. The periodicity is typically well-defined and stable, and hence the signal is quasi-monochromatic. The period ranges from a few to several minutes.

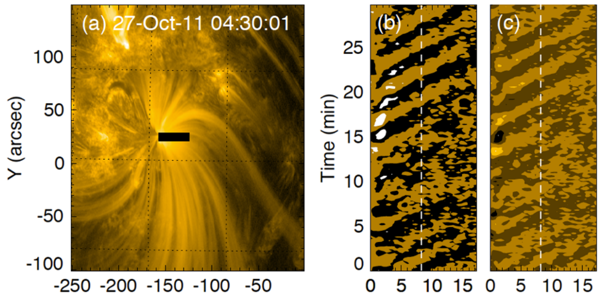

Fig. 29 Example of a propagating quasi-periodic longitudinal oscillation in a coronal plasma fan. (**a**) SDO/AIA 171 Å image of active region NOAA 11330 observed on 27 October 2011 at 04:30:01 UT. A cut that was taken to make the time–distance plot is indicated with a black bar. (**b**) Time-distance plot of the running difference, made along the cut. It covers about 10 cycles of the propagating features. (**c**) The same time-distance plot but made with the background-subtraction method. The diagonal stripes in panels (**b**) and (**c**) indicate the outwardly propagating waves of the EUV intensity. From Yuan and Nakariakov (2012)

It is observed that propagating slow waves are strongly damped. Typically (e.g. De Moortel et al. 2002), it was found that waves with a period of 5 minutes reach in coronal loops or fan-like plasma structures in active regions the height of only 10 Mm, which is 1–2 wavelengths along the wave path. Recently, it was found that long-period (up to 25 minutes), propagating slow waves can reach heights up to 150 Mm (Krishna Prasad et al. 2012), and seem to be omnipresent in the solar corona. Due to the quality factor that is nearly independent of the period (Krishna Prasad et al. 2014), the long-period waves can reach much greater heights before they are damped.

The damping of these compressive waves is thought to be mainly due to classical dissipative processes (Ofman et al. 1999, 2000; Nakariakov et al. 2000), in particular thermal conduction (De Moortel and Hood 2003), and coronal loop/field line expansion (De Moortel and Hood 2004). However, the recent observational results obtained by Krishna Prasad et al. (2014) question whether these damping mechanisms are truly at work, at least in polar plumes, because the frequency dependence of the quality factor of the observed waves does not agree with the theoretically predicted dependence. Also, it should be noted that observational limitation of the intensity fluctuations with height could lead to apparent wave damping, in addition to the physical damping.

7.2 Propagating Kink Waves

As described in Sect. 6.1 the post-flare standing kink oscillations were first detected in coronal loops by TRACE (Aschwanden et al. 1999; Nakariakov et al. 1999), but it was not until several years later that reports were made of propagating kink waves in the corona by Tomczyk et al. (2007) using data from the Coronal Multi-Channel Polarimeter (CoMP).[2] Typical periods are from several minutes to tens of minutes, with a preference for 5 minutes. The primary reason for the delay of this discovery was the small amplitude nature of propagating kink waves ($\approx 1\ \mathrm{km\,s^{-1}}$). A kink wave with a maximum velocity amplitude of $1\ \mathrm{km\,s^{-1}}$ and a period of 5 minutes will only displace the loop by at most 48 km, which is nearly an order of magnitude smaller than the 365 km ($0.5''$) pixel size of TRACE. However, the advanced

---

[2] The rapidly-propagating waves of emission intensity, detected with the Solar Eclipse Coronal Imaging System (SECIS) by Williams et al. (2002) and Katsiyannis et al. (2003) could also be produced by kink waves by the variation of the apparent column depth (Cooper et al. 2003a,b).

Doppler velocity resolution of the ground-based CoMP, which was primarily designed to make accurate off-limb measurements of the Zeeman effect, offered the first opportunity to study these propagating low amplitude and broadband frequency kink waves. Importantly, these waves were found to be ubiquitous and were not seen to be driven by any large scale energy release events such as flares and CMEs, as is the case with coronal loop standing kink waves observed with TRACE and latterly SDO/AIA. We need to point out that effects of phase mixing, line of sight integration, and instrumental effects (resolution, scattering) could account for the apparent low amplitudes of the observed kink waves.

Initially Tomczyk et al. (2007) interpreted these propagating waves as Alfvén waves, because they have phase speed close to the expected Alfvén speed ($\approx 1000\ \mathrm{km\,s^{-1}}$), are strongly guided by the coronal magnetic field and are almost incompressive in character (with intensity variations of $\Delta I/I < 3 \times 10^{-3}$). However, in contrast to its excellent Doppler velocity resolution, the spatial sampling of CoMP is a relatively coarse 4.5 Mm. It was demonstrated by Van Doorsselaere et al. (2008a) that in the flux tube geometry of coronal loops, only kink waves would display the collective behaviour observed with CoMP on such spatial scales. Essentially, only fast magnetoacoustic waves guided by a field-aligned plasma non-uniformity can propagate along the field and have the transverse size (about 8 Mm) much shorter than their longitudinal wave lengths (about 300 Mm). In contrast, torsional Alfvén waves are not collective modes, existing independently on each magnetic surface (see also discussion in Sect. 4). Consequently, they can have different amplitudes, phases and frequencies on each surface and would simply not display the coherence observed over such spatial scales by Tomczyk et al. (2007), especially after Alfvénic perturbations of different magnetic surfaces get out of phase after some time.

Interestingly, after the launch of Hinode in 2006, its highly effective EUV imaging spectrometer (EIS) also detected low amplitude kink waves ($\approx 1\ \mathrm{km\,s^{-1}}$) in coronal loops that were not seen to be generated by either flares or CMEs (Van Doorsselaere et al. 2008c; Erdélyi and Taroyan 2008). Unfortunately, limited by the narrow spectroscopic slit of EIS, these authors could not observe the loop in its entirety, and were therefore not able to establish if the kink waves were propagating or standing. In that sense, the larger field of view of CoMP had the advantage of determining whether the kink waves are propagating or not, but certainly the presence of non-flare and non-CME generated low amplitude kink waves was confirmed independently by both instruments. Subsequently, propagating kink waves have also been detected with the high resolution EUV imager AIA onboard SDO (launched in 2010) in coronal loops, coronal holes, quiet Sun regions and polar plumes (see e.g., McIntosh et al. 2011; Thurgood et al. 2014). Now there have even been multi-instrumental studies of this phenomena with CoMP and SDO/AIA (Threlfall et al. 2013), and also the ultra-high resolution EUV imager Hi-C with SDO/AIA (Morton and McLaughlin 2013).

As standing kink waves in coronal loops were observed to exhibit rather strong damping, it was natural to assume that the same would also be true of propagating kink waves. Observations of kink waves propagating along coronal loops, made with CoMP (Tomczyk and McIntosh 2009) indicate that it may be indeed the case. Using this as motivation, Terradas et al. (2010) calculated that the damping length of kink waves due to resonant absorption should be proportional to the period. Hence, the effect of resonant absorption is to cause longer damping lengths for lower frequencies, i.e., the damping effect of a resonant layer acts like a low-pass filter for propagating kink waves (see discussion in Sect. 5.5). Therefore, the broadband frequency information contained in the CoMP data offered an excellent opportunity to test this model. Verth et al. (2010) used the same data set as Tomczyk and McIntosh (2009) and found that there was qualitative agreement for the estimated quality factors for both standing and propagating waves in coronal loops, as would be expected for the resonant absorption model.

In highly dynamic regions of the corona propagating kink waves have also been observed in the presence of sub-Alfvénic and even Alfvénic flows. Using Hinode/XRT, Cirtain et al. (2007) observed kink waves in a polar coronal hole X-ray jet, which had two distinct flow components, one near the Alfvén speed ($\approx 800\ \mathrm{km\,s^{-1}}$) and another near the sound speed ($\approx 200\ \mathrm{km\,s^{-1}}$). Modelling this particular event Vasheghani Farahani et al. (2009) deduced that in the observationally determined range of parameters, the kink waves were not found to be subject to either the Kelvin–Helmholtz instability or the negative energy wave instability. Hence, they determined that the kink waves must have been excited at the source off the jet and were actually observed as they were propagating upwards. Such propagating kink waves associated polar coronal hole EUV jets have since been observed with SDO/AIA (e.g., Morton et al. 2012; Chandrashekhar et al. 2014).

There is a number of open questions connected with propagating kink waves:

- Is there a link between propagating kink waves and standing undamped kink oscillations?
- What is the driver of the propagating kink waves? What does determine the horizontal size of the wave?
- The very existence of the propagating kink waves requires presence of field-aligned non-uniformities of the plasma density. Can those non-uniformities be identified in the diffuse corona, where the waves are detected?
- What is the wave polarisation, plane, elliptical or circular?

7.3 Transverse Waves in Coronal Streamers

Propagating transverse waves of much longer periods and wavelengths are observed in coronal streamers. Coronal streamers, also called *helmet streamers*, are large cap-like bright structures with long pointed peaks extended outwards the Sun. Morphologically, these coronal structures consist of a loop anchored at the surface of the Sun, above which the externally lying magnetic field lines form a cusp and a radially-stretched current sheet. The current sheet is surrounded by a high-density plasma sheet or slab, also called *a streamer stalk*. The magnetic configuration of helmet streamers clearly resemble the nightside magnetosphere with the magnetotail (Sect. 8).

Quasi-periodic transverse displacements of a streamer stalk (see Fig. 30), excited by a CME development were recently observed with coronagraphs (Chen et al. 2010; Kwon et al. 2013) at the heights above one solar radius from the solar surface. The CME impact acts as an initial perturbation for the transverse wave guided by the plasma non-uniformity. The oscillation periods were estimated in the range from 60 min to 150 min. There is some evidence of the increase in the oscillation period with height. The perturbation propagates along the streamer's current sheet with the apparent phase speed of about 300–500 $\mathrm{km\,s^{-1}}$ (Chen et al. 2010). Different studies showed that the phase speed decreases with height. Also, the oscillation decays very rapidly, with the decay time approximately equal to the oscillation period. The periods and damping times measured at different heights were found to be highly correlated and scale linearly with each other (Kwon et al. 2013). The amplitude of the displacement is 50–100 Mm (up to 20 % of the solar radius). Excitation of the visible transverse motion in streamers is observed in only a very small fraction of the CME deflection events. The CMEs causing the transverse waves have high phase speed, over 1000 $\mathrm{km\,s^{-1}}$.

Observations of transverse waves guided by streamers are still very rare and require targeted search and analysis. The lack of statistically significant observational information about this phenomenon makes its theoretical modelling rather speculative. However, the rareness of these transverse coronal waves poses questions concerning their excitation and its selectivity.

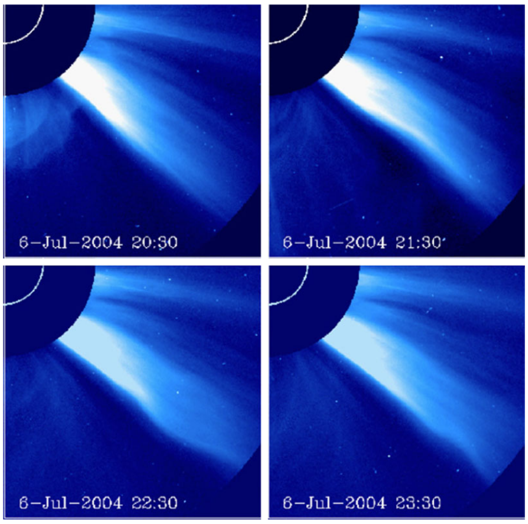

Fig. 30 Transverse motion of a coronal streamer stalk, as an aftermath of the CME impact, seen in the snapshots of coronal images taken in the white light during an artificial eclipse with SOHO/LASCO-C2. The *white circle* in the *top-left corner* of the *images* indicates the solar limb. The wavy displacement propagating outwards at the Southern slope of the bright streamer is the transverse waves. From Chen et al. (2010)

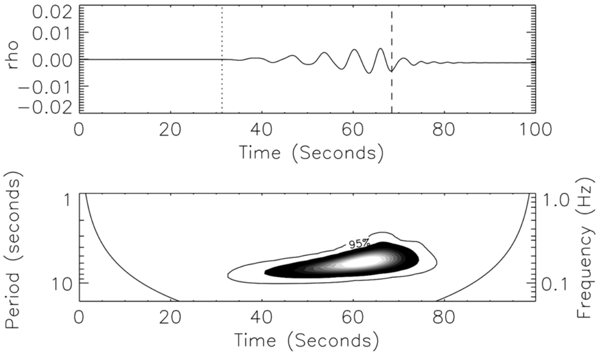

Fig. 31 Numerical simulation of an impulsively generated fast magnetoacoustic wave train propagating along a coronal loop with a density contrast ratio of 5.0 and profile steepness power index equal to 8. *Upper panel*: the characteristic time signature of the wave train. *Lower panel*: wavelet transform analysis of the signal, demonstrating the characteristic "crazy" tadpole wavelet signature. From Nakariakov et al. (2004b)

7.4 Rapidly-Propagating Wave Trains

Magnetoacoustic modes of plasma non-uniformities are subject to geometric dispersion (see Sect. 4). In the low-β plasma (typical for the corona and magnetosphere), dispersion of fast waves is significant. Hence, a broadband initial fast magnetoacoustic perturbation develops in a quasi-periodic wave train as different spectral components propagate at different phase and group speeds because of the dispersion. It has been theoretically predicted that fast magnetoacoustic waves guided by solar coronal plasma structures, can form quasi-periodic wave trains, (Nakariakov et al. 2004b, and references therein). The analysis of the group speed dependence on the longitudinal wave number shows that the long-wavelength spectral components propagate faster than the medium- and short-wavelength ones. This suggests that an impulsively generated fast wave train could have a characteristic signature with three distinct phases: the periodic phase, the quasi-periodic phase and the decay phase (Roberts et al. 1983). Nakariakov et al. (2004b) simulated the formation of the quasi-periodic wave trains in field-aligned plasma slabs with transverse profiles of the plasma density of different steepness. Fast magnetoacoustic wave trains were shown to have a characteristic "crazy" tadpole wavelet (or dynamical Fourier) signature, see Fig. 31. These signatures were detected in the observations in the visible light, and also in decimetric radio bursts (Mészárosová

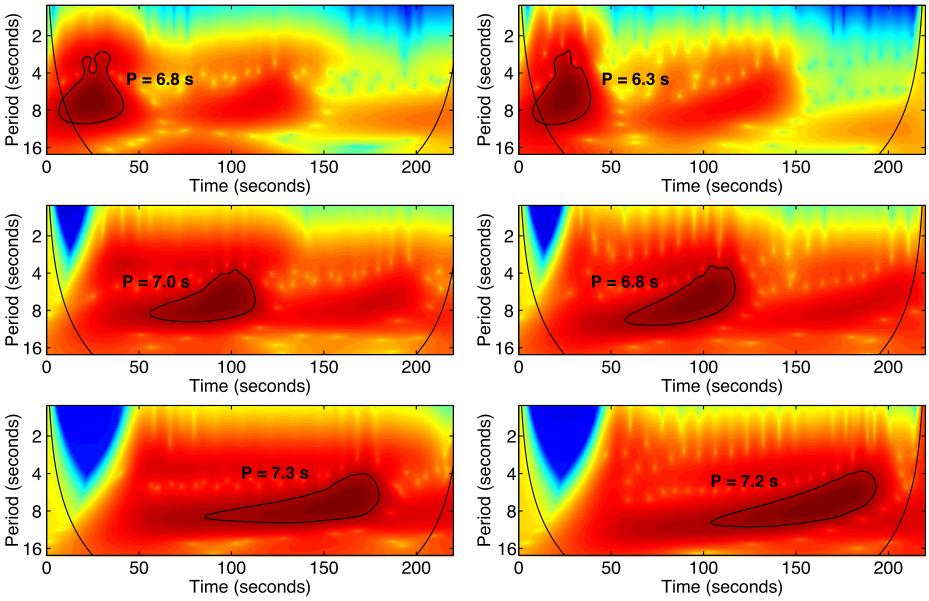

Fig. 32 Wavelet spectra ("the crazy tadpoles") of fast magnetoacoustic wave trains at three different detection points with the increasing distance from the broadband source (*upper*, *middle*, and *lower panel*, respectively). In the *left column*, the results for the density slab are shown, whereas the results for the Harris current sheet can be seen in the *right column*. From Jelínek and Karlický (2012)

et al. 2009). The effect of the amplitude and frequency modulation of coronal fast wave trains is most pronounced if the initial excitation is sufficiently broadband (Nakariakov et al. 2005). Narrowband initial perturbations are not affected by dispersion and remain quasi-monochromatic, see Sect. 7.2.

The so-called spikes (defined as a group of very short and narrowband radio bursts) are observed during the solar flares. Karlický et al. (2011) found the signatures typical for fast magnetoacoustic wave trains formed by dispersion, in decimetre radio spikes. They concluded that these fast wave trains were associated with fast magnetoacoustic waves propagating along the dense plasma slab surrounding the global current sheet (current layer) in turbulent reconnection outflows. These waves modulate the process of acceleration of electrons and hence the generation of plasma and electromagnetic waves, resulting in the radio spikes. Jelínek and Karlický (2012) and Mészárosová et al. (2014) performed a more extended and detailed study of fast sausage wave train dynamics in a plasma slab with a current-sheet, see Fig. 32. The formation of fast wave trains was recovered. It was suggested that these wave trains could modulate the radio fluxes (and even UV fluxes) in various locations in the current-sheet.

A similar effect has also been observed in radio fiber bursts (Karlický et al. 2013), that are fine spectral structures observed in broadband radio emission of solar flares, characterised by fast frequency drift. Their wavelet spectra were found to contain tadpole-like features, as shown in Fig. 31. The frequency drift in the tadpole head is the same as the frequency drift of fiber bursts. This effect can be associated with a fast sausage magnetoacoustic wave train propagation upwards in a stratified atmosphere. The wave train modulates the radio emission produced by super-thermal electrons accelerated and trapped in the flare site.

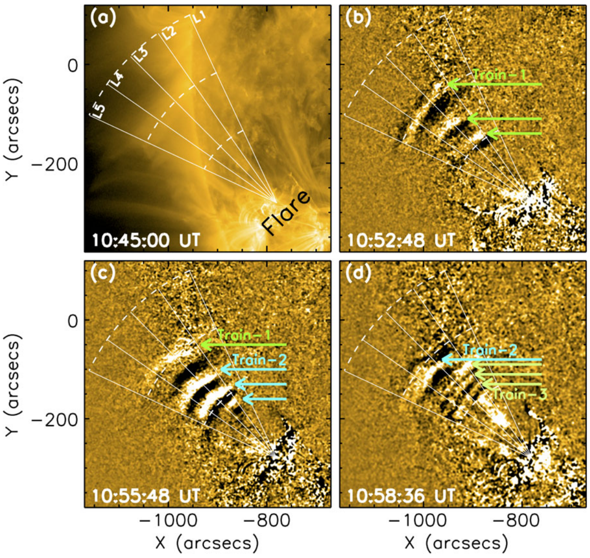

Fig. 33 (**a**) The AIA field-of-view in 171 Å displaying the active region AR11227 and the flare epicentre. (**b**)–(**d**) Running difference images illustrate the fast wave trains. The wave fronts of three distinct wave trains are marked by *arrow* groups in different colours. The *solid lines* (L1–L5) show the funnel. The *dashed arcs* concentric at the flare epicentre, have the radii of 100 Mm, 200 Mm and 300 Mm, respectively. From Yuan et al. (2013)

The advanced time resolution and high sensitivity of SDO/AIA led to the direct observations of coronal fast wave trains in the EUV band (Liu et al. 2011). Figure 33 shows snapshots of several fast waves trains of the EUV emission intensity disturbance propagating along the apparent direction of the magnetic field in the corona. The typical speeds of such wave trains are about 1000 $\mathrm{km\,s^{-1}}$, typical periods of the oscillations of the filling signal are about 60 s and the period varies in time. Typical amplitudes are up to several percent. The waves are detected up to 300 Mm (about half of the solar radius) above the solar surface. Beginnings of individual wave trains coincide with coronal mass ejections or other impulsive energy releases (Yuan et al. 2013).

Ofman et al. (2011) performed the 3D MHD modelling of this phenomena interpreting the oscillations as propagating fast magnetoacoustic waves in a narrow funnel of a dipole field, excited by localised (quasi)-periodic velocity perturbations at the magnetic footpoints of the active region, and found excellent agreement with observations. Pascoe et al. (2013a) developed an advanced numerical model of the dispersive evolution and propagation of fast waves in an expanding magnetic funnel filled in with dense plasma, aiming to interpret coronal EUV fast wave trains. They found that indeed the quasi-periodic fast wave trains are readily formed in plasma funnels. Moreover, the fast wave energy is separated into two wave components—trapped waves which propagate along the funnel axis and leaky components that form similar wave trains outside the funnel. The external wave trains tend to refract upwards. The results were found to be well consistent with observations (Yuan et al. 2013). Moreover, Nisticò et al. (2014) have shown that numerical simulations of rapidly propagating wave trains in an observed active region excellently reproducing the observed behaviour.

8 Flapping Oscillations of Current Sheets

One of the common features of coronal and magnetospheric plasma systems is the occurrence of a thin current sheet separating magnetic field lines of opposite orientation. In particular, such current sheets are observed to be extended into the Earth's magnetotail, occur at the dayside reconnection site, and are believed to appear in solar flares (see Sect. 11.1) and coronal helmet streamers (Sect. 7.3). MHD waves and oscillations of a current sheet have specific properties. In particular, in-situ measurements in the Earth's magnetotail revealed the low-frequency (about 10^{-4}–10^{-1} Hz) magnetic and pressure oscillations of the current sheet (Bauer et al. 1995). One of the most discussed and studied among them are so-called *flapping oscillations* (see, e.g. Korovinskiy et al. 2015, and references therein), which are also observed in the Jupiter and Saturn magnetospheres. Oscillations (waves) of this type are quasi-periodic displacements of the current sheet in the transverse direction (i.e. along the z-axis of the GSM frame of reference in the case of the Earth's magnetotail). Flapping waves are preferentially excited in the central part of the magnetotail at the distances of about 10–30 R_E from the Earth, and propagate towards the flanks (along the y-axis of the GSM frame of reference, so along the magnetotail in the direction perpendicular to the direction of the magnetic field) at typical speeds of about 30–70 $\mathrm{km\,s^{-1}}$, which are about ten times lower than the local Alfvén speed. The waves can be directed both parallel and anti-parallel to the electric current of the sheet. They are often observed several minutes prior to the substorm onset and during substorm growth phase. These observational findings give evidence that the flapping waves have roots deep inside the magnetotail and can be internally linked with the substorm activity. The wavelengths and spatial amplitudes of the flapping waves are statistically found to be about 1–5 R_E and the characteristic frequency is ~ 0.035 Hz.

Two different models were developed to explain flapping waves within the MHD framework. The first one interprets the flapping waves as the ballooning-type mode in the curved magnetic field of the current sheet (Golovchanskaya and Maltsev 2005). The physics of this mechanism is ideologically similar to the physics of the internal gravitational waves in the upper atmosphere. The centrifugal force, acting on a plasma element in the curved magnetic field of the magnetotail, plays the role of the gravity. The buoyancy acts on the displaced plasma element as the restoring force. The wavelength range of the ballooning waves predicted by the theory is quite broad—it can be from a fraction of R_E up to the curvature radius of magnetic field lines of the magnetotail, which is estimated in some cases as ≈ 20 R_E. Thus, in principle, the flapping waves can be interpreted as the ballooning-mode waves. The model predicts both kink-like and sausage-like current sheet displacements. A shortcoming of the theory is that its dispersion relation is derived only for the case when the magnetic curvature radius exceeds the characteristic scale of the flapping waves which is not applicable to all regions of the magnetotail.

The second MHD model of the flapping waves, called the "magnetic double-gradient mechanism", claims that these waves can be caused by the presence of a normal magnetic field component gradient along the current sheet (Erkaev et al. 2007, 2009; Korovinskiy et al. 2015). The characteristic flapping frequency (ω_{flap}), predicted by this model, is determined by the combination of plasma density (n_e) and two magnetic gradients—the tangential (B_x) and normal (B_z) magnetic field components along the normal (z) and tangential (x) directions of the current sheet respectively:

$$\omega_{\mathrm{flap}} = \sqrt{\left(\frac{1}{4\pi n_e m_p} \frac{\partial B_x}{\partial z} \frac{\partial B_z}{\partial x}\right)_{z=0}}, \tag{44}$$

where m_p is the proton mass. For the Harris-like current density profile Erkaev et al. (2009) have found the analytical expression for the group speed of the flapping waves to be,

$$V_{\mathrm{gr}}^{\mathrm{kink,sausage}} \approx \omega_{\mathrm{flap}} \Delta F_{\mathrm{kink,sausage}}(k\Delta), \tag{45}$$

whether flapping waves are really present in the solar corona or not, additional, more detailed spatially-resolved observations are required. At this moment, it is too early to claim that coronal flapping waves, similar to the magnetospheric ones, do exist.

9 Sources of MHD Waves

In the context of the solar corona the mechanisms for the excitation of MHD oscillations are poorly understood. Mainly it is connected with the observational limitations intrinsic to remote sensing. On the other hand, the excitation of MHD waves in the Earth's magnetosphere is reasonably well understood, which creates a solid basis for knowledge transfer.

9.1 External Generation Mechanisms in the Magnetosphere

A large group of magnetospheric MHD wave phenomena is excited by mechanisms acting outside the magnetosphere. The driver of these waves is the solar wind: shear flow at the flanks of the magnetosphere, fluctuations, waves, transient events inherent in the solar wind or generated by the interaction of solar wind and the magnetosphere. Such waves of external origin and their penetration through the turbulent magnetosheath to the magnetosphere require a proper physical explanation.

9.1.1 Shear Flow Instabilities

The solar wind is a turbulent flow, however, even the almost fluctuation-free steady solar wind flow would be able to drive waves at the magnetopause through shear flow instabilities. Among these, the Kelvin–Helmholtz instability (KHI) is the most widely studied (e.g. Pu and Kivelson 1983; Walker 2005) and commonly accepted mechanism (see, e.g. Mazur and Chuiko 2015, and references therein, for the recent status of this research). The KHI can develop at a boundary between two counter-streaming MHD media, such as the magnetopause, by amplifying small scale fluctuations into large amplitude waves and vortices, as schematically illustrated in Fig. 34. Speed fluctuations at the perturbed surface cause pressure fluctuations according to Bernoulli's theorem. Where the pressure has a minimum, fluid elements experience a net force opposite to the pressure gradient. In an incompressible fluid this happens where the flow speed is higher than the bulk speed of the medium, i.e. at the largest displacements. The waves grow due to the instability. In the compressible case, density variations can reduce, or in extreme cases even quench the instability (Walker 2005). In a magnetised plasma, the magnetic field component parallel to the relative shear velocity of

Fig. 34 Schematic illustration of Kelvin–Helmholtz instability onset at the magnetosphere flanks. The excited surface modes are coupled with Alfvén field line oscillations

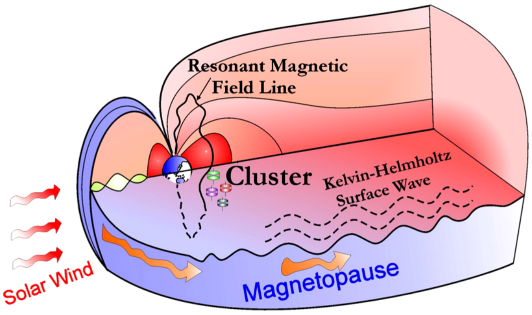

the media also has an important stabilising effect. This is because perturbations due to the instability that acts towards bending field lines are counteracted by the force of magnetic tension.

At the magnetospheric boundary KH waves manifest themselves in the fluctuations of the plasma (density, velocity, temperature) and magnetic field, typically with a period of the order of minutes. Theory of KHI has developed through several stages since it was first proposed. In the first models of the KHI, the instability was considered an infinitely thin tangential discontinuity separating two incompressible fluids. Pu and Kivelson (1983) were the first to study the KHI in a compressible MHD plasma and model the phenomenon at the terrestrial magnetopause. They identified two compressible modes: the quasi-slow mode and the quasi-fast mode, both coupled to evanescent waves on both sides of the magnetopause. The most important effect introduced by the compressibility is the appearance of a second critical flow speed, above which the instability quenched.

A boundary layer of finite width was first investigated by Lee et al. (1981), and the idea was further developed by Walker (1981) and Miura and Pritchett (1982) by including compressibility. In all cases two surface modes were identified, one at each side of the boundary layer. The highest growing rate was found to be achieved at $kd \approx 1$, where k is the wave number and d is the thickness of the boundary layer. As $V_{\mathrm{ph}} = \omega/k$, it also means that for a given thickness d and phase speed V_{ph} a quasi-monochromatic KH wave grows.

All of the above theoretical results were achieved based on models valid only in the linear MHD regime. These models can explain how and where the instability may appear, but cannot describe the fully developed, nonlinear phase of the instability. In particular, development of KHI can increase the thickness of the shear flow interface via generation of the effective viscosity (e.g. Mishin 2005). Global MHD models including the nonlinear development of the KHI, based upon full-MHD numerical modelling, appeared almost a decade ago. Claudepierre et al. (2008) was successful in reproducing two KH modes propagating tailward along the outer and inner edges of the low latitude boundary layer (LLBL) for a southward IMF. These two modes were found to occur for $kd = 0.5$–1.0 and to have different phase velocities and wavelengths, but oscillating at the same frequency. Larger shear flow velocities were found to excite KH waves of higher frequencies. Merkin et al. (2013) found that the KHI has a 3D nature: the magnetopause is perturbed not only in the equatorial plane, but also in the noon-midnight meridional plane. Surface mode perturbations were found to couple to body modes past the terminator plane. They also found field-aligned currents along closed field lines connecting the shear layer and the ionosphere. Their finding that magnetic and plasma pressures are spatially decorrelated is attributed to nonlinear effects. They identified two regions where the waves grow: one closer to the subsolar point (the point on the Earth where the Sun is perceived to be directly in zenith), and another at the flanks. According to this model, the KHI is initiated around 30° off the noon meridian (Guo et al. 2010; Li et al. 2012). The second unstable region starts prior to the terminator and lasts to about $-5\ R_{\mathrm{E}}$ (meaning that this location is in the anti-sunward direction). The plasma closer the subsolar point is less compressible and hence here the growth rate is higher.

Early observations supporting the KHI origin of high latitude Pc4–5 waves were the reversal of wave polarity at noon and amplitude rapidly decaying with increasing distance from the magnetopause. It was found that these waves propagate away from noon with a phase speed that is independent of frequency. These observations are in agreement with theoretical predictions, i.e. with a tailward propagating surface wave coupled to an evanescent wave in the magnetosphere. In the magnetosphere compressive waves of KH origin are coupled to local Alfvén field line resonances. Rolled up KH vortices were identified more frequently on the post noon, dusk-flank (Taylor et al. 2012) indicating that the KHI develops librium, and the decaying kink oscillations occur. Most events (95 %) were established to follow the same scenario. Probably, the efficiency of this mechanism depends on the interaction time of the LCEs with loops and on relative angles between their axes. This should be checked in further researches. The found scenario is consistent with the previously observed domination of the horizontal polarisation of the kink oscillations of loops. However, it should be noted that in 5 % of the studied events it was not possible to unambiguously determine the cause of the oscillations because of limitations of the observational data. It is not excluded that kink oscillations in those events could be excited by some other mechanisms than the discussed above.

Concerning the excitation of propagating kink waves (Sect. 7.2), observational works (e.g. Tomczyk and McIntosh 2009) showed that the waves have a power spectrum in which a power bump at the p-mode frequencies, about 5 minutes, is observed. Actually, the p-modes that are acoustic oscillations of the solar interior do not usually propagate in the corona, as they are evanescent above the photosphere. However, in the presence of magnetic structuring of the plasma, they can perhaps leak upwards and be somehow converted in kink waves. In particular, De Pontieu et al. (2005) proposed that p-modes could reach coronal heights by nonlinear steepening of field-aligned acoustic waves in the case when the field is inclined away from the vertical. More realistic models for such a transfer of p-mode energy in the corona are needed to assess this possibility.

10 Interaction of MHD Waves with Partly-Ionised Boundaries

The ionosphere is the geophysical shell where the energy transfer from the Earth's environment to the atmosphere occurs. Therefore, the description of processes in this region is of key importance for the solar-terrestrial physics, and it is particularly important for the MHD wave interaction with the ionosphere. ULF variations of the terrestrial electromagnetic field are effective tools for a continuous monitoring of dynamical phenomena in the magnetosphere and ionosphere. To apply effectively the ground-based magnetometer data it is important to know how well the ground distribution of the ULF field reflects the relevant wave structure in the magnetosphere.

In the context of the solar corona, the effects of partial ionisation come into play at the footpoints of coronal plasma structures, rooted at the dense and partly-ionised chromosphere. Also, a partly-ionised plasma can be found in solar prominences and cool jets.

10.1 Interaction of Long-Period MHD Waves with the Thin Ionosphere

The analytical solution to the problem of the Alfvén wave interaction with the coupled magnetosphere–ionosphere–atmosphere–ground system can be found under the "thin ionosphere" approximation. This approximation assumes that the wave skin-depth δ_P which is determined by the E-layer Pedersen conductivity σ_P, namely $\delta_\mathrm{P} = \sqrt{2/\mu_0\omega\sigma_\mathrm{P}}$, is larger than the thickness of the ionospheric conductive layer Δh, $\Delta h \ll \delta_\mathrm{P}$. In addition, in the case of fast magnetoacoustic mode incidence, the horizontal wavelength of the wave is to be much larger than the conductive ionospheric layer thickness, $k\Delta h \ll 1$. For ULF waves with the periods longer than 20 s the thin ionosphere approximation is well justified. Using this approximation, the description of the MHD wave transmission through the inhomogeneous anisotropically-conducting ionospheric plasma can be replaced by the consideration of the wave interaction with a thin layer with height-integrated Pedersen and Hall conductances, Σ_P and Σ_H, located at altitude h.

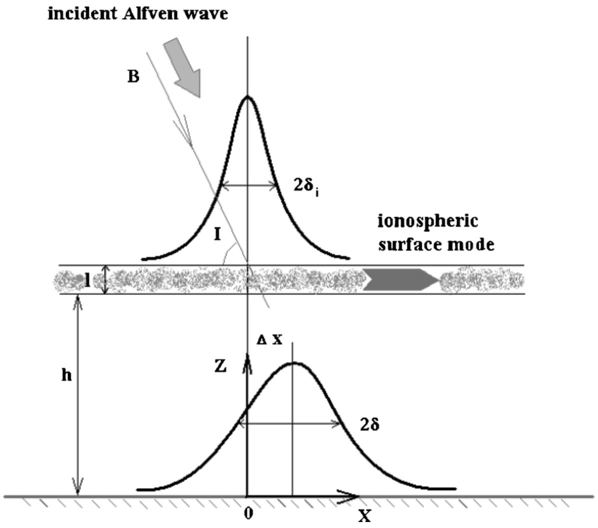

Fig. 40 Illustration of the distortion upon propagation to the ground of the Alfvén wave resonant structure incident on the ionosphere

The theory of MHD wave transmission through the thin ionosphere (Hughes and Southwood 1976) gives rather cumbersome analytical expressions for the coefficient R of the Alfvén plane wave reflection and the coefficient T of its transformation into a magnetic mode in the atmosphere. If one neglects the inductive part of the wave electric field in the ionosphere, related to the secondary compressive mode (the induction Hall effect), and the finite electrical conductivity of the Earth's surface, these expressions reduce to the simple forms

$$R = \frac{b_y^{(r)}(\omega, k)}{b_y^{(i)}(\omega, k)} = \frac{\Sigma_\mathrm{P} - \Sigma_\mathrm{A} \sin I}{\Sigma_\mathrm{P} + \Sigma_\mathrm{A} \sin I}, \qquad T = \frac{b_x^{(g)}(\omega, k)}{b_y^{(i)}(\omega, k)} = \frac{\Sigma_\mathrm{H}}{\Sigma_\mathrm{P}} \sin I \exp(-kh), \tag{58}$$

where I is the local inclination angle of geomagnetic field, and the superscripts (r), (i) and (g) denote the reflected and incident magnetospheric waves, and the ground response, correspondingly. The efficiency of the Alfvén wave reflection from the ionosphere, as follows from Eq. (58), is determined by the contrast between the ionospheric Pedersen conductance Σ_P and the magnetospheric wave conductance $\Sigma_\mathrm{A} = (\mu_0 V_\mathrm{A})^{-1}$. The relationship given by Eq. (58) shows that the ground magnetic response to Alfvén waves is controlled by the ratio between the local wave vector k and the height of the ionospheric current layer h. Large-scale waves with $kh < 1$ produce magnetic response on the ground, whereas small-scale waves with $kh \gg 1$ are screened by the ionosphere from ground-based magnetometers.

More specifically, the ground response to a magnetospheric resonant structure of a spatial scale δ_i is described as

$$b(x) = \frac{1}{2\pi} \int_0^\infty b_y(k) T(k) \exp\bigl(ikx'\bigr) dk \simeq b_0 \frac{\Sigma_\mathrm{H}}{\Sigma_\mathrm{P}} \frac{i\delta_i}{x' + i(\delta_i + h)} \sin I, \tag{59}$$

where b_0 is the amplitude of the latitudinal peak maximum. As follows from Eq. (59) the ground magnetic signal keeps the same form as the incident wave, whereas the maximum amplitude changes by the factor $(\Sigma_\mathrm{H}/\Sigma_\mathrm{P}) \sin I \delta_i/(\delta_i + h)$ and the peak width increases by the factor $(\delta_i + h)/\delta_i$. Thus, the existing models of the Alfvén wave transmission through the ionosphere predict that a spatial structure similar to that above the ionosphere should hold second) Alfvén waves generated by flares in the corona may propagate down to the chromosphere where they will dissipate efficiently due to ion-neutral collisions. This may have important consequences for post-flare chromospheric heating, however, currently due to instrumental limitations it is not possible to observe such high-frequency waves directly.

11 Quasi-Periodic Pulsations in Solar Flares

11.1 Standard Model of a Solar Flare

Generally, solar flares are visible as a sudden increase in the brightness of the Sun (or a part of the solar surface, if the observational instrument allows for spatial resolution) in all observational bands, from radio to gamma-rays. Physical mechanisms responsible for the radiation vary from bremsstrahlung (for hard X-rays and gamma-rays, visible light) and gyrosynchrotron (microwaves) of non-thermal electrons accelerated by the flare trigger, to thermal emission of the hot (up to several tens of million K) plasma evaporated from the denser layers of the solar atmosphere or heated directly in the corona (UV, EUV, microwaves and soft X-rays). Also, in the gamma-ray band the emission is likely associated with nuclear processes, e.g., de-excitation, neutron capture, and positron annihilation, caused by accelerated ions.

During the development of a flare, different physical mechanisms dominate in the emission. According to the timing of the emission recorded in different bands one can distinguish between several phases of a typical solar flare (see, e.g. Benz 2008, for a comprehensive review). In the so-called "preflare phase" one observes increasing EUV and soft X-ray radiation emitted by a gradually heated plasma of the active region where the flare occurs. Later on, a large number of electrically charged particles gets accelerated at the magnetic reconnection site in the active region, causing the "impulsive phase" that typically lasts up to a few minutes only. In this phase hard X-ray, gyrosynchrotron microwave, and gamma-ray emissions rise rapidly, often with many short but intense spikes of emission, each lasting from a fraction of a second to tens of seconds. Some portion of accelerated particles is trapped in the magnetic field of the flaring active region, and gyrates around magnetic field lines producing the emission in the microwave band by the gyrosynchrotron mechanism. The following "flash phase" is characterised by the maxima of soft X-ray and visible light (in particular, Hα that comes from the chromosphere) emission. After that the coronal plasma gradually repairs its initial state in the "decay phase". However the consequent development of a flare still could be recognised in the solar corona as the follow-up magnetic reconfiguration, plasma ejections, various decaying oscillations of various coronal plasma structures, radio bursts, and occasionally as sunquake ripples on the solar surface.

The schematic sketch of the so-called standard (or "Carmichael, Sturrock, Hirayama, Kopp-Pneuman", CSHKP, named after its creators) model of a solar flare, based on the observational phenomenology described above, is shown in Fig. 42. Initially, the magnetic energy is accumulated in active regions of the corona in a form of non-potential magnetic fields. Then some process triggers fast magnetic reconnection in, e.g. the current sheet formed behind of a destabilised ascending plasmoid, causing a rapid release of the free magnetic energy. The current sheet is oriented vertically, somehow resembling the tail in the Earth's magnetosphere. The magnetic energy is converted to the internal energy of the plasma, kinetic energy of bulk flows, e.g. Alfvénic jets or plasmoids, and still poorly understood acceleration of the super-thermal population of charged particles (also called non-thermal, accelerated or energetic particles), usually having the peaking energies in the

Fig. 42 Schematic sketch of the standard model of a solar flare

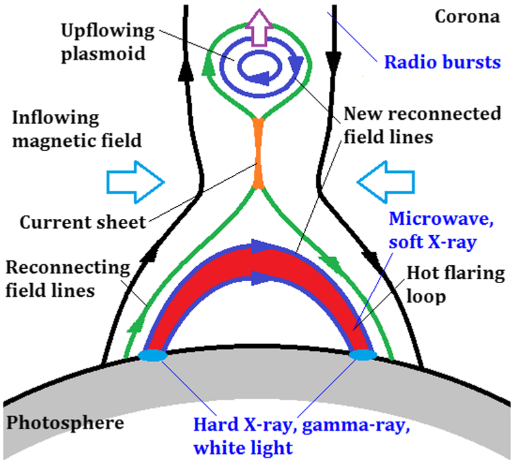

vicinity of 20 keV and extending sometimes to several tens of MeV. The accelerated charged particles move along the field lines, emitting the gyrosynchrotron radiation in the microwave band. The electrons that move towards the solar surface then precipitate into the dense plasma of the lower chromosphere that offers them a thick target. The precipitating non-thermal particles produce the hard X-ray and gamma-ray bremsstrahlung and nuclear emission. The chromospheric material gets heated up to tens of million K and evaporates upward into the corona. This evaporated thermal plasma fills up coronal magnetic flux tubes (coronal loops), emitting soft X-rays. At this stage one can see the appearance of bright "post-flaring" coronal loops in the soft X-ray band. The non-thermal electrons that move upwards interact with the background thermal plasma (see, e.g., the discussion in Sect. 9.2.1) producing various high-frequency radio bursts. This standard model of a flare should be taken as the zero-order approximation only, as it does not include 3D effects. In particular, major solar flares are usually seen to be "two-ribbon": the energy release sites move across the magnetic field, along the neutral line on the surface of the Sun, that separates the footpoints of the opposite magnetic polarity. On the surface of the Sun the sources of the hard X-ray or visible light emission form two "ribbons" that are extended along the magnetic neutral line. In the corona the ribbons are connected by an arcade consisting of a number of isolated loops parallel each other. There are ongoing attempts to generalise the standard model of a flare accounting for 3D effects (see, e.g. Aulanier et al. 2012).

11.2 Observational Manifestation of QPPs

An interesting feature of flaring energy releases are quasi-periodic pulsations (QPPs) often seen in light curves of solar flares as well-pronounced modulation of the emission intensity (see Nakariakov and Melnikov 2009, for a detailed review). These periodic variations of the electromagnetic emission are observed in all bands: the radio, visible light, soft and hard X-rays, and gamma-rays. Typical periods of solar flaring QPPs range from a fraction of a second to several minutes. Statistical studies show that QPPs are a common and perhaps intrinsic feature of flares (Kupriyanova et al. 2010). An example of QPPs is shown in Fig. 43 where the period is of about 40 s, and QPPs are almost synchronous in all observation bands. Moreover it often appears that the periods of QPPs are not stable, and vary during the same event (Nakariakov et al. 2010a; Kupriyanova et al. 2010; Kolotkov et al. 2015). Likewise, QPPs may have well-pronounced amplitude modulation. Usually, the most

A useful piece of information can be obtained from the magnetospheric manifestation of quasi-periodic regimes of reconnection, in sub-storms. In particular, pulsed reconnection in the magnetotail was shown to be connected with Pi2 in Keiling et al. (2006). It was established that a series of 1-min-long *nightside flux transfer event* (NFTE) pulses following each other within 1–3 min, resembled the magnetic field signature of Pi2. NFTEs are believed to form during the reconfiguration of tail magnetic field lines, i.e., reconnection. It was concluded that the quasi-periodic reconnection was both the energy provider and the frequency driver for the Pi2 registered on the ground and also in space. Quasi-periodic magnetic reconnection in the magnetotail can also be responsible for the quasi-periodicity in the *bursty bulk flow* (BBF) events that are about-10-min timescale variable flows observed in the near-Earth and mid-tail plasma sheet.

12 Beyond MHD

Modern magnetospheric observations with a high temporal-spatial resolution during various geophysical processes indicate that a larger power density tends to be concentrated in smaller time and space scales. Thus, impulsive and small-scale processes, despite their relatively short duration and small scale, may involve substantial energy exchange between the media. As an example of impulsive energy exchange in the coupled system magnetosphere–ionosphere–atmosphere one may recall the bursty process with a largest energy release in the terrestrial space plasma—the magnetospheric substorm. The mechanism of the substorm onset has not been identified yet, but probably it is related to small-scale non-MHD processes. For example, kinetic small-scale Alfvénic structures can carry a very localised, but intense, field-aligned electric field, resulting in a downward acceleration of auroral electrons (Chaston et al. 2002a). Likewise, understanding important processes in solar flares, e.g. charged particle acceleration and onset of micro-turbulence, requires employment of micro-physics. For example, the vital role of the anomalous resistivity has already been highlighted above (Sect. 11.4 and 11.5).

12.1 Dispersive Alfvén Waves in the Magnetosphere

For small scale processes, the dispersion relation for shear Alfvén waves, $\omega = \omega_{\mathrm{A}} \equiv k_z V_{\mathrm{A}}$, is modified:

- in the kinetic limit, to $\omega = \omega_{\mathrm{A}}\sqrt{1+(k_\perp \rho_{\mathrm{i}})^2}$, where ρ_{i} is the Larmor ion radius;
- in the inertial limit, to $\omega = \omega_{\mathrm{A}}/\sqrt{1+(k_\perp \lambda_{\mathrm{e}})^2}$, where $\lambda_{\mathrm{e}} = c/\omega_{\mathrm{pe}}$ is the electron inertial length (the collisionless plasma skin depth),

and thus the wave becomes dispersive even in a uniform medium. We should stress that these mechanisms for the MHD wave dispersion are different from the low-frequency geometrical dispersion caused by the waveguiding effect in the presence of a plasma or magnetic field non-uniformity, discussed in Sect. 4.

When dispersive effects are not large, $(\lambda_{\mathrm{e}}, \rho_{\mathrm{i}}) \ll k_\perp^{-1}$, these dispersion relationships can be combined into one $\omega \simeq \omega_{\mathrm{A}}\sqrt{1 \pm (k_\perp \rho_{\mathrm{d}})^2}$, where $\rho_{\mathrm{d}}^2 \simeq \rho_{\mathrm{i}}^2 + \lambda_{\mathrm{e}}^2$ is the dispersion radius. The actual influence of dispersive effects is determined by the structure parameter $\langle \rho_{\mathrm{d}} \rangle$ which is an integral along field lines (Leonovich and Mazur 1995a).

In contrast to waves in ideal MHD approximation, small-scale dispersive Alfvénic structures with scales comparable with the dispersive radius ρ_{d}, possesses intrinsic field-aligned electric field $E_\parallel$,

$$|E_\parallel| = (k_\perp \rho_\mathrm{d})^2 (k_\parallel / k_\perp) |E_\perp|. \tag{74}$$

Due to this field, dispersive Alfvén waves can effectively accelerate and precipitate electrons, which is especially important for the physics of the auroral regions (Borovsky 1993; Stasiewicz et al. 2000) and may be relevant to solar flares. Dispersive Alfvén waves can be driven by compressive magnetoacoustic waves via the mode conversion (Klimushkin and Mager 2014).

In an inhomogeneous system, a shear Alfvén wave tends to evolve into small-scale dispersive Alfvén wave due to the process of phase mixing. The transverse spatial scale of an Alfvén wave in an inhomogeneous plasma increases with time as $k_\perp(t) = \partial_x \omega_\mathrm{A}(x) t$. This effect is simply connected to the intrinsic property of Alfvén waves that are situated at individual magnetic surfaces of constant Alfvén speed perturbing the field and displacing the plasma along those surfaces. Thus Alfvén waves situated at neighbouring magnetic surfaces "do not feel" each other, and can quickly become out of phase. This produces secularly growing transverse gradients, and hence a perpendicular energy cascade to smaller and smaller transverse scales, until the high-frequency dispersion effects come into play. In the saturation state, the typical transverse scale of oscillations in the dispersive Alfvén resonator formed in the magnetosphere between the conjugate ionospheres is $\delta_\mathrm{d} = (a\rho_\mathrm{d}^2)^{1/3}$. This scale, $k_\perp \simeq (a\rho_\mathrm{d}^2)^{-1/3}$, is reached after an elapsed time $\tau_\mathrm{d} = \omega_\mathrm{A}^{-1}(a/\rho_\mathrm{d})^{2/3}$. Estimates show that at auroral latitudes $\langle \rho_\mathrm{d} \rangle$ varies from a few km to a few tens of km. For $a = 400$ km and $\langle \rho_\mathrm{d} \rangle = 1$–$10$ km the transverse scale δ_d determined by dispersive effects is 7–15 km.

12.2 Field-Aligned Potential Drop, Turbulent Layer, and Alfvén Waves

In a collisionless warm (finite-β) plasma a substantial non-resistive potential drop can be produced by mirror forces. The field-aligned electric field $E_\parallel$ is supported by the difference in pitch angle distributions for electrons and ions under conditions of plasma quasi-neutrality. Using stationary distribution functions consistent with a distribution of potential $\phi(s)$ the field-aligned current $j_\parallel$ can be calculated. A total potential difference $\Delta\phi = \phi_\mathrm{m} - \phi_\mathrm{i}$ along a field line, e.g. between the equatorial magnetosphere and ionosphere could be as large as $e\phi \simeq E(B_\mathrm{m}/B_\mathrm{i})$, where E is the particle energy, and $B_\mathrm{m}/B_\mathrm{i}$ is the mirror ratio, and the subscripts m and i indicate the magnetosphere and ionosphere, respectively. This potential drop is necessary to support the field-aligned current in a magnetic trap with a small cone angle, through which current-transporting electrons can reach the bottom ionosphere. In general, $j_\parallel$ is a functional of $\phi(s)$, i.e. $j_\parallel = j(\phi(s))$. Kinetic consideration shows that an Ohm's-type law may exist for the upward current in a mirror-confined plasma for a certain range of potential values. The current–voltage relationship between $j_\parallel$ and the potential drop can be presented in non-local forms,

$$\Delta\phi = Q j_\parallel, \quad \text{or} \quad j_\parallel = K \Delta\phi, \tag{75}$$

where Q is the effective electrical resistance. The field-aligned conductance $K = Q^{-1}$ of a flux tube can be estimated as $K \simeq ne^2/m_\mathrm{e} u_\mathrm{e}$, where m_e, n, and u_e are the mass, concentration, and thermal speed of magnetospheric electrons, respectively (Borovsky 1993). Even this simplified linear current–voltage relationship fits observations rather well. The mirror force produces an effective electric resistance, which may be coined a mirror resistance, accompanied by a dissipation of energy. It is natural to expect that dissipation processes in

P1–3sfe pulsations. These geomagnetic pulsations are observed when the flare exceeds the M4 class (e.g. Parkhomov et al. 2006, 2008). These periodic responses could be attributed to magnetospheric or ionospheric resonant modes. Spectral characteristics of irregular geomagnetic pulsations associated with hard X-rays flares were examined by Lukovnikova and Parkhomov (1984). Observational data obtained with a chain of ground-based magnetometers, for flares over the 1965–1976 year period were analysed, and peak pulsation values with periods of 40, 100, and 300 s were found. Probably, pulsations were induced by three different mechanisms: current fluctuations in the dynamo region of the ionosphere, magnetospheric resonant oscillations, and acoustic waves. However, these suggestions have not been supported yet by detailed data analysis or theoretical modelling. Thus, the relevant physical mechanisms are poorly understood and require detailed modelling and analysis.

14 Conclusions and Perspectives

In this review we have summarised the main observational manifestation and properties of MHD waves in the corona and the magnetosphere, and main results of their theoretical modelling. Despite a similarity between the approaches in solar and magnetospheric physics for the description of wave processes—they are based on the same MHD theory—there are some fundamental differences between coronal and magnetospheric waves as well. In the solar corona, the plasma is the field-aligned filamented and structured, e.g. into closed elongated flux tubes, the loops. Thus, the basic building block of the theory of coronal MHD wave processes is the plasma cylinder oscillations. In the magnetosphere, the plasma is rather homogeneous at least in one direction (azimuthal), so the elemental wave process is oscillations of magnetic shells.

Another difference is that in the magnetosphere, in the entire ULF frequency range, the plasma can be treated as collisionless. At the same time, in the solar atmosphere, some oscillatory modes are in collisional regime (i.e. wavelengths of observed waves, including slow magnetoacoustic waves, exceed the proton mean free path), whereas other modes correspond to a collisionless regime. As a result, in the corona there is a vast observational evidence of slow magnetoacoustic waves (see Sects. 6.3 and 7.1) that in the low-β plasma could degenerate to pure acoustic waves, absent in the collisionless magnetospheric plasma. In the magnetosphere, the lack of high-quality slow mode waves is connected with strong Landau damping, so this mode can be involved in wave processes only as a coupled mode (e.g., poloidal or ballooning modes).

Many long-period MHD wave phenomena in the magnetosphere are global, and involve either the whole magnetosphere (e.g., cavity modes) or its significant part in the wave motion. Thus, their properties are determined by the global geometry of the magnetospheric magnetic field and plasma distribution. In contrast, coronal MHD waves are always of the local nature. Even the events called global coronal waves (Sect. 2) develop from a well-defined epicentre. Moreover, there is still a debate whether these events are connected with MHD waves at all.

Nonetheless, there are plasma objects and configurations in the magnetosphere where the notions developed in the solar physics could be applied. On the dusk side, just outside the nominal plasmapause location, clouds of detached plasmaspheric plasma are regularly observed. Such clouds, in the first approximation, can be considered as flux tubes filled with the dense ionospheric plasma. The possible oscillations of the detached plasma tubes can result in the occurrence of specific localised ULF wave activity in this region. For their identification the models elaborated in the solar physics can be used.

This review identifies several other research topics that would definitely benefit from the knowledge transfer and cross-fertilisation of magnetospheric and coronal MHD wave studies.

The effect of turbulent motions on the MHD wave excitation and propagation needs to be understood. In particular, the excitation of almost monochromatic oscillations such as the decay-less kink oscillations of coronal loops and magnetospheric field-line resonances seem to be related to a similar excitation mechanism. It is the excitation of natural modes of a resonator (actually, predominantly the global mode in both the coronal and magnetospheric cases) by a continuously-operating broadband pumping.

Linear coupling of fast magnetoacoustic and Alfvén waves at the singular resonant surface where the phase speed of the fast waves equals the local Alfvén speed, plays an important role in both magnetospheric and coronal applications. In the magnetospheric applications this effect is directly observed, while in the corona it is still a theoretical model (see Sect. 5.5). It seems to be highly beneficial for both the research communities to perform a detailed comparative study of this effect.

The magnetospheric poloidal Alfvén waves with the large azimuthal wavenumber, slowly propagating sunward in the azimuthal direction are strongly compressive. Moreover, these waves are not fast magnetoacoustic, as the perturbation of the plasma density is seen in anti-phase with the perturbations of the absolute value of the magnetic field. This phenomenon seems to be similar to the magnetoacoustic wave progressing along the neutral line in two-ribbon flares, discussed in Sect. 6.3.

A cusp, either appearing above flaring arcades and in helmet streamers in the corona, or the magnetospheric polar cusp, acts as an accumulation region for fast magnetoacoustic wave energy in both the physical systems. This phenomenon deserves deep investigation both theoretically and observationally, as, in particular, it may be responsible for the formation of quasi-periodic patterns in magnetic energy releases.

The geometry of the Earth's magnetotail is similar to the geometry of coronal helmet streamers. Both these plasma systems are observed to guide MHD waves. Both the systems constitute two waveguides, one is the current sheet (the "warm" waveguide), and the other is the density enhancement surrounding the current sheet (the "cold" waveguide). Discrimination between the modes guided by the different waveguides is an interesting problem, with potential seismological implications. A similar magnetic configuration, a vertical current sheet above the reconnection site, is predicted by the standard model of solar flares. The search for MHD waves in this system is an interesting task that is important for comparative studies.

The effect of virtual compressive resonances has been studied in both magnetospheric and coronal contexts, however independently. The knowledge transfer between our research fields would be highly beneficial, including analytical models that have exact analytical solutions and approximate methods for the analysis of more general cases.

The integral emission curves recorded in both magnetospheric sub-storms and solar flares show quasi-periodic pulsations. The physical mechanisms responsible for QPPs need to be revealed. They may be either associated with MHD oscillations or quasi-periodic regimes of magnetic reconnection (the magnetic dripping, i.e. "pulsed" or "repetitive" reconnection). In the former case, one has to explain how low-amplitude oscillations produce high-amplitude variations of the emission intensity. In the latter case, one needs to determine the conditions for the appearance of this regime, and the relationship of the period with the parameters of the reconnecting current sheet and its environment.

For magnetospheric ULF waves, an important role is played by the partially-ionised layer of the ionospheric plasma at the footpoints of the oscillating magnetic field lines. In the solar corona a similar effect can be caused by the partial ionisation of the chromospheric plasma at the footpoints of, e.g., coronal loops. Some consolidated understanding of the role of the partial ionisation needs to be achieved.

In solar coronal loops, the non-equidistant frequency spectrum of standing kink oscillations is attributed to the non-uniformity of the Alfvén speed with height. Multi-band spectral features of magnetospheric ULF waves, associated with magnetospheric or ionospheric Alfvénic resonators, are used as a reliable tool for the diagnostics of the plasma distribution along geomagnetic field lines. It would be interesting to combine the analytical techniques and methods for the development and application of plasma diagnostics techniques.

ULF variations of the terrestrial electromagnetic field are effective tools for a continuous monitoring of dynamical phenomena in the magnetosphere, ionosphere, and atmosphere. The advanced understanding of ULF wave physics enabled space physicists to develop reliable methods of "hydromagnetic seismology" of the outer space to monitor the plasma density variations in the magnetosphere and ionosphere. However, in contrast with the similar usage of seismic waves for the solid Earth probing, in magnetospheric physics particular sources of ULF disturbances and their spectral properties are practically unknown. Nevertheless, the resonant transformation process, which is inevitably related to the propagation of MHD disturbances from extra-magnetospheric regions to the ground, ensures the existence of a specific resonant frequency for any geomagnetic location. The ground-based methods of hydromagnetic diagnostics of magnetospheric plasma are based on the extraction of this resonant frequency from ULF spectra. Similar techniques, jointly called MHD seismology of the solar corona, are intensively developed and used in the diagnostics of the coronal plasma. In particular, it provides the unique information about the coronal magnetic field, transport coefficients, the adiabatic index, sub-resolution structuring, and the characteristic scale of the stratification.

Despite intensive studies and numerous papers on ULF waves in the magnetosphere, many vital problems still cannot be considered as resolved. Most theoretical models are oversimplified and take into account only some aspects of actual physical phenomena. For example, theoretical models either describe realistic MHD modes, neglecting kinetic effects, or consider wave–particle interaction assuming a simple plane wave approximation. In reality, the integral growth rate of ULF waves is to be determined not only by wave-particle interaction, but the spatial structure of unstable modes.

Traditionally, wave processes in those two space objects—the Earth and Sun, have been studied so far almost independently. We attempted to outline main fundamental MHD wave processes which may occur in these two plasma systems. In addition, well-elaborated physical models designed by the magnetospheric wave communities, which, in our opinion, have a wider application area including solar, space and astrophysical plasma, but have so far obtained very limited attention, comprise the following physical phenomena:

- spectral magnetohydrodynamics, describing discrete and continuous spectra and eigenfunctions of MHD waves in an inhomogeneous plasma immersed into curved magnetic field;
- interaction of MHD waves with a multi-layer interface between the collisionless plasma and non-conductive atmosphere; the occurrence of transmission windows on the frequency domain owing to the ionospheric Alfvénic resonator and MHD waveguide;
- spontaneous excitation of small-scale Alfvénic modes by kinetic instabilities of energetic plasma component;
- Alfvénic energisation of warm electrons owing to kinetic or mirror resistance effects;
- the interaction due to a finite-frequency effect of propagating magnetoacoustic and Alfvén waves in a longitudinally inhomogeneous plasma in regions with open field lines.

In general, the potentials of MHD waves for the monitoring of plasma processes in near-Earth space and solar corona have not been fully exploited yet, and MHD seismology of the magnetosphere and corona just originated. MHD seismological techniques have a great potential in real-time monitoring the physical conditions in the corona and the near-Earth environment, with very interesting implications for space weather, which needs to be revealed and exploited.

Acknowledgements This review is based upon the activities of the international science team "MHD oscillations in the solar corona and Earth's magnetosphere: towards consolidated understanding" supported by the International Space Science Institute, Bern, Switzerland. The authors would like to thank Dr N. Nishitani and Dr A. Yoshikawa for the valuable discussions. The authors acknowledge the support by the STFC Warwick Astrophysics Consolidated Grant ST/L000733/1 (VMN, GN); the European Research Council under the *SeismoSun* Research Project No. 321141 (VMN), BK21 plus program through the National Research Foundation funded by the Ministry of Education of Korea (DHL, VMN); the Leverhulme Trust (GV); the János Bolyai Research Scholarship of the Hungarian Academy of Sciences (BH); grant P209/12/0103 and 16-13277S (GA CR) (MK, PJ); an Odysseus grant of the FWO Vlaanderen, the IAP P7/08 CHARM (Belspo) and the GOA-2015-014 (KU Leuven) (TVD); Program No 9 of the Presidium of the Russian Academy of Sciences (DYK).

Appendix

Abbreviations and acronyms commonly used in solar coronal and Earth's magnetospheric physics:

AAR	Auroral acceleration region
AIA	Atmospheric Imaging Assembly on SDO
BBF	bursty bulk flow events
CBF	coronal bright fronts
CIR	Corotating interaction region
CME	Coronal mass ejection
CSHKP	Carmichael, Sturrock, Hirayama, Kopp-Pneuman (or standard) model of a solar flare
EIS	Extreme Ultraviolet Imaging Spectrometer on Hinode
EIT	Extreme Ultraviolet Imaging Telescope on SoHO
EMIC	Electromagnetic ion-cyclotron
EUV	Extreme Ultraviolet
FLR	field line resonance—an eigenmode of a closed geomagnetic field line
FMS	Fast magnetosonic
FTE	Flux transfer events
IAR	Ionospheric Alfvénic resonator
IMF	Interplanetary magnetic field
IRI	International Reference Ionosphere model
KAWs	Kinetic Alfvén waves
KHI	Kelvin–Helmholtz instability
LLBL	Low latitude boundary layer
LoS	Line-of-sight
MHD	Magnetohydrodynamic
MP	Magnetopause
MSIS	Mass Spectrometer—Incoherent Scatter Model of the upper atmosphere
NFTE	Nightside flux transfer events
NoRH	Nobeyama Radioheliograph

A&A 590, A4 (2016)
DOI: 10.1051/0004-6361/201527306

Astronomy & Astrophysics

Quasi-periodic processes in the flare loop generated by sudden temperature enhancements at loop footpoints

M. Karlický[1] and P. Jelínek[2, 1]

[1] Astronomical Institute of the Czech Academy of Sciences, Fričova 258, 251 65 Ondřejov, Czech Republic
e-mail: `karlicky@asu.cas.cz`
[2] University of South Bohemia, Faculty of Science, Institute of Physics and Biophysics, Branišovská 10, 370 05 České Budějovice, Czech Republic

Received 4 September 2015 / Accepted 8 March 2016

ABSTRACT

Aims. During the impulsive flare phase, the plasma at the flare loop footpoints is rapidly heated by particle beams. In the present paper, we study processes that occur after this sudden heating in a two-dimensional magnetic loop.

Methods. We adopt a 2D magnetohydrodynamic (MHD) model, in which we solve a full set of the ideal time-dependent MHD equations by means of the FLASH code, using the adaptive mesh refinement (AMR) method. Periods in the processes are estimated by the wavelet analysis technique.

Results. We consider a model of the solar atmosphere with a symmetric magnetic loop. The length of this loop in the corona is approximately 21.5 Mm. At both loop footpoints, at the transition region, we initiate the Gaussian temperature (pressure) perturbation with the maximum temperature 14, 7, or 3.5 times higher than the unperturbed temperature. In the corona, the perturbations produce supersonic blast shocks with the Mach number of about 1.1, but well below Alfvén velocities. We consider cases with the same perturbations at both footpoints (symmetric case) and one with different perturbations (asymmetric case). In the symmetric case, the shocks move along both loop legs upwards to the top of the loop, where they interact and form a transient compressed region. Then they continue in their motion to the transition region at the opposite side of the loop, where they are reflected upwards, and so on. At the top of the loop, the shock appears periodically with the period of about 170 s. In the loop legs during this period, a double peak of the plasma parameters, which is connected with two arrivals of shocks, is detected: firstly, when the shock moves up and then when the shock, propagating from the opposite loop leg, moves down. Increasing the distance of the detection point in the loop leg from the top of the loop, the time interval between these shock arrivals increases. Thus, at these detection points, the processes with shorter periods can be detected. After ~500 s the process with the periodically interacting shocks slowly changes to slow mode magnetosonic free oscillation. Furthermore, we detected quasi-periodic processes, even in the chromosphere under the location of the pressure perturbation. These processes can be observed in intensities and Doppler shifts of optical chromospheric lines. In the case with the asymmetric perturbations, we found that the processes are even more complex.

Key words. Sun: flares – Sun: oscillations – magnetohydrodynamics (MHD) – methods: numerical

1. Introduction

In solar flares, oscillations are commonly observed in radio, soft X-ray, hard X-ray, ultraviolet, and even in gamma-ray emissions (Roberts et al. 1984; Fárník et al. 2003; Wang et al. 2005; Nakariakov et al. 2006, 2010).

The period of these oscillations ranges from sub-seconds to tens of minutes (Mészárosová et al. 2006; Tan 2008; Karlický et al. 2010; Kupriyanova et al. 2010; Huang et al. 2014; Nisticò et al. 2014). Several theoretical models have been proposed to explain a generation of these oscillations (Nakariakov & Melnikov 2009).

Many oscillations and various modes of waves, especially in coronal loops, were already numerically studied, see, e.g., Ofman & Wang (2002), De Moortel & Hood (2003), Nakariakov et al. (2004, 2005), Selwa et al. (2005), Jelínek & Karlický (2009, 2010), Konkol et al. (2010), Ofman et al. (2012), Pascoe & De Moortel (2014), Mészárosová et al. (2014). Recent numerical results are summarized by Pascoe (2014).

During the impulsive phase in the "standard" CSHKP solar flare model (Carmichael 1964; Sturrock 1966; Hirayama 1974; Kopp & Pneuman 1976), particle beams, which are accelerated by magnetic reconnection processes in the low corona, propagate downwards along the legs of flare loop and bombard dense chromospheric layers at both its footpoints. Owing to this bombardment, the chromosphere at loop footpoints is rapidly heated and the hard X-ray emission is generated (MacNeice et al. 1984; Mariska & Poland 1985; Fisher et al. 1985a,b,c; Mariska et al. 1989; Karlický 1990; Karlický & Henoux 1992; Hawley & Fisher 1994; Abbett & Hawley 1999; Allred et al. 2005; Brown 1971; Varady et al. 2014).

The chromosphere is also heated by the thermal conduction from a very hot flare plasma (Švestka 1973). However, in the impulsive flare phase, the heating of the chromosphere by the strong particle beams is faster than that by the thermal conduction. Namely, at this flare phase there is not enough hot coronal flare plasma. Thus, the thermal conduction heating of the chromosphere is more important in later flare phases.

Now a question arises: what happens in the flare loop after impulsive heating by particle beams at its footpoints. It is known that the fast and localized heating produces shocks. When these shocks are generated at both loop footpoints then the shocks interact inside the loop. Moreover, the flare loop is a closed system, where shocks can be reflected at boundaries and thus some periodic processes can be expected.

We study just these processes in the present paper. We note that these processes differ from the free oscillations of flare loops that have been studied in previous papers. Similar papers about shocks above and in the post-flare loop have been presented recently by Takasao et al. (2015). But in contrast to the present paper, the authors consider the magnetic reconnection, which is localized above the loop, as a source of the shocks.

In this paper, we consider a symmetric loop described by a two-dimensional (2D) magnetohydrodynamic (MHD) model. Shocks are generated by sudden temperature enhancements at loop footpoints. We study two cases: a) with the same initial perturbation in both loop footpoints (symmetric case) and b) with different perturbations (asymmetric case). We selected perturbations generating the plasma velocities, which are well below Alfvén velocities.

The paper is structured as follows: in Sect. 2, we present our numerical model, including the initial equilibrium and perturbations. The results of numerical simulations and their interpretation are summarized in Sect. 3. Finally, we complete the paper with conclusions in Sect. 4.

2. Model

2.1. Governing equations

Our numerical model describes the gravitationally stratified solar atmosphere, in which the plasma dynamics are described by the 2D, time-dependent ideal MHD equations. We use the FLASH code (Lee & Deane 2009; Lee 2013), where MHD equations are formulated in the conservative form as

$$\frac{\partial \varrho}{\partial t} + \nabla \cdot (\varrho \boldsymbol{v}) = 0, \tag{1}$$

$$\frac{\partial \varrho \boldsymbol{v}}{\partial t} + \nabla \cdot (\varrho \boldsymbol{v}\boldsymbol{v} - \boldsymbol{B}\boldsymbol{B}) + \nabla p_* = \varrho \boldsymbol{g}, \tag{2}$$

$$\frac{\partial \varrho E}{\partial t} + \nabla \cdot [(\varrho E + p_*)\boldsymbol{v} - \boldsymbol{B}(\boldsymbol{v} \cdot \boldsymbol{B})] = \varrho \boldsymbol{g} \cdot \boldsymbol{v}, \tag{3}$$

$$\frac{\partial \boldsymbol{B}}{\partial t} + \nabla \cdot (\boldsymbol{v}\boldsymbol{B} - \boldsymbol{B}\boldsymbol{v}) = 0, \tag{4}$$

$$\nabla \cdot \boldsymbol{B} = 0. \tag{5}$$

Here ϱ is a mass density, $\boldsymbol{v}$ is flow velocity, $\boldsymbol{B}$ is the magnetic field, $\boldsymbol{g} = [0, -g_\odot, 0]$ is the gravitational acceleration with $g_\odot = 274\ \mathrm{ms}^{-2}$. The total pressure p_* is given by

$$p_* = \left(p + \frac{B^2}{2\mu_0}\right), \tag{6}$$

where p is the fluid thermal pressure and B is the magnitude of magnetic field. Specific total energy E in Eq. (3) is expressed as

$$E = \epsilon + \frac{v^2}{2} + \frac{B^2}{2\mu_0 \varrho}, \tag{7}$$

where ϵ is the specific internal energy

$$\epsilon = \frac{p}{(\gamma - 1)\varrho}, \tag{8}$$

with the adiabatic coefficient $\gamma = 5/3$, v is the magnitude of the flow velocity, and $\mu_0 = 1.26 \times 10^{-6}\ \mathrm{Hm}^{-1}$ is the magnetic permeability of free space.

Generally, the terms expressing the radiative losses R_{loss}, thermal conduction T_{cond}, and heating H should be added to the set of MHD equations. In its initial state, it is assumed that the radiative losses and thermal conduction are fully compensated for by the heating H, i.e., $R_{\mathrm{loss}} + T_{\mathrm{cond}} + H = 0$, otherwise the unperturbed atmosphere is not in equilibrium, e.g., owing to the steep temperature gradient in the transition region. Problems appear when the atmosphere is perturbed. Namely, there is no simple expression for the heating term H which, in the unperturbed atmosphere, fully compensates R_{loss} and T_{cond} and, in the perturbed atmosphere, correctly describes the heating. Therefore, for the purpose of our study, we assume that $R_{\mathrm{loss}} + T_{\mathrm{cond}} + H = 0$ is valid during the whole studied processes.

2.2. Initial state

For a still ($\boldsymbol{v} = \boldsymbol{0}$) equilibrium, the Lorentz and gravity forces have to be balanced by the pressure gradient in the entire physical domain

$$-\nabla p + \boldsymbol{j} \times \boldsymbol{B} + \varrho \boldsymbol{g} = \boldsymbol{0}. \tag{9}$$

Assuming a force-free magnetic field, $\boldsymbol{j} \times \boldsymbol{B} = \boldsymbol{0}$, the solution of the remaining hydrostatic equation yields

$$p(y) = p_0 \exp\left[-\int_{y_0}^{y} \frac{1}{\Lambda(\tilde{y})} \mathrm{d}\tilde{y}\right], \tag{10}$$

$$\varrho(y) = \frac{p(y)}{g_\odot \Lambda(y)}. \tag{11}$$

Here

$$\Lambda(y) = \frac{k_{\mathrm{B}} T(y)}{m g_\odot} \tag{12}$$

is the pressure scale-height which, in the case of isothermal atmosphere, represents the vertical distance over which the gas pressure falls off by a factor of e, $k_{\mathrm{B}} = 1.38 \times 10^{-23}\ \mathrm{JK}^{-1}$ is the Boltzmann constant and $\overline{m} = 0.6 m_{\mathrm{p}}$ is the mean particle mass ($m_{\mathrm{p}} = 1.672 \times 10^{-27}$ kg is the proton mass), p_0 in Eq. (10) denotes the gas pressure at the reference level y_{ref}. In our calculations we set and hold fixed $y_{\mathrm{ref}} = 10$ Mm. For the solar atmosphere, we use the temperature profile $T(y)$ as derived by Avrett & Loeser (2008).

The solenoidal condition, $\nabla \cdot \boldsymbol{B} = 0$, is identically satisfied with the implementation of the magnetic flux function, $\boldsymbol{A}$, such as

$$\boldsymbol{B} = \nabla \times \boldsymbol{A}. \tag{13}$$

For the calculation of a 2D magnetic field with symmetric loops, we use $\boldsymbol{A} = [0, 0, A]$ as Konkol et al. (2012) or Jelínek & Murawski (2013):

$$A(x, y) = B_0 \Lambda_B \cos\left(\frac{x - x_0}{\Lambda_B}\right) \exp\left(-\frac{y - y_{\mathrm{ref}}}{\Lambda_B}\right). \tag{14}$$

The magnetic field components (B_x, B_y) are then given by

$$(B_x, B_y) = B_0 \left[-\cos\left(\frac{x - x_0}{\Lambda_B}\right), \sin\left(\frac{x - x_0}{\Lambda_B}\right)\right] \times \exp\left(\frac{y - y_{\mathrm{ref}}}{\Lambda_B}\right). \tag{15}$$

Here B_0 is the magnetic field in the reference level y_{ref} and $\Lambda_B = 2L/\pi$ is the magnetic scale height. We choose the ratio between Alfvén c_{A} and sound c_{s}, speeds as

$$\frac{c_{\mathrm{A}}(x, y_0)}{c_{\mathrm{s}}(y_0)} = \sqrt{\frac{B(x, y_0)}{\gamma \mu_0 p(y_0)}} = 7.07. \tag{16}$$

Table 1. Coordinates of selected detection points, and Alfvén v_A and sound c_s speeds in the initial state at these points.

Detection point	x_D (Mm)	y_D (Mm)	v_A (km s^{-1})	c_s (km s^{-1})
Corona				
1	2.80	4.23	1455	119
2	3.70	5.29	1389	129
3	4.60	6.15	1324	134
4	5.50	6.80	1266	137
5	6.40	7.29	1222	139
6	7.30	7.65	1184	141
7	8.20	7.91	1154	142
8	9.10	8.11	1124	143
9	10.0	8.25	1124	143
10	14.50	6.80	1266	137
Chromosphere				
A	1.00	1.50	83	13.5
B	1.09	1.65	103	13.5
C	1.18	1.80	127	13.5

The plasma β is defined as

$$\beta(x, y) = \frac{p}{p_{\rm mag}} = \frac{2}{\gamma}\left(\frac{c_s}{c_A}\right)^2 . \tag{17}$$

2.3. Perturbations

To generate an evaporation process, at the start of the numerical simulation ($t = 0$ s), the equilibrium in the chromosphere is perturbed by the Gaussian pulse in the temperature (pressure) and has the following form:

$$T = T_0\left[1 + \mathcal{A}\cdot\exp\left\{-\frac{(x - x_{\rm P})^2}{\lambda_x^2}\right]\cdot\exp\left[-\frac{(y - y_{\rm P})^2}{\lambda_y^2}\right]\right\}, \tag{18}$$

where T_0 is the initial temperature, $\mathcal{A}$ is the initial amplitude of the pulse, and λ_x, and λ_y are the widths of the temperature pulse in x and y directions, respectively.

2.4. Wavelet method

For the wavelet analysis we used the Morlet wavelet, which consists of a plane wave modulated by a Gaussian:

$$\Psi(t) = \pi^{-1/4}\exp^{({\rm i}\sigma t)}\exp^{-(t^2/2)}, \tag{19}$$

where the parameter σ allows a trade between time and frequency resolutions. Here we assumed the value of parameter $\sigma = 6$, as recommended by Farge (1992). More details about the wavelet method and its implementation can be found on the web page of R. Sych (`http://pwf.iszf.irk.ru/`) and in the paper by Torrence & Compo (1998).

2.5. Numerical code

To solve the MHD Eqs. (1)–(4), we use the FLASH code, which is well tested, fully modular, parallel, multiphysical, open science, simulation code that implements second- and third-order unsplit Godunov solvers with various slope limiters and Riemann solvers, as well as adaptive mesh refinement (AMR; Chung 2002). The Godunov solver combines the corner transport upwind method for multi-dimensional integration and the constrained transport algorithm for preserving the divergence-free constraint on the magnetic field (Lee & Deane 2009). We used the minmod slope limiter and the Riemann solver (Toro 2006). The main advantage of using the AMR technique is to refine a numerical grid at steep spatial profiles while keeping a coarse grid at the places where fine spatial resolution is not essential. In this case, the AMR strategy is based on controlling the numerical errors in a gradient of mass density that leads to the reduction of the numerical diffusion within the entire simulation region.

For our numerical simulations, we use a 2D Eulerian box of its height $H = 10$ Mm and width $W = 20$ Mm. The spatial resolution of the numerical grid is determined with the AMR method. We use the AMR grid with the minimum (maximum) level of the refinement blocks set to 3 (7). The whole simulation region is covered by 2626 blocks. Since every block consists of 8×8 numerical cells, this number of blocks corresponds to 168 064 numerical cells and the smallest spatial resolution is $\Delta x = \Delta y = 3.9$ km.

At all boundaries, we fix all plasma quantities to their equilibrium values using fixed-in-time boundary conditions, which lead to only negligibly small numerical reflections of incident wave signals.

3. Numerical results

To present our results, we selected the detection points shown in Table 1, where their locations and Alfvén and sound velocities in the initial state at these points are shown. These detection points are distributed along the axis of the loop, which is expressed by the red magnetic field line in Fig. 1.

The detection points 1−9 are in the coronal part and in the left side of the loop. Detection point 9 is at the top of the loop. Namely, in the symmetric case, plasma processes in the loop are symmetric. The detection point 10 is chosen for the asymmetric case, and is located at the right side of the loop, symmetrically to detection point 4. To study associated processes in the chromosphere, under the perturbation point, we also selected detection points A, B, and C.

We consider two perturbation points P_1 and P_2 at the transition region. They are located at $x_{\rm P}^1 = 1.45$ Mm, $y_{\rm P}^1 = 2.25$ Mm,

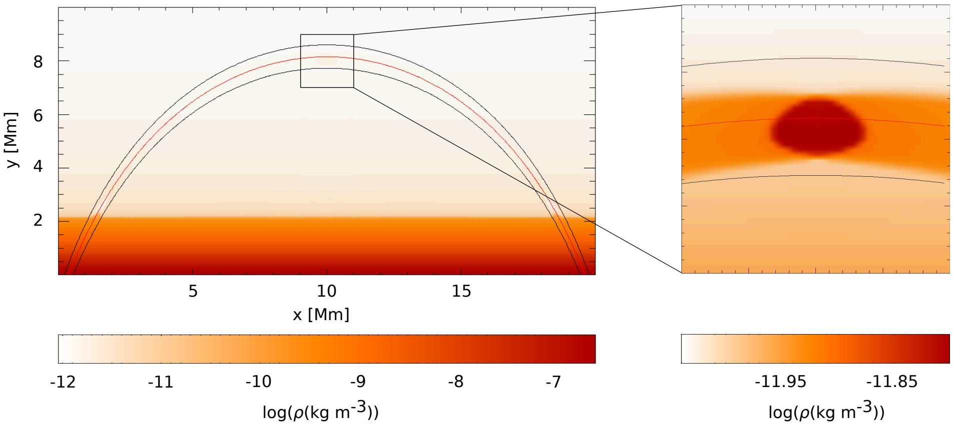

Fig. 1. Spatial distribution of plasma mass density at $t = 71$ s. At this time we observe maximal compression of the plasma at the *top* of the loop (see the zoomed part) owing to the collision of shocks generated by the temperature (pressure) enhancements at loop footpoints. The solid curved lines show representative magnetic field lines. The red one determines the magnetic field line along the loop axis.

Table 2. Parameters of perturbations in computational runs.

Run	$x_{\rm PL}$ (Mm)	$y_{\rm PL}$ (Mm)	$x_{\rm PR}$ (Mm)	$y_{\rm PR}$ (Mm)	$\mathcal{A}_{\rm PL}$	$\mathcal{A}_{\rm PR}$	λ_x (Mm)	λ_y (Mm)
I	1.45	2.25	18.55	2.25	14	14	0.1	0.1
II	1.45	2.25	18.55	2.25	7	7	0.1	0.1
III	1.45	2.25	18.55	2.25	7	3.5	0.1	0.1
IV	1.45	2.25	18.55	2.25	14	14	0.1	0.05

Notes. $\mathcal{A}$ is the perturbation amplitude, x and y are the coordinates. The index PL and PR means the perturbation at the left-side and right-side loop footpoint, respectively, see Fig. 1.

and at $x_{\rm P}^2 = 18.55$ Mm, $y_{\rm P}^2 = 2.25$ Mm, i.e., at both the loop footpoints.

In the symmetric case, the temperature perturbation amplitude is chosen as $\mathcal{A} = 14$ or 7 at both footpoints $\rm P_1$ and $\rm P_2$ and, in the asymmetric case, as $\mathcal{A} = 7$ at $\rm P_1$ and $\mathcal{A} = 3.5$ at $\rm P_2$.

As shown in Table 2, where the parameters of perturbations are summarized, we made several numerical runs. Owing to the similarity of their results, we present here mainly the results of Run I.

In Fig. 1, we show an example of the spatial distribution of the plasma density for Run I with the same perturbations at both loop footpoints (symmetric case), at $t = 71$ s, i.e., at the time of maximal plasma compression at the loop top region. The spatial profiles of the density, velocity, temperature, and magnetic field along the loop axis at the same time are presented in Fig. 2. Comparing these profiles with those in the initial state (dashed lines in Fig. 2) show how dense and hot plasma moves from the transition region to the low corona.

3.1. Quasi-periodic processes in the coronal part of the loop

Now, let us look in more detail at processes in the coronal part of the loop, i.e., at the region with the coordinates $y \geq 2$ Mm.

Analyzing Figs. 1 and 2, we can see that, at the time $t = 71$ s at the top of the loop, a region with plasma that is denser and hotter than the surrounding plasma is formed. This happens owing to the plasma compression during the collision of the shocks moving upwards from both loop footpoints. This region is transient, but it appears periodically with the repeated collisions of the shocks at the top of the flare loop (see the processes described in the following).

The global time evolution of the processes in the corona after the perturbation initiation is shown in Fig. 3, where the time-distance diagram of the mass density along the loop axis is shown. As can be seen in Figs. 2 and 3, after the initiation of temperature perturbations at both footpoints, the heated plasma from the transition region is evaporated to coronal parts of the loop and counter-streaming evaporation shocks are formed. These shocks collide at the top of the loop at $t = 71$ s. In the following times, the shocks continue in their motion to the transition region at the opposite side of the loop, where they are reflected back to the corona (at $t \approx 150$ s), and so on (Fig. 3).

At first, the shocks propagate with a velocity slightly greater than the local sound velocity, see Table 1. Considering their velocity and corresponding plasma flow velocities (Fig. 4), we found that the shocks are of the blast type. Using the relation (Priest 1982)

$$\frac{v_2}{v_1} = \frac{2 + (\gamma - 1)M_{\rm s}^2}{(\gamma + 1)M_{\rm s}^2}, \tag{20}$$

where v_1 and v_2 are the inflow and outflow plasma velocities in the shock frame, we determined the Mach number, $M_{\rm s}$, of these shocks along the loop and in the time interval 40−70 s as about 1.1. Afterwards, their Mach number decreases and shocks slowly change to waves (see the quasi-periodic variations of the plasma velocity, temperature and plasma density at three detection points 5, 7, and 9 in Fig. 4).

During these processes, which are with the low plasma beta parameter, the magnetic field changes only very weakly, see the

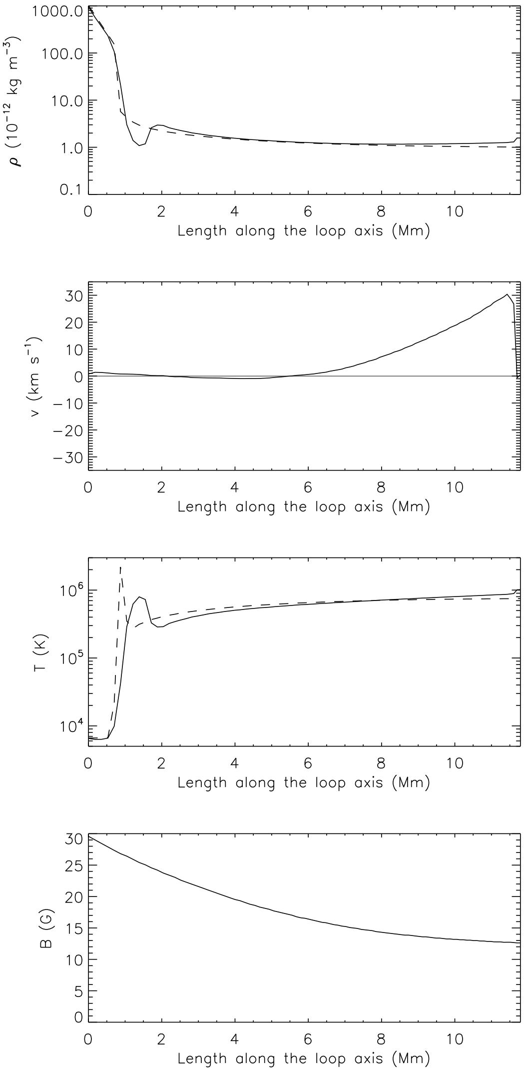

Fig. 2. Profiles of the mass density, velocity, temperature, and magnetic field along the loop axis from the detection point A to the top of the loop at 71 s (i.e., at the same time as in Fig. 1 – full line) and at the initial state with the pressure (temperature) perturbation (dashed line).

time profile of the magnetic field at the top of the loop in Fig. 5. Here, the most distinct change in the magnetic field was detected at the first arrival of the shock at t = 71 s (~0.5 G). Later the amplitude of the magnetic field variation decreases. The amplitude of the magnetic field variation is in the anti-phase to the pressure variation. It shows that these shocks and waves (after ~500 s) are of slow magnetosonic mode.

As already mentioned, at the top of the loop, a region with enhanced temperature and density is periodically formed owing to shock collisions. We propose that this region could be observed in the soft X-rays or EUV lines as a periodic and transient loop-top source. For example, the X-ray bremsstrahlung thermal emission $I(\epsilon_x)$ is proportional to (Tandberg-Hanssen & Emslie 1988)

$$I(\epsilon_x) \sim \frac{n_e^2 V}{\epsilon_x T^{1/2}} \exp(-\epsilon_x/k_B T), \tag{21}$$

where, ϵ_x is the X-ray photon energy, n_e is the plasma density, T is the plasma temperature, V is the region volume, and k_B is the Boltzmann constant. In our case, considering the emission from the constant volume element, we computed the relative X-ray emission intensity (the X-ray emission intensity in ratio to its initial value) at the top of the loop for ϵ_x = 1.549 keV (8 Å), see Fig. 6. As shown here, at t = 71 s (the time of the maximum plasma compression at the loop-top region), the increase in the relative intensity of the X-ray emission is about 1000. This relatively high value is due to the fact that the plasma temperature at the top of the loop is relatively low and the X-ray photon energy ϵ_x = 1.549 keV corresponds to a very steep part of the X-ray spectrum.

Analyzing these quasi-periodic processes further, we recognize a further aspect of these processes that could be observed. Figure 7 presents the pressure variations in nine detection points along the left side of the loop (Table 1). While at the top of the loop (the uppermost profile – detection point 9) there is a simple variation, at detection points in the loop leg variations are more complex; the double peak with the shorter period appears. By increasing the distance of the detection point in the loop leg from the top of the loop, the time interval between peaks in the double peak increases. To explain this effect, we note that each peak in Fig. 7 indicates a passage of the shock through some detection point. One shock arrival to the loop-top detection point is always connected with two shock passages (shock propagating up and shock propagating down) at the loop-leg detection points. Clearly, increasing the distance of the detection point in the loop leg from the top of the loop, the time interval between shock passages increases. From a diagnostic point of view, this means that, in the signal from the loop leg, a shorter period in these processes also appears.

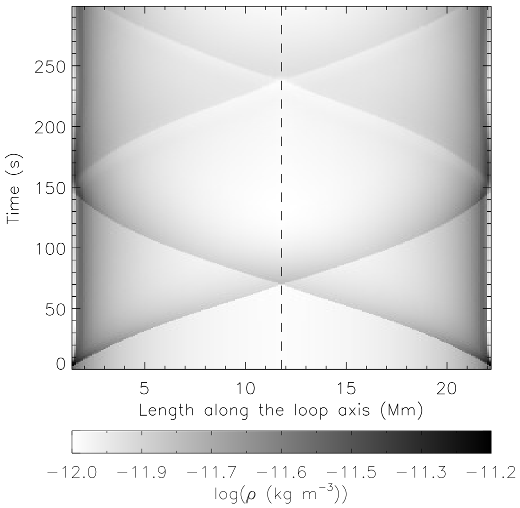

Fig. 3. Time-distance diagram of the mass density along the loop axis in the coronal part of the loop for Run I. The vertical dashed line expresses the loop top position.

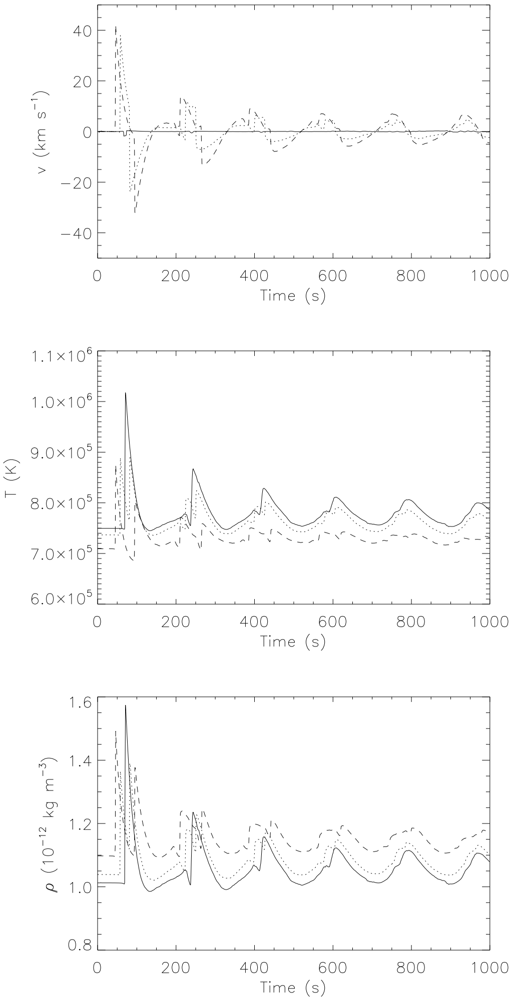

Fig. 4. Time profiles of the plasma velocity, temperature, and mass density at the detection points: 9 (top of the loop; full line), 7 (dotted line), and 5 (dashed line) in the time interval 0−1000 s.

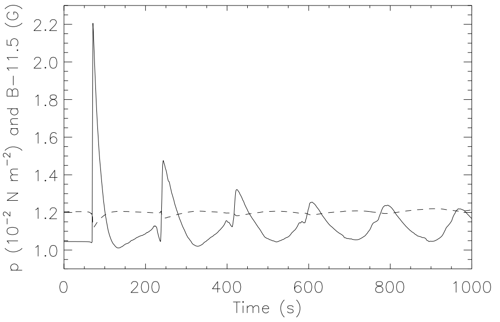

Fig. 5. Comparison of time profiles of the pressure p (full line) and magnetic field B (dashed line) at the top of the loop (detection point 9).

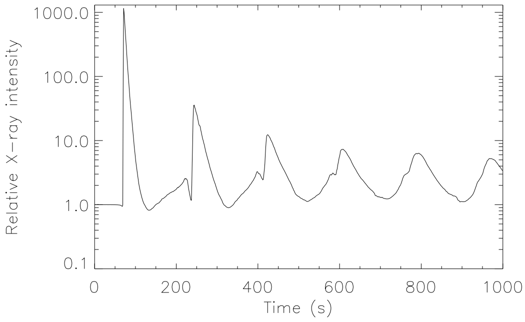

Fig. 6. Time profile of the relative X-ray emission intensity at the top of the loop (detection point 9) for the energy ϵ_x = 1.549 keV (8 Å).

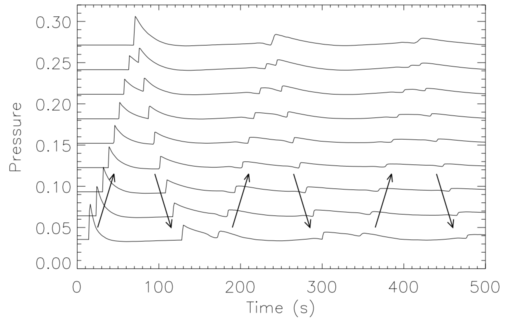

Fig. 7. Series of pressure evolution profiles at nine detection points: From the bottom, the profile at point 1 up to the profile at point 9 (top of the loop) in the time interval 0−1000 s. The arrows show trajectories of shocks.

To show this, we analyzed the pressure variations at the top of the loop (detection point 9) and at the loop leg (detection point 4) by the wavelet technique. The first and the strongest peak in these variations is close to the beginning of the time series, see Fig. 5. To eliminate the edge effects in computed wavelet spectra, we added data with unperturbed pressures (lasting 300 s) before the computed time series. As a result, the analyzed time series now lasts 1300 s.

The results of the wavelet analysis are presented in Fig. 8. As shown in Fig. 8 (upper part) the dominant period of the pressure variation at the top of the loop (detection point 9) is of about 170 s. On the other hand, in Fig. 8 (bottom part) the dominant period of pressure variation at the loop leg (detection point 4) is shorter (~80 s). However, this shorter period is accompanied by the same period as that in the loop-top detection point, but with a lower power.

3.2. Quasi-periodic processes in the chromosphere

Pressure perturbations at loop footpoints generate not only shocks in the coronal part of the loop, but the perturbation also propagates downwards in chromospheric layers, as presented in Fig. 9. An analysis shows that the perturbation is the sound wave propagating with a sound speed of about 13.5 km s^{-1}. During its downward propagation, the chromospheric plasma is heated from ~6500 K up to ~9000 K. Simultaneously, the plasma moves downwards with a velocity of up to ~5 km s^{-1}.

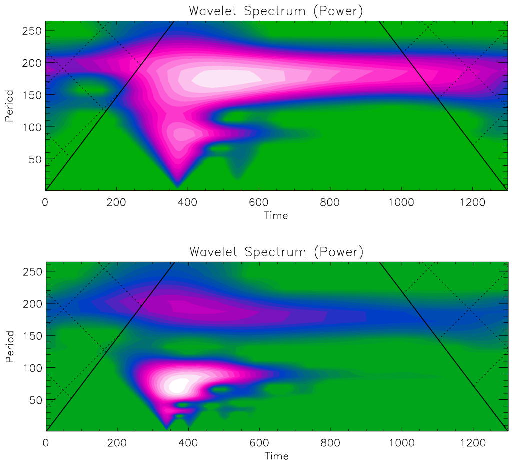

Fig. 8. Wavelet spectrum of the pressure variation at detection point 9 (top of the loop; *upper part*), and at detection point 4 (*bottom part*), symmetric case (Run I). For the periods, see the pink areas. The period and time are in seconds. The hatched regions belong to the cone of influence by edge effects owing to finite-length time series.

After this process, there is the phase with temperature decreases and upward plasma velocities. All these processes repeat in correspondence with the quasi-periodic processes in the coronal part of the loop.

3.3. Comparison of results obtained in different numerical runs

In this paper, we mainly present the results obtained from Run I. Other runs give similar results. For example, the change in the form of the perturbation in Run IV provides only a small decrease in the shock amplitudes, otherwise the results are very similar to Run I.

The most distinct change can be found when comparing Run II (symmetric case) and Run III (asymmetric case). While in the symmetric case, at the symmetrically taken detection points (4 and 10, see Table 1), the time profiles of the pressure, temperature, and plasma density are the same, in the asymmetric case they differ, see Fig. 10. Here the time profiles of the pressure for Run III (asymmetric case) at the detection points 4 and 10 are shown. As can be seen, the shock generated in the left-side loop leg (detected at detection point 4 at the time 42 s) is stronger and appears earlier than that in the right-side loop leg (detected at detection point 10) owing to the higher amplitude of the temperature perturbation at the left-side loop footpoint than that in the right-side loop footpoint. In the following time (at about 120 s) it is the reverse. This is due to that after the interaction of the shocks near the top of the loop, the shocks continue in their motion to the opposite side of the loop, where they are then reflected at the transition region, and so on.

To show these processes in more detail, we computed the time-distance diagram of the mass density along the loop axis in the coronal part of the loop (Fig. 11). Compared to the symmetric case (Fig. 3), the location of the shock interaction is shifted outside of the loop top position. We note that the position of the first shock interaction is on the right side, outside of the loop top position, and the position of the second shock interaction is on the left side, outside the loop top position.

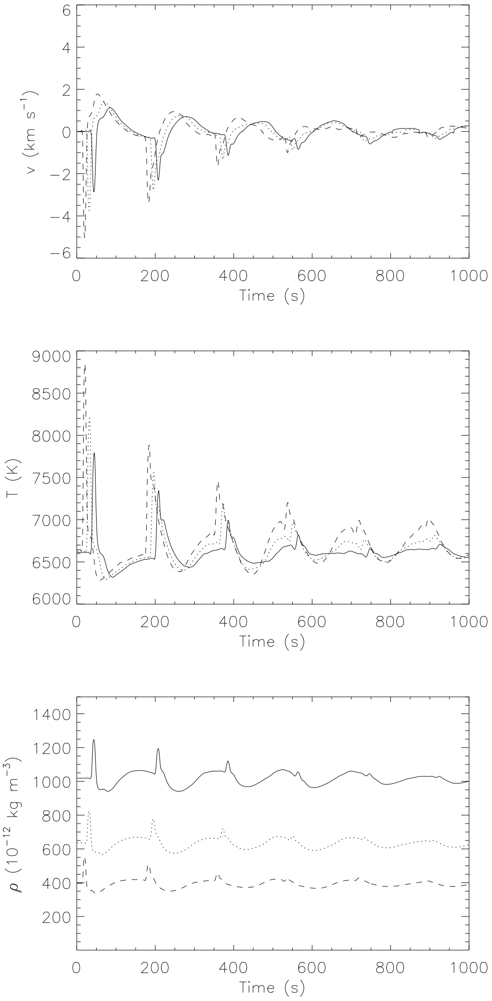

Fig. 9. Time profiles of the plasma velocity, temperature, and mass density at the detection points: A (full line); B (dotted line); and C (dashed line) in the time interval 0−1000 s.

Similar to the symmetric case, we present the wavelet spectra of the pressure variation (Fig. 12). They are computed for the detection point 4 and 10, i.e., symmetrically to the top of the loop. They differ not only in dominant periods in the interval 50−100 s, but the period of about 200 s is only in the wavelet spectrum from detection point 4. These spectra also differ from the wavelet spectrum at detection point 4 for the symmetric case (Fig. 8). We note that, in different detection points, the wavelet spectra can be different.

4. Conclusions

We studied processes in the flare loop after sudden temperature enhancements at loop footpoints. After the initiation of

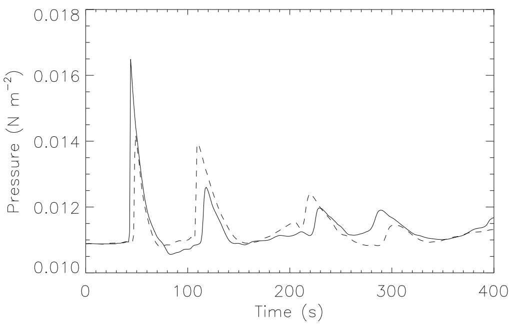

Fig. 10. Time profiles of the pressure for Run III (asymmetric case) at detection points 4 (full line) and 10 (dashed line) in the time interval 0−1000 s.

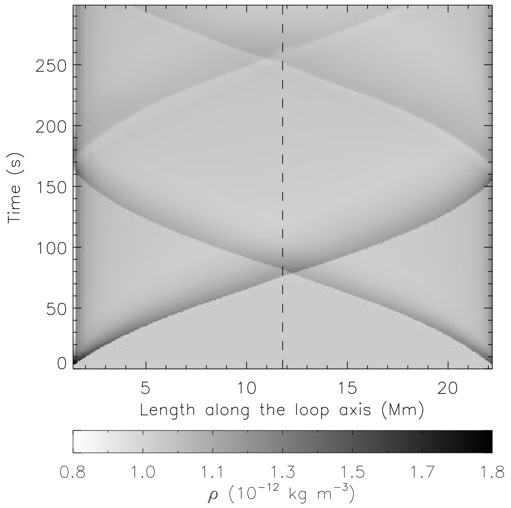

Fig. 11. Time-distance diagram of the mass density along the loop axis for Run III (asymmetric case). The vertical dashed line shows the loop top position.

temperature (pressure) perturbations at loop footpoints, blast shocks that propagate upwards along the loop are generated. In our case, at the beginning of these processes, at t = 40−70 s, the Mach number of these shocks is $M_{\rm s} \sim 1.1$. At the top of the loop, these shocks collide and compress the plasma, forming the region with enhanced plasma density and temperature, see also Falewicz et al. (2015). In the symmetric case, this compressed region appears at the top of the loop, and in the asymmetric case this region is slightly shifted outside of the top of the loop. Although, this compressed region is only transient, it could explain some observed soft X-ray or EUV loop-top sources. Owing to the periodic arrival of shocks to the top of the loop, these loop-top sources should appears periodically. Moreover if, in the loop, some superthermal electrons are trapped, then this transient loop-top region can be observed even in hard X-rays, as was shown by Karlický & Henoux (1994).

After the interaction of these shocks at the top of the loop, the shocks continue in their motion downwards to the transition region on the opposite side of the loop, where they are reflected

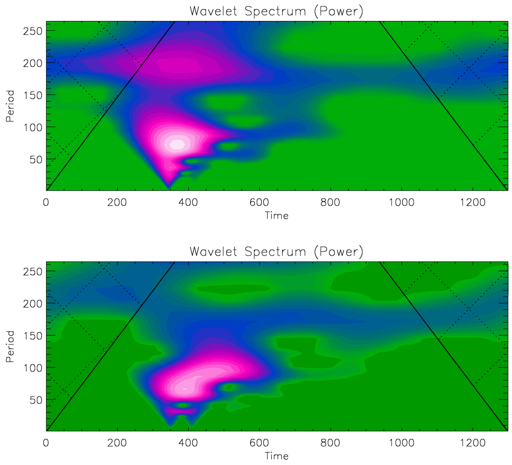

Fig. 12. Wavelet spectrum of the pressure variation at detection point 4 (*upper part*) and 10 (*bottom part*; located symmetrically in the left- and right-side of the loop, see Table 1), asymmetric case (Run III). The period and time are in seconds. The hatched regions belong to the cone of influence by edge effects, owing to finite-length time series.

back to the coronal part of the loop, and so on. These processes generate variations (forced oscillations) of plasma parameters in the flare loop. In a later phase of these processes (after about 500 s), the shocks slowly change to waves. In our case, however, the magnetic field varies very weakly in the anti-phase to the pressure variations. This shows that the presented shocks and waves are of slow magnetosonic mode. It would appear that this type of plasma variations was recently recognized in the EUV observations of the 20 July 2013 flare by Kumar et al. (2015).

In the symmetric loop, which has a length of approximately 21.5 Mm, using the wavelet spectral technique, we found variations in the range of 40−170 s. This shows that the period of these variations depends on the detection point location. While the simplest variations are found at the top of the loop with the dominant period of about ~170 s, at the detection point in the loop leg (detection point 4) the dominant period is shorter (~80 s). Considering the loop length ($L \sim 21.5$ Mm) and the sound speed in the corona ($c_{\rm s} \sim 130$ km s^{-1}), the period found at the top (170 s) can be described by $\sim L/c_{\rm s} = 165$ s. Similarly, the period found in the leg (80 s) can be explained by $\sim L/2c_{\rm s} = 82.5$ s. The factor 2 is due to the contribution of both of the slow shocks.

Increasing the distance in the detection point in the loop leg from the loop top, the time interval between peaks in the double peak increases (Fig. 7). This is due to two passages of shocks through the loop-leg detection point (the shock propagation upward and downward).

In the asymmetric case, the plasma variations and corresponding wavelet spectra are even more complex. The displacement of the interaction point near the loop top is small in spite of the large difference in the amplitude of the initial disturbance between the two foot points. This is because the Mach number of the two shocks is close to unity and they propagate with a similar speed.

We also found that the quasi-periodic processes in the coronal part of the loop are closely associated with processes in the chromospheric layers, located below the perturbation locations.

Here, we found variations in the temperature, plasma velocities, and plasma densities that propagated with the sound velocity ($\sim$13.5 km s^{-1}). These quasi-periodic variations certainly change intensities and produce Doppler shifts of the optical chromospheric lines, which means that these processes should be observable.

Acknowledgements. The authors thank the referee for constructive comments that improved the paper. M.K. and P.J. acknowledge support from Grants P209/12/0103 and 16-13277S of the Grant Agency of the Czech Republic and European grant FP7-SPACE-2013-1 F-CHROMA (No. 606862) and the Marie Curie FP7-PIRSES-GA-2011-295272 RadioSun project. The authors also express their thanks to Prof. Kris Murawski for valuable discussions and Dr. Robert Sych for his wavelet package `http://pwf.iszf.irk.ru/`. The FLASH code used in this work was developed by the DOE-supported ASC/Alliances Center for Astrophysical Thermonuclear Flashes at the University of Chicago.

References

Abbett, W. P., & Hawley, S. L. 1999, ApJ, 521, 906
Allred, J. C., Hawley, S. L., Abbett, W. P., & Carlsson, M. 2005, ApJ, 630, 573
Avrett, E. H., & Loeser, R. 2008, ApJS, 175, 229
Brown, J. C. 1971, Sol. Phys., 18, 489
Carmichael, H. 1964, NASA SP, 50, 451
Chung, T. J. 2002, Computational Fluid Dynamics (Cambridge, UK: Cambridge University Press)
De Moortel, I., & Hood, A. W. 2003, A&A, 408, 755
Falewicz, R., Rudawy, P., Murawski, K., & Srivastava, A. K. 2015, ApJ, 813, 70
Farge, M. 1992, Ann. Rev. Fluid Mech., 24, 395
Fárník, F., Karlický, M., & Švestka, Z. 2003, Sol. Phys., 218, 183
Fisher, G. H., Canfield, R. C., & McClymont, A. N. 1985a, ApJ, 289, 434
Fisher, G. H., Canfield, R. C., & McClymont, A. N. 1985b, ApJ, 289, 425
Fisher, G. H., Canfield, R. C., & McClymont, A. N. 1985c, ApJ, 289, 414
Hawley, S. L., & Fisher, G. H. 1994, ApJ, 426, 387
Hirayama, T. 1974, Sol. Phys., 34, 323
Huang, J., Tan, B., Zhang, Y., Karlický, M., & Mészárosová, H. 2014, ApJ, 791, 44
Jelínek, P., & Karlický, M. 2009, Eur. Phys. J. D, 54, 305
Jelínek, P., & Karlický, M. 2010, IEEE Transactions on Plasma Science, 38, 2243
Jelínek, P., & Murawski, K. 2013, MNRAS, 434, 2347
Karlický, M. 1990, Sol. Phys., 130, 347
Karlický, M., & Henoux, J.-C. 1992, A&A, 264, 679
Karlický, M., & Henoux, J.-C. 1994, A&A, 283, 202
Karlický, M., Zlobec, P., & Mészárosová, H. 2010, Sol. Phys., 261, 281
Konkol, P., Murawski, K., Lee, D., & Weide, K. 2010, A&A, 521, A34
Konkol, P., Murawski, K., & Zaqarashvili, T. V. 2012, A&A, 537, A96
Kopp, R. A., & Pneuman, G. W. 1976, Sol. Phys., 50, 85
Kumar, P., Nakariakov, V. M., & Cho, K.-S. 2015, ApJ, 804, 4
Kupriyanova, E. G., Melnikov, V. F., Nakariakov, V. M., & Shibasaki, K. 2010, Sol. Phys., 267, 329
Lee, D. 2013, J. Comput. Phys., 243, 269
Lee, D., & Deane, A. E. 2009, J. Comput. Phys., 228, 952
MacNeice, P., Burgess, A., McWhirter, R. W. P., & Spicer, D. S. 1984, Sol. Phys., 90, 357
Mariska, J. T., & Poland, A. I. 1985, Sol. Phys., 96, 317
Mariska, J. T., Emslie, A. G., & Li, P. 1989, ApJ, 341, 1067
Mészárosová, H., Karlický, M., Rybák, J., Fárník, F., & Jiřička, K. 2006, A&A, 460, 865
Mészárosová, H., Karlický, M., Jelínek, P., & Rybák, J. 2014, ApJ, 788, 44
Nakariakov, V. M., & Melnikov, V. F. 2009, Space Sci. Rev., 149, 119
Nakariakov, V. M., Tsiklauri, D., Kelly, A., Arber, T. D., & Aschwanden, M. J. 2004, A&A, 414, L25
Nakariakov, V. M., Pascoe, D. J., & Arber, T. D. 2005, Space Sci. Rev., 121, 115
Nakariakov, V. M., Foullon, C., Verwichte, E., & Young, N. P. 2006, A&A, 452, 343
Nakariakov, V. M., Inglis, A. R., Zimovets, I. V., et al. 2010, Plasma Physics and Controlled Fusion, 52, 124009
Nisticò, G., Pascoe, D. J., & Nakariakov, V. M. 2014, A&A, 569, A12
Ofman, L., & Wang, T. 2002, ApJ, 580, L85
Ofman, L., Wang, T. J., & Davila, J. M. 2012, ApJ, 754, 111
Pascoe, D. J. 2014, RA&A, 14, 805
Pascoe, D. J., & De Moortel, I. 2014, ApJ, 784, 101
Priest, E. R. 1982, Solar magneto-hydrodynamics (Dordrecht, Holland: D. Reidel Pub.), 195
Roberts, B., Edwin, P. M., & Benz, A. O. 1984, ApJ, 279, 857
Selwa, M., Murawski, K., & Solanki, S. K. 2005, A&A, 436, 701
Sturrock, P. A. 1966, Nature, 211, 695
Takasao, S., Matsumoto, T., Nakamura, N., & Shibata, K. 2015, ApJ, 805, 135
Tan, B. 2008, Sol. Phys., 253, 117
Tandberg-Hanssen, E., & Emslie, A. G. 1988, The physics of solar flares (Cambridge, New York, USA: Cambridge Uni. Press), 114
Toro, E. F. 2006, Int. J. Numerical Methods in Fluids, 52, 433
Torrence, C., & Compo, G. P. 1998, Bull. Am. Met. Soc., 79, 61
Švestka, Z. 1973, Sol. Phys., 31, 389
Varady, M., Karlický, M., Moravec, Z., & Kašparová, J. 2014, A&A, 563, A51
Wang, T. J., Solanki, S. K., Innes, D. E., & Curdt, W. 2005, A&A, 435, 753